

Development of Advanced Numerical Tools for Dynamic Analysis of Aquaculture Structures

by

Hui Cheng

Thesis submitted in fulfilment of
the requirements for the degree of
PHILOSOPHIAE DOCTOR
(PhD)



Faculty of Science and Technology
Department of Mechanical and Structural Engineering
and Materials Science
2022

University of Stavanger
NO-4036 Stavanger
NORWAY
www.uis.no

©2022 Hui Cheng

ISBN: 978-82-8439-078-9

ISSN: 1890-1387

PhD: Thesis UiS No. 641

谨以此文献给我的家人、导师、同行和朋友们

To my family, supervisors, peers in fisheries and aquaculture engineering, and friends.

程晖

Hui Cheng

Preface

This thesis is submitted in partial fulfillment of the requirements for the degree of Doctor of Philosophy (PhD) at the University of Stavanger (UiS), Norway. The research work has been carried out at the Faculty of Science and Technology, Department of Mechanical and Structural Engineering and Material Science, in the period from September 2018 to April 2022. This PhD project was funded by the University of Stavanger.

Hui Cheng

2022

Acknowledgments

First and foremost, I would like to express my sincere gratitude to my main supervisor, Prof. Muk Chen Ong, who offered me the PhD position. His continuous support, stringent guidance and careful training were the keys to the accomplishment of this PhD research. It was a great pleasure and honor to work under his supervision. The deep, interesting, and sometimes intense discussions on broad topics will become priceless memories of my life.

I would like to thank my co-supervisors, Assoc. Prof. Lin Li and Assoc. Prof. Karl Gunnar Aarsæther. Their knowledge and experiences are essential for every breakthrough in my research. The rich and plentiful discussions on the hydrodynamics of aquaculture structures were fascinating, and I am extremely grateful to have been able to work with them during my time in Norway. And besides, I learned a lot of practical programming skills during my stay in Tromsø, which now is my most visited city in Norway.

I would like to thank Asst. Prof. Hao Chen from the University of Glasgow. He generously shared his knowledge and codes about the porous media model for aquaculture nets. His excellent previous works contributed considerable contents and ideas to my PhD research. I would also like to thank Digvijay Patankar from the Indian Institute of Technology, Jean Pierre Aubry from La Machine and the anonymous in the Code_Aster forum for providing help in using Code_Aster.

I would like to thank Prof. Liuyi Huang, who was the first to bring me into the fisheries and aquaculture engineering field. His philosophy of life and strict research attitude are always my pursuits. I would also like to express my appreciation to Prof. Fenfang Zhao for her considerate company during my first year in Norway. The start-up phase of my PhD study would never be such smooth and easy without your help. Moreover, the badminton skills you taught me are indeed useful in my later exercises.

I would like to thank Prof. Yongchun Yang for his visit. His recipe for the pan-fried steamed bun always reminds me of the taste from home. I would also like to thank my friend Xuesong Bai for his generous sponsorship, so I could attend the Aqua Nor exhibition at Trondheim together with a large group of experts. Their industrial perspectives considerably improved the applicability of my PhD study.

I would like to thank my colleagues and friends who created a joyful and motivating environment. The knowledge sharing among PhD and post-doctoral fellows at the Marine Advanced Computation (MAC) group created a great chance to learn from different research fields.

Finally, many thanks to my family and friends for their encouragement, understanding and support during the time I studied abroad, especially during the COVID period.

Abstract

Numerical methods to accurately predict dynamic responses of marine aquaculture structures are essential in the engineering design process, because these structures can be subjected to large wave and current loads in the ocean environment, which causes complex structural motion and deformation. However, only a few numerical programs for the dynamic analysis of aquaculture structures can be accessed by the public without permission.

In order to meet the high demand for a ready-for-use program, a numerical module for an open-source Finite Element Analysis (FEA) program, Code_Aster, is developed in this PhD study. This numerical module includes various wave models (*e.g.*, Airy waves, Stokes 2nd order waves and irregular waves) and hydrodynamic force models (*e.g.*, Morison model, Screen model and flow velocity reduction due to wake effects). Moreover, a coupling algorithm to handle the wake effects of thin, flexible and highly permeable structures with complex geometries is also implemented to solve the complex fluid-structure interaction (FSI) problem in marine aquaculture engineering. The accuracy of structural response prediction can be improved using the coupling algorithm with the open-source Computational Fluid Dynamics (CFD) solver, OpenFOAM, which can solve the complex flow field around the structures. Detailed verifications and validations are firstly conducted with considerations of different net solidities, inflow angles, incoming current velocities and net dimensions. Subsequently, the newly

developed numerical module is applied to study dynamic responses of traditional fish cages, grid moored fish farms and a large semi-submersible aquaculture structure for practical engineering design and optimization purposes.

The structural responses of traditional fish cages with different design parameters (including circumferences of floating collar, depths of net bag, submerged weights) are comprehensively analyzed under pure current conditions. Based on the parametric analysis with a large number of numerical simulations, regression functions for the most concerning aspects are provided for engineering usages in the design process. These regression functions can save considerable time for experiments and numerical simulations in the design of traditional fish cages.

The structural responses of grid moored fish farms are analyzed with respect to combinations of mooring line breakages and current directions. Based on the numerical results, suggestions to improve the design of the mooring system are given. It is also recommended to monitor the positions of buoys during in-situ operations. When one of the mooring line breaks, the maximum tension increment in the mooring system can be estimated based on the displacement of the buoys. This estimation can help the farmer to decide whether the damaged mooring line should be repaired immediately.

The global responses of a semi-submersible offshore aquaculture structure are investigated under irregular waves and current conditions

which correspond to a return period of 50 years. The numerical model shows a reasonable agreement with published experimental results and demonstrates that the newly developed numerical module can be applied to the dynamic analysis of offshore aquaculture structures.

List of publications

List of research papers presented in the thesis

1. **Cheng, H.**, Li, L., Aarsæther, K.G., Ong, M.C., 2020. Typical hydrodynamic models for aquaculture nets: A comparative study under pure current conditions. *Aquacultural Engineering* 90, 102070.
<https://doi.org/10.1016/j.aquaeng.2020.102070>
2. **Cheng, H.**, Li, L., Ong, M.C., Aarsæther, K.G., Sim, J., 2021. Effects of mooring line breakage on dynamic responses of grid moored fish farms under pure current conditions. *Ocean Engineering* 237, 109638.
<https://doi.org/10.1016/j.oceaneng.2021.109638>
3. **Cheng, H.**, Ong, M.C., Li, L., Chen, H., 2022. Development of a coupling algorithm for fluid-structure interaction analysis of submerged aquaculture nets. *Ocean Engineering* 243, 110208.
<https://doi.org/10.1016/j.oceaneng.2021.110208>
4. **Cheng, H.**, Li, L., Ong, M.C., 2022. Comparative study of five commonly used gravity type fish cages under pure current conditions. *Ocean Engineering* 250, 110977.
<https://doi.org/10.1016/j.oceaneng.2022.110977>
5. **Cheng, H.**, Ong, M.C., Li, L., 2022. Dynamic simulations of an offshore aquaculture structure under combined wave and current conditions. (OMAE2022, accepted)

List of research papers not included in the thesis

1. **Cheng, H.**, Aarsæther, K.G., Li, L., Ong, M.C., 2020. Numerical Study of a Single-Point Mooring Gravity Fish Cage with Different Deformation-Suppression Methods. *Journal of Offshore Mechanics and Arctic Engineering* 142, 041301. <https://doi.org/10.1115/1.4046115>
2. Sim, J., **Cheng, H.**, Aarsæther, K.G., Li, L., Ong, M.C., 2021. Numerical Investigation on the Cage-to-Cage Wake Effect: A Case Study of a 4×2 Cage Array. *Journal of Offshore Mechanics and Arctic Engineering* 143, 051301. <https://doi.org/10.1115/1.4049831>
3. Mjåtveit, M.A., **Cheng, H.**, Ong, M.C., Lee, J., 2022. Comparative study of circular and square gravity-based fish cages with different dimensions under pure current conditions. *Aquacultural Engineering* 96, 102223. <https://doi.org/10.1016/j.aquaeng.2021.102223>

Table of Contents

Preface	III
Acknowledgments	V
Abstract.....	VII
List of publications	XI
1 Introduction.....	1
1.1 Research background.....	1
1.2 State of the art in aquaculture structural designs.....	8
1.3 Challenges in structural design	15
1.4 Research objectives and scope.....	19
1.5 Thesis outline	20
2 Hydrodynamic modelling of marine aquaculture structures	23
2.1 Introduction to netting.....	24
2.2 Hydrodynamic loads on twines, ropes and pipes	29
2.3 Hydrodynamic loads on net panels	35
2.4 Flow velocity reduction	46
2.4.1 Twine-to-twine wake effect.....	48
2.4.2 Net-to-net wake effect.....	49
2.4.3 Cage-to-cage wake effect	53
2.5 Comparative study on hydrodynamic force models.....	55
2.5.1 Drag under different current velocities.....	55
2.5.2 Drag and lift under different inflow angles	61
2.6 Conclusions and recommendations.....	66
3 Structural modelling of marine aquaculture structures	69
3.1 Introduction to the structural modelling methods	70
3.1.1 Mass-spring model (0D).....	71
3.1.2 Truss finite element model (1D).....	73
3.1.3 Triangular finite element model (2D).....	75
3.1.4 Tetrahedral/hexahedral finite element model (3D).....	77
3.2 Structural model.....	79
3.2.1 Finite element constitution	79

3.2.2	Governing equations for dynamic analysis.....	80
3.2.3	Mesh grouping method.....	83
3.3	Implementation of hydrodynamic force models	84
3.3.1	Simulation process	84
3.3.2	Features of the UiS-Aqua numerical module	85
3.4	Validation for the structure solver.....	91
3.4.1	Net hanging in the air	91
3.4.2	Fish cage under the action of water flow.....	93
3.5	Conclusions.....	104
3.6	Appendix. Derivation of the mesh grouping method.	106
3.6.1	Mass equivalent.....	107
3.6.2	Stiffness equivalent	108
3.6.3	Environmental loads equivalent	109
4	Coupling algorithm for fluid-structure interaction analysis.....	113
4.1	Introduction to the fluid-structure interaction problem in marine aquaculture structure.....	114
4.2	Fluid model.....	118
4.2.1	Governing equations	118
4.2.2	Fluid velocity in the porous media model	119
4.2.3	Turbulence modelling.....	121
4.2.4	Boundary conditions for fluid	123
4.3	Dynamic porous media model	124
4.3.1	Topological method.....	124
4.3.2	Conservation of momentum	127
4.3.3	Flow velocity correction.....	129
4.4	Coupling algorithm	131
4.5	Comments on the previous coupling algorithm	133
4.6	Validation for the coupling algorithm.....	135
4.6.1	Convergence studies.....	135
4.6.2	Fixed net panel	138
4.6.3	Two flexible net panels	143
4.6.4	Full-scale fish cage.....	151
4.7	Conclusions.....	165
4.8	Appendix. Derivation of the flow velocity correction	167
5	Application to the design of traditional fish cages	173
5.1	Introduction.....	174

5.2	Descriptions of the traditional fish cage.....	176
5.3	The studied parameters and conditions	179
5.4	Results and discussion	185
5.4.1	Cultivation volume in still water	185
5.4.2	Cultivation volume under current conditions	192
5.4.3	Volume prediction under current conditions	206
5.4.4	Drag under current conditions	212
5.4.5	Drag prediction under current conditions	220
5.5	Conclusions.....	226
6	Application to the dynamic analysis of grid moored fish farms	229
6.1	Introduction.....	230
6.2	Description of the fish farm system	234
6.2.1	Fish cage description.....	234
6.2.2	Single-cage fish farm	236
6.2.3	1×4 multi-cage fish farm.....	239
6.3	Environmental conditions	242
6.4	Results and discussion	244
6.4.1	Single-cage fish farm	244
6.4.2	Multi-cage fish farm.....	254
6.4.3	Mooring system design consideration	261
6.4.4	Observations during operation	264
6.5	Conclusions.....	267
7	Application to offshore aquaculture structure.....	269
7.1	Introduction.....	270
7.2	Description of the offshore aquaculture structure	273
7.3	Validation of the numerical model.....	275
7.3.1	Free decay test.....	275
7.3.2	Dynamic responses under pure wave conditions	276
7.4	Application in irregular waves and currents	279
7.5	Conclusions.....	287
8	Conclusions and future work	289
8.1	Conclusions.....	289
8.2	Recommendations for the future work.....	291
	References.....	293

1 Introduction

1.1 Research background

The human population has increased from approximately 3.1 billion in 1961 to 7.8 billion in 2020 and is expected to exceed 9 billion by 2050. According to a recent report by the Food and Agriculture Organization of the United Nations (FAO, 2020), fish provided about 3.3 billion people with almost 20% of their average *per capita* intake of animal protein. Figure 1-1 shows the world capture fisheries and aquaculture production. The contribution of the aquaculture industry to global fish production was 46% in 2018. Although the capture fisheries provided most of the global fish production until now, the fast-growing aquaculture will surpass it in the coming years. Thus, aquaculture, rather than the stagnant capture fisheries, will be the main driving force behind the growth of global fish production and will be the solution to the increasing food demand from the growing population.

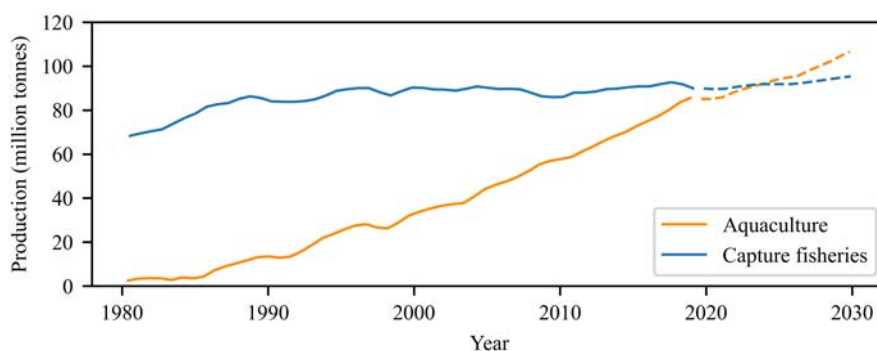


Figure 1-1. World capture fisheries and aquaculture production in live weight (FAO, 2020).

1.1 Research background

Aquaculture is a fast-growing industry. Over the past decades, the aquaculture industry has evolved from having a relatively minor role to playing a mainstream part in the global food system (Naylor *et al.*, 2000, 2021). According to the biannual report by FAO (2020), global fish consumption increased at an average annual rate of 3.1% from 1961 to 2017. This rate was almost twice of the annual world population growth (1.6%) for the same period. Figure 1-2 shows the world aquaculture production from 1998 to 2018. The farmed finfish production, including inland, marine and coastal aquaculture, was 54.3 million tonnes and accounted for 47.4% of the global aquaculture production in 2018 (FAO, 2020).

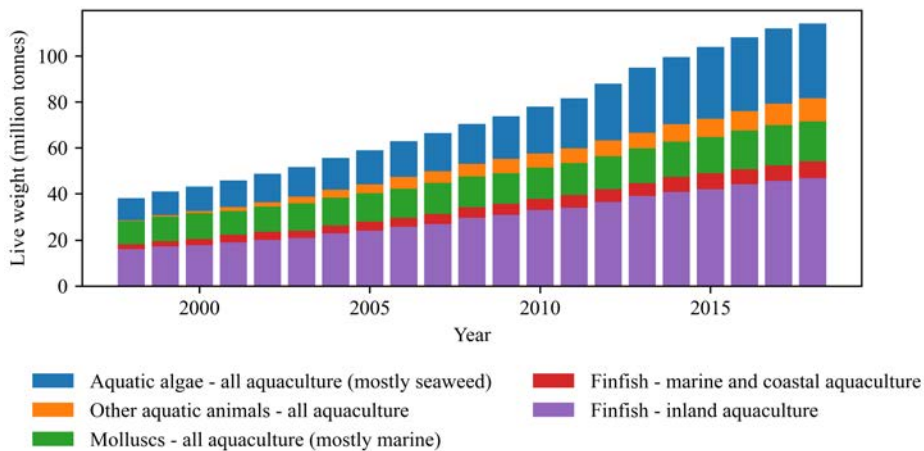


Figure 1-2. World aquaculture production (FAO, 2020).

In order to achieve the carbon-neutral goal, aquaculture is a promising solution for providing high-quality protein within a low carbon footprint. However, fish consumption only accounted for 17% of

1 Introduction

the total animal protein worldwide, and this percentage is much lower in Oceania, Northern America and Europe (FAO *et al.*, 2020). There is tremendous potential for aquaculture to raise dietary diversity in these areas. It requires less land and freshwater to produce fish meats than any other animal meats (Froehlich *et al.*, 2018). Moreover, finfish aquaculture has fewer greenhouse gas emissions compared to land-based animal agriculture (Davis *et al.*, 2016; Schubel and Thompson, 2019). Thus, fish meat which is a substitute for land-based animal meats, should be promoted in daily life to meet the carbon-neutral goal.

As shown in Figure 1-3, most of the finfish are currently produced from marine captures (FAO, 2020). However, the total marine catches have been relatively stable since the late-1990s, ranging from 78 Mt to 81 Mt per year (Figure 1-1). Thus, the increment of food demands due to the increasing population needs to be addressed by aquaculture. Currently, land-based aquaculture produces most of the finfish and plays an important role in world food security. However, the expansion of this land-based aquaculture can negatively affect fresh water, soil and biodiversity (Costello *et al.*, 2020). This can weaken the ability of the inland environment to produce other food products. While the ocean covers 71% of Earth's surface, marine aquaculture contributes only 5.3% to the world's total finfish production (FAO, 2020). As the ocean has abundant high-quality water and virtually unlimited space, marine aquaculture has enormous potential for the supply of nutritious food in the future.

1.1 Research background

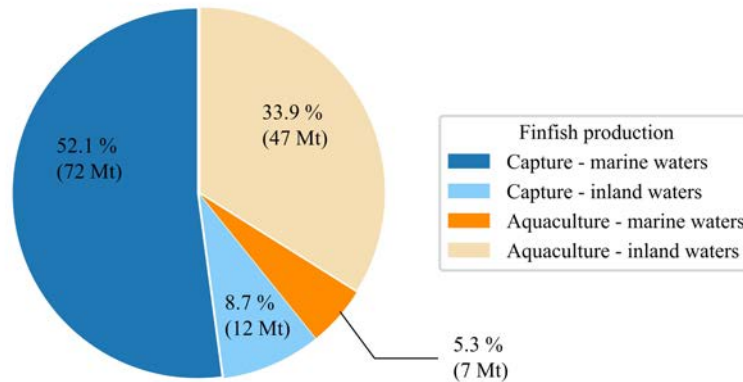


Figure 1-3. Fraction of world finfish production in 2018 (FAO, 2020).

While world aquaculture production has considerably increased in the past 20 years, as shown in Figure 1-2, marine finfish aquaculture is almost stagnating (Johannesen *et al.*, 2021). The causes are various and partly related to government policies, parasite infestations and complete exploitation of suitable farming sites. The effects of pathogens, parasites and pests (PPP), water pollution as well as harmful algal blooms still challenge the sustainability of marine aquaculture (Naylor *et al.*, 2021).

In order to reduce the risks from PPP and algal blooms, offshore aquaculture in the deep and open ocean is proposed and shows a promising potential (Lester *et al.*, 2018). Offshore aquaculture is designed to raise a large volume of fish while minimizing spatial conflicts (e.g., with wild-capture fisheries and coastal leisure) and coastal environmental impacts (e.g., degradation of benthos, eutrophication of water and sea lice infestations). Figure 1-4 shows the concept of offshore

1 Introduction

aquaculture in terms of locations (DNV GL, 2018). According to Cardia and Lovatelli (2015), offshore aquaculture can benefit the fish welfare and the ecosystem through better water exchange and dispersal of waste over a larger area. Moreover, technological advances of offshore aquaculture structures can improve the on-site work environments and reduce the risks of operations.

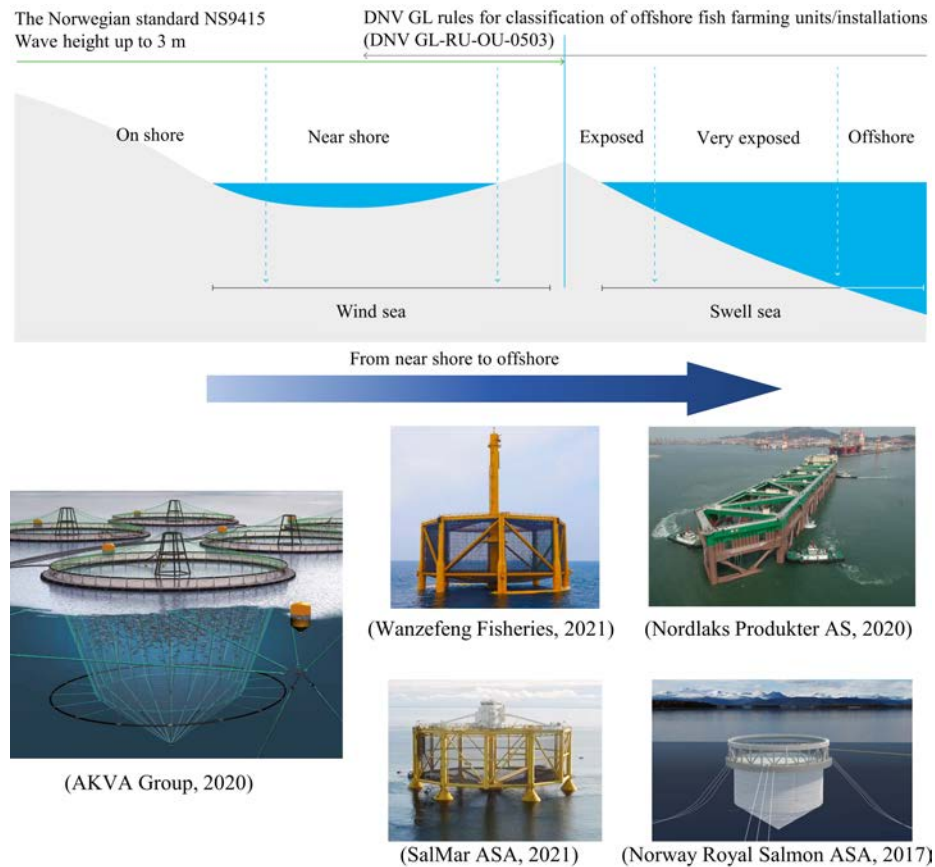


Figure 1-4. The classification of fish farming (reproduced from DNV GL, 2018).

1.1 Research background

Currently, offshore aquaculture structures are mainly designed for high market value cultured species. Among all the finfish species, salmonids (mainly Atlantic salmon¹ and Rainbow trout) have been the most important commodity traded in terms of international traded value since 2013. Although cultured salmonids only accounted for 1.8% of the global finfish production, they accounted for 30% of the total international finfish traded value in 2018 (FAO, 2020). The development of this high market value finfish species attracts significant investments to upgrade conventional farming facilities in marine aquaculture. According to the Norwegian Seafood Research Fund, the aquaculture value chain has invested more than NOK 115 billion in Norway since 2000 (Blomgren *et al.*, 2019).

However, moving the aquaculture structures to the deep and open ocean is not easy. On the exposed sites, large waves and currents are usually expected, which can significantly increase the environmental loads on aquaculture structures. The reliable design of the aquaculture structures is one of the keys to ensuring the sustainability of offshore aquaculture. Currently, Norway and China are leading the offshore aquaculture industry with the introduction of massive semi-submersible aquaculture structures. The novel facilities require precise and reliable design to operate at offshore sites. Given the large capital costs, offshore

¹ Atlantic salmon grows best in the sites where water temperatures are in the range of 6 ~ 16 °C, and salinities are close to oceanic levels (33-34‰). Water flows need to be sufficient to eliminate waste and to supply well oxygenated water (approximately 8 ppm). Maximum stocking densities of up to 20 kg/m³ are usual. Atlantic salmon are usually raised in sea sites for up to 2 years, and then are harvested from 2 kg upwards.

1 Introduction

aquaculture is growing cautiously and has been confined mainly to small-scale pilot projects in many other countries (Naylor *et al.*, 2021).

For marine aquaculture structures, the net is regarded as the most critical component. As shown in Figure 1-4, the net is the only barrier that surrounds the farmed fish and prevents fish escapes. The hydrodynamic loads on the net are also the largest contributors among the environmental loads on a marine aquaculture structure. According to the experiments by Cheng (2017), the hydrodynamic loads on the net can account for 85% of total loads on a conventional fish cage under pure current conditions. Thus, accurate predictions of the deformation and drag on the nets are needed in structural designs, both for ensuring fish welfare and for dimensioning the mooring system.

1.2 State of the art in aquaculture structural designs

In order to investigate the deformation and cultivation volume of fish cages, considerable research works have been done using experimental and numerical methods. Lader and Enerhaug (2005) measured the forces and geometry of a fish cage under the action of uniform water flow in a flume tank. Lader *et al.* (2007a, 2007b) investigated the wave forces acting on and damping mechanism of a fish cage. Bi *et al.* (2015) conducted a series of laboratory experiments to investigate the damping effect of the net cage on wave propagation. Moe-Føre *et al.* (2016) conducted a series of experiments to investigate the structural responses of high solidity net cages in uniform flow. Their detailed analysis and documentation provided valuable benchmark data for the subsequent research. Zhao *et al.* (2015a) investigated hydrodynamic characteristics of a large fish farm containing eight cages with a model scale of 1:40. Their results showed that obvious flow-velocity reduction exists inside the cages of the multi-cage configuration. Dong *et al.* (2021) measured the drag, cage deformation and flow field inside and around a scaled net cage model in a flume tank. Their results showed a complex fluid-structure interaction owing to the significant deformation of the flexible net. Bi *et al.* (2020) conducted laboratory experiments to investigate the effects of farmed fish on the drag acting on fish cages. Their results suggested that the farmed fish has a negligible contribution to the drag acting on the cage. All of these experimental studies provide reliable results for understanding the structural responses of aquaculture structures and for validating the later developed numerical program.

1 Introduction

In addition to the above experimental studies on the global dynamic responses of fish cages, there are also considerable experiments focusing on the local hydrodynamic characteristics of net panels and twines. Løland (1991) and Balash *et al.* (2009) found that the drag coefficient for a net panel is equivalent to the drag coefficient for cylinders modified with a function of net solidity. According to experimental data from Tsukrov *et al.* (2011), copper nets (smooth) had significantly lower drag in steady currents than nylon nets (rough) of similar solidity. The experimental data from Lader *et al.* (2014) indicated that the drag on the knotted net is up to 10% higher than that of the knotless net, given the same environmental condition. Tang *et al.* (2018a) later found that the drag generated by knots accounted for 15-25% of the total force on a net panel based on an experimental study. Bi *et al.* (2018) investigated the biofouling effect on the hydrodynamic characteristics of net panels and found that the accumulation of biofouling can lead to over 10 times more hydrodynamic load on nets. Tang *et al.* (2018b) found that the hydrodynamic loads on net panels were affected significantly by net configurations and the Reynolds numbers. They proposed a formula to calculate the drag coefficient based on the measured forces on a cylindrical cruciform element in a flume tank. The aforementioned experimental studies provided essential drag and lift coefficients which can be used by appropriate hydrodynamic force models to calculate the environmental loads on nets.

While the experimental research offers down-scaled, controllable and repeatable conditions for reliable analysis (Buck and Langan, 2017),

1.2 State of the art in aquaculture structural designs

the complex dynamic behavior of a full-scale aquaculture structure is still largely uncertain from quantitative points of view (Klebert *et al.*, 2013; Ruzzo *et al.*, 2021). The hydrodynamic responses of a flexible fish cage mainly depend on gravity (buoyancy), elastic and viscous phenomena, which cannot be simultaneously scaled using any scaling laws. In order to investigate the structural responses of full-scale fish cages, several in-house specialized numerical codes have been developed in recent years and validated against experiments, and a few of these in-house codes turned into commercial software afterward.

Løland and Slaattelid (1993) developed a computer program, NETSIM, to calculate the deformations of conventional fish cages under the action of currents and waves, based on a two-dimensional theory. It was probably the first computer program for the design of fish cages in Norway, and it had significant influence on later computer programs.

Through years of developments by Berstad *et al.* (2014, 2013, 2008) at Aquastructures AS, the computer program AquaSim became one of the leading analysis tools in the aquaculture industry in Norway.

Priour (1999) proposed a triangular element to calculate the deformation of nets using the Finite Element Method (FEM), and successfully applied this method to the simulations of fishing gears and fish cages (Priour, 2005).

1 Introduction

Tsukrov *et al.* (2003) developed the Aqua-FE computer program (the latest version of the software is called Hydro-FE) and successfully applied it to the dynamic analyses of fish cages and mussel longlines (Shainee *et al.*, 2013; DeCew *et al.*, 2010; Knysh *et al.*, 2021, 2020).

Li *et al.* (2006a, 2006b) and Zhao *et al.* (2007a, 2007b, 2007c) developed the computer program DUT-FlexSim with considerable validation works to calibrate their numerical models. Zhao *et al.* (2015b) compared the above two programs (Aqua-FE and DUT-FlexSim) with available experimental data and concluded that both programs have sufficient accuracy for the design of fish cages.

With the contributions of considerable researchers working at SINTEF Ocean (Endresen *et al.*, 2013, 2014; Reite *et al.*, 2014; Skjong *et al.*, 2021; Su *et al.*, 2021, 2019; Endresen and Klebert, 2020), the computer program FhSim was successfully developed with considerable verifications and applied to various applications, such as fish cages in rough seas, trawl net system and aquaculture operation.

Lee (2002) and Cha and Lee (2002) developed a numerical tool for fishing gears and later applied it to fish cage analysis (Lee *et al.*, 2008; Lee *et al.*, 2015; Park *et al.*, 2021). This numerical tool turned into commercial software, SimuTrawl, SimuPurse and SimuLine, under the company MPSL.

1.2 State of the art in aquaculture structural designs

Takagi *et al.* (2002) developed a numerical tool, NaLA, using similar numerical models as the work in Lee (2002), and applied it to estimate the dynamic responses of gill net, purse seine and fish cage (Suzuki *et al.*, 2003; Shimizu *et al.*, 2007; Takagi *et al.*, 2014). Moreover, a handful of in-house codes also showed their ability to simulate the structural responses of fish cages (Wan *et al.*, 2020; Wang *et al.*, 2016; Huang *et al.*, 2007; Chen *et al.*, 2021; Kristiansen, 2013).

A summary of the commonly used programs and codes for the dynamic analysis of marine aquaculture structures is shown in Table 1-1. The two green-shaded programs, *i.e.*, ANSYS and ABAQUS, are general-purpose FEM programs and provide a wide range of element types for different structural analyses. Although these general-purpose FEM programs have been utilized in many industrial applications, special developments such as hydrodynamic force models for nets and wake effects, are still needed in order to achieve accurate numerical results. The following three blue-shaded programs are developed for ocean engineering applications and can be applied to the design of marine aquaculture structures with proper hydrodynamic modifications. The rest of the programs/codes are originally developed in fishing and aquaculture industries for the design of marine aquaculture structures and fishing gears.

Although considerable numerical programs and codes have been proposed with a large number of publications (references in Table 1-1), most of them are either commercial programs or still in-house codes. To

1 Introduction

the author's knowledge, most of the programs/codes listed in Table 1-1 cannot be accessed by the public without permission. Thus, the marine aquaculture industry needs a ready-for-use numerical tool for the dynamic analysis of marine aquaculture structures.

1.2 State of the art in aquaculture structural designs

Table 1-1. A summary of numerical programs and codes for dynamic analysis of fish cages.

Programs or code	Hydrodynamic force model	Structural model	Reference
ANSYS	Morison	Truss, pipe, beam	Cheng <i>et al.</i> , 2018; Cui <i>et al.</i> , 2014
ABAQUS	Morison	Truss, beam	Moe-Føre <i>et al.</i> , 2016; Moe-Føre <i>et al.</i> , 2015; Li <i>et al.</i> , 2013
Orcaflex	Morison	Truss, mass-spring	Cifuentes and Kim, 2017b; Cifuentes and Kim, 2017a; Cifuentes and Kim, 2015; Li <i>et al.</i> , 2020
SIMA	Morison/Screen	Truss	Li and Ong, 2017; Faltinsen and Shen, 2018; Li <i>et al.</i> , 2018
ProteusDS	Morison	Mass-spring	Turner <i>et al.</i> , 2017
Hydro-FE\ Aqua-FE	Morison	Truss	Shainee <i>et al.</i> , 2013; DeCew, 2011; DeCew <i>et al.</i> , 2010; Tsukrov <i>et al.</i> , 2003
AquaSim	Morison	Truss, beam, membrane	Berstad and Aarsnes, 2018; Berstad and Heimstad, 2017; Reichert, 1994
FhSim	Morison/Screen	Triangles, mass-spring	Reite <i>et al.</i> , 2014; Endresen <i>et al.</i> , 2013; Endresen <i>et al.</i> , 2014; Skjong <i>et al.</i> , 2021; Su <i>et al.</i> , 2021, 2019; Endresen and Klebert, 2020
DUT-FlexSim	Morison	Mass-spring	Li <i>et al.</i> 2006a, 2006b Zhao <i>et al.</i> 2007a, 2007c
SimuTrawl\ SimuPurse\ SimuLine	Screen	Mass-spring	Lee <i>et al.</i> , 2005; Lee <i>et al.</i> , 2008; Lee <i>et al.</i> , 2015; Park <i>et al.</i> , 2021
NaLA	Morison	Mass-spring	Takagi <i>et al.</i> , 2002; Tsukrov <i>et al.</i> , 2003; Suzuki <i>et al.</i> , 2003; Shimizu <i>et al.</i> , 2007; Takagi <i>et al.</i> , 2014
DynamiT	Morison	Mass-spring	Vincent, 1999

1 Introduction

1.3 Challenges in structural design

Four major challenges arise in predicting structural responses of marine aquaculture structures under complex environmental conditions. As shown in Figure 1-5, these four challenges are: (a) How to model the ambient flow field around the structure, (b) How to accurately model environmental loads on structures, (c) How to correctly calculate the dynamic responses of the large-scale flexible nets with a feasible and fast method and (d) How to address the fluid-structure interaction problem for nets.

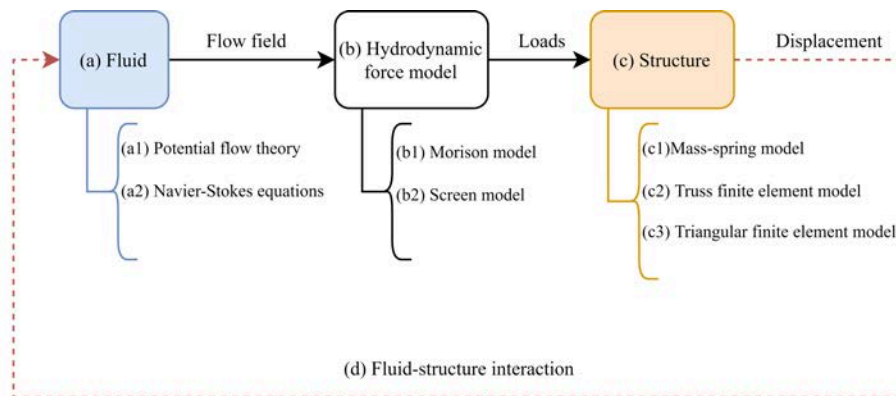


Figure 1-5. A simple flow chart for the fluid-structure interaction problem.

The first challenge is crucial for modelling nets under the action of currents and waves, and it is one of the most important preconditions for the subsequent challenges (b) and (c). In a real fish farm, the structures at different positions are usually subjected to different flow velocities due to wake effects. The environmental loads on structures are dependent on the ambient flow field, which can be modelled by (a1) potential flow

1.3 Challenges in structural design

theory or (a2) Navier-Stokes equations. Based on the flow field, the environmental loads may be calculated based on the integration of pressure and surface friction on the wetted area of the structure without using hydrodynamic force models. However, this integration method usually demands large computational resources (considering both computational time and CPU cores) and is impractical for calculating the hydrodynamic loads on the nets of an aquaculture structure. Wang *et al.* (2021) investigated the current load on a fixed net panel using the Large Eddy Simulation (LES) method, where the drag on a 0.02 m² net panel was calculated using 50 million grids. This 0.02 m² net panel only accounts for about 0.00008% of the total net area of the aquaculture structure in Figure 1-6(a). Thus, the environmental loads on aquaculture structures are usually calculated using hydrodynamic force models.

The second challenge arises due to the structural complexity. As described above, the environmental loads need to be modelled in order to reduce the computational demand. Usually, the environmental loads on nets are predicted by the two hydrodynamic force models, *i.e.*, (b1) Morison model (DeCew *et al.*, 2010; Zhao *et al.*, 2007) and (b2) Screen model (Løland 1991; Aarsnes *et al.*, 1990; Lee *et al.*, 2008; Balash *et al.*, 2009; Kristiansen and Faltinsen, 2012). Both models take the flow field as an input argument and return the hydrodynamic loads. The main difference between the two types of models is the object of reference for calculating the environmental loads. The Morison model takes a single twine as the object, while the Screen model takes a net panel as the object. A systematic comparison between the two types of hydrodynamic

1 Introduction

force models was shown in Cheng *et al.* (2020), where the authors suggested employing the Screen model for the dynamic analysis of aquaculture structures to amend common defects of Morison models. Thus, an appropriate hydrodynamic force model is one of the keys to the dynamic analysis of aquaculture structures.

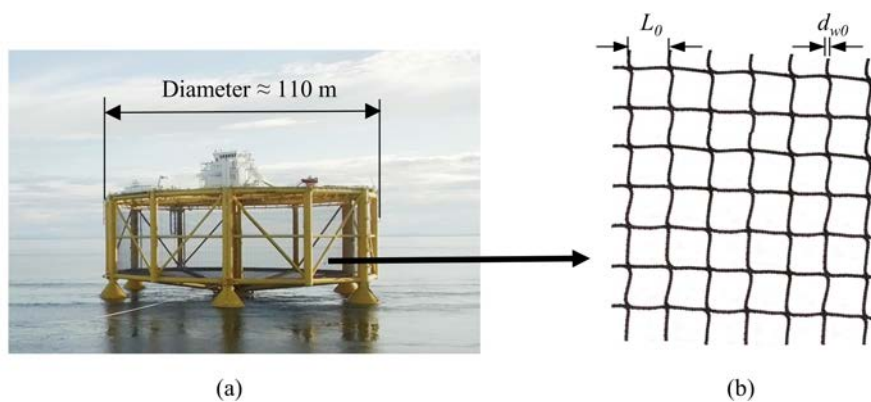


Figure 1-6. Illustration of nets in an aquaculture structure. (a) A large aquaculture structure with a diameter of 110 m (reproduced from SalMar ASA, 2021). (b) A piece of typical net in aquaculture structures with a mesh size L_0 of 30 - 50 mm and a twine diameter of 2 - 4 mm.

The third challenge arises as it is impractical to directly model the whole nets in aquaculture structures by each twine. The nets in an aquaculture structure usually comprise millions of twines which require an enormously large number of elements for modelling. For example, more than 30 million one-dimensional truss finite elements are needed to directly model the nets in the aquaculture structure, as shown in Figure 1-6(b). In addition, the dynamic response of aquaculture structures is nonlinear because the environmental loads depend on time, motion and deformation of the structure. According to Antonutti *et al.* (2018), this

1.3 Challenges in structural design

nonlinearity can cause high-frequency oscillations and bring challenges to the convergence of numerical simulations. Thus, an appropriate spatial discretization method together with a stable solution technique is required according to the research focus.

The last challenge arises due to the high porosity and flexibility of nets. As illustrated in Figure 1-6, an aquaculture structure usually comprises thousands of square meters of nets. These nets are usually flexible and can allow large displacements and deformations under the loads from current and wave. The deformed nets can, in turn, affect the flow field. The affected flow field can significantly affect the structural responses of the nets and the global movement of aquaculture structures (Bi *et al.*, 2013; Cheng *et al.*, 2020; Zhao *et al.*, 2013), especially when the structures (partly) are located in the wake field of an upstream net. This typical fluid-structure interaction (FSI) problem needs to be properly addressed in the fully coupled numerical simulations.

1 Introduction

1.4 Research objectives and scope

The main objectives of this thesis are to study complex dynamic responses of and flow physics around aquaculture structures under the action of currents and waves, and contribute to the structural design of aquaculture structures. In order to fulfill the main objectives and address the challenges described in Section 1.3, the following sub-objectives are defined:

- (1) To assess the existing hydrodynamic force models and provide recommendations for the model selection.
- (2) To propose a coupled simulation method for the complex FSI problem of aquaculture nets.
- (3) To provide practical engineering method for the most concerning aspects in the design process of traditional fish cages.
- (4) To provide recommended in-situ operation procedures to reduce the risks of accidental failures in fish farms.
- (5) To study the dynamic responses of a large semi-submersible aquaculture structure under irregular waves and currents.

1.5 Thesis outline

This thesis consists of seven chapters. A brief description of each chapter is provided as follows:

Chapter 1: This chapter introduces the research background, objectives, and scope of this thesis.

Chapter 2: This chapter presents a comprehensive review of the two types of hydrodynamic force models, *i.e.*, Morison model and Screen model, and the flow velocity reduction. The selection of hydrodynamic force models depends on the underlying structures and desired accuracy. Eleven commonly used hydrodynamic force models are reviewed comprehensively in this chapter, with the consideration of different current velocities, inflow angles and net solidities. The numerical results from the different hydrodynamic force models are compared against existing experimental data under pure current conditions. Suggestions for the selection of appropriate hydrodynamic force models are provided based on the model comparison.

Chapter 3: This chapter reviews the main structural modelling methods for marine aquaculture structures. The structural model used in this thesis is comprehensively described and validated against published experiments. Static and dynamic simulations are conducted with the consideration of different net structures.

1 Introduction

Chapter 4: This chapter presents the coupling algorithm for the two open-source numerical toolboxes, *i.e.*, OpenFOAM and Code_Aster. Compared to previous approaches, the present coupling algorithm can simplify the procedures of the model preparation by removing additional data-fitting processes for porous coefficients. Meanwhile, it can improve the accuracy of structural responses by employing a fluid solver to calculate the flow field and an advanced Screen model to calculate the hydrodynamic forces. The coupling algorithm is comprehensively described and validated with published experiments for both fixed and flexible nets. Different solidities, inflow angles, incoming velocities and dimensions of nets are also considered. The comparisons of flow velocity in the wake, deformation of flexible nets and drag on the full-scale fish cage, show that the numerical results obtained from the present coupling algorithm are in good agreement with experimental data.

Chapters 5 ~ 7: These chapters present the applications of the newly developed numerical module to the design of traditional fish cages, the dynamic responses of grid moored fish farms and the dynamic responses of a large semi-submersible aquaculture structure.

Chapter 8: Conclusions and recommendations for the future work are presented.

1.5 Thesis outline

2 Hydrodynamic modelling of marine aquaculture structures

The content is partly published as:

Cheng, H., Li, L., Aarsæther, K.G., Ong, M.C., 2020. Typical hydrodynamic models for aquaculture nets: A comparative study under pure current conditions. *Aquacultural Engineering* 90, 102070.

2.1 Introduction to netting

The net¹, or more specifically the netting, is regarded as the most critical component in a marine aquaculture structure. The hydrodynamic loads on a piece of net are dependent on the ambient flow velocity and its hydrodynamic characteristics. The hydrodynamic characteristics of nets are related to their physical properties, including materials, mesh shapes, twine shapes and net weaving methods. Table 1-1 summarizes the related physical properties of the commonly used nets in fishing and aquaculture industries.

Table 2-1. Physical properties of common nets in fishing and aquaculture industries.

Materials	Silicon-bronze Polyamide (PA) Polyester (PES) Polyethylene (PE) Polypropylene (PP) Polyethylene terephthalate (PET) Ultra-high molecular weight polyethylene (UHMWPE)
Mesh shape	Square Rhombus Hexagon
Twine shape	Monofilament Twisted Braided
Net weaving method	Knotless Knotted Welded Double-twisted

¹ People usually use “net” on many different occasions, and “netting” is more accurate when referring to the material made of string, thread or twine, with spaces in between. In this thesis, these two words refer to the same subject.

2 Hydrodynamic modelling of marine aquaculture structures

Different materials and twine shapes make the net's surface roughness different. Higher surface roughness will generate larger turbulence regions; and thus, higher drag (Balash *et al.*, 2009). According to experimental data from Tsukrov *et al.* (2011), copper nets (smooth) exhibit significantly lower drag resistance in steady currents than nylon nets (rough) of similar solidity. Different net weaving methods can also lead to different hydrodynamic characteristics. The experimental data from Lader *et al.* (2014) indicates that the drag on the knotted net is up to 10% higher than that of the knotless net, given the same environmental condition. Figure 2-1 shows four commonly used nets in marine aquaculture structures, and the hydrodynamic characteristics of these nets are quite different. In order to quantify the hydrodynamic characteristics of different nets, quantitative parameters, such as twine diameter and mesh size, are needed in addition to these qualitative physical properties (Table 1-1). The definitions of twine diameter and mesh size are shown in Figure 2-2.

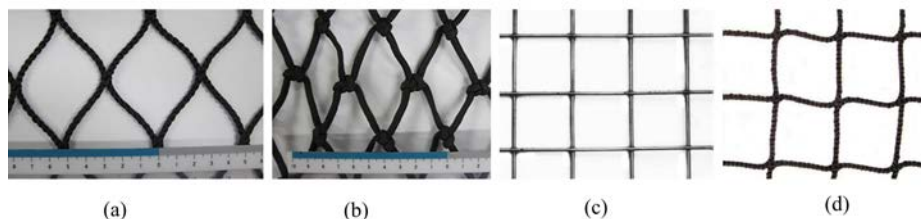


Figure 2-1. Different types of nets: (a) Knotless nylon net with rhombic mesh (Tang *et al.*, 2018), (b) Knotted nylon net with rhombic mesh and Single English knot (Tang *et al.*, 2018), (c) Welded silicon-bronze net (Tsukrov *et al.*, 2011) and (d) Knotless nylon net with square mesh.

2.1 Introduction to netting

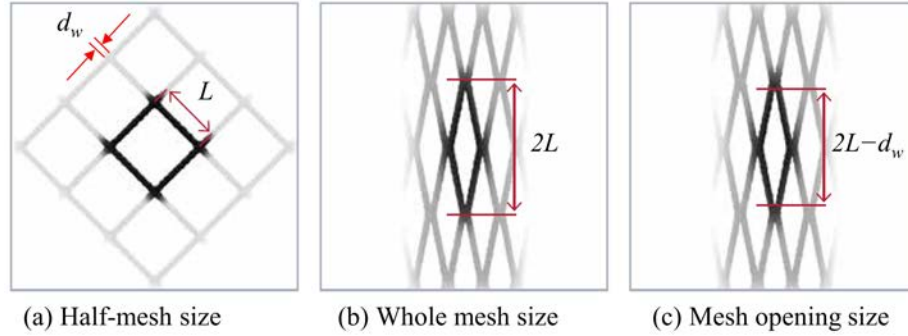


Figure 2-2. Definitions of mesh size (reproduced from AKVA Group 2020).

Through a large number of experimental studies (Tsukrov *et al.*, 2011, Tang *et al.*, 2018, Lader *et al.*, 2014, Balash *et al.*, 2009), researchers found that hydrodynamic characteristics of nets are also dependent on the two dimensionless variables, Reynolds number (Re) and solidity (Sn), defined as follows:

$$Re = \frac{U d_w}{\nu} \quad (2-1)$$

$$Sn = \frac{d_w(2L - d_w)}{L^2} \quad (2-2)$$

where U is the undisturbed water velocity, ν is the kinematic viscosity of the fluid, d_w is the twine diameter, L is the half-mesh size. For a typical net in marine aquaculture structures, the values of Sn are in the range of 0.1 ~ 0.4, and the values of Re are in the range of 100 ~ 10 000.

2 Hydrodynamic modelling of marine aquaculture structures

In comparison to the definition of Re in Eq.(2-1), some researchers (Kristiansen and Faltinsen, 2012; Balash *et al.*, 2009) defined Re with local flow velocity, such as $Re = \frac{Ud_w}{\nu(1-Sn)}$. This definition leads to a higher Re compared to Eq.(2-1), when applying to the same situation. Thus, users need to pay special attention when different hydrodynamic force models are applied to the dynamic analyses of marine aquaculture structures.

Sn is a key parameter for hydrodynamic characteristics. For a net panel, the drag is mainly dependent on the value of Sn without obvious effects of d_w and L , which both define Sn itself (Klebert *et al.*, 2013). From the perspective of physics, Sn is the ratio between the projected net area (the area of dark lines in Figure 2-3) and the outline area of the net panel ($= a \times b$, as shown in Figure 2-3). Thus, the values of Sn are always between 0 ~ 1, where 1 means an impermeable membrane.

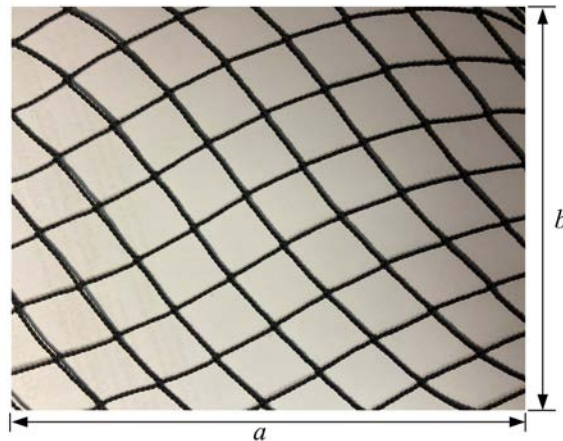


Figure 2-3. Illustration of a net panel with the length of a and the width of b .

2.1 Introduction to netting

For an ideal knotless square net, a mathematical expression for S_n is given in Eq.(2-2). For knotted nets and other mesh shapes, the expression can be different. Besides, the digital image processing (DIP) method can also be used to estimate the S_n of a net panel. The value of S_n is processed as the ratio between pixels in different colors in the DIP method (Yu, 2017). In general, the DIP method and Eq.(2-2) have less than 4% discrepancy in the S_n estimation for typical nets in marine aquaculture structures (Tsukrov *et al.*, 2011). Nevertheless, the DIP method is still the most precise method for measuring the S_n . Moreover, one should notice that the S_n measured in the dry air may be changed when the net panel is submerged in water and stretched by weight.

As the environmental loads on marine aquaculture structures are usually complex under the action of currents and waves, hydrodynamic force models are required to calculate the environmental loads on structures and transfer the loads to the structural solver in dynamic analyses. Two main types of hydrodynamic force models can be applied to calculate the environmental loads on marine aquaculture structures: Morison model (Section 2.2) and Screen model (Section 2.3).

2.2 Hydrodynamic loads on twines, ropes and pipes

The Morison type hydrodynamic force model can be applied to a line-like structure, such as rope, cable, and the twine of nets. When the Morison model is applied to calculate the environmental loads on a net panel, the loads are calculated based on individual twines. As shown in Figure 2-4(a), a small segment of the twine in a net panel can be taken as a cylinder. Thus, the net panel is a combination of many intersected cylinders. In practice, the environmental load on the line-like structure is usually decomposed into two components: normal drag (\mathbf{F}_n , Eq.(2-3)) and tangential drag (\mathbf{F}_t , Eq.(2-4)):

$$\mathbf{F}_n = \frac{1}{2} C_n \rho L d_w |\mathbf{u}^r_n| \mathbf{u}^r_n \quad (2-3)$$

$$\mathbf{F}_t = \frac{1}{2} C_t \rho L d_w |\mathbf{u}^r_t| \mathbf{u}^r_t \quad (2-4)$$

where L is the length of the line-like structure, d_w is the diameter of the line-like structure, ρ is the fluid density. \mathbf{u}^r_n and \mathbf{u}^r_t are the normal and tangential velocity of fluid relative to the line-like structure. C_n and C_t are the drag coefficients in normal and tangential directions, respectively. A 2D illustration of the force directions is given in Figure 2-4(b).

The drag coefficients C_n and C_t are crucial in the calculation of the environmental loads as they determine how much the environmental loads is applied in numerical simulations. In practice, C_n and C_t are

2.2 Hydrodynamic loads on twines, ropes and pipes

obtained from well-designed experiments. For example, Kebede *et al.* (2020) designed a delicate experiment in a flume tank and investigated the hydrodynamic properties of different ropes at various water velocities and angles of attack. Their results showed that the drag coefficients of helix ropes and conventional ropes have no statistical difference when $4.51 \times 10^2 < Re < 1.24 \times 10^4$.

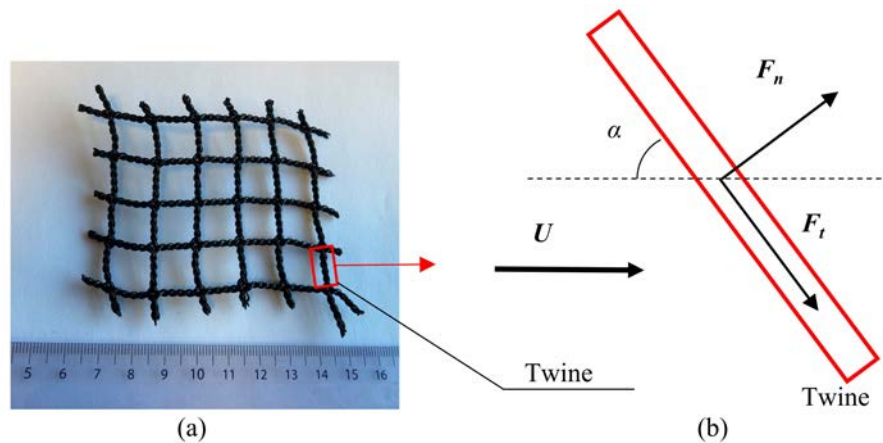


Figure 2-4. A 2D illustration of the environmental loads on a line-like structure. F_n and F_t are the normal and tangential drag, respectively. The angle of attack α is the angle between the current direction and the axis of a line-like structure.

Table 2-2 summarizes the two drag coefficients for twines in a net panel from the published literature (see the references in Table 2-2). From M1 to M5, the expressions of C_n increase in complexity. M1 and M2 treat the normal drag coefficient as a constant value independent of Re . M3 and M4 include the variable Re to improve the accuracy of C_n at different fluid flow regimes. M5 includes another variable, S_n , to include the effect of net solidity.

2 Hydrodynamic modelling of marine aquaculture structures

According to Table 2-2, the value of C_t is approximately 1/10 of the value of C_n . Therefore, even though C_t is not included in M2 and M5 (Cifuentes and Kim, 2017a; Wan *et al.*, 2002), the simulation results are still acceptable. Figure 2-5 shows the values of C_n in the five models together with the C_n of a smooth cylinder. It indicates that when $100 < Re < 10\ 000$, the values of C_n in M1-M5 are similar, and the values are between 1.1 and 1.3, which are close to C_n of a smooth cylinder in the subcritical Reynolds number region.

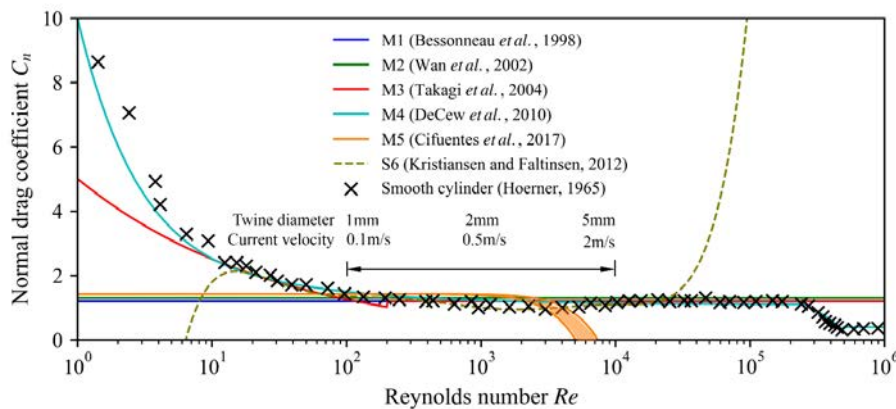


Figure 2-5. Normal drag coefficients (C_n) versus Reynolds number (Re) according to different hydrodynamic force models. Because C_n in M5 model changes with different solidities (Sn), the filled area represents its variation range for its applicable solidities ($0.172 < Sn < 0.208$). The normal drag coefficient of the twine in S6 is a polynomial function according to its formulae (Kristiansen and Faltinsen, 2012). The normal drag coefficients for a smooth cylinder and the typical Re region (100-10 000) for twines are also shown in this figure.

2.2 Hydrodynamic loads on twines, ropes and pipes

Table 2-2. Hydrodynamic coefficients in Morrison model, when $100 < Re < 10\,000$.

Model	C_n	C_t	Reference
M1	1.2	0.1	Bessonneau and Marichal, 1998
M2	1.3	-	Wan <i>et al.</i> , 2002
M3	$\begin{cases} 10^{0.7} Re^{-0.3} & (Re < 200) \\ 1.2 & (Re > 200) \end{cases}$	0.1	Takagi <i>et al.</i> , 2004
M4	$\begin{cases} \frac{8r}{sRe} (1 - 0.87s^{-2}) & 0 < Re < 1 \\ 1.45 + 8.55Re^{-0.9} & 1 < Re < 30 \\ 1.1 + 4Re^{-0.5} & 30 < Re < 2.33e5 \\ -3.41 \times 10^{-6}(Re - 5.78 \times 10^5) & 2.33e5 < Re < 4.92e5 \\ 0.401 \left(1 - e^{\frac{-Re}{5.99 \times 10^5}} \right) & 4.92e5 < Re < e7 \end{cases}$	$\begin{cases} \pi\mu(0.55\sqrt{Re} + 0.084Re^{2/3}) \end{cases}$	DeCew <i>et al.</i> , 2010; Choo and Casarella, 1971; Zhao <i>et al.</i> , 2007a; Tsukrov <i>et al.</i> , 2000
M5	$-3.2891 \times 10^{-5}(Sn^2Re)^2 + 0.00068(Sn^2Re) + 1.4253$	-	Cifuentes and Kim, 2017a

2 Hydrodynamic modelling of marine aquaculture structures

The advantage of the Morison model lies in its format. Since the formulation of Morison mode is coincident with the line-like elements in structural models, the application of a Morison model is directly compatible with the structural model. Thus, it is easy to implement the Morison model into FEM programs to calculate the hydrodynamic loads. As shown in Table 1-1, the Morison model is the most popular among the software and codes. Moreover, the Morison model can be easily applied to many line-like structures in marine applications, such as mooring lines, cables and ropes.

However, the Morison model has these drawbacks: (1) The velocity decomposing follows the independence principle, while this principle is only partially successful in correlating measured force data (Zdravkovich, 2003); (2) The Morison model can overestimate the drag when the angle of attack (α) is small as it is not able to capture the interaction between the twines (Kristiansen and Faltinsen, 2012); (3) The Morison model will lead to significant errors when applying to a net with large Sn . Before the Morison model was applied to the design of fish cages, this model was usually applied to the design of fishing gears, such as the front part of trawling net, demersal seine net and gillnet. For the nets in fishing gears, Sn has a small effect on the C_n because the value of Sn in the fishing net is usually very small. Thus, the effect of solidity on the drag coefficients has not been included in Morison model. M5 (Cifuentes and Kim, 2017a) is the first model to consider the effect of solidity. However, one should note the strict application area of M5, since the negative quadratic term in C_n can result in unrealistic values for

2.2 Hydrodynamic loads on twines, ropes and pipes

large values of the Sn or/and Re . In order to mitigate these defects of Morison model, Screen model is proposed.

2.3 Hydrodynamic loads on net panels

In Screen model, the hydrodynamic loads are calculated based on a flat net panel. The twines (and knots) in the net panel are considered as an integrated structure. In practice, the hydrodynamic loads on the net panel are decomposed into two components, either relative to the panel or relative to the flow. In most of the models, the hydrodynamic loads are decomposed, relatively to the direction of the water velocity, into drag and lift (\mathbf{F}_D and \mathbf{F}_L in Eqs.(2-5) and (2-6)).

$$\mathbf{F}_D = \frac{1}{2} C_D \rho A_t |\mathbf{u}^r|^2 \mathbf{i}_D \quad (2-5)$$

$$\mathbf{F}_L = \frac{1}{2} C_L \rho A_t |\mathbf{u}^r|^2 \mathbf{i}_L \quad (2-6)$$

$$\mathbf{i}_D = \frac{\mathbf{u} - \mathbf{v}}{|\mathbf{u} - \mathbf{v}|} \quad (2-7)$$

$$\mathbf{i}_L = \frac{(\mathbf{u} - \mathbf{v}) \times \mathbf{e}_n \times (\mathbf{u} - \mathbf{v})}{|(\mathbf{u} - \mathbf{v}) \times \mathbf{e}_n \times (\mathbf{u} - \mathbf{v})|} \quad (2-8)$$

where A_t is the outline area of the net panel, \mathbf{u}^r is the fluid velocity relative to the net panel, \mathbf{i}_D and \mathbf{i}_L are unit force vectors to indicate the directions of drag and lift forces. C_D and C_L are the drag and lift coefficients. The coefficients are determined from experimental data, and they are usually dependent on the Re , Sn and inflow angle θ (see the definition in Figure 2-6). In the simulation, the coordinates of every node

2.3 Hydrodynamic loads on net panels

are known. Thus, A_t and unit normal vector e_n of the net panel can be calculated based on the nodal coordinates as follows:

$$A_t = \frac{1}{2} |\overrightarrow{P_1P_2} \times \overrightarrow{P_1P_4}| \quad (2-9)$$

$$e_n = \frac{\overrightarrow{P_1P_2} \times \overrightarrow{P_1P_4}}{|\overrightarrow{P_1P_2} \times \overrightarrow{P_1P_4}|} \quad (2-10)$$

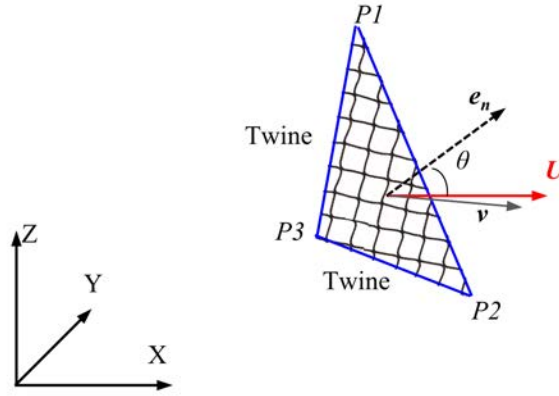


Figure 2-6. Illustration of a net panel. The inflow angle θ of the net panel is defined as the angle between e_n and U .

According to Fridman (1973), the hydrodynamic loads on a net panel can also be decomposed into normal drag (F_N) and tangential drag (F_T), which are related to the orientation of the net panel. The expressions of these two components (Eqs.(2-11) and (2-12)) have a similar form with the Morison model (Eqs.(2-3) and (2-4)), except that the reference area is changed from the projected area of a net twine $d_w L$ to the outline area of a net panel A_t .

2 Hydrodynamic modelling of marine aquaculture structures

$$\mathbf{F}_N = \frac{1}{2} C_N \rho A_t |\mathbf{u}^r_n| \mathbf{u}^r_n \quad (2-11)$$

$$\mathbf{F}_T = \frac{1}{2} C_T \rho A_t |\mathbf{u}^r_t| \mathbf{u}^r_t \quad (2-12)$$

where \mathbf{u}^r_n and \mathbf{u}^r_t are the normal and tangential components of the fluid velocity relative to the net panel. C_N and C_T are the normal and tangential drag coefficients of the net panel, which are dependent on the Re and Sn . The relationships of \mathbf{F}_N , \mathbf{F}_T , \mathbf{F}_D , \mathbf{F}_L and θ are shown in Figure 2-7. The relationships of C_D , C_L , C_N , C_T are given in Eqs.(2-13) and (2-14).

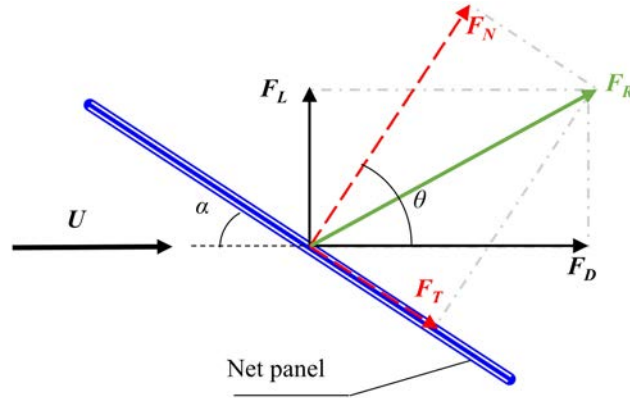


Figure 2-7. A 2D illustration of hydrodynamic loads on a net panel. \mathbf{F}_R is the resultant force which can be decomposed to drag \mathbf{F}_D and lift \mathbf{F}_L , or normal drag \mathbf{F}_N and tangential drag \mathbf{F}_T . The inflow angle θ is defined as the angle between the normal vector of the net panel and the flow direction.

$$C_D = C_N \cos \theta \cos^2 \theta + C_T \sin \theta \sin^2 \theta \quad (2-13)$$

$$C_L = C_N \sin \theta \cos^2 \theta - C_T \cos \theta \sin^2 \theta \quad (2-14)$$

2.3 Hydrodynamic loads on net panels

Table 2-3. Hydrodynamic coefficients in Screen model.

Model	C_D	C_L	Applicable conditions	Reference
S1	$0.04 + (-0.04 + Sn - 1.24Sn^2 + 13.75Sn^3)\cos \theta$	$(0.575Sn - 3.545Sn^2 + 10.15Sn^3)\sin 2\theta$	$0.13 < Sn < 0.35$	Aarnes <i>et al.</i> , 1990
S2	$0.04 + (-0.04 + 0.335Sn + 6.545Sn^2 - 4.885Sn^3)\cos \theta$	$(-0.055Sn + 2.35Sn^2 - 1.765Sn^3)\sin 2\theta$	$0.13 < Sn < 0.35$	Løland, 1991
S3	$C_{D0}(a_1\cos\theta + a_3\cos 3\theta)$ $C_{D0} = C_{d_{cylinder}} \frac{Sn(2 - Sn)}{2(1 - Sn)^2}$	$C_{L0}(b_2\sin 2\theta + b_4\sin 4\theta)$ $C_{L0} = (0.5C_{D0} - C_{L45})/\sqrt{Z}$ $C_{L45} = \pi C_{N45}/(8 + C_{N45})$ $C_{N45} = C_{cylinder} \frac{Sn}{2(1 - Sn)^2}$	$0 < Sn < 0.5$ $31.6 < Re < 10\ 000$	Kristiansen and Faltinsen, 2012
S4*	$3(Re)^{-0.07}Sn$	$0.1(Re)^{0.14}Sn$	$10 < Re < 50\ 000$	Fridman, 1973
S5	-	-	-	Lee <i>et al.</i> , 2005
S6	for knottless net $C_D = C_{cylinder}(0.12 - 0.745Sn + 8.035Sn^2)\cos^3 \theta$ for knotted net $C_D = \left(\frac{C_{d_{cylinder}} + \frac{C_{d_{sphere}}\pi L d_w}{8D^2}}{\pi L d_w / 8D^2} + \frac{C_{d_{sphere}}\pi L d_w}{8D^2}\right)(0.12 - 0.745Sn + 8.035Sn^2)\cos^3 \theta$	-	$0.051 < Sn < 0.235$	Balash <i>et al.</i> , 2009

*S4: The expressions of S4 are for C_N and C_T

2 Hydrodynamic modelling of marine aquaculture structures

Table 2-3 summarizes the two hydrodynamic coefficients for net panels in Screen model together with their applicable conditions, based on the published literature (see the references in Table 2-3). Figure 2-8 and Figure 2-9 present the values of C_D and C_L of S1-S6 with respect to θ and Sn , within their applicable conditions. For S4, the hydrodynamic coefficients, C_N and C_T , are converted to C_D and C_L using Eqs.(2-13) and (2-14) for a better comparison. For S3, S4 and S6, Re is assumed as a constant of 1 000 in Figure 2-8 and Figure 2-9. For S3, the harmonic terms (a_3 and b_4) should increase with the increasing solidity, but no quantitative relationship is given by Kristiansen and Faltinsen (2012). Thus, the harmonic terms in S3 are set according to the experimental data reproduced by Shimizu *et al.* (2018), where $Sn = 0.29$, $a_1 = 0.83$ $a_3 = 0.15$. For S5, which is applied to the program SimuTrawl, SimuPurse and SimuLine (Table 1-1), formulation of C_D and C_L was not disclosed in the published article (Lee *et al.*, 2005). The values of C_D and C_L are read from the Fig.5 in (Lee *et al.*, 2005) and are assumed linearly proportional to Sn and independent of Re .

As shown in Figure 2-8, the values of C_D decrease with increasing θ as expected. S1 and S2 have a similar shape, and their C_D almost overlaps with the cosine function. In comparison, the values of C_D in S3 - S6 are decreased faster than the cosine function with the increasing θ . According to the expressions of S3 and S6, the drag coefficient is zero when $\theta = 90^\circ$. It means that the drag on a net panel is zero when the water flow is parallel to the net panel, which is irrational as there must be a drag, although very small. If one applies S3 and S6 to the design of a

2.3 Hydrodynamic loads on net panels

square fish cage, the drag can be underestimated when half of the nets are parallel to the water flow. Compared to S3 and S6, S1 and S2 may be more rational and closer to reality when $\theta \neq 90^\circ$.

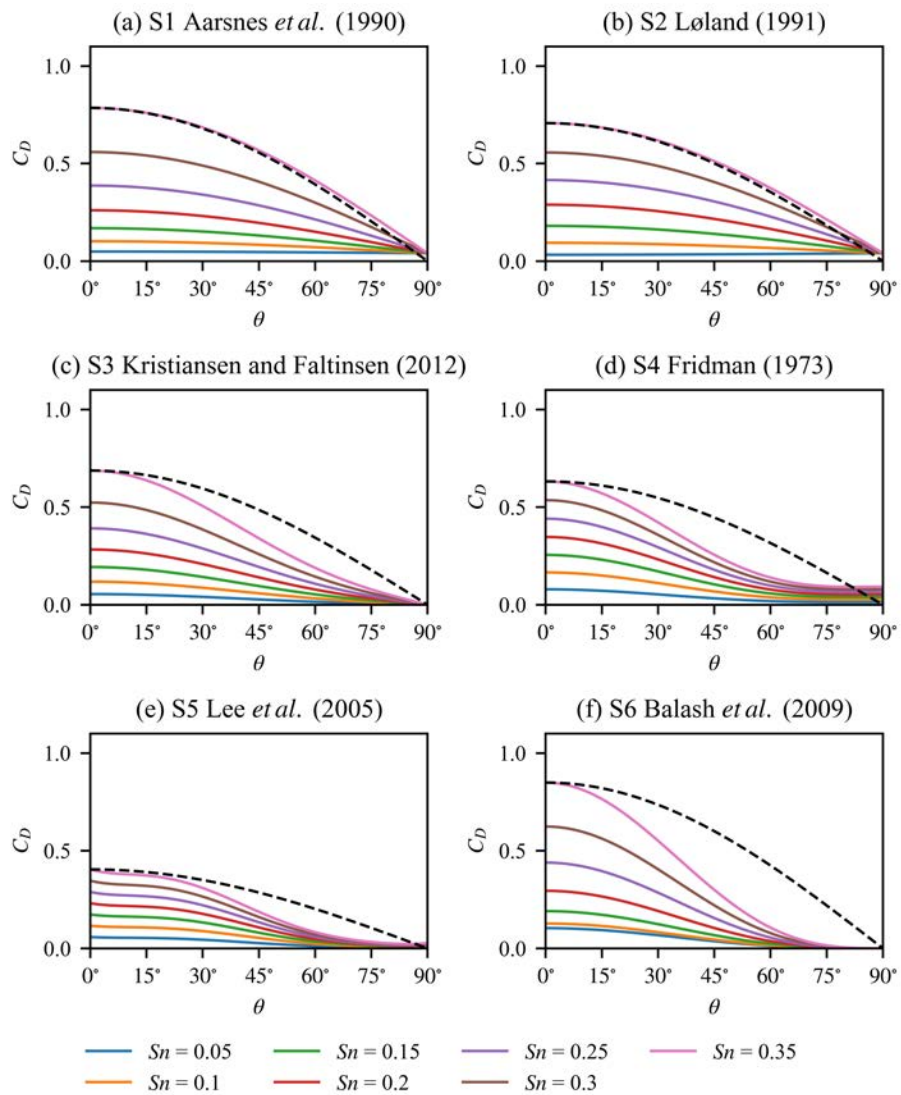


Figure 2-8. Drag coefficients of S1-S6. The dashed lines in each subplot are $C_{D(\theta=0^\circ)} \cos \theta$.

2 Hydrodynamic modelling of marine aquaculture structures

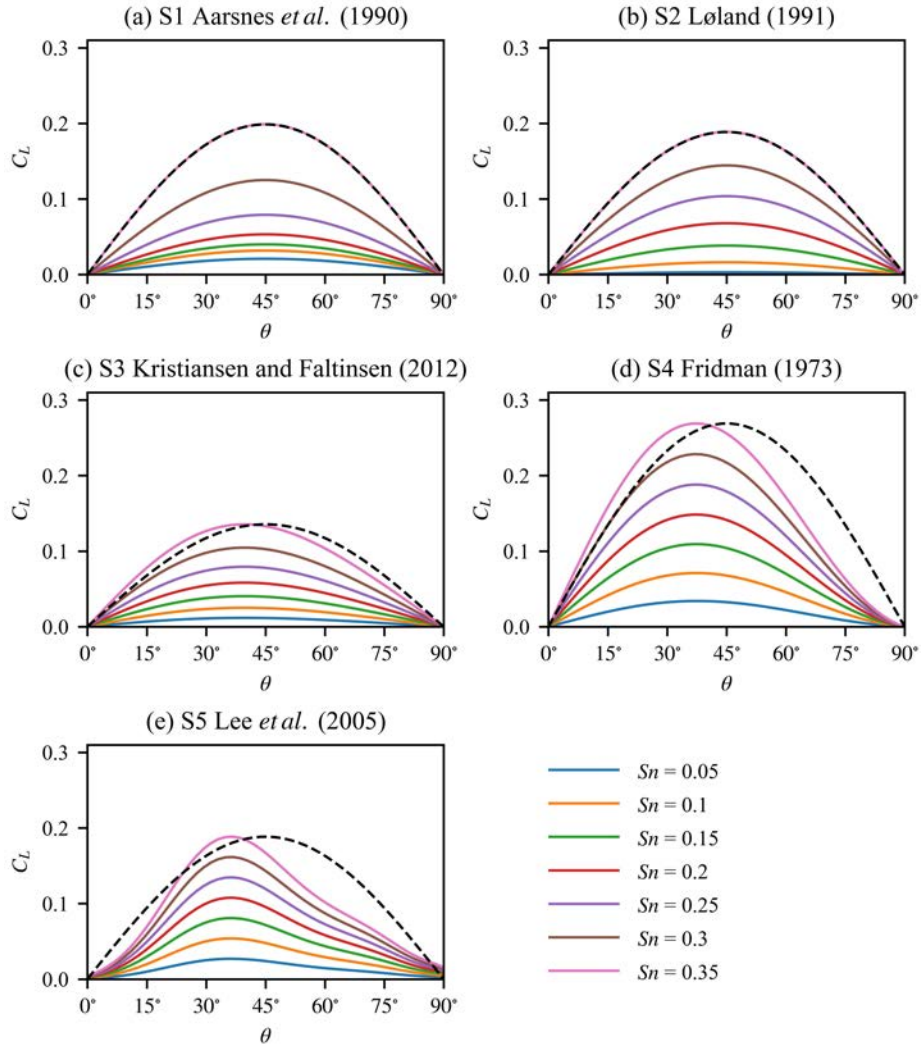


Figure 2-9. Lift coefficients of S1 – S5. The dashed lines in each subplot are $\max(C_L)\sin 2\theta$.

According to Figure 2-9, the values of C_L first increase and then decrease with the increasing θ . This characteristic of C_L for a net panel is similar to that of an airfoil. It is rational that the values of C_L are 0 when the water flow is parallel or perpendicular to the net panel. The

2.3 Hydrodynamic loads on net panels

curves of S1 and S2 are overlapped with the sine function of 2θ . While for S3, S4 and S5, the crests of curves are located between 30° and 45° . In addition, the crest location can be easily tuned through the harmonic term in S3, based on available experimental results. S6 is not presented in Figure 2-9 due to the lack of formulas for C_L .

As shown in Figure 2-8 and Figure 2-9, the values of C_D and C_L have significantly different characteristics with respect to θ . The ratios between C_L and C_D in S1-S5 are presented in Figure 2-10. The values of C_L/C_D can indicate the relationship between lift and drag on a net panel. The appropriate hydrodynamic force model should have a rational C_L/C_D and the values of C_L/C_D should agree with the observed lift/drag in experiments. In Section 2.5, these values of C_L/C_D will be compared against published experimental results. As shown in Figure 2-10, the values of C_L/C_D in S1 and S2 are very small (less than 0.5). However, the values of C_L/C_D in S3 -S5 can be larger than 1, and their C_L/C_D is almost independent with Sn . These characteristics are quite irrational. When the Sn is small, the net panel becomes more permeable to the water flow. The more permeable net panel means that the gaps between twines are larger, and thus, should have a smaller C_L/C_D . Thus, from this point of view, the characteristics of C_L/C_D in S2 are more rational than the others.

2 Hydrodynamic modelling of marine aquaculture structures

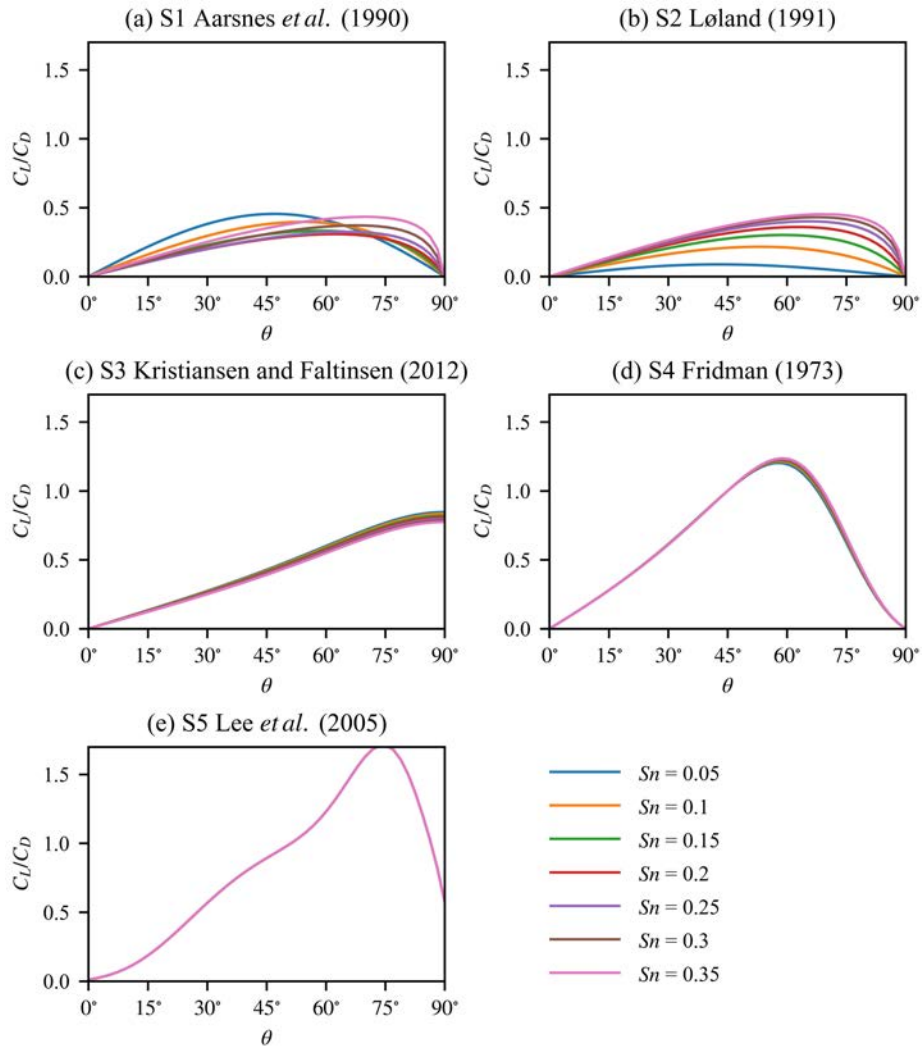


Figure 2-10. The values of C_L/C_D in S1-S5.

Through a large number of experiments (Klebert *et al.*, 2013, Zhou *et al.*, 2015, Tang *et al.* 2018), researchers found that the hydrodynamic coefficients are highly dependent on Sn . Thus, Sn is considered as an essential physical parameter in Screen model and is included in S1-S6

2.3 Hydrodynamic loads on net panels

(see Table 2-3). In general, the values of C_D and C_L increase with increasing Sn , which indicates that the drag and lift on a net panel will become larger when Sn gets larger, and the other conditions are the same. Figure 2-11 shows the values of C_D for knotless nylon net panels when $\theta = 0^\circ$ with respect to Sn from the available experimental data (Zhou *et al.*, 2015; Tsukrov *et al.*, 2011; Gansel *et al.*, 2015). The regression curves in Figure 2-11 are fitted using the ordinary least squares method. The coefficients of determination (R^2) show that the cubic regression fits the data better than the simple linear regression. This observation complies with the expressions in S1 (Aarsnes *et al.*, 1990) and S2 (Løland, 1991).

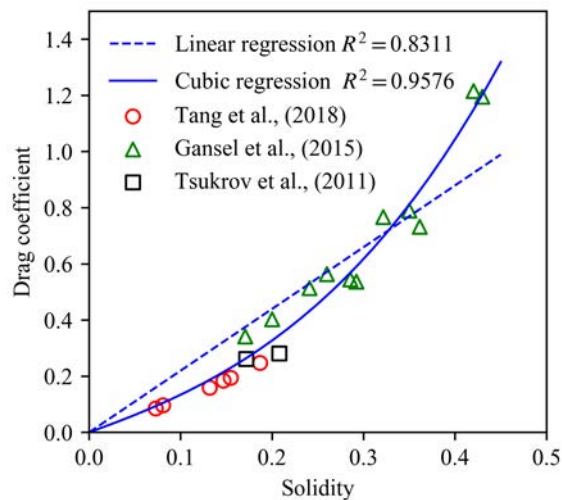


Figure 2-11. Drag coefficient versus solidity for nylon nets when $\theta=0^\circ$. The scatter points come from different experimental results. R^2 is the coefficient of determination.

2 Hydrodynamic modelling of marine aquaculture structures

The flow patterns around nets and twines will change with Re , and thus influence the values of hydrodynamic coefficients. For S1, S2 and S5, the values of C_D and C_L are independent of Re , as they do not include Re in their expressions. For S3, S4 and S6, Re is included in the expressions of C_D and C_L . According to Figure 2-5, the effect of Re might be negligible since the drag coefficient of a net twine is almost constant when $100 < Re < 10\ 000$.

Screen models are seldom used in general-purpose FEM programs (see Table 1-1) for dynamic simulations of fish cages, due to the complexity of implementation. Usually, the motions and deformations of aquaculture nets are calculated based on the line-like elements (truss, pipe or beam) in the general-purpose FEM programs. In order to implement Screen models into the existing FEM programs, other types of elements (shell or plane) or an external module must be introduced to calculate the hydrodynamic loads and extra steps are required to map the hydrodynamic loads to the line-like elements. From the perspective of programming, Screen model may require more algorithms than Morison models to fulfill dynamic analyses of fish cages. Thus, Screen models are not commonly used in the software and codes, referring to Table 1-1.

2.4 Flow velocity reduction

In the context of aquacultural engineering, the wake is the region downstream from the permeable nets, where the flow velocity is reduced and the flow is often turbulent (Cheng *et al.*, 2020; Sim *et al.*, 2021; Zhao *et al.*, 2013a; Zhao *et al.*, 2013b). The effect of wake is an essential and complex mechanism in the dynamic analyses of permeable structures, such as the nets in fish cage and fishing gear. In a real fish farm, nets at different positions usually experience different flow velocities due to wake effects.

In most of the dynamic analyses of fish cages, the structural solver calculates the equilibrium between the external and internal forces of the structure and neglects the fluid mechanics. If no special precautions are taken to include the wake effect, the hydrodynamic loads on the downstream nets can be overestimated. And thus, the predicted motions and deformations of the fish cage can be wrong. In general, there are two ways to include the wake effect in the fish cage simulation. One can couple a structural solver with a fluid solver to include the fluid-structure interaction (Chen and Christensen, 2017). Although this method can be very accurate, the high demands for computational resources make this method hardly applied to real-time simulations.

Alternatively, one can use the quasi-static assumption to “register” a wake region in the structural solver, where the flow velocity is tuned to be smaller than the non-wake effect region (Endresen *et al.*, 2013).

2 Hydrodynamic modelling of marine aquaculture structures

For the latter method, the wake effect for a conventional fish farm (where 4~8 fish cages are moored in a grid shape) can be subdivided into three types according to the applicable regions. As shown in Figure 2-12, the three types are (1) twine-to-twine wake effect; (2) net-to-net wake effect; (3) cage-to-cage wake effect.

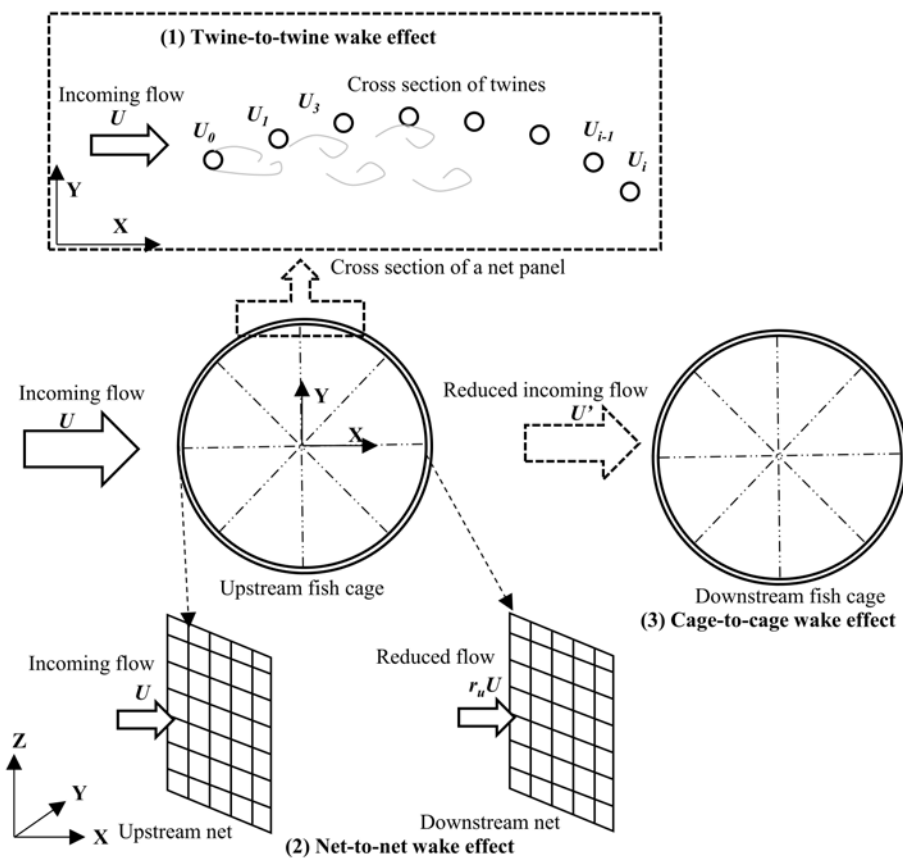


Figure 2-12. Illustration of different wake effects. (1) Twine-to-twine wake effect, where a grid of $i+1$ cylinders (cross-section of a net panel) are exposed to an incident current velocity U . The U_i ($i = 0, 1 \dots$) denotes the velocity experienced by cylinder i , which is modified due to the presence of upstream cylinders. (2) Net-to-net wake effect, where the upstream (left) net panel is exposed to an incoming current velocity U . The net-to-net wake effects from the upstream net panel result in a reduced flow ($r_u U$) at the downstream net. (3) Cage-to-cage wake effect, where the incoming flow for the downstream (right) fish cage is anisotropic and might be smaller than the incoming flow for the upstream (left) fish cage.

2.4.1 Twine-to-twine wake effect

The twine-to-twine wake effect represents the interactions between net twines in a net panel, where the applicable region is in the order of 1 cm. In a net panel, the flow velocity of the downstream twine is smaller than that of the upstream twine when $\theta > 70^\circ$. According to the analysis by Endresen *et al.* (2013), when $\theta = 90^\circ$, the predicted drag on a net panel without considering the twine-to-twine wake effect can be maximumly 8 times larger than that in the experiment. Thus, the twine-to-twine wake effect has significant effects on hydrodynamic loads prediction, especially when θ is large, and this effect should be included in the hydrodynamic force model.

The Morison model has a natural drawback on the implementation of the twine-to-twine wake effect. In order to include this effect in the Morison model, one needs to make a function to describe the flow pattern behind a cylinder. For example, the wake shape around a 2D circular cylinder in an infinite fluid can be calculated based on Blevins formula (Blevins, 1984), as given in Eq.(2-15).

$$U' = U \left(1 - 1.02 \sqrt{\frac{C_d}{6 + x/d_w}} \exp \left\{ \frac{-(y/d_w)^2}{0.0767 C_d (6 + x/d_w)} \right\} \right) \quad (2-15)$$

where U' is the flow velocity for the downstream cylinder at coordinate (x, y) , U is undisturbed flow velocity in front of the cylinder, d_w is the diameter of the cylinder, and C_d is the drag coefficient. In Morison models, excessive numerical calculations and sophisticated algorithms

2 Hydrodynamic modelling of marine aquaculture structures

are required to determine the spatial relationships among a large number of twines in the numerical model. This, it is difficult to consider this wake effect in Morison model.

On the other hand, the twine-to-twine effect is naturally included in Screen model, since the hydrodynamic coefficients of net panels already implicitly include the interactions between twines. Thus, no special algorithm is required when applying the Screen model to the dynamic analysis of fish cages under the action of currents and waves.

2.4.2 Net-to-net wake effect

The net-to-net wake effect represents the interaction between nets inside a single fish cage, where the applicable region is around 30~50 m (dependent on the diameter of the fish cage). Approximately half of the nets in a cylindrical fish cage will experience the net-to-net wake effect. If the net-to-net wake effect is neglected in the dynamic analyses of fish cages, the mooring force can be overestimated up to 22% (Faltinsen and Shen, 2018). In practice, a flow velocity reduction factor (r_u) is adopted in software and codes to represent the net-to-net wake effect. Eq.(2-16) is a typical expression for the net-to-net wake effect, where r is the flow velocity reduction factor ($0 < r_u < 1$), $\mathbf{U}_{upstream}$ is the ambient flow velocity in front of a fish cage. According to this equation, the downstream nets experience a smaller flow velocity compared to the upstream nets.

2.4 Flow velocity reduction

$$\mathbf{U}_{downstream} = r_u \mathbf{U}_{upstream} \quad (2-16)$$

In numerical simulations, whether a net is located in the wake can be determined based on its position, the center of the fish cage and the incoming flow direction (see Figure 2-13). Then, r_u can be set as an attribute of the downstream nets once after the initialization of the structural solver, and the value of r_u can keep constant during the whole dynamic simulation.

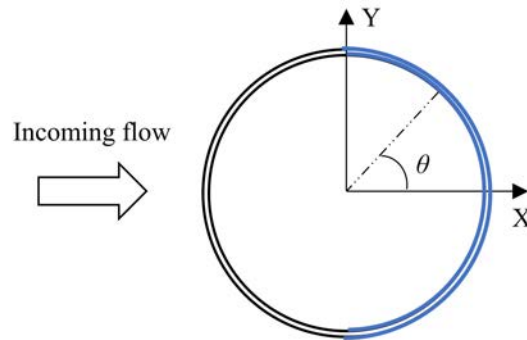


Figure 2-13. Illustration of the method to identify the nets which experience the net-to-net wake effect caused by upstream nets in a cylindrical fish cage. The fish cage is shown from the top, and the blue part is the rear half of a cage where the nets will experience a reduced flow.

An accurate r_u is critical for predicting the hydrodynamic loads on the nets in the wake (the blue part in Figure 2-13). Table 2-4 presents the values of r_u from experiments and theoretical analyses, based on the published literature (see the references in Table 2-4). In this table, the value of r_u is related to Sn , Re and θ . However, the value of r_u from the most commonly used engineering method, $r_u = 1 - 0.46 C_{D(\theta=0^\circ)}$, is consistent with different inflow angles. That means all the downstream nets in the rear half of a cylindrical fish cage (*e.g.*, see the blue part in

2 Hydrodynamic modelling of marine aquaculture structures

Figure 2-13) experience the same reduced flow velocity, which is contrary to the experimental results reported by Bi *et al.* (2013).

Table 2-4. Comparison of flow velocity reduction factors (r).

r_u	Sn	Re	Reference
0.82-0.98 (average:0.9)	0.135-0.272	70-590	Bi <i>et al.</i> , 2013
0.69	0.128-0.223	170 -1438	Zhan <i>et al.</i> , 2006
$1-0.46C_{D(\theta=0^\circ)}$	0.13-0.32	1400-1800	Løland, 1991; Aarsnes <i>et al.</i> , 1990; Kristiansen and Faltinsen, 2012
0.85	0.20-0.22	-	Patursson, 2008
0.8	-	198-660	Zhao <i>et al.</i> , 2007a; Zhao <i>et al.</i> , 2007b

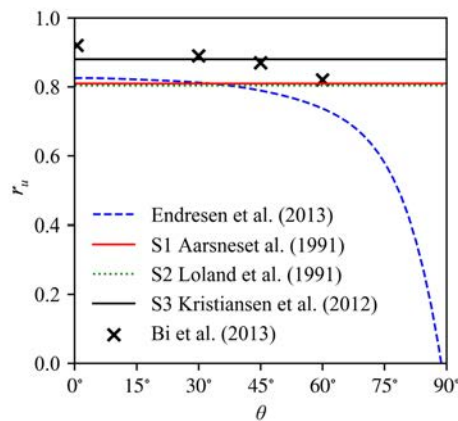


Figure 2-14. The relationship between flow velocity reduction factors (r_u) and inflow angles (θ) when $Sn = 0.243$ and $Re \approx 450$. In the experiment, the net is a knotless square PE net with $L = 20\text{mm}$ and $d_w = 2.6\text{mm}$. The velocity probe is located 0.6m behind the net panel.

Figure 2-14 shows the value of r_u with respect to θ for downstream net panels in a cylindrical fish cage. In this figure, the experimental

2.4 Flow velocity reduction

results from Bi *et al.* (2013) are presented and compared with theoretical values. The experimental data indicate that the value of r_u should reduce with increasing θ of the upstream net. However, only the result from Endresen *et al.* (2013) agrees with the trend. The other three from Aarsnes *et al.* (1991), Løland *et al.* (1991) and Kristiansen and Faltinsen (2012), using the engineering method, $r_u = 1 - 0.46 C_{D(\theta=0^\circ)}$, give a constant r_u with respect to different θ and disagree with the experimental results.

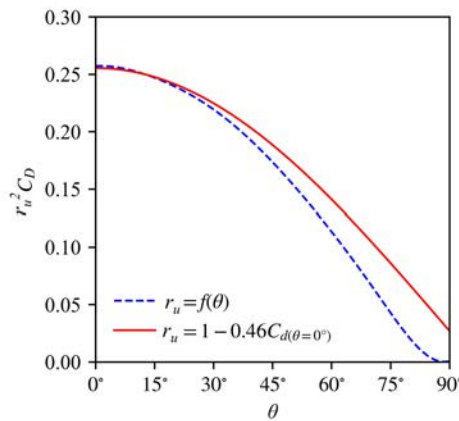


Figure 2-15. Equivalent drag coefficients ($r_u^2 C_D$) of the downstream nets for different θ .

Figure 2-15 shows the equivalent drag coefficients ($r_u^2 C_D$) of the downstream net panels when $Sn = 0.243$ using the methods from Endresen *et al.* (2013) and Aarsnes *et al.* (1991). Because the drag is proportional to the square of the flow velocity, $r_u^2 C_D$ can be used to represent the equivalent drag coefficient of a net panel in the wake. In Figure 2-15, the value of C_D is calculated based on the S1 model for both

2 Hydrodynamic modelling of marine aquaculture structures

curves. For the dashed line, r_u is calculated according to Endresen *et al.* (2013). For the solid line, r_u is calculated by $1-0.46C_{D(\theta=0^\circ)}$ according to Aarsnes *et al.* (1990). As shown in Figure 2-15, the equivalent drag coefficients of downstream net panels based on the two flow velocity reduction factors are similar when $\theta < 30^\circ$. However, with increasing θ , the equivalent drag coefficient using the constant r_u is larger than the one using the variable r_u . It means around 2/3 of the downstream net panels in a cylindrical fish cage will be assigned larger hydrodynamic loads if the constant r_u is applied to the dynamic analysis of fish cages.

2.4.3 Cage-to-cage wake effect

The cage-to-cage wake effect represents the interaction between cages in a fish farm, where the applicable region can be a few hundred of meters (dependent on the fish farm size). In the marine aquaculture industry, fish cages are usually grouped in arrays as a fish farm. Due to the block effect of the upstream cages, the flow velocity for the downstream cages can be different from the upstream cage.

In the previous study (Løland *et al.* 1991), an engineering method for the velocity reduction behind a net panel ($r_u = 1 - 0.46 C_D$) was used to represent the wake effect between cages. According to the numerical simulations by Bi and Xu (2018), the flow velocity around a fish cage is reduced by 38.3% at the back and increased by 14.4% at the two sides. According to the experiment by Turner *et al.* (2016), the wake after a fish cage is nonuniform, and the flow velocity is reduced up to 62%

2.4 Flow velocity reduction

behind the fish cage and increased 19% underneath the fish cage. In addition, high levels of large-scale turbulence were also observed behind a fish cage (Turner *et al.*, 2016). However, the engineering method can only give a uniform reduced flow throughout the entire wake, and this is unphysical and unrealistic. Therefore, the engineering method cannot sufficiently describe the wake behind a fish cage.

The cage-to-cage wake has not been fully implemented into any FE solver or codes now due to its complexity. The wake topology is dependent on the environmental conditions, the status of the upstream fish cage and the spatial relationships among the fish cages. Although the wake shape and velocity profiles can be pre-predicted through accurate computational fluid dynamics (CFD) simulations, complex and verified algorithms are still needed to implement such pre-predictions into a FE solver for fish farm analyses. In the latest work by Sim *et al.* (2021), the cage-to-cage wake effect is implemented into a numerical program, FhSim, to investigate its influences on the responses of a 4×2 multi-cage fish farm. The results indicate that the total drag loads of the 8 fish cages can be overestimated up to 128% and the total cultivation volume of the 8 cages can be underestimated as much as 42%, when the wake effect is neglected in the numerical simulation. From the performed numerical simulations, the impacts of wake effects on drag loads, cultivation volumes, and tensions in anchor lines are clearly observed.

2 Hydrodynamic modelling of marine aquaculture structures

2.5 Comparative study on hydrodynamic force models

Four net panels, which are widely used in the aquaculture industry, are selected from available experimental data (Tang *et al.*, 2018; Tsukrov *et al.*, 2011) to study the applicability and accuracy of the aforementioned hydrodynamic force models with respect to net structures, ambient flow velocities and inflow angles. The parameters of the four studied net panels are given in Table 2-5, and photos of the four net panels are shown in Figure 2-1. The size of the net planes in the numerical simulation is $1\text{m} \times 1\text{m}$, and the four edges of the net planes are fixed in the simulation.

Table 2-5 Parameters of the studied four net panels.

Net	Twine diameter (mm)	Half-mesh size (mm)	Sn	Material	Knots	Mesh orientation
N1	3.17	46.87	0.132	Nylon	Knotless	45°
N2	3.66	43.13	0.177	Nylon	Knotted	45°
N3	2.05	25.42	0.1512	Silicon-bronze	Knotless	0°
N4	2.85	25.87	0.2056	Nylon	Knotless	0°

2.5.1 Drag under different current velocities

Figure 2-16 shows the drag on the four net planes under different flow velocities when $\theta = 0^\circ$ using the eleven hydrodynamic force models (*i.e.*, M1-M5 and S1-S6). In general, the drag loads on net panels increase with the increasing flow velocity, but their increasing speeds are dependent on the hydrodynamic characteristics of net panels. The

2.5 Comparative study on hydrodynamic force models

predicted drag loads using hydrodynamic force models should agree with the experimental measurements.

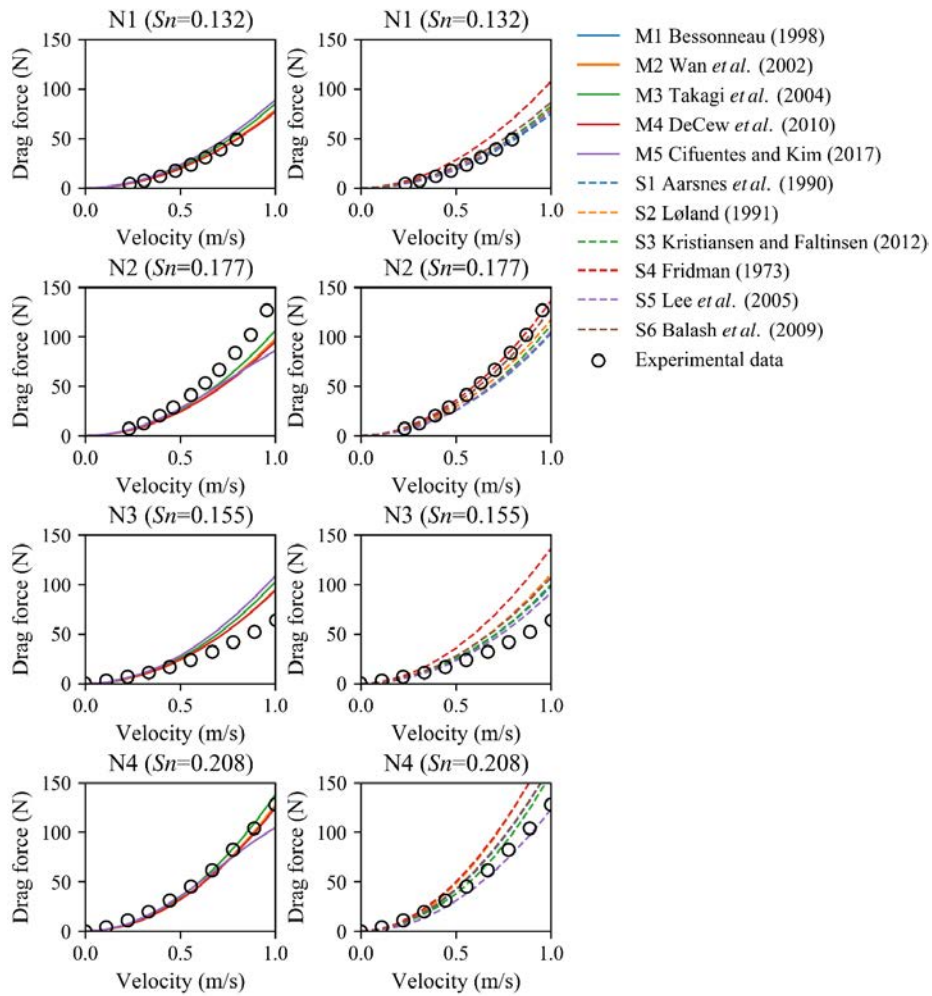


Figure 2-16. Drag on the four studied net panels for different current velocities when the incoming flow is perpendicular to the net panels ($\theta=0^\circ$). The left subplots are the simulation results using Morison model M1-M5 (solid lines). The right subplots are the simulation results using Screen model S1-S6 (dashed lines).

2 Hydrodynamic modelling of marine aquaculture structures

Different materials can make the twine surface roughness different, and the smooth surface can reduce the hydrodynamic loads on the net. For the silicon-bronze net (N3), all the hydrodynamic force models overestimate the drag compared to the experimental data, especially when the flow velocity is larger than 0.5 m/s. When the flow velocity is 1 m/s, the discrepancies between the experimental data and the predicted forces are varied from 43% to 113%. However, for the Nylon nets (N1 and N4), the discrepancies between experimental data and the predicted forces can be as low as 0.4%. Since all the eleven hydrodynamic force models were developed based on fibred nets whose surface is rougher than that of metal nets, they cannot be directly applied to the smooth metal nets. Moreover, the experimental results reported by Cha *et al.* (2013) revealed that the value of C_D for chain-link copper alloy nets is smaller than that of the fabric nets with similar Sn , only when $\theta < 60^\circ$. When the $\theta > 60^\circ$, the larger thickness of copper alloy nets due to the net weaving method, can cause larger drag than the fabric nets. Additional research work is necessary to have a better understanding of the hydrodynamic differences between fabric nets and copper alloy nets.

Solidity is an important factor for the prediction of hydrodynamic loads. In general, the larger solidity can induce a larger drag. The predicted drag for N4 (highest-solidity net from N1-N4) using Morison model can fit the experimental data well, except for M5 when the flow velocity is 1 m/s. According to the expression of C_n in M5, the value of C_n can be negative when $Sn^2 Re > 218$. That means when the Sn is 0.3

2.5 Comparative study on hydrodynamic force models

and the Re is higher than 2 400, C_n can be negative. Thus, one should notice this strict applicable condition when using this model.

The knots on a net panel can bring additional hydrodynamic loads. Compared to N4, N2 has a smaller S_n , which means the drag on N2 should be smaller than N4 when both net panels are under the action of the same flow velocity. However, due to the existence of knots on N2, the drag loads on these two net panels are almost the same under the action of the same flow velocity. For the knotted net (N2), Morison model can underestimate the drag loads if the effect from knots is neglected. These phenomena are in line with the findings from Lader *et al.* (2014), in which the drag on knotless nets is up to 10% less than that on knotted nets. For the knotted net (N2), the predicted drag loads using Screen model show better agreement with the experimental data. In particular, the predicted drag loads based using S4 and S6 are very close to the experimental data, because these two models have included the effect of knots.

However, it is also observed that not all the Screen models can well predict the drag on a net panel. S4 model always overestimates the drag on knotless net panels (N1, N3 and N4). One should notice that this model was proposed more than 40 years ago. At that time, the marine aquaculture industry was just in its infancy compared to the fishing industry. The researchers used fishing nets, most likely knotted nets, to generate this hydrodynamic force model. Thus, predicted drag using S4 can only agree well with the drag on knotted nets.

2 Hydrodynamic modelling of marine aquaculture structures

Although the solidity has a clear physical meaning, the expressions to estimate the value of S_n are quite different in the S1-S4. Table 2-6 compares the estimated values of S_n of N1 and N4 using the expressions in S1-S4 against the measurements from experiments. For N1, all the estimated values of S_n used in S1-S4 are within 5% difference of the experimental value. However, for N4, the relative difference between the estimated S_n and experimental value can be as large as 10.1%. This large difference can affect the accuracy of the predicted hydrodynamic loads. Thus, the predicted drag on N4 (high solidity net) has large deviations than that on N1 (low solidity net) when using the Screen model. In addition, when attaching the net panels to the frame, a pre-tension is usually needed to keep the net stable in the desired shape for conducting experiments. The different pre-tensions can cause the twines to have different degrees of elastic deformation. Thus, the measured S_n in experiments can be different for the same net panel when the pre-tension is different.

The mesh orientation has negligible effects on drag in numerical simulations when $\theta = 0^\circ$. The concept of mesh orientation is shown in Figure 2-17. For Morison model, the total drag on a net panel is the sum of the drag on each twine. The sum of the projected area of the twines does not change with the different mesh orientations. For Screen model, the drag loads are calculated based on the outline area of a net panel whose area is also unchangeable with the changing orientation. Thus, the predicted drag loads based on both types of hydrodynamic force models are independent of the mesh orientation when the flow is perpendicular

2.5 Comparative study on hydrodynamic force models

to the net panel. However, drag loads on the two net panels with the same Sn (illustrated in Figure 2-17), can be different when $\theta \neq 0^\circ$ (Balash *et al.*, 2015). A numerical study indicates that when $\theta > 45^\circ$, the drag on net(b) is larger than that on net(a), given the same other conditions (Bi *et al.*, 2017).

Table 2-6. Solidities of N1 and N4.

		Experimental value		Estimated value		
Model	-	S1	S2	S3	S4	
Formula	-	$\frac{2d_w}{L}$	$\frac{d_w(2L + 0.5d_w)}{L^2}$	$\frac{d_w(2L - d_w)}{L^2}$	$\frac{2d_w}{L}$	
	Solidity	0.132	0.1352	0.1375	0.1307	0.1352
N1	Relative difference ¹	-	2.4%	4.2%	-0.9%	2.4%
	Solidity	0.2056	0.2203	0.2264	0.208	0.2203
N4	Relative difference ¹	-	7.2%	10.1%	1.3%	7.2%

¹Relative difference = (estimated estimation - experimental value)/experimental value \times 100%.

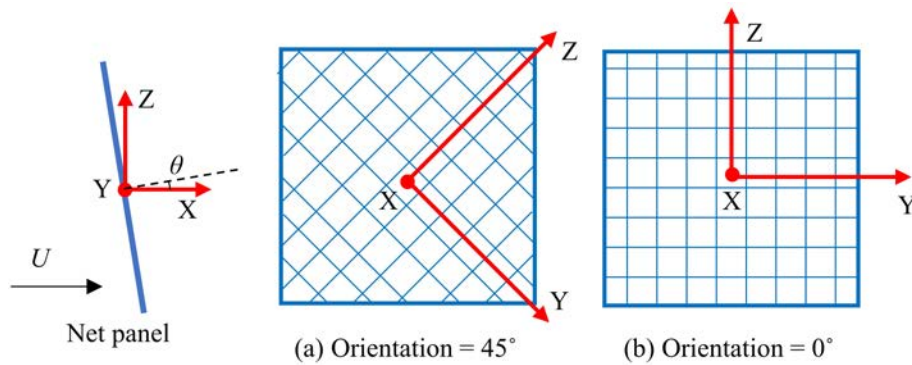


Figure 2-17. Illustration of the inflow angle θ (left) and mesh orientation (right). The two net panels have the same solidity and mesh size.

2 Hydrodynamic modelling of marine aquaculture structures

2.5.2 Drag and lift under different inflow angles

In practice, most of the nets in a fish cage are not perpendicular to the flow direction, especially when the fish cage is under the action of currents and waves. Thus, it is important to compare the hydrodynamic load under different θ . Due to limited experimental data, only N1 and N2 have the experimental results under different θ . Since most of the hydrodynamic force models are not applicable to the knotted net (N2), we only discuss the loads on N1 in this section. Figure 2-8 shows the drag, lift, and the ratio of lift to drag with respect to different θ when the flow velocity is 0.6 m/s.

According to the experimental data by Tang *et al.* (2018), the drag on the net panel decreases with the increasing θ . As shown in Figure 2-18, the predicted drag loads based on M1-M5 are similar, and all agree with the experimental data when $\theta < 70^\circ$. While $\theta > 70^\circ$, all the Morison model M1-M5 can overestimate the drag due to the absence of the twine-to-twine wake effect. That means the drag on at least 22% of a cylindrical fish cage can be overestimated. The overestimated drag loads could lead to inaccuracy in the prediction of displacements and cultivation volumes. Thus, simulations using Morison model can be low accuracy when the fish cage has large deformation (Moe-Føre *et al.*, 2016).

For Screen model, not all the models agree with the experimental results well. S3, S5 and S6 underestimate the drag loads when $\theta > 30^\circ$; S4 overestimates the drag loads when $\theta < 30^\circ$ and underestimates the drag loads when $\theta > 30^\circ$; only S1 and S2 agree with the experimental

2.5 Comparative study on hydrodynamic force models

data quite well for all θ . According to the drag coefficients in Figure 2-8, only S1 and S2 are in line with the cosine function with the increasing θ . The drag coefficients of S3-S6 decrease much faster than the cosine function. That is the reason why the drag loads are underestimated by S3-S6 when $\theta > 30^\circ$. It is observed that the drag loads using S3 and S6 models are zero when $\theta = 90^\circ$. That unphysical value contradicts the experiment data by Zhou *et al.* (2015). Therefore, S1 and S2 are more accurate than S3-S6 in the drag prediction for the N1 net panel.

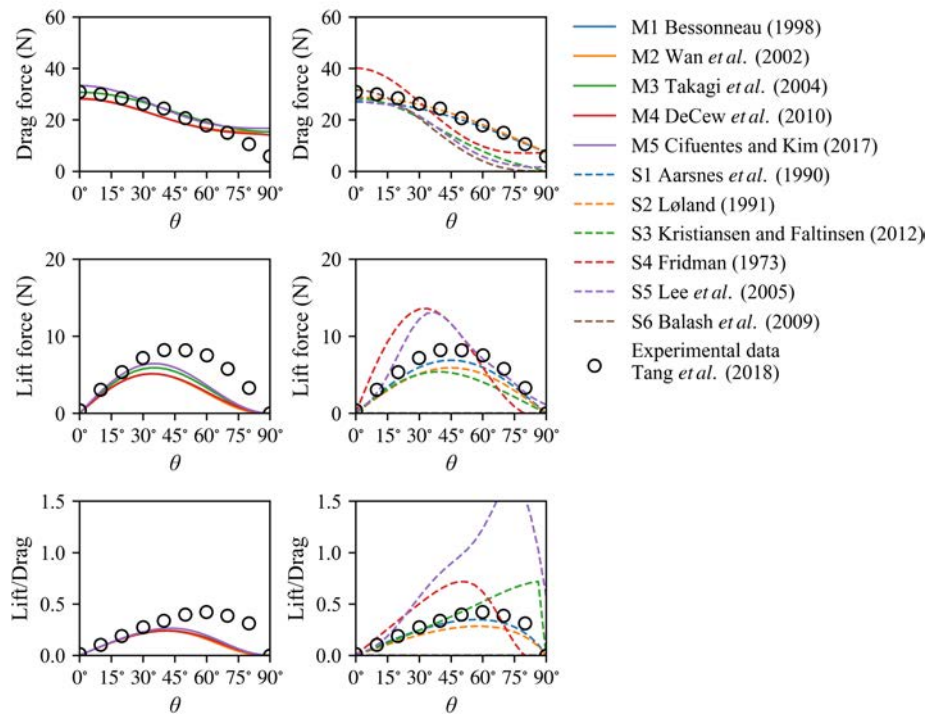


Figure 2-18. Drag and lift with respect to different inflow angles when the flow velocity is 0.6m/s. The left subplots are the simulation results using Morison model M1-M5 (solid lines). The right subplots are the simulation results using Screen model S1-S6 (dashed lines).

2 Hydrodynamic modelling of marine aquaculture structures

The lift first increases and then decreases with the increasing θ according to the experimental data by Tang *et al.* (2018), as shown in Figure 2-18. In general, the lift curves are in line with the shape of the sine function. For Morison model M1-M5, the predicted lifts are similar to each other, and all of them are smaller than the experimental results when $\theta > 30^\circ$. The underestimations of lift might cause underestimations of fish cage deformations. Screen model S4-S5 overestimate the lift force when $15^\circ < \theta < 45^\circ$ due to their large lift coefficients; S1 -S3 slightly underestimate the lift when $30^\circ < \theta < 60^\circ$; S6 has zero lift due to the lack of formulas for C_L .

The lift-to-drag ratio is a dimensionless parameter, showing the relationship between lift and drag. This parameter is important in the aerodynamic design of airfoils. As shown in Figure 2-18, the experimental data indicate that the maximum lift-to-drag ratio is 0.5. Because of the large porosity of net panels, the water flow can easily pass through the net panel. Thus, it is expected to observe this small lift-to-drag ratio in the experiment. For the Morison model M1-M5, the curves of the lift-to-drag ratio are close to each other. The results using M1-M5 can well agree with the experimental results when $\theta < 30^\circ$ but underestimate the lift-to-drag ratio when $\theta > 30^\circ$. For Screen model, the curves of the lift-to-drag ratio are distinct among S1-S5: S1 and S2 are close to the experimental results; S3 can agree with the experimental results when $\theta < 60^\circ$ but overestimate the lift-to-drag ratio when $\theta > 60^\circ$; S4 does not agree with the experiments for all θ . The curve of lift-to-drag ratio using S5 can be larger than 1 when $\theta > 60^\circ$, which is two times

2.5 Comparative study on hydrodynamic force models

higher than the experimental value. This irrational relationship could lead to incorrect simulations where S5 is applied to the dynamic analyses of fish cages.

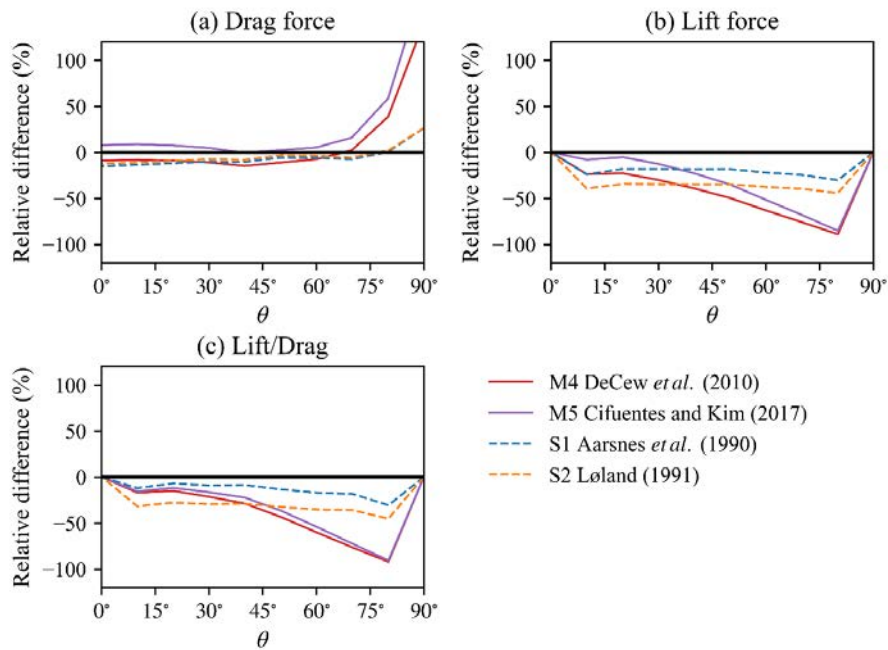


Figure 2-19. The relative difference between predicted and experimental results. The relative difference = (predicted results-experimental results) / experimental results $\times 100\%$.

Based on the aforementioned discussion on the drag and lift, four hydrodynamic force models, *i.e.*, M4, M5, S1 and S2, are chosen to calculate the relative difference between their predicted results and the experimental results. As shown in Figure 2-19 (a), the drag loads predicted by the four models are within 5% of the experimental results when $\theta < 70^\circ$. However, the drag loads predicted by Morison models are more than twice of the experimental results when $\theta > 70^\circ$, due to the lack

2 Hydrodynamic modelling of marine aquaculture structures

of the twine-to-twine wake effect. These overestimations were also observed by Endresen *et al.* (2013).

According to Figure 2-19(b), the lifts predicted by M4-M5 are less than half of the experimental results when $\theta > 45^\circ$. The underestimated lift together with the overestimated drag might lead to incorrect results when $\theta > 45^\circ$. Thus, the global responses of fish cages can be wrong. On the other hand, the lift and lift-to-drag ratios predicted by S1-S2 agree with the experimental results better than those predicted by M4-M5, especially when $\theta > 45^\circ$. In particular, the relative difference of S1 is less than 10% in Figure 2-19(c).

2.6 Conclusions and recommendations

In Chapter 2, the Morison model and the Screen model for calculating hydrodynamic loads on aquaculture nets are reviewed. Based on the results in the comparative study, the following conclusions are given:

1. When the water flow is perpendicular to the net panel ($\theta = 0^\circ$), the drag on knotless nylon nets can be well predicted by all the hydrodynamic force models except for S4, which is originally for knotted nets. The discrepancies between experimental data and the predicted forces can be as low as 0.4% when the flow velocity is 1 m/s.
2. For metal nets with smooth surfaces, all the hydrodynamic force models overestimate the drag. That is because all these models were initially developed for twisted or braided nets with rough surfaces. Further investigations are needed to develop a new hydrodynamic force model for metal nets.
3. Knots can bring additional drag on nets. The Morison model can underestimate the drag on knotted nets if the effects from knots are not considered. As for the Screen model, the drag on the knotted net can only be well predicted by S4 and S6.
4. When the water flow is not perpendicular to the net panel ($0^\circ < \theta \leq 90^\circ$), drag predicted by the Morison modes are within 5% of the experimental results if $\theta < 70^\circ$. However, the predicted drag can be two times higher than the experimental results when $\theta > 70^\circ$, due to the lack of the twine-to-twine wake effect. As for the

2 Hydrodynamic modelling of marine aquaculture structures

Screen model, which can include the twine-to-twine wake effect implicitly, the predicted drag is within 10% of the experimental results for all inflow angles.

5. For modelling the hydrodynamic loads on nets, the Morison model has a significant defect compared to the Screen model. Because the Morison model does not include the twine-to-twine wake effect, the hydrodynamic loads on a net panel can be overestimated when the inflow angle is large. This will make the dynamic analyses inaccurate and unreliable for the structural design.

2.6 Conclusions and recommendations

3 Structural modelling of marine aquaculture structures

The content is partly published as:

Cheng, H., Li, L., Aarsæther, K.G., Ong, M.C., 2020. Typical hydrodynamic models for aquaculture nets: A comparative study under pure current conditions. *Aquacultural Engineering* 90, 102070.

Cheng, H., Li, L., Ong, M.C., 2022. Comparative study of five commonly used gravity type fish cages under pure current conditions. *Ocean Engineering* 250, 110977.

3.1 Introduction to the structural modelling methods

In order to understand the dynamic responses of marine aquaculture structures as well as other net-included marine structures under the action of currents and waves, considerable studies have been conducted based on the three methods: physical model experiments, numerical simulations and field measurements. According to the Moore's law (Moore, 1968), the computational power was tremendously increased, and the cost of computers was declined in the last 60 years. Thus, numerical simulations become the inexpensive and time-saving method compared to the other two methods. Therefore, many numerical modelling methods have been proposed in the past decades.

Based on the shape and dimension of the element, the structural elements can be categorized into zero-dimensional (0D) element, one-dimensional (1D) element, two-dimensional (2D) element and three-dimensional (3D) element, according to Okereke and Keates (2018). For modelling the global response of marine aquaculture structures, three models, *i.e.*, mass-spring model, truss finite element model and triangular finite element model, are commonly used. These three models will be discussed in the following subsections. The selection of models is dependent on the application, level of details required from the model, technical know-how for the user and availability of computational resources for running FEM programs.

3 Structural modelling of marine aquaculture structures

3.1.1 Mass-spring model (0D)

The mass-spring model is simple and has been widely applied to various applications. In this model, the net is modeled as a set of lumped mass points and interconnected massless springs. All the loads, such as drag, buoyancy, gravity and tension, will be summed up based on individual mass points. The equation governing the motion of mass points is given as:

$$(m + m_a)\ddot{\mathbf{q}} = \mathbf{F}_{D(\dot{\mathbf{q}})} + \mathbf{B}_{(\mathbf{q})} + \mathbf{W}_{(\mathbf{q})} + \mathbf{T}_{(\mathbf{q})} \quad (3-1)$$

where m and m_a are the mass and the added mass of point, \mathbf{q} is the displacement of the mass point, \mathbf{F}_D is the drag, \mathbf{B} is the buoyancy, \mathbf{W} is the gravity, and \mathbf{T} is the tension in the spring between mass points. The variable in the bracket of each load represents the dependent variable. Figure 3-1 shows a more complex mass-spring model for a netting, where the shear force and bending moment are also considered in addition to the axial force (tension). However, for most nets in fish cages and fishing gears, the dynamic responses of the structure can be accurately simulated even only considering the axial force.

As shown in Table 1-1, the mass-spring model is employed in many programs and codes, especially in the specialized program/code for the design of marine aquaculture structures and fishing gears. Bessonneau and Marichal (1998) proposed a method using the mass-spring model to study the dynamics of submerged nets with applications

3.1 Introduction to the structural modelling methods

to trawl nets. Lader *et al.* (2001) developed a simple 2D model using the mass-spring model to analyze the dynamic response of net panels; and Lader *et al.* (2003) extended the 2D model to 3D model with an application to the dynamic analysis of a fish cage. Cha and Lee (2002) and Lee (2002) developed a mass-spring model for the dynamic analysis of midwater trawl, and Lee *et al.* (2008) later applied the model to the dynamic simulation of a fish cage under the action of currents and waves. Takagi *et al.* (2004), Huang *et al.* (2006) and Zhao *et al.* (2007) developed the mass-spring model and applied it to the dynamic analysis of fish cages. Their numerical models can give accurate predictions compared with validation experiments.

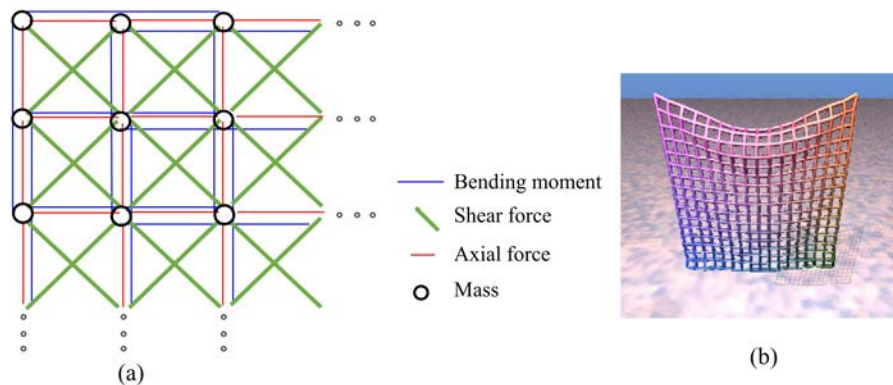


Figure 3-1. The mass-spring model for netting. (a) shows the springs with respect to different loads. (b) shows the deformation of netting by gravity (reproduced from Provot, 1995).

Strictly speaking, this mass-spring model is not a standard element in typical FEM (Okereke and Keates, 2018). The lumped mass technique, where point masses are defined at nodes, usually comes together with the mass-spring model (Xu and Qin, 2020). This method

3 Structural modelling of marine aquaculture structures

has been widely used for cloth simulations in computer graphics, video games and film industries (Provot, 1995). Although this model has a wide range of applications, critical numerical issues, such as numerical oscillation, numerical damping and locking issues, need to be well addressed in the numerical simulation.

3.1.2 Truss finite element model¹ (1D)

The truss finite element model is also commonly used for the dynamic analysis of marine aquaculture structures, and it has also been applied to many other industrial applications. This element type was originally developed for structural analyses of small-displacement structures. With further development, this element can be used for dynamic analyses of structures with large displacement and rotation in marine environments. The element name may be changed accordingly, such as “LINK180” in ANSYS, “CABLE” in Code_Aster and “T3D3” in ABAQUS. The equations governing the global motion of the structure can be:

$$[M + M_a]\ddot{\mathbf{q}} + [C]\dot{\mathbf{q}} + [K]\mathbf{q} = \mathbf{F}_D(\dot{\mathbf{q}}) + \mathbf{B}(\mathbf{q}) + \mathbf{W}(\mathbf{q}) \quad (3-2)$$

where the $[M+M_a]$ is the mass matrix, $[K]$ is the global stiffness matrix, $[C]$ is the damping matrix, \mathbf{F}_D is the hydrodynamic loads, \mathbf{B} is the buoyancy and \mathbf{W} is the weight. Figure 3-2 shows the application of

¹ The element name may be varied in different programs or codes.

3.1 Introduction to the structural modelling methods

“CABLE” element to simulate the deformation of a fish cage under the action of water flow.

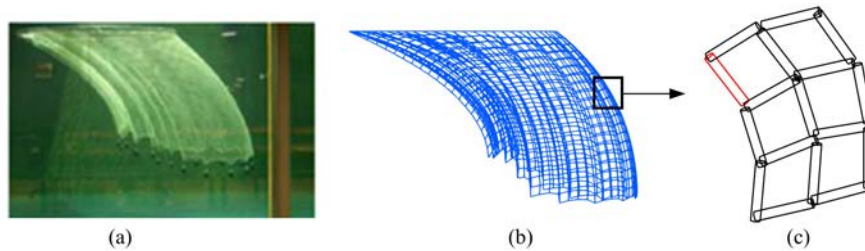


Figure 3-2. Illustration of the truss finite element model for modelling a fish cage. (a) shows the deformation of a fish cage under the action of water flow (reproduced from Moe-Føre *et al.*, 2016). (b) shows a numerical simulation result using a line-like finite element (reproduced from Cheng *et al.*, 2020). (c) shows the connection of elements, where the hydrodynamic load on the red bar can be calculated using the Morison type hydrodynamic force model as shown in Section 2.2.

Tsukrov *et al.* (2003) proposed a consistent finite element (a line-like element) to analyze the structural responses of offshore aquaculture fish cages under the action of currents and waves. This finite element is developed in the Aqua-FE computer program (the latest version of the software is called Hydro-FE), and it is successfully applied to the dynamic analyses of fish cages and mussel longlines (Shainee *et al.*, 2013; DeCew *et al.*, 2010; Knysh *et al.*, 2021, 2020). Moe *et al.* (2010) modeled the fish cage with the truss finite element and found the tensions in ropes and netting of full-size fish cages were much below the design capacity. Li *et al.* (2013) studied the dynamic responses of a fish cage in waves and currents using ABAQUA program. Cheng *et al.* (2018) studied deformations of and drag on a single-point mooring fish cage using ANSYS program.

3 Structural modelling of marine aquaculture structures

The spatial discretization process is similar to the mass-spring model and truss finite element model. For modelling netting, the nodes are usually located at the intersection of twines (or the knots), and the elements are usually aligned with the twine. For modelling a rope, the elements are usually linked with nodes and are aligned with the rope. The main difference between these two models is the governing equations and their solving method. The solution techniques of Eq.(3-1) are usually based on the backward Euler method or the Runge-Kutta methods. The solution techniques of Eq.(3-2) are usually based on the Newmark- β method for the time integration and the Newton-Raphson iteration scheme to find nodal displacement at every time step. According to the comparison by Zhao *et al.* (2015), the two models have a similar accuracy compared against the model experiments. Both models can be utilized to design marine aquaculture structures provided an appropriate safety factor.

3.1.3 Triangular finite element model (2D)

An interesting triangular finite element proposed by Priour (1999) can also be applied to the dynamic analysis of nettings. In the book by Priour (2013), the construction of the triangular finite element for netting is described in detail. This model was originally proposed for the dynamic analyses of fishing gears, especially the trawl net. Later, it was successfully applied to the dynamic analyses of fish cages (Priour, 2014; Moe-Føre *et al.*, 2015).

3.1 Introduction to the structural modelling methods

Figure 3-3 illustrates the application of triangular finite element to a net panel. In this 2D element, the properties of the physical mesh shape (as shown in Table 2-1) can be described by the local shape and stiffness matrix, and the edges of the triangular finite element are not necessarily aligned with the twines. Thus, in the spatial discretization process, the nodal positions do not need to change according to the physical mesh shape, *i.e.*, the same set of nodes and elements can be applied to the modelling of square, rhombic and hexagonal netting. This can save considerable effort in the spatial discretization process.

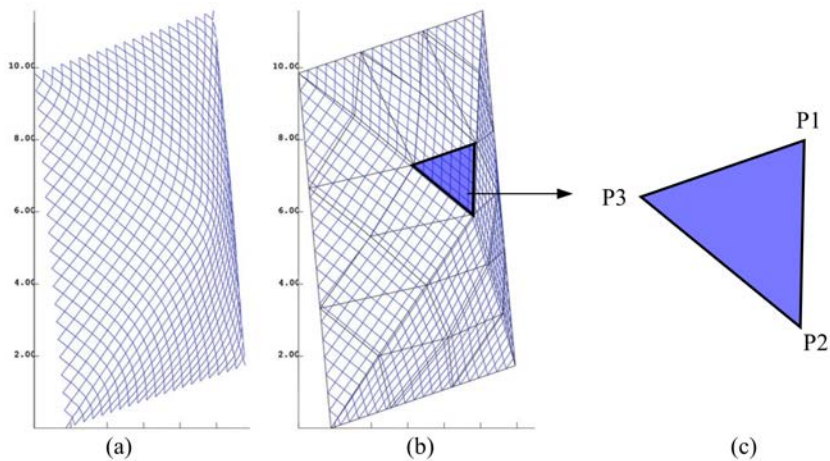


Figure 3-3. The triangular finite element model for netting. The illustration is reproduced from Priour (2013). (a) is a piece of netting with a rhombus mesh shape. (b) is the represented numerical model using the triangular finite element model proposed by Priour (2013). (c) is one triangular finite element where the hydrodynamic load can be calculated using the Screen type hydrodynamic force model as shown in Section 2.3.

Essentially, equations governing the global motion of the structure are the same with Eq.(3-2) as described in Section 3.1.2. Only the assemblies of the local matrices to the global matrices are different due

3 Structural modelling of marine aquaculture structures

to the different element shapes. Thus, the same solution techniques of Eq.(3-2) are also valid for the triangular finite element model.

3.1.4 Tetrahedral/hexahedral finite element model (3D)

These 3D finite elements are well developed in many general-purpose FEM programs and are applied to many complex problems in structural mechanics. However, the 3D finite elements are not commonly used for the global dynamic analysis of netting-related structures under the action of currents and waves, because the global dynamic analyses usually do not need a high level of details, such as the stress distribution on the cross-section of a rope and the stress distribution on a knot in a net panel. For the sake of thesis completeness, these elements are briefly introduced by showing a few examples.

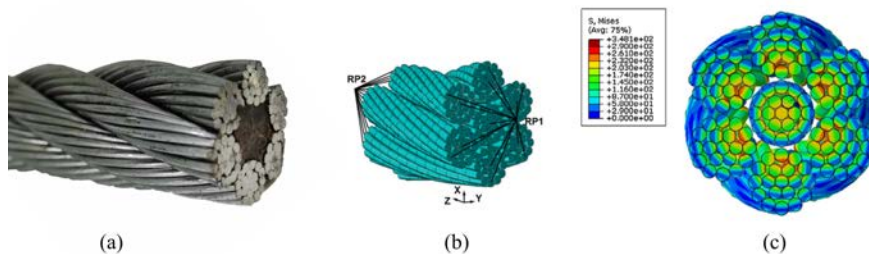


Figure 3-4. Mechanical analysis of a section of rope (reproduced from Wang *et al.*, 2013). (a) shows a section of steel wire rope. (b) shows the numerical model of the net panel using a 3D solid finite element. (c) shows the distribution of equivalent stress on the cross-section under an axial strain of 0.001.

Figure 3-4 and Figure 3-5 present the application of the 3D finite element in the mechanical analysis of the rope and netting. These 3D elements are suitable for the mechanical analysis of a local component in marine aquaculture structures.

3.1 Introduction to the structural modelling methods

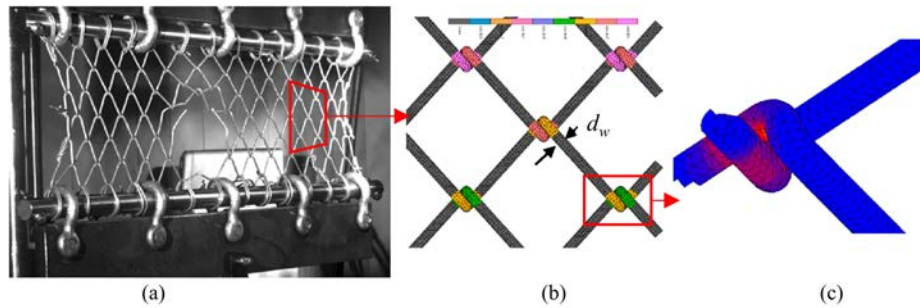


Figure 3-5. Mechanical analysis of a piece of chain-link netting (reproduced from Drach *et al.*, 2016). (a) shows the tension strength testing of the chain-link net panel. (b) shows the numerical model of the net panel using a 3D solid finite element. (c) Distribution of the equivalent stress at the local position.

3.2 Structural model

3.2.1 Finite element constitution

The structural element used in this thesis is a one-dimensional finite element denoted as “CABLE” in the structural solver, which was initially developed to calculate the mechanical behavior of overhead electrical lines. This element has perfectly flexible characteristics and cannot sustain any bending moments and torsion. As this element type allows great displacements in the nonlinear dynamic analysis, it is suitable for representing highly flexible line-like structures. Thus, the “CABLE” element is suitable for modelling cable and nets (Antonutti *et al.*, 2018). As illustrated in Figure 3-6, one “CABLE” element has six nodal degrees of freedom (DOFs, three components at each node) in the global coordinate system, which corresponds to the translations at its two nodes. The linear shape functions (N) are used to express the deformation of the element (\hat{q}) in the global coordinate system as a function of the vector of DOF (q):

$$\hat{q} = \begin{bmatrix} 1 - \xi & 0 & 0 \\ 0 & 1 - \xi & 0 \\ 0 & 0 & 1 - \xi \end{bmatrix} \begin{bmatrix} q_x^i \\ q_y^i \\ q_z^i \end{bmatrix} + \begin{bmatrix} \xi & 0 & 0 \\ 0 & \xi & 0 \\ 0 & 0 & \xi \end{bmatrix} \begin{bmatrix} q_x^j \\ q_y^j \\ q_z^j \end{bmatrix} \quad (3-3)$$

where ξ is the strain, and the two square matrixes are the shape functions (N).

3.2 Structural model

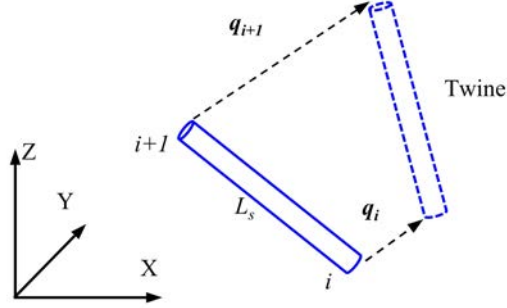


Figure 3-6. Illustration of the “CABLE” element.

$$[\mathbf{M}] = \frac{\rho_s \pi d_{ws}^2}{4} \int_{x=0}^{L_s} \mathbf{N} \mathbf{N}^T dx \quad (3-4)$$

$$[\mathbf{K}] = \frac{\pi d_{we}^2 E}{4} \int_{x=0}^{L_s} \mathbf{B} \mathbf{B}^T dx \quad (3-5)$$

The mass matrix (\mathbf{M}) and stiffness matrix (\mathbf{K}) for one structural element are shown in Eqs.(3-4) and (3-5), where $\mathbf{B} = \mathbf{J}^{-1} \frac{\partial \mathbf{N}}{\partial x}$ is the element strain-displacement transformation matrix, \mathbf{J} is the Jacobian matrix, d_{ws} is the structural diameter, d_{we} is the elastic diameter, and L_s is the length of one element. The detailed explanations of d_{ws} and d_{we} are given later in Section 3.2.3. After assembling the contributions from individual elements and concentrating all the environmental loads to nodes, the structural responses are calculated using Eq.(3-6).

3.2.2 Governing equations for dynamic analysis

In this thesis, the structural responses are calculated based on the FEM, where the net is divided into a set of one-dimensional elements. The

3 Structural modelling of marine aquaculture structures

equation governing the motions of nodes in the Cartesian coordinate system is:

$$[\mathbf{M}]\ddot{\mathbf{q}} + [\mathbf{K}]\mathbf{q} = \mathbf{F}_g + \mathbf{F}_b + \mathbf{F}_h \quad (3-6)$$

where \mathbf{q} is the time-dependent vector of nodal displacements, \mathbf{M} is the mass matrix, \mathbf{K} is the stiffness matrix, \mathbf{F}_g is the nodal force vector due to gravity, \mathbf{F}_b is the nodal force vector for buoyancy forces, and \mathbf{F}_h is the nodal force vector for the hydrodynamic loads, which can be calculated using the models presented in Sections 2.2 and 2.3. \mathbf{F}_g is simple and only calculated once in the initialization step, and they are constant throughout numerical simulations. \mathbf{F}_b is the buoyancy and is calculated based on the relative position of structures to the water level.

The system is highly nonlinear because \mathbf{F}_h depends on the time, the square of nodal velocities, and structural deformations. According to Antonutti *et al.* (2018), the system nonlinearity can cause high-frequency oscillations and bring challenges for the simulations to reach convergence. In the present structural solver, the solution technique for Eq.(3-6) is based on the unconditionally stable Hilber-Hughes-Taylor- α (HHT- α) method, which introduces low numerical damping in the low-frequency band and high damping at the high-frequency band. The temporal integration of Eq.(3-6) is:

3.2 Structural model

$$\begin{aligned} M\ddot{q}_{i+1} + (1 - \alpha)Kq_{i+1} + \alpha Kq_i \\ = (1 - \alpha)(F_s + F_h)_{i+1} + \alpha(F_s + F_h)_i \end{aligned} \quad (3-7)$$

$$q_{i+1} = q_i + \Delta t \dot{q}_i + \Delta t^2 [(0.5 - \beta)\ddot{q}_i + \beta\ddot{q}_{i+1}] \quad (3-8)$$

$$\dot{q}_{i+1} = \dot{q}_i + \Delta t [(1 - \gamma)\ddot{q}_i + \gamma\ddot{q}_{i+1}] \quad (3-9)$$

where Δt is the time increment. The parameters α , β and γ are satisfied:

$$0 \leq \alpha \leq \frac{1}{3}, \quad \beta = \frac{(1 + \alpha)^2}{4}, \quad \gamma = \frac{1}{2} + \alpha \quad (3-10)$$

3 Structural modelling of marine aquaculture structures

3.2.3 Mesh grouping method

In a full-scale fish cage, the netting is usually composed of thousands of small twines. It is impractical to build a numerical model twine by twine. A mesh grouping method is usually applied to the spatial discretization process to reduce the computational effort (Cheng *et al.*, 2018; Zhao *et al.*, 2007). In the present structural model, the material properties of the numerical model are assumed the same as that of the physical net. In order to acquire the correct solutions, the \mathbf{M} , \mathbf{K} , \mathbf{F}_s and \mathbf{F}_h in Eq.(3-6) should be consistent between the physical and numerical nets. To satisfy the consistency of the aforementioned variables, three derived diameters, *i.e.*, structural diameter (d_{ws}), elastic diameter (d_{we}) and hydrodynamic diameter (d_{wh}), are applied in the spatial discretization process. The detailed derivation is illustrated in Section 3.6, and only the final relationships between the three numerical diameters and the physical twine diameter (d_{w0}) are presented here:

$$\lambda = L_s / L_0; d_{ws} \approx \sqrt{\lambda} d_{w0}; d_{wh} = \lambda d_{w0} \quad (3-11)$$

where λ is the ratio between the half mesh size of the numerical net (L_s) and the half mesh size of the physical net (L_0). For a full-scale fish farm facility, λ is usually in the range of 20 to 80.

3.3 Implementation of hydrodynamic force models

The general-purpose FEM program, Code_Aster, is selected as the structural solver in this thesis. Code_Aster was developed in Électricité de France (EDF) for the thermo-mechanical study of structures (EDF, 1989-2017). With over 30-year development, this software offers 400 types of finite elements and a broad range of solvers. It can conduct many types of FEM analyses, such as static, dynamic, vibrational analyses and modal analyses. Since this FEM program is open-source, it can be extended with additional functionalities. However, this FEM program has very few applications to dynamic analyses of structures under the action of currents and waves (Antonutti *et al.*, 2018).

In order to conduct dynamic analyses of marine aquaculture structures under the framework of Code_Aster, a numerical module is developed in this thesis. This module, named as UiS-Aqua, is stored in this repository (<https://github.com/hui-aqua/HydroModules>), together with detailed documentation and examples. The simulation process with this module is described in Section 3.3.1.

3.3.1 Simulation process

The flowchart for the simulation process is presented in Figure 3-7, together with the UiS-Aqua module highlighted by the red dashed box. The UiS-Aqua module is invoked at each time step to calculate the hydrodynamic loads on the nets, ropes and pipes, and to map these loads onto corresponding nodes. Two types of hydrodynamic force models,

3 Structural modelling of marine aquaculture structures

i.e., Screen model and Morison model, can be applied to different components to improve the accuracy. Moreover, UiS-Aqua can also be applied to coupled simulations with OpenFOAM (see Figure 4-6).

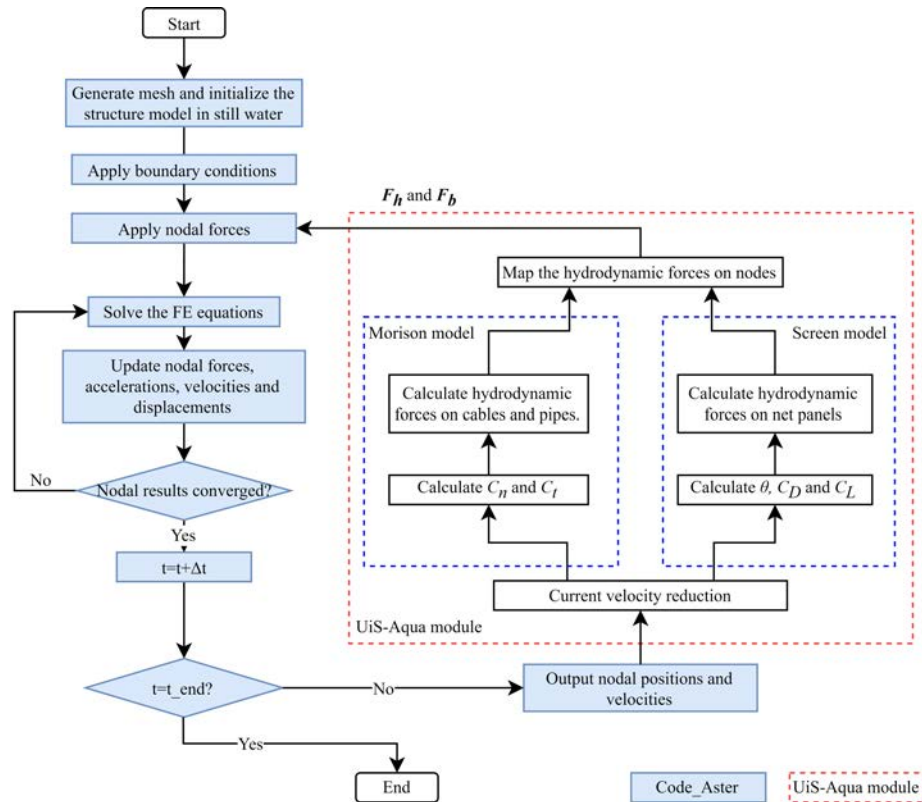


Figure 3-7. Flowchart for the simulation process under the framework of Code_Aster.

3.3.2 Features of the UiS-Aqua numerical module

This newly developed module mainly includes the three submodules: *enviromentModules*, *hydroModules* and *meshModules*. Figure 3-8 shows the main contents of this module in a tree-like format. This module is written in Python programming language with many advanced features.

3.3 Implementation of hydrodynamic force models

3.3.2.1 Modularity

The UiS-Aqua is developed in a modular style with the goal of minimizing dependencies. The code is split into different files and submodules based on the corresponding functionalities, as shown in Figure 3-8.

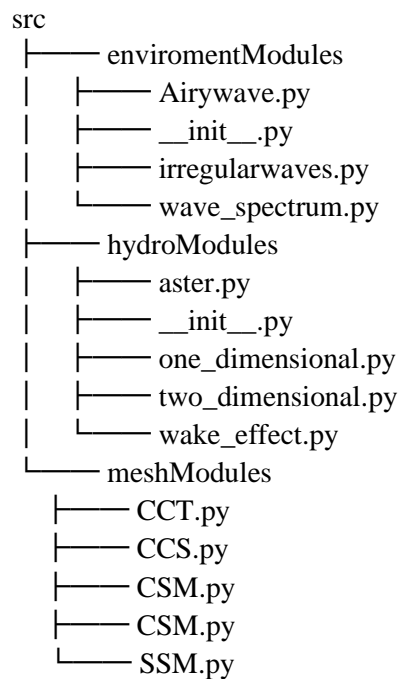


Figure 3-8. Contents of the UiS-Aqua numerical module in a tree-like format.

In *hydroModules*, a wide range of hydrodynamic force models are provided for different nets in dynamic analyses of aquaculture structures. The flow velocity reduction due to wake effects is also included in this submodule. Besides, a template for the user-defined hydrodynamic force model is also provided for the study of new nets in the future. In

3 Structural modelling of marine aquaculture structures

enviromentModules, various wave models, such as Airy waves, Stokes 2nd order waves and irregular waves, are provided. In *meshModules*, the numerical models for commonly used traditional fish cages can be easily built up based on the main design parameters.

Moreover, the submodules can be imported to different projects or other modules. As shown in Figure 3-9, “irregularwaves.py” imports “Airywave.py” for the irregular random waves, based on the summation of sinusoidal wave components. Thus, the code is readable, reliable and maintainable without too much effort.

```
import numpy as np
from . import Airywave as wave

class summation:
    """
    Irregular random waves, representing a real sea state,
    can be modelled as a summation of sinusoidal wave components.
    DNV-RP-C205, Section 3.3.2.1
    """
    def __init__(self, waveSpectrum, water_depth, wave_direction):
        """
        Parameters
        -----
        waveSpectrum: A n*2 array list of wave spectrum, the first column is
w, the second is the S(w)
        water_depth: water depth of the sea, assume flat sea floor. A position
number | float | Unit [m]
        wave_direction: direction of wave propagation. | float | Unit [degree]
        """
        self.water_depth = water_depth
        self.list_of_waves = []
```

3.3 Implementation of hydrodynamic force models

```
d_fre = abs(waveSpectrum[1, 0]-waveSpectrum[0, 0])
for each in waveSpectrum:
    xi = np.sqrt(2 * d_fre * each[1])
    wave_period = 2 * np.pi / each[0]
    self.list_of_waves.append(wave.Airywave(
        xi * 2, wave_period, water_depth, wave_direction,
        np.random.uniform(0, 360)))
```

Figure 3-9. A piece of code in irregularwaves.py

3.3.2.2 Embeddability

Due to the embeddability feature of the Python programming language, the UiS-Aqua can be embedded with the Code_Aster, which is written using the Fortran programming language. With the UiS-Aqua, Code_Aster can be applied to computationally efficient decoupled simulations to analyze the dynamic responses of fish cages. Moreover, UiS-Aqua can also be invoked in other open-source programs for different purposes, *e.g.*, the two-way coupled simulations with OpenFOAM in Chapter 4 for the complex FSI problem in marine aquaculture structures.

3.3.2.3 Vectorization

Usually, processing a large array of data using Python can be slow as compared to other programming languages, *e.g.*, C/C++. The main reason for this slow computation is due to the dynamic nature of Python and the lack of compiler-level optimizations. In UiS-Aqua, a vectorization technique from Numpy module is implemented to deal with a large array of data. The functions defined by Numpy module are highly optimized that can significantly reduce the elapsed time of code.

3 Structural modelling of marine aquaculture structures

An example shown in Figure 3-10 illustrates the significant speed-up of the vectorization technique. This example mimics a function inside of “irregularwaves.py”. This function can return a time-series wave particle velocity (u_x , u_y , u_z) at one position based on the summation of the velocity from sinusoidal wave components. In this example, the first function uses the Python for-loop to do the summation and the second function uses the vectorized array operation with Numpy module. The results show that the vectorized array operation can be 1 284 times faster than the pure Python equivalents.

```
import numpy as np
from timeit import Timer

time_list = np.arange(0, 3600, 1)
n_wave = 3000
n_time = len(time_list)
waves_velocities = np.zeros((n_wave, len(time_list), 3))
for i in range(n_wave):
    waves_velocities[i] = np.random.rand(n_time, 3)

def sum_using_forloop():
    velocity_with_time = np.zeros((n_time, 3))
    for i in range(n_time):
        for j in range(n_wave):
            velocity_with_time[i] += waves_velocities[j, i]

def sum_using_numpy():
    velocity_with_time = np.zeros((n_time, 3))
    velocity_with_time = np.sum(waves_velocities, axis=0)

time_forloop = Timer(sum_using_forloop).timeit(1)
time_numpy = Timer(sum_using_numpy).timeit(1)
```

3.3 Implementation of hydrodynamic force models

```
print("Summing elements takes %.9f units using for loop" % time_forloop)
print("Summing elements takes %.9f units using numpy" % time_numpy)
```

output:

```
Summing elements takes 26.986129200 units using for loop
Summing elements takes 0.021073700 units using numpy
```

Figure 3-10. Compare the performance of a non-vectorized summation to a vectorized one.

3.4 Validation for the structure solver

3.4.1 Net hanging in the air

3.4.1.1 Case setup

The numerical model is set up based on the experiment by Lee *et al.* (2005). In the experiment, the net is 12×18 meshes in squared shape with twine diameter $d_w = 0.4$ mm and half mesh size $L = 100$ mm. The Young's modulus of the twine is 119.37 MPa. The four corners are fixed, and three sinkers, whose masses are 0.5 kg, 1.5 kg and 0.7 kg from left to right in Figure 3-11 (a), are hung in the middle of the net. In the numerical simulation, the characteristics and configuration of the net are the same as those in the experiment. The net is modeled by 424 line-like elements and 213 nodes. The three hung sinkers are represented by three concentrated vertical forces, which are 5 N, 15 N and 7 N from left to right. The density of the twine is assigned 1 125 kg/m³ by assuming the material is Nylon (Moe *et al.*, 2010).

3.4.1.2 The shape of the netting

The final shape of the net from the numerical simulation is shown in Figure 3-11(b). Regarding the iterative convergence, the criterion is that the maximum force residue is less than 2e-5. The simulation converges after 200 iterations by using 25.7 s. Regarding the consistency in the solution, the balance of forces in the vertical direction is checked. The total reaction force on the four fixed nodes in the vertical direction is 27.06 N which is equal and opposite to the sum of the wight of the net

3.4 Validation for the structure solver

0.06 N and the three concentrated forces 27 N. Through the two examinations, the FEM program, Code_Aster, is proved feasible to simulate the flexible net.

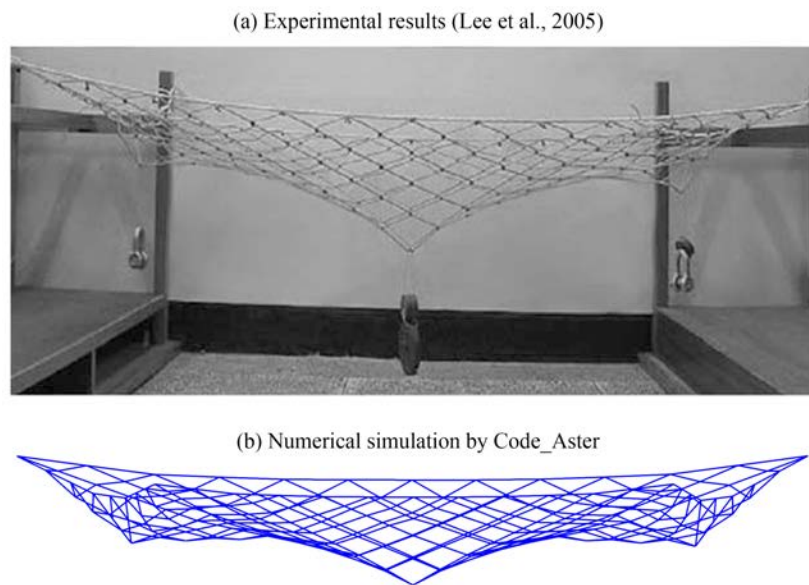


Figure 3-11. Comparison of the net shape between the experimental and the numerical results.

3 Structural modelling of marine aquaculture structures

3.4.2 Fish cage under the action of water flow

In this section, the Screen model S1, is selected to be used to reproduce the experiment by Moe-Føre *et al.* (2016) using the present numerical model. Since the twine-to-twine wake effect is already included in S1 implicitly, and its effect has been discussed in Section 2.4.1, this section is focused on the accuracy of the present numerical model and the net-to-net wake effect.

3.4.2.1 Case setup

The main parameters for the numerical models and corresponding experimental models are listed in Table 3-1. The nodes in the upper circumference of the numerical model are restricted from translational motion, representing the rigid and fixed steel ring in the physical model. In the experiments by Moe-Føre *et al.* (2016), each sinker is a circular steel cylinder with a diameter of 4 cm, a length of 6 cm, and a submerged weight of 5.15 N, as given in Table 3-1. In the numerical model, the 16 sinkers are represented by 16 vertical concentrated forces corresponding to the submerged weight. Figure 3-12 shows the physical and numerical fish cage models in still water. It can be observed that both the physical and numerical fish cages are slightly stretched in Z-direction due to the weights.

3.4 Validation for the structure solver

Table 3-1. The parameters of the fish cage.

	Experimental model	Numerical model
Cage diameter (m)	1.75	1.75
Cage height (m)	1.50	1.50
Submerged weight (N)	5.15×16	5.15×16
Weight diameter (m)	0.04	-
Weight height (m)	0.06	-
Twines Young's modulus (MPa)	40	40
Twines density (kg/m^3)	1140	1140
Net half mesh (mm)	25.5 (8.3) *	85.9 (85.9)
Net twine thickness (mm)	2.42 (1.41)	4.44 (2.59) **
Solidity	0.194 (0.347)	0.194 (0.347)

* The values in the bracket are for the high solidity net.

** The net twine thickness in the table refers to the structural diameter (d_{ws}). For the elastic diameter (d_{we}) and the hydrodynamic diameter (d_{wh}), please refer to Eq.(3-11).



Figure 3-12. The fish cage in still water is shown from the side: (a) the physical fish cage model by Moe-Føre *et al.* (2016). (b) the numerical fish cage model. The numerical model is subjected to the flow along the x-axis.

3 Structural modelling of marine aquaculture structures

The two forms of flow velocity reduction factor are applied to numerical models to study the wake effect. The expressions of the flow velocity reduction factor are shown as below:

$$r_u = f_1(Sn) = 1 - 0.46C_{D(Sn, \theta=0^\circ)} \quad (3-12)$$

$$r_u = f_2(Sn, \theta) = \max\left(\frac{\cos \theta + 0.05 - 0.38Sn}{\cos \theta + 0.05}, 0\right) \quad (3-13)$$

where Sn is the solidity of net, and θ is the inflow angle. Eq.(3-12) is the most commonly used formula in the dynamic analysis of fish cages (Løland, 1991; Aarsnes *et al.*, 1990; Kristiansen and Faltinsen, 2012; Moe-Føre *et al.*, 2016), in which r is dependent on solidity and keeps constant for all the rear half nets. Eq.(3-13) is a new regression formula using the least-squares method based on the sum of velocity reductions after cylinders according to Eq.(2-15). Moreover, the new formula considers solidity as well. According to the new formula Eq.(3-13), the nets with larger θ induce smaller flow velocity in their wake region. The comparisons between the two formulas with experimental results by Bi *et al.* (2013) and Patursson (2008) are shown in Figure 3-13. Based on the experimental results, values of r decrease with the increasing inflow angle. Compared to the commonly used formula, $r_u = f_1(Sn)$, the new formula, $r_u = f_2(Sn, \theta)$, shows better agreement with the experimental results.

3.4 Validation for the structure solver

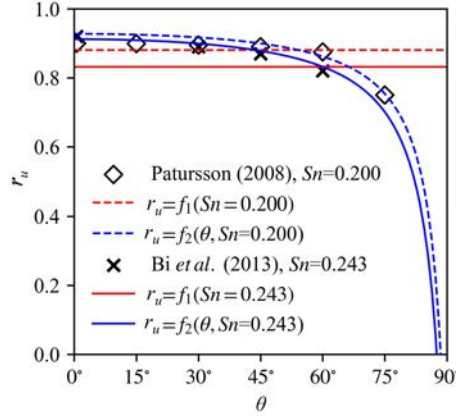


Figure 3-13. Comparison of the two formulas for r against experimental data.

3.4.2.2 Convergence studies

As it is the first time that the open-source FEM program, Code_Aster, is applied to the dynamic analysis of marine aquaculture structures, the feasibility of the solver should be assessed at the very beginning. In order to demonstrate the reliability of the implementation of the UiS-Aqua module with the FEM program Code_Aster, convergence studies on both computational mesh and time step are performed at first. The detailed setup of the numerical model is given later in Section 3.4.2.

In the convergence study of computational meshes, five different sets of computational meshes shown in Table 3-2, are created for the fish cage with a high solidity net in Table 3-1. Drag loads on the fish cage are estimated by using the five sets of computational meshes under a flow velocity of 1 m/s. As shown in Figure 3-14(a), the relative differences of drag loads are less than 3%, which demonstrates that the present mesh grouping method, as discussed in Section 3.2.3 and Section 3.6, is

3 Structural modelling of marine aquaculture structures

accurate for aquaculture nets. As shown in Table 3-2, with the increasing number of nodes (elements), the computer memory and computational time are increased, and the difference of the drag compared to the finest computational mesh (Mesh 5) is reduced. In order to achieve the results within 1% difference compared to the finest computational mesh (Mesh 5) and keep the computational costs low, Mesh 3 is chosen for the subsequent simulations. Using Mesh 3, the numerical model consists of 64 elements (64 nodes) with 85.90 mm length around the circumference and 16 elements (17 nodes) with 93.75 mm length over the depth. The total numbers of elements and nodes are 2 112 and 1 088 in the numerical model, respectively.

In the convergence study of time steps, four different time steps listed in Table 3-3 are applied in the simulations by using Mesh 3. Drag loads on the fish cage under different time steps are calculated under a water flow velocity of 1 m/s. As shown in Figure 3-14(b), the drag loads first increase then decay fast with oscillations as the time increases; After 6 s, all the simulations reach equilibrium. As shown in Table 3-3, the drag loads on the fish cage calculated with the four time steps reach the same value at the end of simulations. Increasing the time step can significantly reduce the computational time. Since the simulations are calculated under pure current conditions without any oscillating load, the studied time steps have neglectable influences on the final results as long as the simulation is converged. Therefore, the subsequent simulations are calculated using Mesh 3 with a time step of 0.2 s and a duration of 10 s.

3.4 Validation for the structure solver

Table 3-2. Mesh size, computational time and estimated drag with time step = 0.1s.

Mesh	Mesh 1	Mesh 2	Mesh 3	Mesh 4	Mesh 5
Number of nodes	320	672	1088	1840	2592
Number of elements	608	1296	2112	3600	5088
Length of element (mm)	171.81	114.54	85.90	68.72	57.27
$\lambda=L/8.3$	20.7	13.8	10.3	8.3	6.9
Computer memory (MB)	386.83	536.97	550.22	1007.80	1260.84
Computational time (s)	312.1	1169.8	2175.6	5189.2	10641.0
Drag (N)	210.0	211.9	212.6	213.3	213.6
Deviation	1.69%	0.94%	0.47%	0.14%	-

Table 3-3. Computational time and drag using Mesh 3 with different time steps.

Time step	$\Delta t=0.02s$	$\Delta t=0.05s$	$\Delta t=0.1s$	$\Delta t=0.2s$
Computational time (s)	9919.8	4005.8	2175.6	1201.8
Drag (N)	212.6	212.6	212.6	212.5

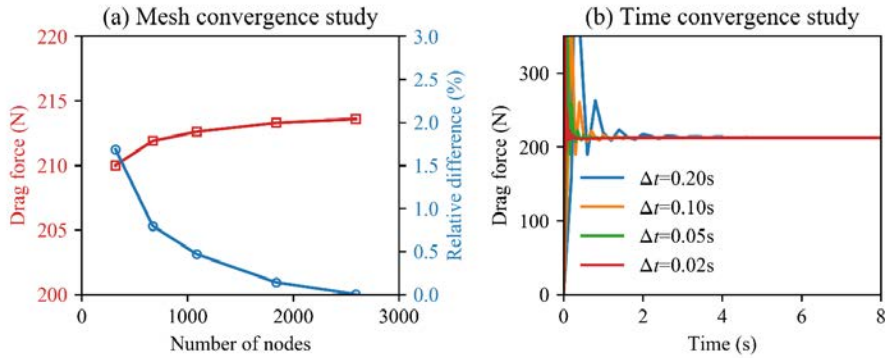


Figure 3-14. Convergence studies on both computational mesh and time step. In (a) Mesh convergence study, the relative difference is calculated by taking the drag in Mesh 5 as a reference value.

3 Structural modelling of marine aquaculture structures

3.4.2.3 Comparison of the cage deformation

Figure 3-15 and Figure 3-16 show the deformations of fish cages subjected to different current velocities with $Sn = 0.194$ and 0.347 , respectively. In the two figures, the red model uses $f_1(Sn)$ for the net-to-net wake, and the blue model uses $f_2(Sn, \theta)$ for the net-to-net wake. From the side view, the two models with different net-to-net wake effects have significant distinctions in the deformation, especially at the rear part. The model using $f_1(Sn)$ has larger deformation at the rear half of the fish cage. According to Figure 2-15 and discussions in Section 2.4, the equivalent drag coefficients of the downstream nets with a constant flow velocity reduction factor are much larger than the one with the variable flow velocity reduction factor, especially when $\theta > 30^\circ$. Therefore, the rear half of the cage experiences smaller drag and has less deformation when $f_2(Sn, \theta)$ is applied. In addition, the deformations at the frontal half of the fish cage are similar in the two numerical models, because the frontal nets experience the same current velocity in both models.

3.4 Validation for the structure solver

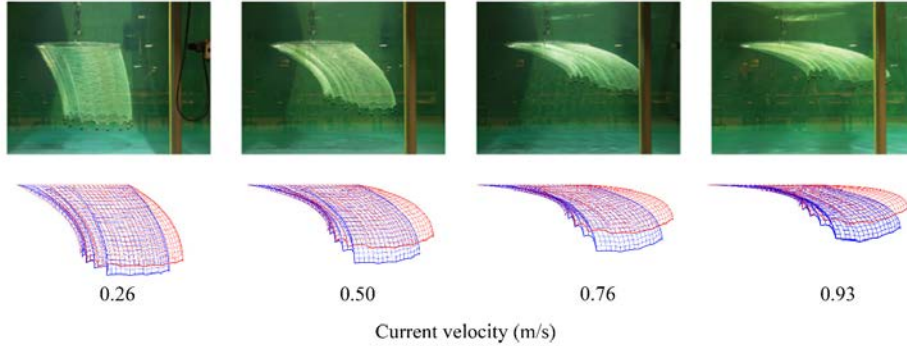


Figure 3-15. Comparison of experimental and numerical results subjected to different current velocities, $Sn = 0.194$. The red model uses $r_u = f_1(Sn)$ for the net-to-net wake, and the blue model uses $r_u = f_2(Sn, \theta)$ for the net-to-net wake.

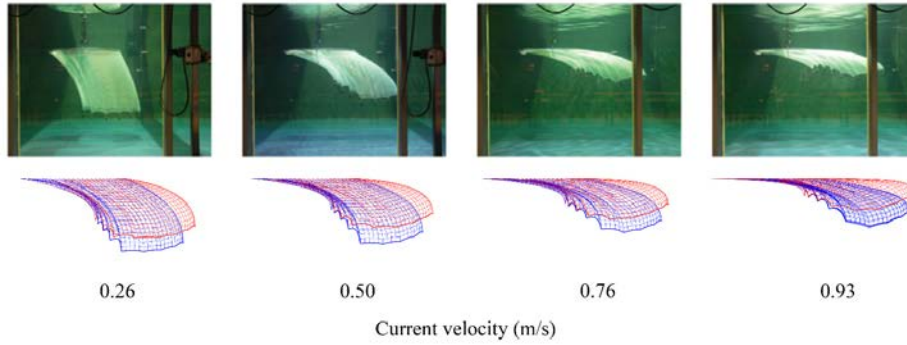


Figure 3-16. Comparison of experimental and numerical results subjected to different current velocities, $Sn = 0.347$. The red model uses $r_u = f_1(Sn)$ for the net-to-net wake, and the blue model uses $r_u = f_2(Sn, \theta)$ for the net-to-net wake.

Figure 3-17 shows the normalized height of the fish cage in numerical simulations with the two net-to-net wake effects. The normalized height is calculated as the height of fish cages at a given current velocity divided by the initial height of the fish cage (1.53 m). Since the bottom nodes of the fish cage are not in a horizontal plane, the height of the fish cage is calculated as the vertical distance between the lowest node and highest node. It can be observed that the height decreases with increasing current velocity. The height of the model

3 Structural modelling of marine aquaculture structures

using $f_2(Sn, \theta)$ is clearly larger than that using $f_1(Sn)$, and the distinctions become significant with increasing current velocity. In particular, when the $Sn = 0.347$, the normalized height of the fish cage is 0.26 for the model using $f_1(Sn)$, and 0.45 for the model using $f_2(Sn, \theta)$. The distinction in the height of fish cage can influence the design of the feeding system and on-site operations related to nets, as the height of the fish cage should be provided to make a precise decision.

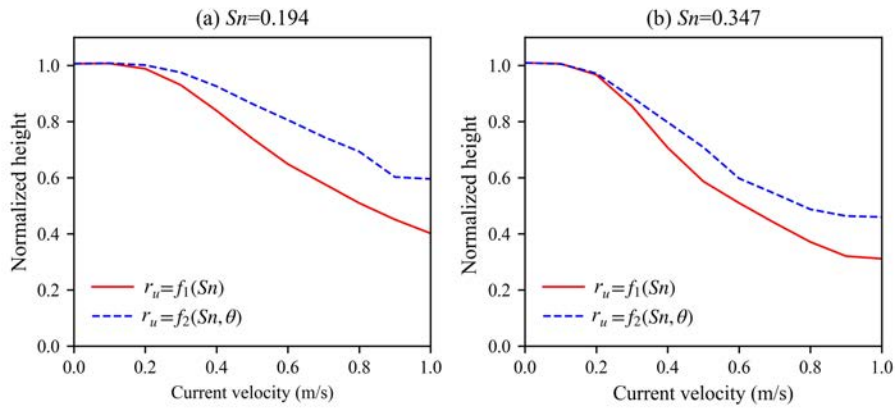


Figure 3-17. The normalized height of fish cages in numerical simulations with the two net-to-net wake effects.

3.4.2.4 Comparison of the drag

Figure 3-18 compares the drag from the numerical simulations using the two forms of r_u against experimental data from Moe-Føre *et al.* (2016). According to the experimental results: (1) the drag on the fish cage with low solidity ($Sn = 0.194$) net is nearly proportional to the current velocity; (2) the drag on the fish cage with high solidity ($Sn = 0.347$) net

3.4 Validation for the structure solver

increases slower with increasing current velocity when the velocities are above 0.5 m/s than that at lower velocities.

The calculated drag loads using both net-to-net wake models increase with increasing current velocity, and they are close to the experimental results when the current velocity is less than 0.5 m/s. Compared to the experiments conducted by Moe-Føre *et al.* (2016), the model using $f_1(Sn)$ overestimates the drag, especially when the current velocity is high, and the overestimations are more evident for the higher solidity fish cage. For the model using $f_2(Sn, \theta)$, the slope of the drag curve decreases when the current velocity exceeds 0.5 m/s, and the predicted drag loads agree with the experimental results quite well. In particular, the maximum difference between the numerical and experimental results is only 5% when using $f_2(Sn, \theta)$. And the drag on the fish cage can be as large as 30% higher than the experimental results when applying $f_1(Sn)$. According to the experimental photos in Figure 3-16, the fish cage has large deformation, *i.e.*, the nets have large θ , when the current velocity is high. Together with the comparison in Figure 3-13, which indicates that $f_1(Sn)$ highly overestimates the flow velocity reduction factor when $\theta > 70^\circ$, the drag on the downstream nets can be overestimated when applying $f_1(Sn)$. Therefore, the total drag on the fish cage is overestimated when using $f_1(Sn)$.

The comparison of the two net-to-net wake effects indicates that the commonly used expression, $f_1(Sn)$ is not sufficient to model the

3 Structural modelling of marine aquaculture structures

interaction between the fluid flow and nets (hydro-elasticity). The variable flow velocity reduction factor, $f_2(Sn, \theta)$, is recommended for numerical simulations of the fish cage with high solidity nets and subjected to high current velocities.

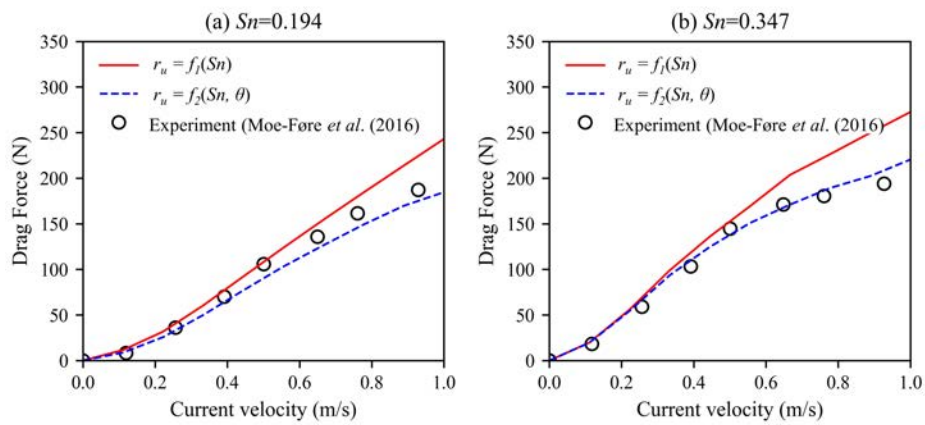


Figure 3-18. Measured and calculated drag in different current velocities using the two net-to-net wake effects.

3.5 Conclusions

In Chapter 3, the implementation of UiS-Aqua to the general-purpose FEM program, Code_Aster, is comprehensively described. Extensive validation studies are performed in both static and dynamic analyses. In general, deformations of nets and drag loads on the fish cage agree well with the validation data. Moreover, the following conclusions are drawn based on the validations:

1. It is the first time that Code_Aster, the open-source FE solver developed by EDF R&D, has been used to simulate nets in marine aquaculture facilities. The successful application is fulfilled through the external module in the present work.
2. Verifications based on computational mesh and time step convergences and validations with experimental results are achieved. It is shown that by employing the newly developed external module in Code_Aster, the present numerical model can predict the response of a flexible fish cage under pure current conditions with satisfactory accuracy. In particular, the maximum difference between the numerical and experimental results is only 5% in drag prediction.
3. The new formula proposed in the present work can fix the evident defect in the previous formula for the net-to-net wake effect. With the help of the new formula, the discrepancy between the predicted and experimental drag on a fish cage can be reduced from 30% to 5%.

3 Structural modelling of marine aquaculture structures

4. The drag on a single fish cage is overestimated by the existing Screen models, especially when high-solidity nets experience large deformation. This is due to the inappropriate net-to-net wake effect. The consistent flow velocity reduction factor, which is commonly used in the fish cage simulation, can overestimate the current velocities on downstream nets. Thus, the total drag on a fish cage can be as large as 30% higher than the experimental results.

3.6 Appendix. Derivation of the mesh grouping method.

This section gives an introduction on how to reduce the number of elements using the present mesh grouping method. As mentioned in Section 3.2.3, the principle is to keep \mathbf{M} , \mathbf{K} , \mathbf{F}_g , \mathbf{F}_b and \mathbf{F}_h in Eq.(16) consistent between the physical net and numerical net. In the numerical model, the fluid density (ρ_{fluid}), the fluid velocity (\mathbf{u}), the density of twine (ρ_{twine}) and Young's modulus of twine (E) are consistent with the physical value, and λ is the ratio between the half mesh size of the numerical net (L_n) and the half mesh size of the physical net (L_p).

As shown in Figure 3-19, the nets in the two blue dashed boxes should have the same mass (\mathbf{M}), stiffness (\mathbf{K}) and environmental loads (\mathbf{F}_g , \mathbf{F}_b and \mathbf{F}_h). To satisfy the consistency, three derived diameters, *i.e.*, structural diameter (d_{ws}), elastic diameter (d_{we}) and hydrodynamic diameter (d_{wh}), are used in the numerical model building. Below, the relationships between the three diameters and the physical twine diameter (d_{w0}) are derived.

3 Structural modelling of marine aquaculture structures

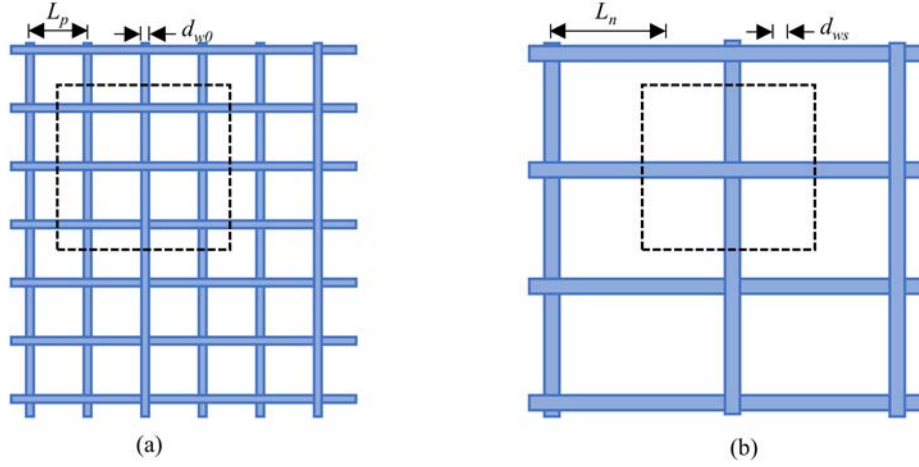


Figure 3-19. Illustration of the mesh grouping method with $\lambda = L_n / L_p = 2$.

3.6.1 Mass equivalent

As shown in Figure 3-19, the mass of the physical net in the blue dashed box is:

$$M_p = \rho_{twine} \left(2\lambda \frac{\pi}{4} d_{w0}^2 \lambda L_p - \lambda^2 \frac{\pi}{4} d_{w0}^2 d_{w0} \right) \quad (3-14)$$

And the mass of the numerical net in the blue dashed box is:

$$M_n = \rho_{twine} \left(2 \frac{\pi}{4} d_{ws}^2 L_n - \frac{\pi}{4} d_{ws}^2 d_{ws} \right) \quad (3-15)$$

Because $M_p = M_n$, the structural diameter d_{ws} should satisfy:

3.6 Appendix. Derivation of the mesh grouping method.

$$d_{ws} = \lambda \sqrt{\frac{2L_p - d_{w0}}{2L_n - d_{ws}}} d_{w0} \quad (3-16)$$

For typical aquaculture nets, $2L_p \gg d_{w0}$ and $2L_n \gg d_{ws}$. Thus, the square root term can be simplified as:

$$\sqrt{\frac{2L_p - d_{w0}}{2L_n - d_{ws}}} \approx \sqrt{\frac{1}{\lambda}} \quad (3-17)$$

Then the structural diameter can be obtained as:

$$d_{ws} \approx \sqrt{\lambda} d_{w0} \quad (3-18)$$

3.6.2 Stiffness equivalent

Because typical aquaculture nets have a negligible bending stiffness and cannot carry any compression load, the stiffness of the physical net in the blue dashed box can be written as:

$$K_p = \lambda \frac{\pi}{4} \frac{d_{w0}^2 E}{\lambda L_p} \begin{bmatrix} 1 & 0 \\ 0 & 1 \end{bmatrix} \quad (3-19)$$

And the stiffness of the numerical net in the blue dashed box is:

3 Structural modelling of marine aquaculture structures

$$K_n = \frac{\pi d_{ws}^2 E}{L_n} \begin{bmatrix} 1 & 0 \\ 0 & 1 \end{bmatrix} \quad (3-20)$$

Based on $K_p = K_n$, then the elastic diameter can be obtained as:

$$d_{we} = \sqrt{\lambda} d_{w0} \quad (3-21)$$

3.6.3 Environmental loads equivalent

3.6.3.1 Gravity and buoyancy loads

The $\mathbf{F}_g - \mathbf{F}_b$ on the physical net and numerical model are given in Eqs.(3-22) and (3-23)

$$\begin{aligned} F_{sp} = \rho_{fluid} g \left(2\lambda \frac{\pi}{4} d_{w0}^2 \lambda L_p - \lambda^2 \frac{\pi}{4} d_{w0}^2 d_{w0} \right) \\ - \rho_{twine} g \left(2\lambda \frac{\pi}{4} d_{w0}^2 \lambda L_p - \lambda^2 \frac{\pi}{4} d_{w0}^2 d_{w0} \right) \end{aligned} \quad (3-22)$$

$$\begin{aligned} F_{sn} = \rho_{fluid} g \left(2 \frac{\pi}{4} d_{ws}^2 L_n - \frac{\pi}{4} d_{ws}^2 d_{ws} \right) \\ - \rho_{twine} g \left(2 \frac{\pi}{4} d_{ws}^2 L_n - \frac{\pi}{4} d_{ws}^2 d_{ws} \right) \end{aligned} \quad (3-23)$$

Similar to the derivation for the mass conservation, the diameter for the gravity and buoyancy forces is the same as the one for the mass. Therefore, it can use the same parameter, d_{ws} , to calculate the gravity and buoyancy forces.

3.6 Appendix. Derivation of the mesh grouping method.

3.6.3.2 Hydrodynamic loads

For both Morison and Screen models, the hydrodynamic forces are calculated based on the following equation:

$$\mathbf{F}_h = \frac{1}{2} C_d \rho_{fluid} A |\mathbf{u} - \mathbf{v}| (\mathbf{u} - \mathbf{v}) \quad (3-24)$$

In Morison models, the hydrodynamic coefficients depend on the physical twine diameters (d_{w0}) and the reference area A is the projected area of twines. The projected area of twines in the physical net is:

$$A_p = 2\lambda d_{w0} \lambda L_p - \lambda^2 d_{w0}^2 \quad (3-25)$$

The projected area of the twines in the numerical net is:

$$A_n = 2d_{wh} L_n - d_{wh}^2 \quad (3-26)$$

Based on $A_p = A_n$, the hydrodynamic diameter should satisfy:

$$d_{wh} = \lambda d_{w0} \quad (3-27)$$

In Screen models, the hydrodynamic coefficients depend on the solidity or the twine diameters (d_{w0}) of the physical net. The reference

3 Structural modelling of marine aquaculture structures

area A in the numerical model is the net panel area, which is the same as the physical net. The solidity of the physical net is:

$$Sn_p = \frac{d_{w0}(2L_p - d_{w0})}{L_p^2} \quad (3-28)$$

And the solidity of the numerical net is

$$Sn_n = \frac{d_{wh}(2L_n - d_{wh})}{L_n^2} \quad (3-29)$$

Based on $Sn_p = Sn_n$, the derived hydrodynamic diameter satisfies the same relationship in Eq.(3-27). In summary, Eqs.(3-18), (3-21) and (3-27) have been used in the present mesh grouping method to reduce the computational effort.

3.6 Appendix. Derivation of the mesh grouping method.

4 Coupling algorithm for fluid-structure interaction analysis

The content is partly published as:

Cheng, H., Ong, M.C., Li, L., Chen, H., 2022. Development of a coupling algorithm for fluid-structure interaction analysis of submerged aquaculture nets. *Ocean Engineering* 243, 110208.

4.1 Introduction to the fluid-structure interaction problem in marine aquaculture structure

In a real fish farm, nets at different positions usually experience different flow velocities due to wake effects. In the context of marine aquaculture structures, the wake is the region downstream from the permeable nets, where the velocity is reduced, and the flow is often turbulent (Cheng *et al.*, 2020; Sim *et al.*, 2021; Zhao *et al.*, 2013a; Zhao *et al.*, 2013b). For a typical cylindrical fish cage, approximately half of the nets, located at the rear side of the cage, experience the wake flow generated by the front part of the cage. Thus, knowing how the flow velocity is reduced in the wake is the key for calculating the forces on marine aquaculture structures, particularly since the force is proportional to the square of velocity in the hydrodynamic force models, giving a large contribution (Lekang, 2019). Neglecting the wake effects in numerical analyses can cause unreliable structural responses of the whole fish cage (Chu *et al.*, 2020; Rickard, 2020; Chen *et al.*, 2021). According to the study by Faltinsen and Shen (2018), the anchor force of a single fish cage can increase by up to 22% if wake effects are not included in numerical analyses. Moreover, the wake effects play a vital role in the design of a fish farm which is usually comprised of several fish cages (Bi and Xu, 2018; Sim *et al.*, 2021).

Different methods have been proposed to estimate the wake effects for marine aquaculture structures. In general, they can be categorized into two approaches. The first approach is to assign a pre-defined

4 Coupling algorithm for fluid-structure interaction analysis

empirical flow velocity reduction factor (r_u) onto the downstream nets in order to lower the hydrodynamic forces. The value of r_u can be acquired from theoretical analyses and experimental results. Løland (1991) proposed an engineering approach, *i.e.*, $r_u = 1 - 0.46C_{D(\theta=0^\circ)}$ where C_D is the drag coefficient of a net panel and θ is the inflow angle, to calculate the flow velocity reduction factor. Lee *et al.* (2008) conducted water-tank experiments with plane nets under different inflow angles, solidity and flow velocities, and found that r_u reduced with increasing inflow angles. Cheng *et al.* (2020) proposed a new formula based on previous experimental data, considering both the solidity and inflow angle of net panels. The new formula showed a better agreement with experimental results than the previous methods. However, the first approach simplifies the wake effect by assigning a constant r_u onto the downstream nets to turn down the hydrodynamic forces, without considering the directions of the flow. The second approach is to solve the fluid field through and around marine aquaculture structures using proper fluid models. Recently, the computational fluid dynamic (CFD) method combined with a porous media model was proposed by Simonsen *et al.* (2006) to calculate the flow field around nets. The advantage of this method is that it is not necessary to conduct numerous experiments to acquire r_u , which can save considerable time and cost. Patursson *et al.* (2010) applied experiment-based porous media resistance coefficients in ANSYS Fluent to model the flow through and around nets. Their promising results inspire researchers to combine the CFD method with commonly used finite element methods. Further studies showed that combining CFD

4.1 Introduction to the fluid-structure interaction problem in marine aquaculture structure

simulations and structural analyses can acquire more accurate structural responses than pure structural analyses (Bi *et al.*, 2014a; Yao *et al.*, 2016). Moreover, results from CFD simulations are valuable for the understanding of nutrients and materials transport (Alver *et al.*, 2016; Oppedal *et al.*, 2011) and pollutant distribution (Xu and Qin, 2020) in fish farming sites. Thus, combining CFD simulations and structural analyses has become a new trend in the design of marine aquaculture structures.

The interaction between flexible nets and fluid is a typical fluid-structure interaction (FSI) problem and requires solving the governing equations in both the fluid and structure domains. For this FSI problem, one of the most noticeable contributions is the immersed boundary method (IBM), which was initially proposed by Peskin (1972). The interaction between the fluid and structure is usually accomplished by distributing nodal forces and interpolating nodal velocities between the Eulerian and Lagrangian domains using the Dirac delta function (Wang and Zhang, 2009). Because flexible nets can experience large deformations in the three-dimensional domain, a class of non-boundary-fitted methods is usually chosen to track the moving boundaries (Wang *et al.*, 2017). In this method, the fluid and solid domains are discretized separately using a fixed Eulerian grid and a moving Lagrangian grid, respectively. Due to the different discretization methods, the coupling information cannot be directly transferred between the two domains. Thus, it is challenging to build the relation for these two meshes to impose the coupling condition (de Tullio and Pascazio, 2016; Jiang *et*

4 Coupling algorithm for fluid-structure interaction analysis

al., 2018). Moreover, according to Yan *et al.* (2020), the conventional IBM had a major disadvantage for fiber-like immersed structures, *e.g.*, the cables and nets in the present study, because fiber-liked structures occupy negligible volume in the fluid domain. Thus, a new coupling algorithm is needed to study the effect of nets, which are thin (2 - 4 millimeters of twine diameter), flexible and highly permeable structures, on the flow field through and around a large marine aquaculture structure (hundreds of meters) in a computationally affordable way.

In this thesis, the structural responses are solved by Code_Aster, while the complex fluid flows are solved by OpenFOAM. The two solvers are well-verified according to the research works by Févotte and Lathuilière (2017) for Code_Aster and Robertson *et al.* (2015) for OpenFOAM. As the structural model is detailly discussed in Chapter 3, only the fluid model is presented in this chapter.

4.2 Fluid model

4.2.1 Governing equations

In the present study, the flow field is calculated based on the Finite Volume Method (FVM), and the fluid domain is divided into a grid of cells. The equations governing the incompressible flow based on Eulerian cells include a continuity equation and momentum equations:

$$\nabla \cdot \mathbf{u} = 0 \quad (4-1)$$

$$\begin{aligned} \frac{\partial \mathbf{u}}{\partial t} + \mathbf{u} \cdot \nabla \mathbf{u} = & -\frac{1}{\rho} \nabla p + \nabla \cdot [(\nu + \nu_T)(\nabla \mathbf{u} + \nabla \mathbf{u}^T)] + \mathbf{g} \\ & + \mathbf{S}_{pz} \end{aligned} \quad (4-2)$$

where \mathbf{u} is the velocity of the fluid, p is the pressure, ν is the fluid kinematic viscosity, ρ is the fluid density, \mathbf{g} is the gravity acceleration, \mathbf{S}_{pz} is the source term due to the existence of net. The source term \mathbf{S}_{pz} is added to the cells in porous zones to account for the hydrodynamic loads on nets. A dynamic porous media (DPM) model is developed to find the porous zones (shown as blue cells in Figure 4-1) and to assign the correct \mathbf{S}_{pz} onto the exact cells. Explanations for the DPM model are presented in Section 4.3.

4 Coupling algorithm for fluid-structure interaction analysis

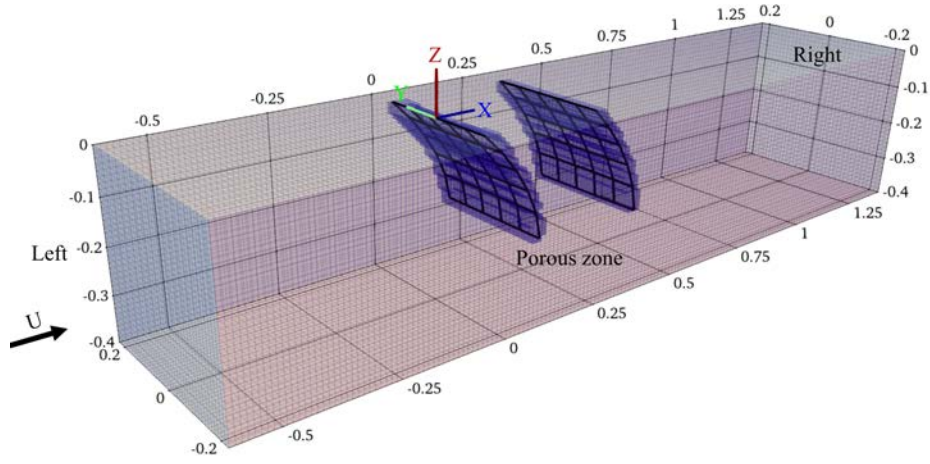


Figure 4-1. Illustration of the computational domain for fluid. This illustration corresponds to the validation case in Section 4.6.3. The blue cells represent the porous zones in the fluid model. The black lines inside the porous zones are the structural model, which is composed of one-dimensional elements.

4.2.2 Fluid velocity in the porous media model

Unlike the porous media models for coastal structures (Jensen *et al.*, 2014), the present DPM model does not need to modify \mathbf{u} in governing equations. As shown in Figure 4-2, \mathbf{U}_c is the fluid velocity at the cell centroid, which is defined as a volume-averaged velocity where averaging is done over the volume containing both fluid and solid domains. In Figure 4-2 (a), \mathbf{U}_c is no doubt smaller than the intrinsic averaged velocity (\mathbf{U}_{ia}), where the averaging is done over the fluid domain only. According to the conservation of mass, the relationship between \mathbf{U}_c and \mathbf{U}_{ia} can be expressed as $\mathbf{U}_c = \alpha \mathbf{U}_{ia}$, where α is the porosity of the porous zone, defined as the ratio of the volume occupied by the fluid to the total volume of the porous zone. For Figure 4-2 (b), α can be calculated as:

4.2 Fluid model

$$\alpha = \frac{A_t T - \frac{\pi}{4} S n A_t d_{w0}}{A_t T} = 1 - \frac{\pi d_{w0}}{4 T} S n \quad (4-3)$$

where $S n$ is the solidity of nets, d_{w0} is the diameter of the actual twine, A_t is the area of a net panel, and T is the thickness of the porous zone. Moreover, one should notice that $S n$ is a planar concept for the structural model, while α is a volumetric concept for the fluid model. Eq.(4-3) is the bridge between these two concepts.

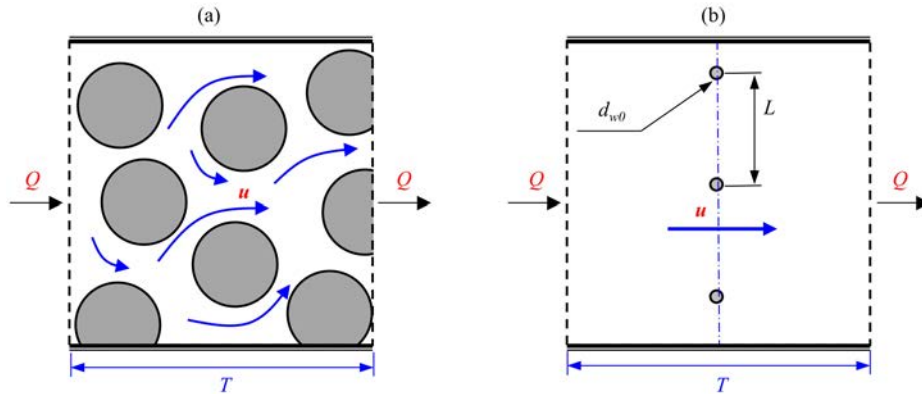


Figure 4-2. A 2D illustration of the velocity at the cell centroid (U_c) with different porous media models. The dark grey circles represent solid. A square box represents one cell in the fluid solver. Based on the conservation of mass, the flux Q through the cell is constant, which leads to an increasing velocity u in the pore area. (a) In the commonly used porous media model for coastal structures, the solids are filled in the porous zone and increase the intrinsic velocity (Jesus *et al.*, 2012). (b) In the dynamic porous media (DPM) model for nets, the fiber-like solids (twines) concentrate along a line and occupy a negligible volume of the porous zone.

As illustrated in Figure 4-2, the twine diameter is in the order of 10^{-3} m, and the dimension of a whole fish cage is in the order of 10^2 m. When the water flow velocity is 1 m/s, the value of Re is in the order of 10^3 based on the twine diameter. With different such a broad range of scales in dimension and large Re , it would be computationally

4 Coupling algorithm for fluid-structure interaction analysis

unaffordable to model the fluid with a fine mesh that can capture the complex flow separation from the twines. Furthermore, such a complex and high-resolution flow field around small twines might be redundant for the design of marine aquaculture structures. Thus, for the fiber-like structure in the present study, the thickness of the porous zone is much larger than the diameter of the actual twine. Hereby, $T \gg d_{w0}$ and $\alpha \approx 1$ based on Eq.(4-3). Thus, the porosity correction is unnecessary to include in the governing equations for the simulations of nets.

4.2.3 Turbulence modelling

As observed in the experiments by Bi *et al.* (2013), a transition zone is formed near a net panel due to different flow velocities inside and outside the wake. The flow in the transition zone is a typical free shear flow. Chen and Christensen (2017) compared four types of turbulence models, *i.e.*, k - ε model, k - ω model, k - ω SST model and realizable k - ε model, to simulate this free shear flow near a net. According to their comparisons, these four turbulence models give similar results regarding the flow velocities in the wake. Thus, the k - ε model of Jones and Launder (1973) is employed in the present model as the turbulence closure for the RANS equations.

$$\frac{Dk}{Dt} = \nabla \cdot [(\nu + \sigma_k \nu_T) \nabla k] + G_k - \varepsilon \quad (4-4)$$

$$\frac{D\varepsilon}{Dt} = \nabla \cdot [(\nu + \sigma_\varepsilon \nu_T) \nabla \varepsilon] + C_{1\varepsilon} \frac{\varepsilon}{k} G_k - C_{2\varepsilon} \frac{\varepsilon^2}{k} \quad (4-5)$$

$$G_k = \frac{\nu_T}{2} (\nabla \mathbf{u} + \nabla \mathbf{u}^T)^2 \quad (4-6)$$

$$\nu_T = C_\mu \frac{k^2}{\varepsilon} \quad (4-7)$$

where $\sigma_k=1.0$, $\sigma_\varepsilon=1.3$, $C_{1\varepsilon}=1.44$, $C_{2\varepsilon}=1.92$, $C_\mu=0.09$. The initial values of the turbulence quantities (k and ε) are estimated as follows:

$$k = \frac{3}{2} (\mathbf{u}I)^2; \quad \varepsilon = \frac{C_\mu^{0.75} k^{1.5}}{L_T} \quad (4-8)$$

where I is the turbulence intensity, L_T is the turbulence length scale. The values of these parameters are provided separately in the validation studies in Section 4.6.

The effect of nets is negligible in turbulence modelling. Physically, when the flow passes through a net, the turbulent kinetic energy (TKE) can increase around the net due to the existence of individual twines in the net, but TKE dissipates very fast with a power law in the wake region (Laws and Livesey, 1978). In order to precisely model the turbulence around a net, extensive studies and well-validated experimental data are needed. However, for a typical fish cage in which the distance between upstream net and downstream nets is usually from 20 to 50 meters (Halwart *et al.*, 2007), the TKE generated by the upstream nets should dissipate into negligible scale before the flow travels to the downstream nets. Thus, the additional source terms to address TKE are not included in Eqs.(4-4) and (4-5).

4 Coupling algorithm for fluid-structure interaction analysis

4.2.4 Boundary conditions for fluid

The flow field is solved using the Pressure Implicit with Splitting of Operators (PISO) algorithm. The spatial schemes for gradient, Laplacian and divergence are Gauss linear, bounded Gauss linear upwind, and Gauss linear limited corrected. All the simulations in Section 4.6 are three-dimensional and with a similar fluid domain, as shown in Figure 4-1. The boundary conditions for fluid are listed as follows:

- (1) Left: A uniform velocity is given as the inlet condition. p is set as zero normal gradient. The values of \mathbf{u} , k and ε on the left boundary vary in different cases and will be given along with the description of each case in Section 4.6.
- (2) Right: A fixed zero pressure is set as outlet condition. \mathbf{u} , k , and ε are set as zero normal gradient.
- (3) Top, bottom, front and back: p , k , and ε are specified as zero normal gradient. \mathbf{u} is set as a slip condition. According to Patursson (2008), near-wall treatment has a negligible effect on the numerical results when the nets are far away from the wall. Thus, no near-wall treatment is employed in the simulations.

4.3 Dynamic porous media model

The porous zones, representing nets in the fluid domain, are governed by a dynamic porous media (DPM) model in the present study. Two main functions in this model, *i.e.*, (1) find the cells that belong to the porous zones, and (2) assign the correct \mathbf{S}_{pz} onto the exact cells, are explained in detail in this section.

4.3.1 Topological method

In order to represent the deformation of nets in fluid, a topological method is needed to map the Lagrangian nodes to the Eulerian grids. As the nets are flexible and can have violent movements under strong current flows, it is challenging for the DPM model to identify the positions of the net panels. In the present study, an improved topological method is developed based on the research work reported by Chen and Christensen (2017) to map the geometries. As discussed by Martin *et al.* (2020) and Chen and Christensen (2017), the original method can lead to missing cells (the circled cells in Figure 4-3(b)) at intersections of porous zones when the two adjacent net panels have different θ . These missing cells can have side effects on the downstream wake when the net has large deformation.

4 Coupling algorithm for fluid-structure interaction analysis

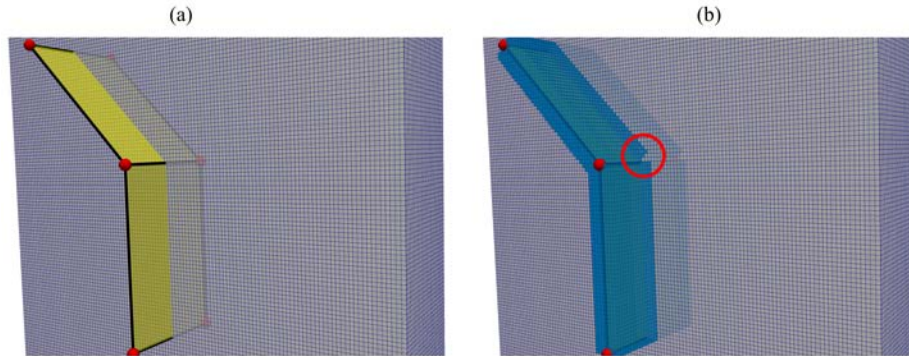


Figure 4-3. Illustration of the topological method. (a) The yellow rectangles represent net panels with different θ . The red points represent the vertices that define the location of net panels. The black lines represent the “CABLE” elements. (b) The blue cells are the porous zones in the fluid domain. The red circle indicates the missing cells.

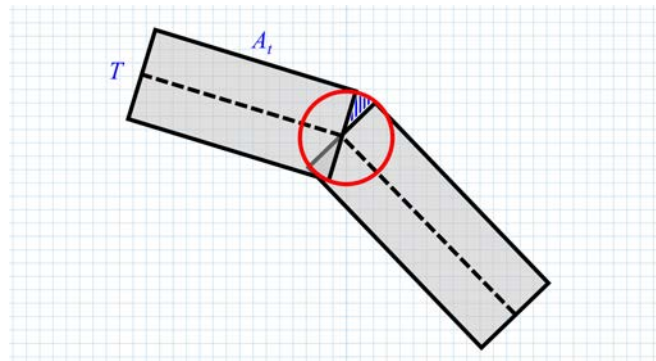


Figure 4-4. Two-dimensional illustration of the improved topological method in the present study. When it comes to three-dimensional space, the two black rectangles represent the porous zones that are extruded by a thickness of T based on the net panels, and the red circle represents a circular cylinder that is extruded along the common edges of two adjacent net panels.

In order to address the problem of missing cells, an improved topological method is developed in the present study. A cell is recognized in porous zones if its centroid is located in the volume extruded based on net panel by a thickness of T . Besides, an additional

4.3 Dynamic porous media model

procedure is introduced to retrieve the missing cells. As illustrated in Figure 4-4, the red circle (with a diameter of D) between the two porous zones (with a thickness of T) covers the gaps and retrieves the missing cells in the gaps. The ratio of D/T determines how many cells in the gaps can be retrieved.

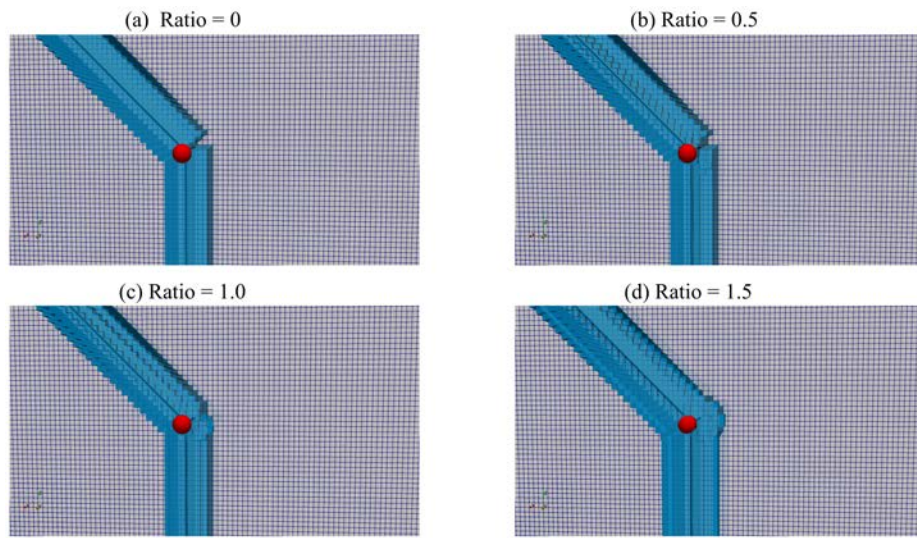


Figure 4-5. The effect of different D/T on cell retrieval.

Figure 4-5 shows the influence of D/T on the cell retrieval. $D/T = 0$ corresponds to the results of the original topological method proposed by Chen and Christensen (2017). With increasing D/T , more fluid cells at intersections of porous zones are retrieved. The present study adopts $D/T = 1$, as it can retrieve exactly all the missed cells in the gaps, neither more nor less than expected. Apart from the red circle, a conditional statement is added to exclude duplicated cells. Thus, the volume of one porous zone, V_{pz} , can be expressed as follows:

4 Coupling algorithm for fluid-structure interaction analysis

$$V_{pz} = TA_t = \sum_{i=1}^m V_i \quad (4-9)$$

where m is the number of cells in one porous zone, A_t is the area of one net panel, T is the thickness of one net panel in the fluid solver, and V_i is the volume of a fluid cell.

4.3.2 Conservation of momentum

As shown in Figure 1-6, nets consist of millions of small twines in a marine aquaculture structure. The twines are intersected with each other and form a porous membrane-like structure. In various industrial situations where a well-resolved grid or even a reduced resolution grid is unaffordable, a porous media model is usually adopted to study the flow field around the porous structure (Roelofs and Shams, 2019). Essentially, a porous media model handles the flow field by adding an extra momentum source term in the governing momentum equations (the S_{pz} in Eq.(4-2)). According to the study by O'Neill (2006), the source term can be expressed by a polynomial function of the velocity at the cell centroid, and expressed using the following general form:

$$S_{pz} = \sum_{i=1}^n C_i \mathbf{u}_c^i \quad (4-10)$$

4.3 Dynamic porous media model

where the coefficients C_i are acquired by data fitting, n is the degree of the polynomial, and \mathbf{u}_c is the velocity of the fluid. Usually, $n = 2$ is sufficient for most engineering applications (O'Neill, 2006). In the present study, the value of \mathbf{S}_{pz} is calculated based on the conservation of momentum instead of the data fitting from fluid experiments that measure the pressure difference (*e.g.*, experiments by Zhong *et al.* (2014)).

The conservation of momentum should be fulfilled during the data exchange between the fluid and structural solvers. Based on Newton's Third Law, the hydrodynamic loads on nets and the resistance forces on the fluid are equal in magnitude and opposite in direction. Thus, the relation between the hydrodynamic loads on a single net panel and the loss of the fluid momentum in the corresponding porous zone can be expressed by Eq.(4-11), where the volume integral is conducted over the porous zone. The purpose of adopting a porous media model in the present study is not to study the complex flow separations near the nets, but to handle the wake effects in the region downstream of the nets. Thus, \mathbf{S}_{pz} can be treated as a constant through the cells in a porous zone representing a single net panel in the fluid domain. Hereby, the volume integral on the left-hand side of Eq.(4-11) reduces to the product of porous zone (TA_t) volume and \mathbf{S}_{pz} , as given in Eq.(4-12). On the right-hand of Eq.(4-12), the hydrodynamic load $\mathbf{F}_h = \mathbf{F}_D + \mathbf{F}_L$, and is calculated using Eqs.(2-5) and (2-6). Thus, the value of source term in

4 Coupling algorithm for fluid-structure interaction analysis

one fluid cell with a volume of V_i can be written as Eq.(4-13) for convenience.

$$\iiint_V \rho \mathbf{S}_{pz} \, dx \, dy \, dz = -\mathbf{F}_h \quad (4-11)$$

$$\rho T A_t \mathbf{S}_{pz} = -\mathbf{F}_h \quad (4-12)$$

$$\begin{aligned} \mathbf{S}_{pz} &= \frac{-\mathbf{F}_h}{\rho T A_t} V_i \\ &= -\frac{1}{2} \left| \sqrt{\frac{2}{2 - (C_D + C_L)}} \mathbf{U}_c - \mathbf{v} \right|^2 \frac{C_D \mathbf{i}_D + C_L \mathbf{i}_L}{T} V_i \end{aligned} \quad (4-13)$$

4.3.3 Flow velocity correction

In the present study, the hydrodynamic loads on nets are calculated using the forces model that is derived from experiments. According to the formulae in Eqs.(2-5) and (2-6), the hydrodynamic loads are functions of the undistributed incoming flow velocity \mathbf{U}_∞ . While, in the FSI analyses, the fluid solver extracts the flow velocity at the center of porous zones (\mathbf{U}_c). Thus, a velocity correction process is needed to convert \mathbf{U}_c to \mathbf{U}_∞ , so that, the existing hydrodynamic force models can be applied in the simulations.

4.3 Dynamic porous media model

Usually, the force coefficients (*i.e.*, C_D and C_L) in the existing hydrodynamic force models are derived based on the undisturbed flow velocity $U_{-\infty}$, because the value of $U_{-\infty}$ is easy to measure in laboratory experiments (*e.g.*, the towing speed in towing tank experiments or the flow velocity in recirculating flume experiments). These force coefficients are usually obtained from experiments that approximate the ideal conditions of a finite net panel in an infinite flow field. However, these ideal conditions are challenging to achieve in practice.

One should notice that $U_{-\infty}$ can be different for nets at the different positions of a marine aquaculture structure due to the wake effects. The different $U_{-\infty}$ brings challenges to the calculation of hydrodynamic loads on nets. In the present study, the wake effects are solved by a fluid model, and the flow velocity at the centroid of a net panel U_c can be obtained directly from the fluid solver. The final relationship between $U_{-\infty}$ and U_c is presented in Eq.(4-14), and the detailed derivations can be found in Section 4.8.

$$U_{-\infty} = \sqrt{\frac{2}{2 - (C_D + C_L)}} U_c \quad (4-14)$$

4.4 Coupling algorithm

The two solvers in the present study, *i.e.*, Code_Aster and OpenFOAM, are written in an object-oriented manner and open source. Hereby, it is feasible to couple the two solvers to study the FSI problem. The coupling is achieved through our in-house module, which allows information exchange between the two solvers. The two-way coupling algorithm is illustrated in Figure 4-6, and the main procedures are:

- (1) At the beginning of simulations, the two solvers load the physical parameters from a dictionary file and initialize the model according to the configuration of nets. In the initialization, porous zones are created in the fluid solver, and net panels are created in the structural solver.
- (2) The fluid solver solves the flow field using the PISO algorithm.
- (3) The velocities in porous zones are extracted from the fluid solver and corrected using Eq.(4-14).
- (4) The *hydroModules* from UiS-Aqua employs the corrected velocities to calculate the hydrodynamic loads on nets based on Screen model.
- (5) The hydrodynamic loads on nets are mapped onto the corresponding structural nodes.
- (6) Based on the received hydrodynamic loads, the structural solver calculates the structural responses using the HHT- α algorithm.

4.4 Coupling algorithm

- (7) The DPM model updates the shapes of porous zones based on the topological method in Section 4.3.1 and the value of S_{pz} in fluid cells using Eq.(4-13).
- (8) The fluid solver calculates the flow field with the newly updated porous zones as in Step (2). Hereby, a full loop to solve the FSI problem is built.

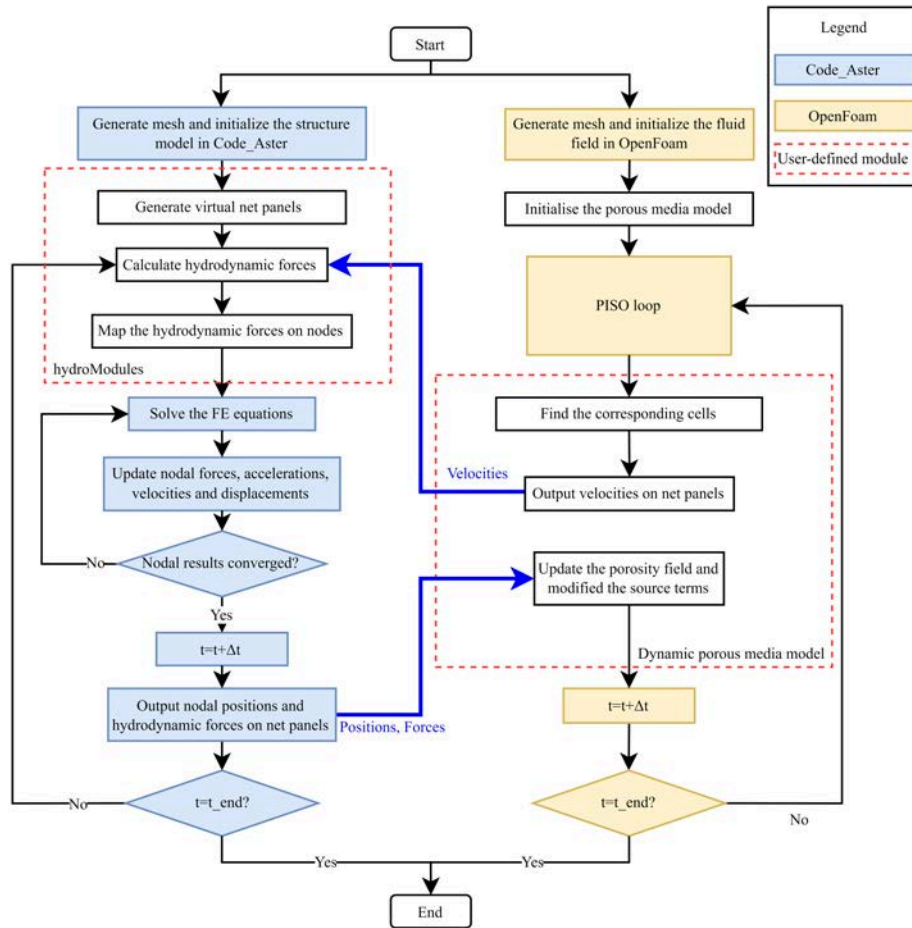


Figure 4-6. Flow chart showing the coupling algorithm.

4.5 Comments on the previous coupling algorithm

The present coupling procedure is conceptually similar to the IBM (Pepona and Favier, 2016; Griffith and Patankar, 2020; Wang *et al.*, 2017) for moving structures, but it employs a different way to convert the fluid pressure into a structural load. This is because the conventional IBM for impermeable solid cannot be used for the highly permeable nets. In the present coupling algorithm, the DPM model is developed to handle the porous nets in a computationally affordable way. Although the names of the additional source term S_{pz} vary in different publications (O'Neill, 2006; Patursson *et al.*, 2010; Martin *et al.*, 2020), the methods are conceptually similar. Essentially, S_{pz} is added to the momentum equations to account for the resistance of nets. Compared to Martin *et al.* (2020), the present coupling algorithm fulfills the law of momentum conservation which is a fundamental principle for reliable results. Compared to the coupling algorithm using the “force balance” concept (Bi *et al.*, 2014b; Yao *et al.*, 2016), the present time-stepping algorithm is more advanced and applicable to both steady and unsteady flow conditions.

Different from the previous studies (Patursson *et al.*, 2010; Bi *et al.*, 2014a; Chen and Christensen, 2016) where the hydrodynamic forces were calculated using Morison models, the present algorithm employs the advanced Screen models to calculate the hydrodynamic forces. According to Cheng *et al.* (2020), the advanced Screen models can improve the accuracy of the environmental load, which is a basis for

4.5 Comments on the previous coupling algorithm

structural responses. Moreover, compared to the approach proposed by Paturrsson *et al.* (2010) and Chen and Christensen (2016), the new algorithm properly removes the additional process for fitting the porous coefficients, which implicitly includes the velocity correction. Because considerable experimental and theoretical studies on Screen models are already published (Fridman, 1973; Aarsnes *et al.*, 1990; Løland, 1991; Balash *et al.*, 2009; Kristiansen and Faltinsen, 2012; Bi *et al.*, 2018), the force coefficients C_D and C_L can be directly obtained from these published articles and applied in the present algorithm. Thus, the present algorithm can simplify the procedures for the model preparation and improve the accuracy of the structural responses.

4.6 Validation for the coupling algorithm

In this section, a series of experiments conducted by Paturrsson *et al.* (2010), Bi *et al.* (2014a), and full-scale sea trials conducted by Gansel *et al.* (2018) are taken as references for the validation study of the present coupling algorithm. A convergence study is performed at first to determine the appropriate spatial resolution for the simulations. Then, the flow velocities behind a fixed net panel under several inflow angles (θ) are compared with the experimental data by Paturrsson *et al.* (2010). After that, the deformations of two flexible net panels are compared with the experimental data by Bi *et al.* (2014a). Finally, the drag loads on the full-scale fish cage under different flow velocities are calculated and compared to the sea trials by Gansel *et al.* (2018).

4.6.1 Convergence studies

In this study, hexahedral orthogonal grids are employed to discretize the fluid domain in the fluid solver. Although the thickness of the porous zone has a negligible effect on the simulations results (Paturrsson *et al.*, 2010), the number of cells across the porous zone might affect the results (Chen and Christensen, 2016). Thus, a grid convergence study should be performed to determine $T/\Delta x$, where T is the thickness of the porous zone, and Δx is the cell size. The grid convergence study is carried out with three sets of grids (G1-G3) for the cases in Paturrsson *et al.* (2010). The detailed setup of the numerical model is given later in Section 4.6.1, and the results for the convergence study are shown in Figure 4-7 and

4.6 Validation for the coupling algorithm

Table 4-1. The deviation in Table 4-1 is calculated based on the finest grid resolution (G3).

As shown in Table 4-1, G2 can achieve very close results compared to the finest grid regarding the drag F_D and flow velocity in the wake. However, G1 overpredicts F_D by 7.7 % compared to the finest grid. As the three sets of grids use the same hydrodynamic force coefficients from Paturrsson *et al.* (2010) to calculate the drag, the discrepancies of F_D in numerical results by the three sets of grids are only induced by the differences of U_c . The large discrepancies between G1 and G3 indicate that $T/\Delta x=1$ might be too coarse to solve the fluid field around the net. As for the flow velocities in the wake, which is extracted from the red spot in Figure 4-8, discrepancies of the results from G1-G3 are less than 1%. Therefore, it can conclude that the numerical simulation is converged when $T/\Delta x \geq 3$. For the subsequent simulations, $T/\Delta x = 3$ is chosen for the spatial resolution in the fluid solver. Regarding the structural mesh, the convergence study by Cheng *et al.* (2020) has demonstrated that the results using different numbers of elements have a maximum 1.69% deviation. Thus, the structural mesh mainly considers the calculational domains and computational costs.

The time-step convergence study is also performed for the nets in pure currents. The conclusion is similar to Cheng *et al.* (2020), where four time steps, *i.e.*, 0.02s, 0.05s, 0.1s and 0.2s, were applied. Since the simulations are calculated under pure current conditions without any oscillating loads, the above time steps have negligible influences on the

4 Coupling algorithm for fluid-structure interaction analysis

final results. Thus, a time step 0.1 s is selected for all the subsequent simulations considering the Courant–Friedrichs–Lewy (CFL) number. In the following simulations, the maximum CFL number is 0.3.

Table 4-1. Results of convergence study for a fixed net panel in steady flow when $\theta = 0^\circ$

Grid	Cells	$T/\Delta x$	F_D (N)	Deviation	u (m/s)	Deviation
G1	20 352	1	35.602	7.70%	0.4344	0.73%
G2	560 952	3	33.431	1.14%	0.4381	0.11%
G3	2 638 494	5	33.056	-	0.4376	-

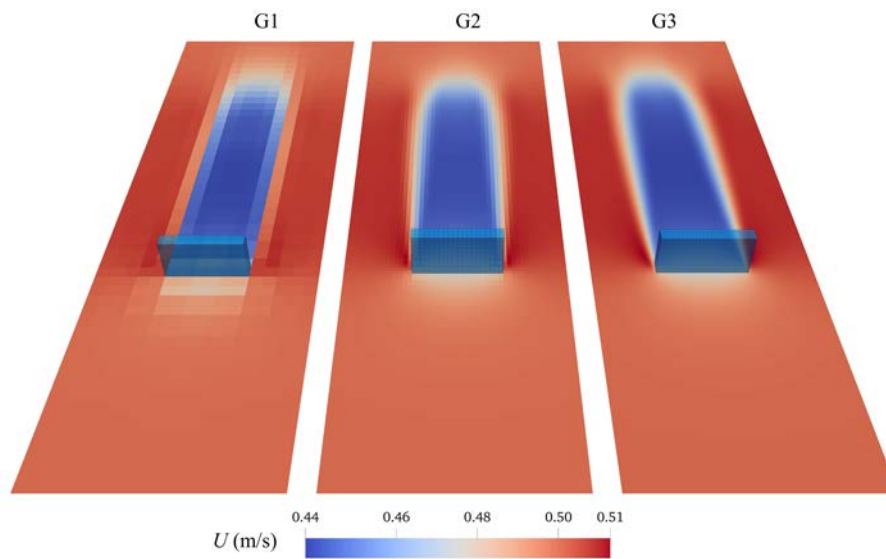


Figure 4-7. Mesh convergence study with different $T/\Delta x$.

4.6.2 Fixed net panel

4.6.2.1 Case setup

The first validation is based on the experiments by Paturrsson *et al.* (2010). In the experiments, a net panel was fixed to a square frame and towed under various inflow angles and velocities. The net panel was made of a 1 m × 1 m knotless nylon material with $d_{w0} = 2.8$ mm, $L = 29$ mm and $Sn = 0.2$. The purpose of this validation is to test whether the flow field behind a net panel can be correctly predicted. The flow velocity reduction factor r_u is used in this validation to indicate the accuracy of the numerical simulations. r_u is calculated as the ratio between the velocity at the probe (the red circle in Figure 4-8) and the undisturbed incoming velocity.

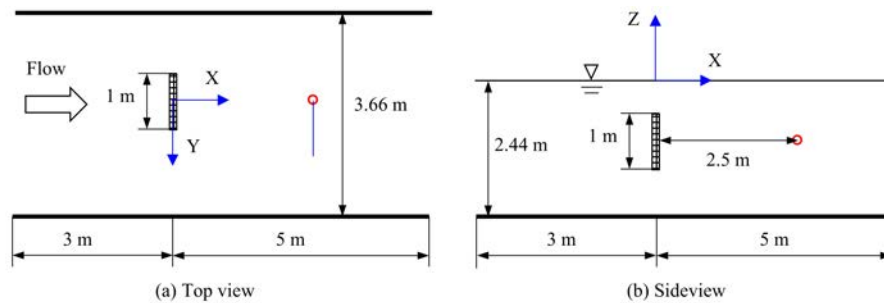


Figure 4-8. Sketch of the fluid domain for the reproduction of the experiment by Paturrsson *et al.* (2010) Top view is shown on the left, side view is shown on the right. The flow velocities in the wake are measured at the red circle.

The sketch of the simulation domain is shown in Figure 4-8. In the numerical model, G3 is chosen for the spatial resolution in the fluid solver, and 220 elements with $\lambda = 3.45$ are used to represent the net in the structural solver. For the boundary conditions in the fluid solver, $\mathbf{u} =$

4 Coupling algorithm for fluid-structure interaction analysis

0.5 m/s, $k = 3.75 \times 10^{-5} \text{ m}^2\text{s}^{-2}$ and $\varepsilon = 2.5 \times 10^{-7} \text{ m}^2\text{s}^{-3}$ are set as fixed values on the inlet boundary according to the data provided by Paturrsson *et al.* (2010). In the structural model, the nodes on the four edges are fixed to represent the setup in the experiments. The square frame which was used to support the net is not modeled in the present simulations. The hydrodynamic forces on net panels are calculated using the force coefficients in Table 4-2, which are derived based on the experimental data from Paturrsson *et al.* (2010).

4.6.2.2 Flow patterns behind the single net panel

Figure 4-9 presents the flow velocity field and the streamlines on the X-Y plane at $Z = -1.22 \text{ m}$ when $\theta = 45^\circ$ and $U_\infty = 0.5 \text{ m/s}$. The wake region behind the net panel is visible and has approximately the same width as the projected width of the net panel. The magnitude of the flow velocity in the wake is smaller than U_∞ . Since the drag on the net can cause a loss of momentum on the fluid, it is reasonable to observe a flow velocity reduction in the wake. Besides the velocity reduction, the flow is also deflected by the net panel, shown as the slightly bent streamlines in Figure 4-9. When $\theta = 45^\circ$, the fluid flow can cause a lift force on the net. The lift force can, in turn, lead the flow to an opposite direction according to Newton's third law. This flow deflection is also reported by Reynolds (1969). Therefore, the existence of the net can reduce the flow velocity and also change the flow direction.

4.6 Validation for the coupling algorithm

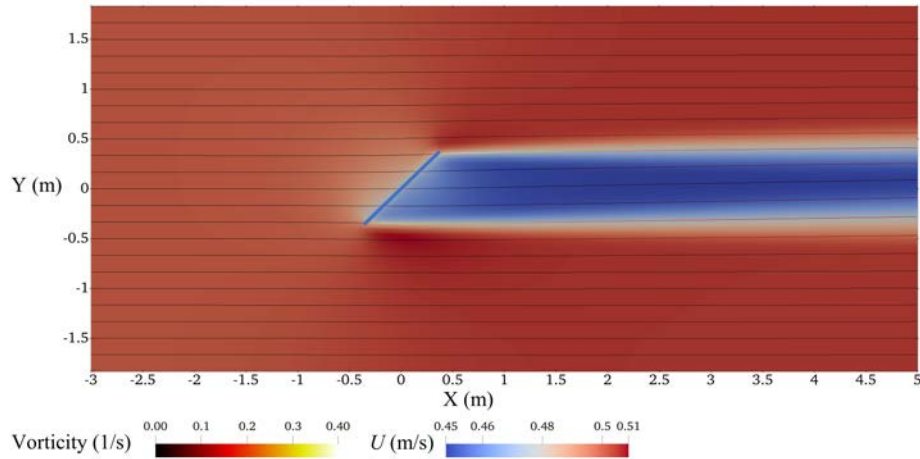


Figure 4-9. The velocity contour from the present numerical model on the X-Y plane at $Z = -1.22$ m when $\theta = 45^\circ$ and $U_\infty = 0.5$ m/s. The blue line represents the net panel.

The turbulence model is necessary for simulating the flow field in the wake region. According to Laws and Livesey (1978), the net panel in the present study works like a turbulence-suppressing screen in a wind tunnel, which can produce a steady and uniform flow. Thus, it is expected to observe a steady and uniform flow behind the net panel in Figure 4-9. According to the numerical results by Martin *et al.* (2020) and Chen and Christensen (2017), the flow field in the wake region showed a stripe pattern when the turbulence model was absent. The stripe pattern indicates that the flow field in the wake has a sharp velocity gradient and high nonuniformity. As a turbulence model is employed in the present study, the turbulent diffusion causes momentum exchange in-between the layers with different velocities. The momentum exchange reduces the velocity variation. Thus, the turbulence model can remove the unphysical sharp velocity gradient and produce a uniform wake flow.

4 Coupling algorithm for fluid-structure interaction analysis

Moreover, the uniform flow is theoretically better than the stripe-pattern flow for calculating the hydrodynamic forces on nets. Because the hydrodynamic forces are calculated using the extracted flow velocity from the fluid solver, the stripe-pattern flow can cause a large-variation load. Hereby, dynamic responses of the whole structure can be unstable and unreliable. An example of an unstable numerical result is reported by Chen and Christensen (2017). Therefore, it is suggested to add a turbulence model in simulations in order to achieve physical and stable solutions.

4.6.2.3 Flow velocity profiles behind the net panel

Figure 4-10 shows the flow velocity profiles along the blue line in Figure 4-8 from the numerical simulations with different inflow angles. The circles in this figure represent the experimental measurements provided by Paturrsson *et al.* (2010). According to the flow velocity profiles, the velocity gradually decreases from the flank of the towing tank to the center plane of the towing tank. Near the flank of the towing tank, the flow velocity is approximately 3% higher than U_{∞} . This velocity increment is the result of mass conservation. Around the center plane of the towing tank, the flow velocity is reduced due to the loss of momentum. In general, the velocity profiles from the numerical simulations agree well with the experimental measurements except for the two measurements at $Y = 0.43$ m. When $\theta = 0^\circ$ and 30° , the velocity probe is located in the wake region generated by the frame. As the frame is not modeled in the numerical simulation, it is reasonable to observe the discrepancy of the velocities at $Y = 0.43$ m when $\theta = 0^\circ$ and 30° . The

4.6 Validation for the coupling algorithm

engineering approach proposed by Løland (1991) is shown in Figure 4-10 for comparison. It indicates that the engineering approach fits well with the experimental measurements at the center plane of the towing tank when $\theta < 60^\circ$.

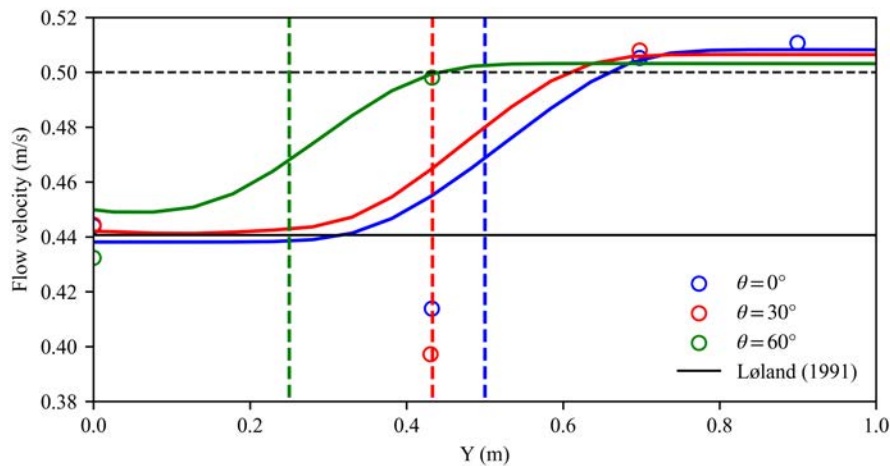


Figure 4-10. Flow velocity profiles from numerical simulations. The vertical dashed lines show the position of the vertical frame for the different inflow angles.

4.6.2.4 Flow velocity reduction factor

In general, the flow velocity reduction factor (r_u) can be accurately predicted by the present model. As shown in Table 4-2, the differences between the predicted r_u and the experimental results are within 1.5% when $\theta < 60^\circ$. The large deviation is only seen when the inflow angle $\theta = 75^\circ$. For the cases when $\theta > 60^\circ$, the large deviation can be explained mainly by the two reasons. First, the experimental data might have errors when $\theta > 60^\circ$ by using the experimental setup in Paturrson *et al.* (2010). As reported by Tang *et al.* (2018, 2019), a special-designed experiment together with a streamlined frame is essential for measuring the drag

4 Coupling algorithm for fluid-structure interaction analysis

when $\theta > 60^\circ$. If the flawed force coefficients are employed by the present FSI method, the hydrodynamic forces and the flow field can be inaccurate. Second, the rigid frame is not modeled in the present study due to the insufficient descriptions in Paturrson *et al.* (2010). As shown in Figure 4-10, if the probes are located in the wake region generated by the frame, the measured velocity will be reduced significantly. When $\theta = 75^\circ$, the probe (the red circle in Figure 4-8) is affected by the frame. Thus, the measured velocity is reduced significantly. For these two reasons, it is expected to observe the large deviations when $\theta > 60^\circ$.

Table 4-2 Deviations for the flow velocity reduction factor between numerical simulations and experimental data by Paturrson *et al.* (2010) when $U_\infty = 0.5$ m/s.

	θ	0°	15°	30°	45°	60°	75°
Exp.	C_D	0.258	0.243	0.210	0.157	0.106	0.077
	C_L	0	0.037	0.064	0.075	0.069	0.035
	r_u	0.889	0.886	0.889	0.885	0.865	0.738
Sim.	r_u	0.876	0.880	0.882	0.896	0.899	0.902
	Deviations	-1.45%	-0.79%	-0.45%	1.24%	3.70%	22.67%

4.6.3 Two flexible net panels

4.6.3.1 Case setup

The second validation is performed based on the experiments by Bi *et al.* (2014a), where two flexible net panels are under the action of steady currents. The purpose of this validation is to test whether the present coupling algorithm can accurately predict the deformations of flexible nets and the downstream flow velocity. In the experiment, the tops of the

4.6 Validation for the coupling algorithm

two net panels were fixed on bars just below the free surface. On the bottom of the net panels, steel bars with a density of $8\,610\text{ kg/m}^3$ were mounted as sinkers. The length and diameter of the steel bars were 0.3 m and 6 mm , respectively. Each net panel is a $0.3\text{ m} \times 0.3\text{ m}$ knotless polyethylene net with $d_{w0} = 2.6\text{ mm}$, $L = 20\text{ mm}$ and $Sn = 0.26$.

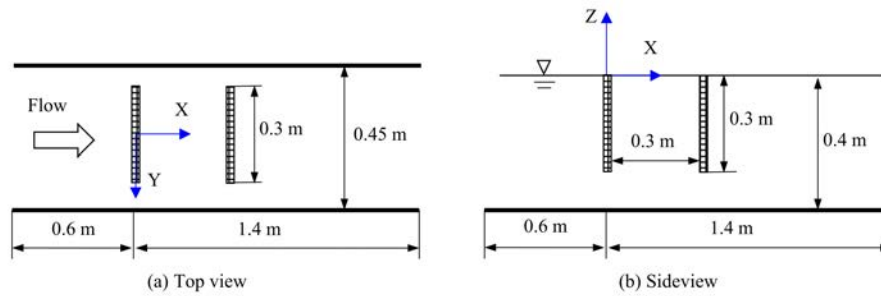


Figure 4-11. Sketch of the simulation domain for the reproduction of the experiment by Bi *et al.* (2014a). The top view is shown on the left, and the side view is shown on the right.

The sketch of the simulation domain is presented in Figure 4-11. In the present numerical model, 2 872 800 cells with $T/\Delta x = 3$ are used for the spatial resolution in the fluid solver, 120 elements with $\lambda=3.0$ are used in the structural solver to represent the two net panels. According to the experiments (Bi *et al.*, 2014a), the turbulence intensity is 4.37% when $U_\infty = 0.226\text{ m/s}$. Thus, $u = 0.226\text{ m/s}$, $k = 1.46 \times 10^{-4}\text{ m}^2\text{s}^{-2}$, $\varepsilon = 2.88 \times 10^{-5}\text{ m}^2\text{s}^{-3}$ are set as the inlet boundary conditions in the fluid solver. In the structural model, nodes on the top of the net panels are fixed to represent the setup in the experiments. Regarding the hydrodynamic forces, C_D and C_L are acquired by fitting the measured data from Bi *et al.* (2014a). The two force coefficients are expressed as follows:

4 Coupling algorithm for fluid-structure interaction analysis

$$C_D = 0.04 + 0.4921\cos\theta + 0.1873 \cos^2 \theta \quad (4-15)$$

$$C_L = 0.4159\sin 2\theta - 0.169 \sin^2 2\theta \quad (4-16)$$

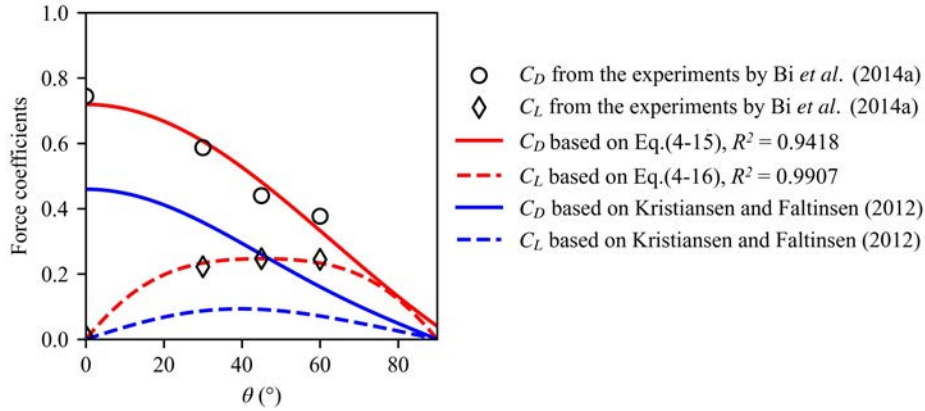


Figure 4-12. The force coefficients from experimental measurements by Bi *et al.* (2014a).

Figure 4-12 shows the force coefficients of the fixed flat net panel based on experimental measurements by Bi *et al.* (2014a). In the experiments, the drag and lift forces on the net panel were measured under four inflow angles when $U_{-\infty} = 0.170$ m/s. Because both the fixed and flexible net panels were made of the same net, the force coefficients of the fixed net panel can be applied to the two flexible net panels. As shown in Figure 4-12, the force coefficients in Eqs.(4-15) and (4-16) well agree with the experimental data. However, the force coefficients, which are derived based on a finite net panel in an infinite flow field by Kristiansen and Faltinsen (2012), are significantly smaller than those based on the experiments by Bi *et al.* (2014a). The large discrepancies

4.6 Validation for the coupling algorithm

can be explained by the two reasons. First, the forces on the net panel were measured in a flume tank with a limited width by Bi *et al.* (2014a). The ratio between the width of the net panel and the width of the flume tank W_n/W_t is =0.67. As explained in Section 4.3.3, the force coefficients should be measured in the ideal condition where a finite net panel is placed in an infinite flow field. When the width of the flume tank is insufficient, the existence of the net panel can speed up the flow velocity on the net due to the mass conservation. The speed-up velocity can cause an increment in the hydrodynamic forces. Hereby, the forces coefficients in the experiments by Bi *et al.* (2014a) are higher than the force coefficients proposed by Kristiansen and Faltinsen (2012). Second, the differences in materials and geometrical parameters of the nets can also contribute to the discrepancy of the force coefficients. This discrepancy can cause different structural responses in numerical simulations, which are revealed in Figure 4-14(a).

4.6.3.2 Structural deformation

As shown in Figure 4-13, the presented numerical model can reproduce the experimental results (Bi *et al.*, 2014a) in the three-dimensional domain. The flow velocity reduction behind the net panels can be observed. The results at the two planes, *i.e.*, $Y = 0$ m and $Z = -0.15$ m, will be used to compare with the numerical results by Kristiansen and Faltinsen (2012) as well as the numerical and experimental results by Bi *et al.* (2014a) in the subsequent discussion.

4 Coupling algorithm for fluid-structure interaction analysis

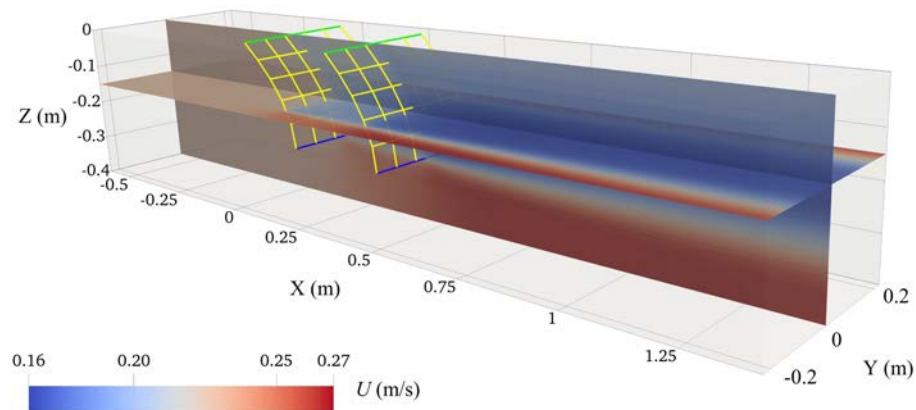


Figure 4-13. Deformation of the two flexible net panels when $U_{\infty} = 0.226$ m/s. The yellow lines represent the nets. The green lines represent fixed parts of the nets. The blue lines represent the steel bars attached to the net bottom.

Figure 4-14(a) shows the deformations of the two flexible net panels obtained from the present numerical simulation, Kristiansen and Faltinsen (2012) and Bi *et al.* (2014a). Figure 4-14(b) shows the corresponding experimental measurements reported by Bi *et al.* (2014a). Compared to the numerical results using the force coefficients based on Kristiansen and Faltinsen (2012), the present results using Eqs.(4-15) and (4-16) show a better agreement with the experimental results (Figure 4-14(b)). The better agreement indicates that: (1) the numerical results are sensitive to the force coefficients; (2) the numerical simulation should use the force coefficients as accordant to the experiments as possible. Although the hydrodynamic force model proposed by Kristiansen and Faltinsen (2012) has been tested in many studies and achieved acceptable results (Yao *et al.*, 2016; Martin *et al.*, 2020), the mismatched force coefficients make the simulations fail to predict the deformations of the net panels correctly. Compared to the numerical

4.6 Validation for the coupling algorithm

results by Bi *et al.* (2014a), the results by using Eqs.(4-15) and (4-16) show only a small discrepancy. This small discrepancy might come from the differences in hydrodynamic force models, coupling algorithms and structural models.

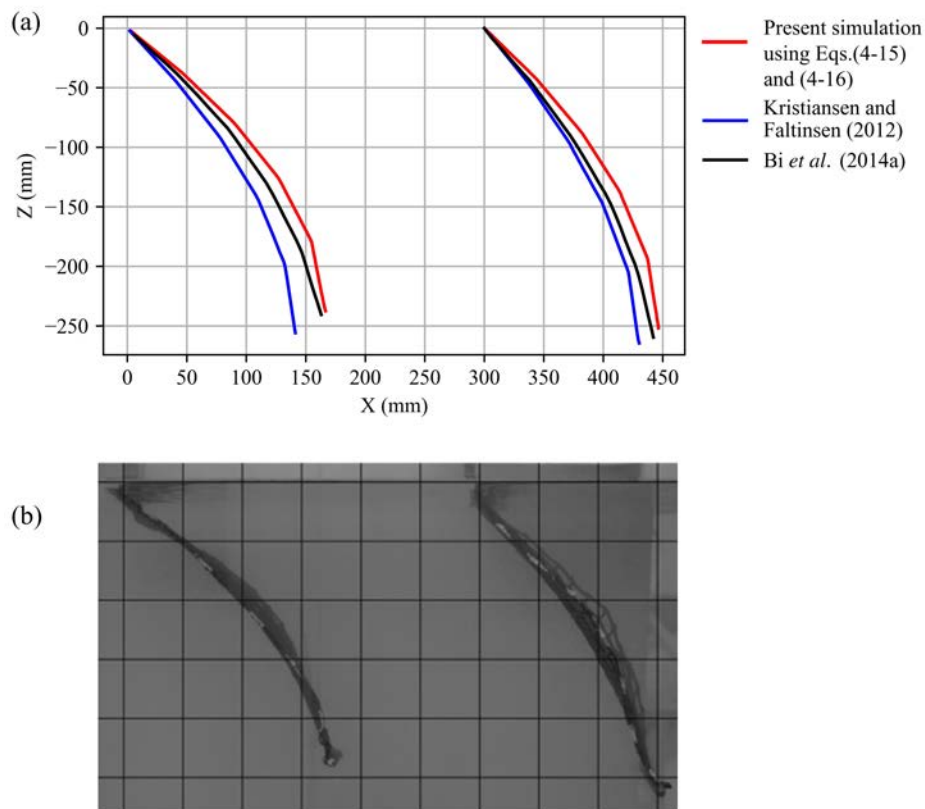


Figure 4-14. Deformations of two flexible net panels when $U_{\infty} = 0.226$ m/s. (a) Numerical simulation results: The red lines use the force coefficients in Eqs.(4-15) and (4-16); The blue lines use the force coefficients based on Kristiansen and Faltinsen (2012), *i.e.*, S3; The black lines are from Bi *et al.* (2014a), where the hydrodynamic forces are calculated using the Morison model, and the nets are modeled using a lumped-mass method. (b) Experimental results by Bi *et al.* (2014a).

4 Coupling algorithm for fluid-structure interaction analysis

4.6.3.3 Flow patterns behind the two net panels

Figure 4-15 shows the flow field around the two flexible net panels using the present coupling algorithm together with force coefficients in Eqs.(4-15) and (4-16). As observed, the flow velocity below and in the flanks of the net panels increases by 20% compared to U_{∞} . The velocity increment is relatively large compared to that from the experiments by Paturrsson *et al.* (2010), where Wn/Wt is =0.27, and the flow velocity in the flanks of the net panel only increases 3%. The large velocity increment also demonstrates that the width of the flume tank in Bi *et al.* (2014a) is insufficient to eliminate the near-wall effects. As for the flow in the wake region, the velocity decreases 10%-15% after the flow passes each net panel. According to the streamlines in Figure 4-15, the diversion of flow direction is small and only occurs near the edges of the net panels.

Besides the deformations, the flow velocity from the present numerical simulation also agrees with the experimental data well. As shown in Figure 4-16, the maximum difference between the numerical results using Eq.(4-16) and the experimental data is only 1.4%. Because of the conservation of momentum, which is explained clearly in Section 4.3.2, it is expected that the flow velocity behind the two net panels obtained by using the force coefficients from Kristiansen and Faltinsen (2012) is higher than that by using Eq.(4-16). The engineering approach proposed by Løland (1991) is also included in Figure 4-16 for comparison. It is observed that the flow velocity behind the two net panels by using this engineering approach is 40% smaller than the experimental data. If the smaller flow velocity is applied in the design of

4.6 Validation for the coupling algorithm

fish cages, the drag on the whole fish cage can be underestimated. With the underestimated drag, the structural design may be non-conservative.

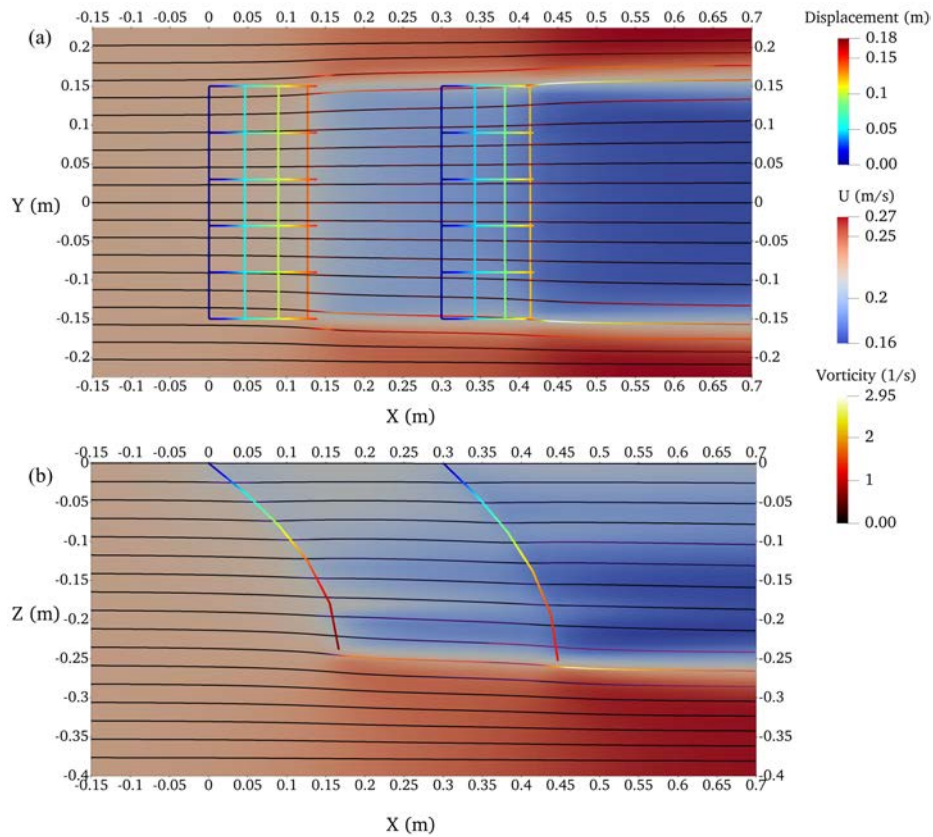


Figure 4-15. Flow velocity field around the flexible net panels. (a) Contours on the horizontal plane $Z = -0.15$ m; (b) Contours on the vertical plane $Y = 0$ m.

4 Coupling algorithm for fluid-structure interaction analysis

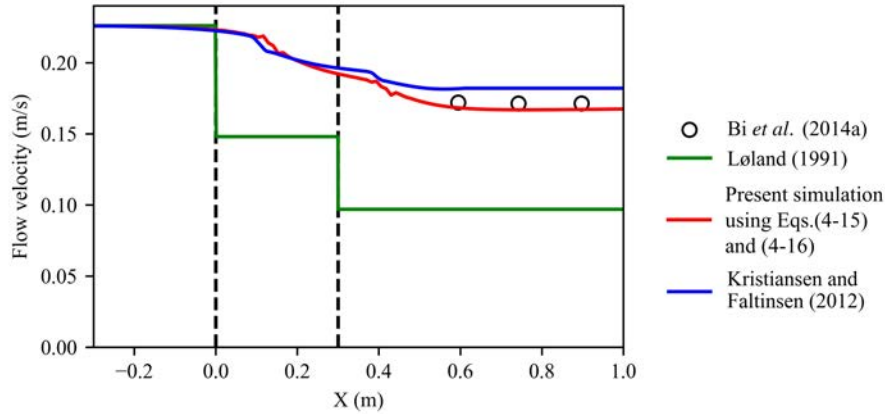


Figure 4-16. Flow velocity along the line $Y = 0$ m on the plane $Z = -0.15$ m. The two vertical dash lines show the initial positions of the net panels.

4.6.4 Full-scale fish cage

4.6.4.1 Case setup

The third validation is performed based on a full-scaled fish cage from sea trials by Gansel *et al.* (2018). The purpose of this validation is to test whether the present method can accurately predict the drag and the deformation of a full-scaled marine aquaculture structure. As discussed by Gansel *et al.* (2018), the numerical methods used in that study cannot properly predict the drag on the full-scale fish cage because the flow field cannot be well addressed. With the present coupling algorithm, both the structural responses and the flow field are coupled and solved simultaneously. Thus, the sea trials can be properly reproduced. To the authors' knowledge, there is no published result on modelling a full-scale fish cage under different current conditions by using the FSI method. Challenges on determining the spatial resolutions and boundary conditions are raised in the numerical simulations

4.6 Validation for the coupling algorithm

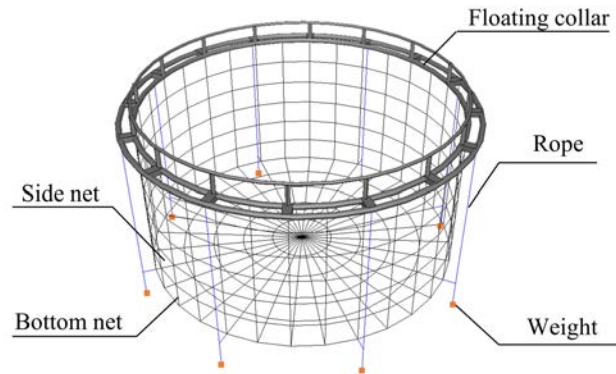


Figure 4-17. Illustration of the fish cage model in the present study.

An illustration of the fish cage in the seal trials by Gansel *et al.* (2018) is shown in Figure 4-17. Eight concrete weights are attached to the floating collar and submerged to 7 meters below the water surface on the outside of the net-pen with even spacing along the circumference. The main parameters of the full-scale fish cage in the sea trials and numerical simulations are given in Table 4-3.

In the numerical model, 2 906 299 cells with $T/\Delta x = 3$ are used in the fluid solver, 704 elements with $\lambda = 66.67$ are used in the structural solver. In order to increase the resolution around the fish cage, the grid in the fluid solver is refined in the vicinity of the fish cage. A grid convergence has been carried out with the same procedure as described in Section 4.6.1, and the final spatial resolution is shown in Figure 4-18.

4 Coupling algorithm for fluid-structure interaction analysis

Table 4-3. The parameter of the full-scale fish cage in sea trials and numerical simulations.

	Full-scale model	Numerical model
Cage diameter (m)	12	12
Cage height (m)	6	6
Submerged weight (Kg)	35×8	35×8
Bottom ring (kg/m)	0.5	0.5
Twines Young's modulus (MPa)	400	400
Twines density (kg/m ³)	1140	1140
Net half mesh size (mm)	15	1000*
Net twine diameter (mm)	2	16.33*
Solidity	0.27	0.27

* The net half mesh size in the numerical model is larger than the Full-scale model because of the mesh grouping method proposed by Cheng *et al.* (2020). The net twine diameter in the table refers to the structural diameter (d_{ws}). For the elastic diameter (d_{we}) and the hydrodynamic diameter (d_{wh}), please refer to Section 3.6.

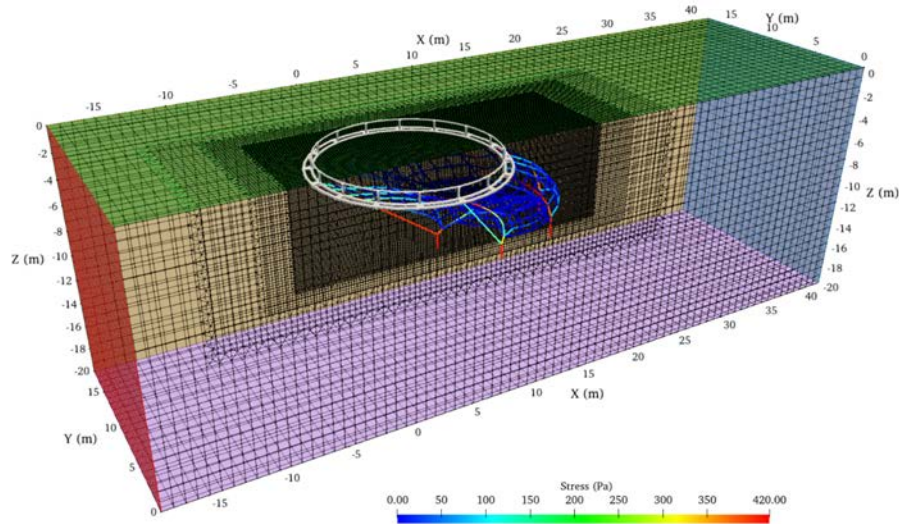


Figure 4-18. The computational grid in the fluid solver and the deformed fish cage in the structural solver. The grid is refined in the vicinity of the circular cage. The computational grid is slipped on plane $Y = 0$ m in order to show the structural responses.

4.6 Validation for the coupling algorithm

In the sea trials by Gansel *et al.* (2018), the fish cage was towed at five different speeds in a fjord when the wave effects could be neglected. In order to minimize the effect of the bow wave caused by the boat, the fish cage is placed 350 meters behind the towing boat. According to the measurements in the sea trials, the flow velocities and directions are stable over the depth of the fish cage. Thus, it is reasonable to set a uniform velocity condition at the inlet boundary in the fluid solver. Hereby, five uniform velocities, *i.e.*, 0.156 m/s, 0.312 m/s, 0.509 m/s, 0.732 m/s and 1.056 m/s, are set on the inlet boundary for each simulation. k and ε are estimated using Eq.(4-8) based on the assumptions that medium turbulence ($I = 5\%$) occurs in the sea trials, and the turbulence length scale L_T is equal to the diameter of the fish cage. In the structural model, the nodes on the floating collar are fixed to represent the setup in the sea trial. The hydrodynamic force model in the simulations follows the suggestions from Gansel *et al.* (2018). The force coefficients are originally proposed by Kristiansen and Faltinsen (2012). The expression can be found in Table 2-3.

4.6.4.2 Structural responses

As shown in Figure 4-19, the drag on the fish cage first increases to a peak value then decays as time increases. After 100 s, the simulation reaches equilibrium. The depth of bottom nets, defined as the depth of the lowest node on bottom nets, follows the opposite trend of the drag. Although the simulation is performed under pure current conditions, oscillations are still observed in the present numerical results. These oscillations come from the nonlinearity of the system, which is also

4 Coupling algorithm for fluid-structure interaction analysis

reported by Antonutti *et al.* (2018). In the present results, the standard deviation for the time-series drag over the last 100 s is 1.8% of the mean drag, which is smaller than that in the sea trial measurements by Gansel *et al.* (2018). Thus, the oscillations in the numerical results are acceptable. For the subsequent discussions, the time-averaged results over the last 100 s are used.

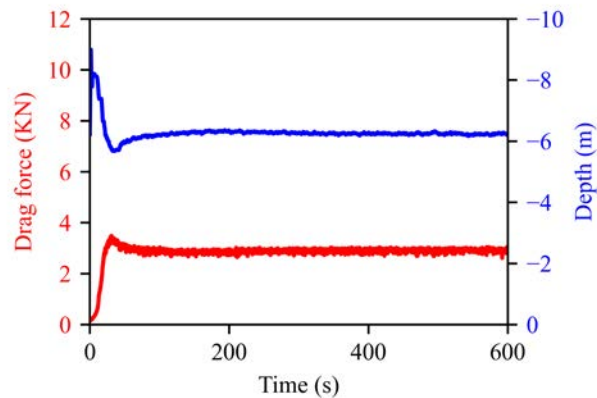


Figure 4-19. Time series of the drag on the fish cage and the depth of bottom nets from the numerical results when the towing speed is 0.509 m/s.

Figure 4-20 shows the comparison of the numerical results from the FSI method and the non-FSI method, along with results from sea trials. The two numerical methods use the same structural model and hydrodynamic force model, and the only difference between the two methods is the way to handle the wake effects. The FSI method models the wake effects by CFD simulations and uses the present FSI algorithm to couple the fluid and structural solvers. In contrast, the non-FSI method simplifies the wake effects by assigning flow velocity reduction factors

4.6 Validation for the coupling algorithm

(r_u) onto the downstream nets without coupling with the fluid solver. In the latter method, r_u is calculated according to the engineering approach proposed by Løland (1991).

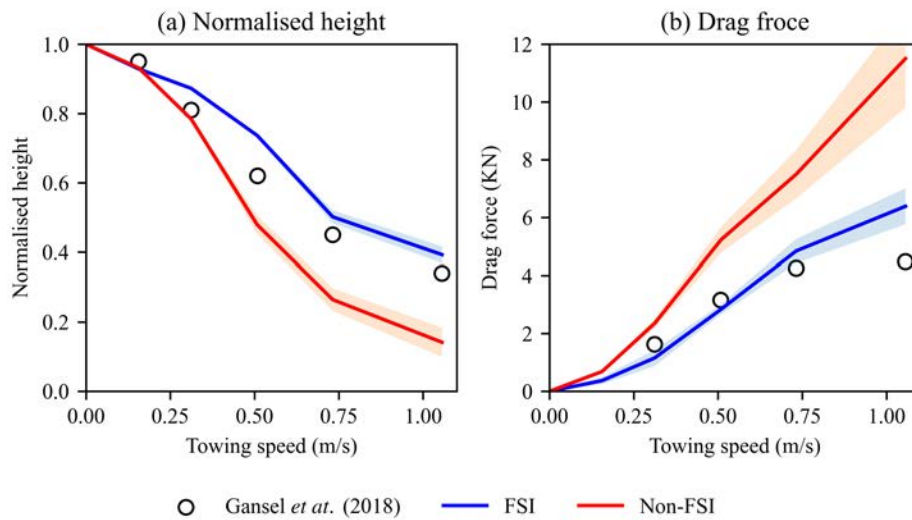


Figure 4-20. Results from the two numerical methods and sea trials. The shadows show the 99.7% confidence intervals.

In Figure 4-20 (a), the normalized height is calculated as the height of the fish cage at a given current velocity divided by the initial height of the fish cage (6 m). Since the bottom nodes of the fish cage are not in a horizontal plane, the height of the fish cage is calculated based on the average depth of the nodes on the bottom nets. This averaged depth is the same as the data processing in the sea trials (Gansel *et al.*, 2018). It can be observed that the height decreases with the increasing current velocity. The height of the fish cage by the non-FSI method is smaller than that of sea trial measurements, and the difference becomes distinct with the increasing current velocity.

4 Coupling algorithm for fluid-structure interaction analysis

Compared with the non-FSI method, the results from the FSI method show better agreement with the sea trials regarding the drag. As shown in Figure 4-20 (b), the drag loads by the non-FSI method are much higher than the sea trial measurements. In particular, the predicted drag can be twice larger than the sea trial measurement when the towing speed is 1.056 m/s. In comparison, the differences between the predicted forces by the FSI method and the sea trial measurements are less than 10% when the flow velocity is smaller than 1 m/s. For the case with towing speed of 1.056 m/s, the large deviation can be explained by the two reasons: First, the measurement may have large uncertainties when the towing speed is 1.056 m/s. According to Gansel *et al.* (2018), the sea trial measurements were the averaged values over 10 minutes in the sea trial. When the fish cage was towed at 1.056 m/s, the wake behind the boat reached the fish cage after 6 minutes. As half of the time-series measurements were affected by the wake, the result by the sea trials at 1.056 m/s may have errors. Second, the bow wave caused by the towing boat can affect the uniformity of the incoming flow velocity at this high towing speed. As described by Gansel *et al.* (2018), an obvious shear flow was observed on the vertical plane $Y=0$ m when the towing speed was 1.056 m/s. Since descriptions of the shear flow are insufficient, the exact boundary condition cannot be reproduced in the numerical simulation. Thus, it is reasonable to observe the large difference between the numerical simulations and the sea trial measurements when the towing speed is 1.056 m/s.

4.6 Validation for the coupling algorithm

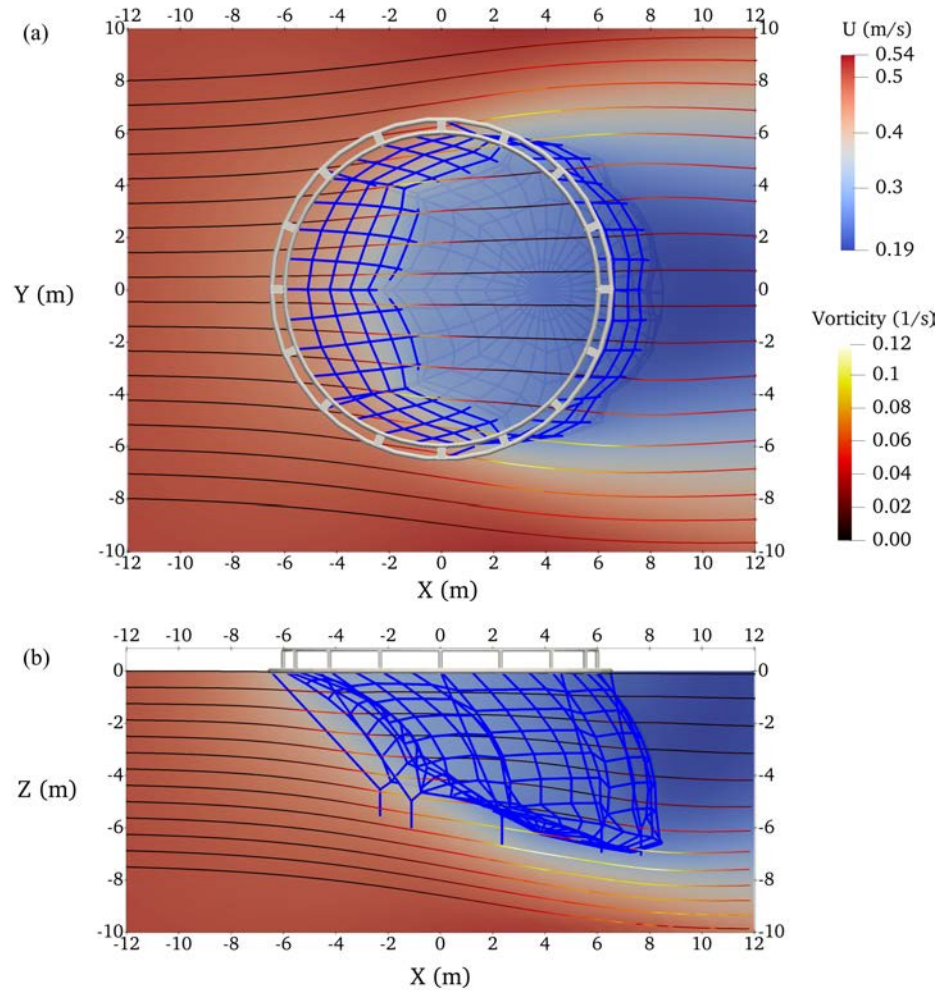


Figure 4-21. Flow velocity field around the fish cage when the towing speed = 0.508 m/s. (a) Contours on the horizontal plane $Z = -3$ m; (b) Contours on the XZ plane $Y = 0$ m.

4.6.4.3 Flow patterns behind and around the fish cage

Figure 4-21 shows the flow velocity field together with the deformations of the fish cage from the present numerical simulations. As observed from this figure, the flow velocity increases approximately by 6.09% compared to the towing speed at the bottom and flanks of the fish cage.

4 Coupling algorithm for fluid-structure interaction analysis

When the fluid encounters the deformed fish cage, a part of the fluid follows the guidance of curved nets. Due to the mass conservation, the flow velocity is expected to increase at the bottom and flanks of the fish cage. The flow velocity decreases up to 62.67% after the flow passes the fish cage. According to the streamlines on the horizontal plane (Figure 4-21 (a)), the flow around the fish cage is almost laminar. This indicates that the TKE at the region downstream of the fish cage is insufficient to generate large vortices with a length scale of L_T . As shown in Figure 4-21 (b), downward flows are observed inside and below the fish cage. These downward flows are reasonable and physical, according to Newton's Third Law. As the lift force on the front nets is upward, the lift force can, in turn, push the flow downward. Hence, the flow velocity and direction on the downstream nets are different from the upstream nets. Accordingly, it is expected that the FSI method has more accurate predictions on the responses of the full-scale fish cage than the non-FSI method, as the non-FSI method employs the engineering approach that only reduces the magnitude of flow velocity.

Figure 4-22 shows the detailed velocity profiles around the fish cage from the FSI simulations. In general, the X-component flow velocity U_x is symmetric about the $Y = 0$ m plane, and the flow velocity reduces significantly near this symmetric plane compared to the incoming flow velocity. The width of the velocity reduction region is around 1.5 ~ 2 times of the fish cage diameter, and this width increases with increasing X coordinate along the incoming flow direction. Compared to the study by Gansel *et al.* (2012), the widths in the present

4.6 Validation for the coupling algorithm

study are slightly larger than their results from the towing tank experiments, where the width is about 1.1~1.4 times the cage diameter. This discrepancy of widths may be due to that the experiments in Gansel *et al.* (2012) used rigid metal nets, while the present study considers flexible nylon nets. The different net materials can make their twines have different surface roughness and thus may cause different flow separations around the twines of nets. Consequently, the wake of the cage can have different widths. Besides, the deformation properties can also cause the discrepancy of wake widths. The deformed nets can guide part of the flow to the bottom. Hence, the fluid at the region downstream of the cage does not have enough momentum to keep the velocity gradient. Besides, the velocity profiles also vary with depth. At a deeper position, the velocity profile has smaller variations. However, the engineering approach proposed by Løland (1991) can only give an averaged estimation, but it cannot give the variations with depths and horizontal position.

4 Coupling algorithm for fluid-structure interaction analysis

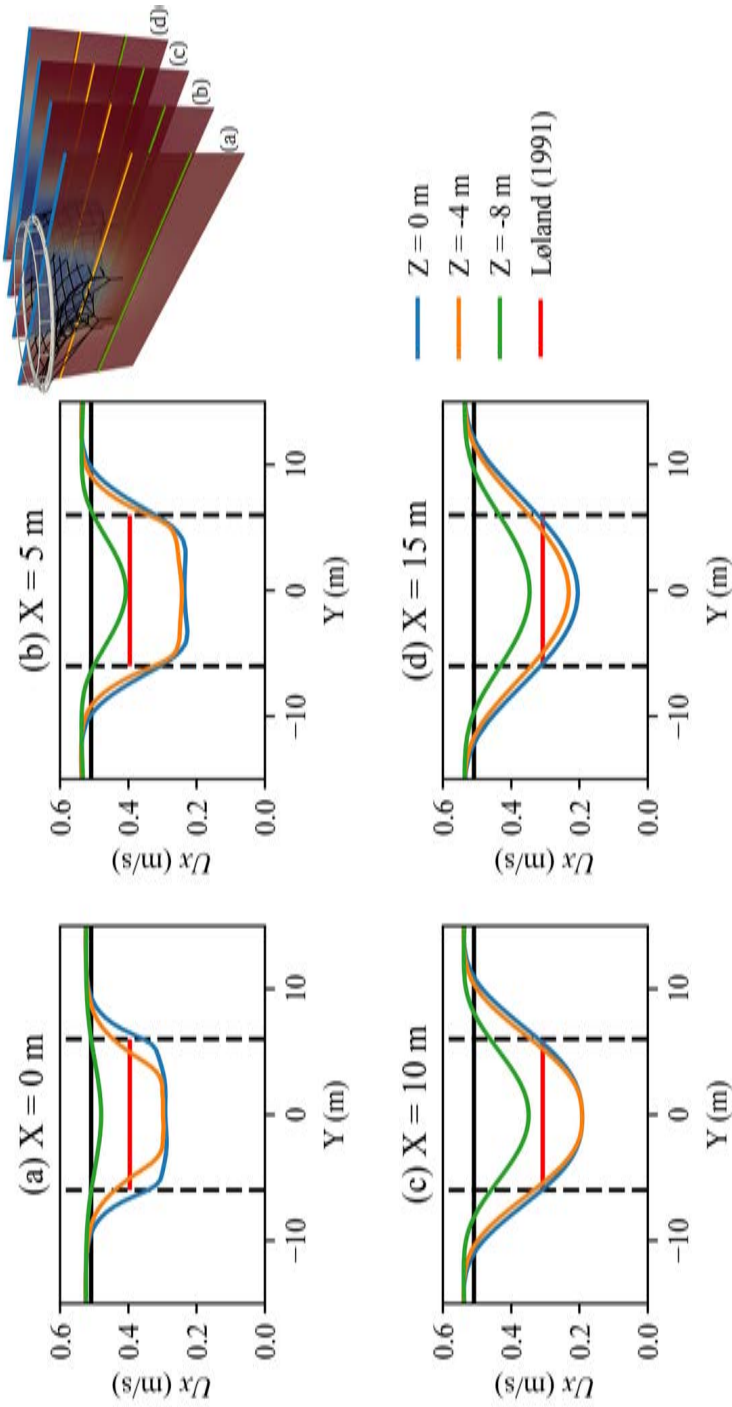


Figure 4-22. Flow velocity profile on four vertical Y-Z planes, which are illustrated at the upper right corner. The undistributed flow velocity (0.508 m/s) is plotted using black lines for reference. The vertical dashed lines indicate the diameter of the fish cage.

4.6 Validation for the coupling algorithm

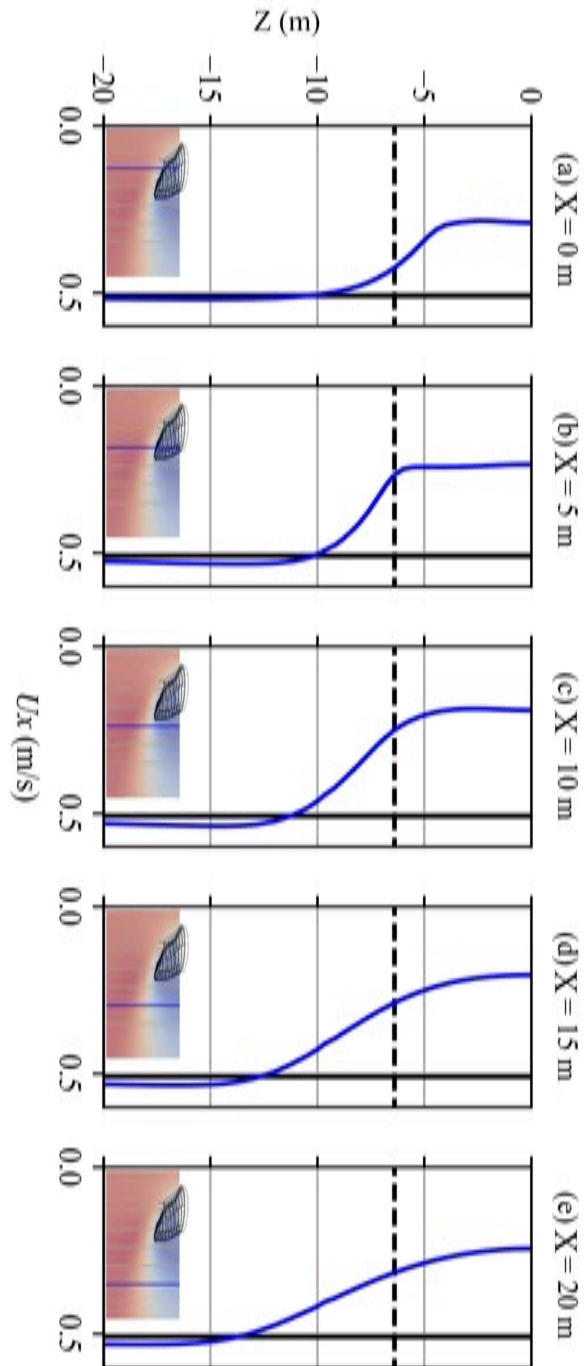


Figure 4-23. Flow velocity profile on XZ plane with $Y=0$. The illustration in the lower left of each subplot figure shows the location of the velocity profile. The dashed lines indicate the Z-position of the deepest node on the fish cage. The undistributed flow velocity (0.508 m/s) is plotted using black lines for reference.

4 Coupling algorithm for fluid-structure interaction analysis

Figure 4-23 shows the flow velocity profiles on the X-Z plane with $Y = 0$ m at different X positions. The height of the velocity reduction region is 1.4 ~2 times of the fish cage height, and this height increases along the flow direction (X direction). Significant flow velocity reductions are observed between the free surface and the bottom of the fish cage. The lowest velocity occurs near the free surface right behind the whole fish cage, as shown in Figure 4-23(c). Below the fish cage (around $Z = -6.4$ m), the flow velocity slowly increases and reaches slightly higher values than the undistributed flow velocity for all the presented profiles. This faster flow velocity may help to sweep away the fish feces and uneaten feeds, but this may differ due to the terrains at different sites.

4.6.4.4 Elapsed time for numerical simulations

All the simulations presented in this chapter are performed on a desktop computer with an eight-core CPU, Intel® Xeon® CPU E5-2620 v4 @ 2.10 GHz, and 32GB memory. From the perspective of general computational efficiency, the elapsed time for running the numerical simulations is shown in Table 4-4. It shows that the elapsed time increases with the increasing number of elements and cells. Regarding the simulations of the two flexible net panels, the elapsed time in the study by Bi *et al.* (2014) was 18 h, which is sixteen times longer than the elapsed time in the present study.

4.6 Validation for the coupling algorithm

Table 4-4. Elapsed time for running numerical simulations.

Case	Number of elements	Number of cells	Simulation time (s)	Elapsed time (h)	
				FSI	Non-FSI
Single fixed net panel $\theta = 0^\circ, 15^\circ, 30^\circ, 45^\circ, 60^\circ, 75^\circ$	220	560 952	80	3.3-3.5	-
Two flexible net panels $U_\infty = 0.266$ m/s	120	202 686	60	1.1	-
Full-scale fish cage $U_\infty = 0.156$ m/s, 0.312 m/s, 0.509 m/s, 0.732 m/s, 1.056 m/s	704	2 906 299	600	18.9- 19.1	6.9

4.7 Conclusions

In this chapter, a new coupling algorithm for fluid-structure interaction analysis of fluid flow through and around flexible nets is developed. The new coupling algorithm can benefit from combining the Finite Element Method (FEM) and Finite Volume Method (FVM). It can predict the structural responses of flexible nets and the surrounding flow field with higher accuracy. The new coupling algorithm properly removes the additional data-fitting process for porous coefficients and adopts the Screen model to calculate the hydrodynamic forces. The two improvements can simplify the numerical procedures and improve the accuracy of numerical simulations. Besides, the new coupling algorithm employs the time-stepping procedure for the data transfer between the fluid and structural solvers and fulfills the law of momentum conservation. These two features ensure that the present method can achieve reliable results in both steady and unsteady conditions.

By applying the present coupling algorithm, Code_Aster and OpenFOAM can work together to simulate structural responses of the thin, flexible and high permeable nets in large marine aquaculture structures. Extensive validation studies are performed, considering different solidities, inflow angles, incoming velocity and dimensions of nets. In general, velocities in the wake region, deformations of nets and drag loads of the fish cage agree well with the validation data. Thus, the extensive validations in the present study provide strong confidence for users to apply the new coupling algorithm in a variety of numerical

4.7 Conclusions

simulations related to the nets in marine aquaculture structures. Furthermore, the following conclusions are drawn based on the validations:

- (1) The hydrodynamic force coefficients are vital for numerical simulations. As discussed in Section 4.6.1, the numerical results can have a large deviation up to 22.67% when $\theta = 75^\circ$ if the employed C_D is unreliable. According to Section 4.6.3, the appropriate hydrodynamic force coefficients are essential to reproduce the experiments accurately
- (2) A turbulence model is suggested to employ in the fluid model in order to remove the unphysical sharp velocity gradient in the wake region. Hereby, the environmental loads on the downstream structures have small fluctuations, and the numerical simulations can easily achieve stable results.
- (3) The engineering approach provided by Løland (1991) is insufficient to address the changes in the flow field around a fish cage. As shown in Sections 4.6.1-4.6.4, the existence of nets can affect both the magnitude and direction of the fluid flow. However, the engineering approach only approximates the wake effect as a flow velocity reduction without considering the direction changes.

4.8 Appendix. Derivation of the flow velocity correction

In the present study, the hydrodynamic loads on nets are calculated using the model that is derived from experiments. According to the formulae (Eqs.(2-5) and (2-6)), the hydrodynamic loads are functions of the undistributed incoming flow velocity $U_{-\infty}$. While, in the FSI analyses, the fluid solver extracts the flow velocity at the center of porous zones (U_c). Thus, a process of velocity correction is needed to convert U_c to $U_{-\infty}$, so that, the existing hydrodynamic force models can be applied in the simulations.

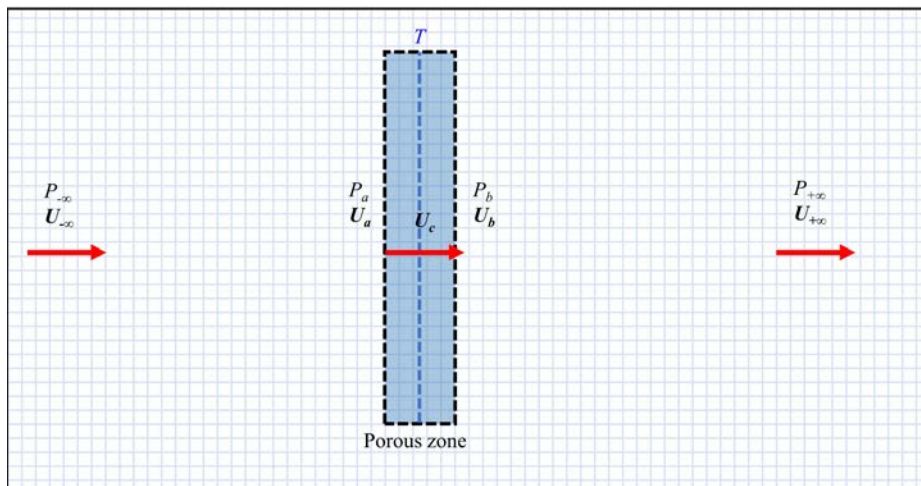


Figure 4-24. Illustration of the notations for velocity and pressure. The black dash box represents a porous zone. The blue dash line is the centerline of the porous zone. T is the thickness of the porous zone.

The derivation in this chapter is based on Bernoulli's principle without consideration of gravity. As shown in Figure 4-24, subscript a represents the variables (pressure and velocity) in front of the porous

4.8 Appendix. Derivation of the flow velocity correction

zone; subscript b represents the variables at the rear of the porous zone. The subscript ∞ represents the variables in the far-field, while $-\infty$ represents the undistributed variables, and $+\infty$ represents the variables in the wake. Because the source term is only added to the cells in porous zones, it is reasonable to assume that the energy is constant along the streamlines that are in front of the porous zone and behind the porous zone. Thus, two Bernoulli equations can be achieved:

$$p_{-\infty} + \frac{1}{2}\rho(\mathbf{U}_{-\infty})^2 = p_a + \frac{1}{2}\rho(\mathbf{U}_a)^2 \quad (4-17)$$

$$p_b + \frac{1}{2}\rho(\mathbf{U}_b)^2 = p_{+\infty} + \frac{1}{2}\rho(\mathbf{U}_{+\infty})^2 \quad (4-18)$$

As shown in Figure 4-24, the pressure variations in front of and behind the porous zone are approximately equal. Thus, it can assume that:

$$p_a - p_{-\infty} = p_{+\infty} - p_b \quad (4-19)$$

The porous zone has at least one layer of cells, and the source term is added to the cell centroids. Approximately, the velocity is linearly reduced along the streamline in porous zones (from a to b) as the source terms are the same among the cells in a porous zone. The thickness of the porous zone is reasonably small compared to the length of the whole computational domain. Thus, it is proper to assume that:

4 Coupling algorithm for fluid-structure interaction analysis

$$\mathbf{U}_a + \mathbf{U}_b = 2\mathbf{U}_c \quad (4-20)$$

The hydrodynamic force on the net panel causes a pressure jump across the porous zone. Based on Newton's Third Law, Eq.(4-21) can be given. The expression on the left-hand side of Eq.(4-21) comes from the definition of drag in laboratory experiments.

$$\frac{1}{2}C_D\rho A_t(\mathbf{U}_{-\infty})^2 = (p_a - p_b)A_t \quad (4-21)$$

Eq.(4-17) + Eq.(4-18) can get:

$$\begin{aligned} p_b + p_{-\infty} + \frac{1}{2}\rho(\mathbf{U}_{-\infty})^2 + \frac{1}{2}\rho(\mathbf{U}_b)^2 \\ = p_a + p_{+\infty} + \frac{1}{2}\rho(\mathbf{U}_{+\infty})^2 + \frac{1}{2}\rho(\mathbf{U}_a)^2 \end{aligned} \quad (4-22)$$

Combing Eq.(4-22) with Eq.(4-21), it can get:

$$\begin{aligned} p_{-\infty} - p_{+\infty} + \frac{1}{2}\rho(\mathbf{U}_{-\infty})^2 + \frac{1}{2}\rho(\mathbf{U}_b)^2 \\ = \frac{1}{2}C_D\rho(\mathbf{U}_{-\infty})^2 + \frac{1}{2}\rho(\mathbf{U}_{+\infty})^2 + \frac{1}{2}\rho(\mathbf{U}_a)^2 \end{aligned} \quad (4-23)$$

If the pressures at the far-field ($p_{-\infty}$ and $p_{+\infty}$) can be assumed approximately equal, then Eq.(4-22) can be rewritten as:

4.8 Appendix. Derivation of the flow velocity correction

$$(1 - C_D)(U_{-\infty})^2 = (U_{+\infty})^2 + (U_a)^2 - (U_b)^2 \quad (4-24)$$

Eq.(4-17) – Eq.(4-18) can get:

$$\begin{aligned} p_{-\infty} - p_b + \frac{1}{2}\rho(U_{-\infty})^2 - \frac{1}{2}\rho(U_b)^2 \\ = p_a - p_{+\infty} + \frac{1}{2}\rho(U_a)^2 - \frac{1}{2}\rho(U_{+\infty})^2 \end{aligned} \quad (4-25)$$

Combing Eq.(4-25) with Eq.(4-19), it can get:

$$(U_{+\infty})^2 = (U_b)^2 + (U_a)^2 - (U_{-\infty})^2 \quad (4-26)$$

Replacing $(U_{+\infty})^2$ in Eq.(4-24) with Eq.(4-26), it can get:

$$(2 - C_D)(U_{-\infty})^2 = 2(U_a)^2 \quad (4-27)$$

Combing Eq.(4-27) with Eq.(4-20), the undistributed incoming flow velocity can be expressed as:

$$(U_{-\infty})^2 = \frac{2}{(2 - C_D)} \left(U_c + \frac{U_a - U_b}{2} \right)^2 \quad (4-28)$$

As shown in Figure 4-25, $U_c \gg \frac{U_a - U_b}{2}$. Thus, Eq.(4-28) can be approximated as:

4 Coupling algorithm for fluid-structure interaction analysis

$$\mathbf{U}_{-\infty} = \sqrt{\frac{2}{2 - C_D}} \mathbf{U}_c \quad (4-29)$$

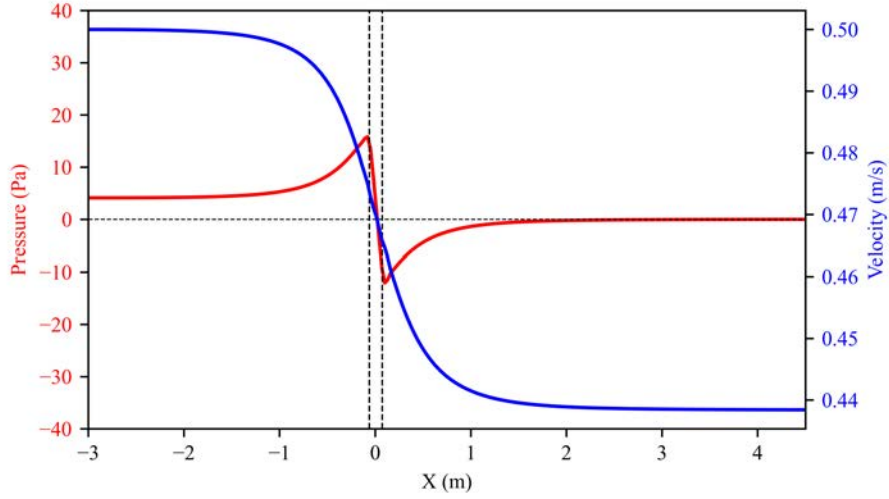


Figure 4-25. Illustration of velocity and pressure distribution in front of and behind a net panel. The vertical dash lines represent the thickness of a porous zone.

One should notice that Eq.(4-29) is derived based on the assumption that the flow direction is perpendicular to the net panel, *i.e.*, the inflow angle $\theta = 0^\circ$. When $\theta \neq 0^\circ$, the lift force should be considered. At this point, all the preceding derivation is still valid except that Eq.(4-21) is changed to:

$$\frac{1}{2}(C_D + C_L)\rho A_t(\mathbf{U}_{-\infty})^2 = (p_a - p_b)A_t \quad (4-30)$$

Therefore, the final relationship between \mathbf{U}_c to $\mathbf{U}_{-\infty}$ is:

4.8 Appendix. Derivation of the flow velocity correction

$$U_{-\infty} = \sqrt{\frac{2}{2 - (C_D + C_L)}} U_c \quad (4-31)$$

According to the experimental data by Bi *et al.* (2013) and Bi *et al.* (2014a), U_c can be acquired by averaging the velocities on the centrelines of the porous zones from the Fig. 11 in Bi *et al.* (2013). C_D and C_L can be calculated by using the Table 1 in Bi *et al.* (2014a). As shown in Table 4-5, the flow velocities calculated using Eq.(4-31) agree well with the experimental results.

Table 4-5. Comparison of the flow velocity at the center of a porous zone when $U_{\infty} = 0.17$ m/s.

Inflow angle	0°	30°	45°	60°
C_D	0.744	0.587	0.440	0.322
C_L	0.011	0.222	0.247	0.245
U_c^*	-	0.135	0.134	0.139
$U_c^\#$	0.134	0.131	0.138	0.144
Deviation	-	-3.1%	2.9%	3.5%

U_c^* : The velocities are averaged based on the centerlines of the porous zones in Fig. 11 from Bi *et al.* (2013).

$U_c^\#$: The velocities are calculated using Eq. (4-31)(4-21).

5 Application to the design of traditional fish cages

The content is partly published as:

Cheng, H., Li, L., Ong, M.C., 2022. Comparative study of five commonly used gravity type fish cages under pure current conditions. *Ocean Engineering* 250, 110977.

5.1 Introduction

Fish cages are commonly used facilities in aquaculture. More than 150 fish species and 12 species of prawn, lobster and crab have been grown in cages (Beveridge, 2004). Over the past six decades, enormous types of fish cages have been proposed and developed (Chu *et al.*, 2020; Guo *et al.*, 2020; Huguenin, 1997; Xu and Qin, 2020; Sievers *et al.*, 2021; Shainee *et al.*, 2013a). However, the number of cage types today is smaller than it was two decades ago (Beveridge, 2004). Capital cost, which always comes at first, has become the overriding design criterion for industrial-scale fish farming, and this has led to an optimized design of cages by considering shape, size, and material). The gravity type fish cage, using High-Density Polyethylene (HDPE) pipes as the skeleton to provide frame and buoyancy and using weight to keep cultivation volume, is now the first choice for most marine aquaculture sites. Since they are relatively inexpensive and convenient to build, this type of fish cage has been the dominant production technology for marine finfish aquaculture in many countries, such as Norway, China, Japan, Chile, and Australia. For the countries with a low level of industrialization, this cage technology has enormous potential for expansion, especially in inland and coastal waters (Cardia and Lovatelli, 2015; Edwards, 2015; Shainee *et al.*, 2013b).

One of the main challenges for the gravity type fish cage is to ensure a sufficient cultivation volume for fish welfare. As the netting of a fish cage is usually flexible and may have large deformations under

5 Application to the design of traditional fish cages

environmental loads, the cultivation volume can significantly decrease under severe currents and waves (Johannesen *et al.*, 2021). In order to investigate the deformation and cultivation volume of fish cages, considerable research works have been done using experimental and numerical methods. A review of these research works is presented in Section 1.2.

Moreover, there is a need for the aquaculture industry to evolve from experienced-based design to knowledge-based design by verified numerical simulations, especially when the modern fish farm is growing up in developing countries. This chapter investigates the structural responses of different cage designs using UiS-Aqua and provides practical guides for cage constructions in the future.

5.2 Descriptions of the traditional fish cage

As illustrated in Figure 5-1, a typical fish cage usually comprises three main components (from top to bottom): floating collar, net bag, and weights. These three components determine the features of a fish cage. In addition, top net (for submersible cage or to prevent predation of birds), jumping net (to prevent fish jumping out of the cage) and skirt net (to reduce infestation of salmon lice) may be installed depending on the site conditions.

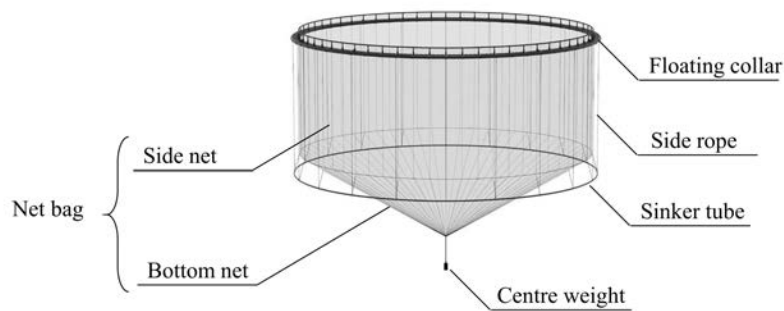


Figure 5-1. Illustration of a gravity type fish cage (reproduced from AKVA Group 2020).

The floating collar, usually sitting at the water level, provides buoyancy force to sustain the cage floating, helps to maintain the net bag shape, serves as a work platform for operators, and offers handles to mooring lines for keeping the cage's position (Lekang, 2019). The structural design of the floating collar varies according to the available material, site condition and cage size. With years of development, the

5 Application to the design of traditional fish cages

commonly used material for the floating collar is HDPE now due to its durability in sunlight and relatively low price.

The weight, usually located at the bottom of a fish cage, is used to keep the net bag down and maintain as much effective volume as possible for the farmed fish (Lekang, 2019). In general, different forms of weight can be applied to a fish cage, such as (1) multiple-sinker weight (multiple sinkers attached to floating collars using side ropes), (2) single-sinker weight (only one single weight attached to the bottom net) and (3) sinker tube (one continuous pipe attached to the bottom net). Strong currents will decrease the cultivation volume, and increasing weights can suppress this. However, care must be taken because adding weights will increase the current forces on the net bag and increase the dynamic forces on the net bag caused by the waves (stretch and slack). The performance of these three forms of weight in steady current will be discussed in this chapter.

The net bag is regarded as the most critical part of a fish cage as it is the only barrier that protects the site environment from fish escapes. However, the netting should only keep the fish confined inside the net bag and should not have any structural functions, such as bearing loads and supporting cage shape (Cardia and Lovatelli, 2015). Nowadays, synthetic materials, *e.g.*, Polyamide (PA, or nylon) and Polyethylene (PE), predominate in the aquaculture industry, because they are relatively cheap, strong and flexible (Lekang, 2019). The rope, acting as the skeleton of the netting, is usually the main structural component to

5.2 Descriptions of the traditional fish cage

ensure the strength and robustness of the net bag. All the weights of a cage are borne by the ropes and usually carried by the floating collar, in order to avoid the tearing damage on netting.

5 Application to the design of traditional fish cages

5.3 The studied parameters and conditions


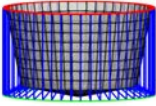

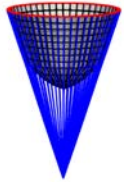
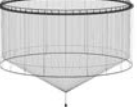
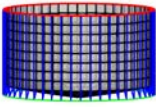

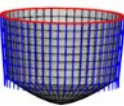

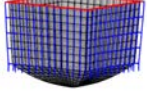
In the present study, five widely used gravity fish cages are modeled using the well-validated structural model presented in Chapter 3. The hydrodynamic loads on ropes and nets are calculated using Morison model and Screen model, respectively. The common properties of the main components are listed in Table 5-1. These properties come from operating farms in the industry and have been applied in previous studies (Cheng *et al.*, 2021; Endresen *et al.*, 2014). Table 5-2 summarizes the main different characteristics of these five fish cages, and the three-letter cage names reflect the characteristics of the three components from top to bottom.

Table 5-1. The common properties of the main components for all the fish cage models

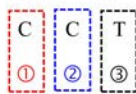
Component	Parameter	Value	Unit
Netting	Twine diameter	2.85	mm
	Mesh length	25.87	mm
	Density	1140	kg/m ³
	Young's modulus	2	GPa
	Solidity	0.2056	-
	Mesh shape	Square	-
Sinker Tube	Section diameter	0.35	m
	Pipe thickness	0.0185	m
	Density	958	kg/m ³
	Young's modulus	3	GPa
Rope	Section diameter	50	mm
	Density	1100	kg/m ³
	Young's modulus	1	GPa
	Horizontal interval	2.5	m

5.3 The studied parameters and conditions

Table 5-2. A summary of the main characteristics of the studied fish cages.

Cage name ¹	Illustration ²	Numerical model ³	Description
CCT			CCT model is a truncated-cone shape cage with a double-pipe circular floating collar to provide buoyancy force and a single-sinker weight to weight down the net.
CCS			CCS model is a truncated-cone shape cage with a double-pipe circular floating collar to provide buoyancy force and a single-sinker weight to weight down the net.
CST			CST model is a straight shape cage with a double-pipe circular floating collar to provide buoyancy force and a single-sinker weight to weight down the net.
CSM			CSM model is a straight shape cage with a double-pipe circular floating collar to provide buoyancy force and multiple sinkers to weight down the net.
SSM			SSM model is a straight shape cage with a double-pipe square floating collar to provide buoyancy force and multiple sinkers to weight down the net.

1: Cage name



①	②	③
The shape of floating collar	The shape of net bag	The form of weight
C: Circular shape S: Square shape	C: Truncated-cone shape S: Straight shape	T: Sinker tube S: Single-sinker weight M: Multiple-sinker weight

2: The illustrations are gathered from a user manual created by AKVA Group (2020).

3: In the numerical model, the colored components refer to the floating collar (red), ropes (blue), nettings (grey) and sinker tube (green).

5 Application to the design of traditional fish cages

In order to investigate the effects of the design parameters on the cultivation volumes and drag loads, 5 circumferences of floating collar (C), 5 depths of net bag (H), 5 design submerged weight (W) and 9 current velocities (U) are considered in the parametric study. Together with the 5 types of fish cages, there are $5 \times 5 \times 5 \times 9 \times 5 = 5625$ cases in total. A summary of the studied parameters is shown in Table 5-3.

Table 5-3. Summary of the studied parameters.

Parameter	Variable	Value	Unit
Circumference of floating collar	C	100, 120, 140, 160, 180	m
Depth of net bag	H	10, 20, 30, 40, 50	m
Weight*	W	40, 50, 60, 70, 80	kg/m
Current velocity	U	0, 0.1, 0.2, 0.3, 0.4, 0.5, 0.6, 0.7, 0.8	m/s

* Weight: In the present study, the weight refers to the submerged weight per meter of circumference (Cardia and Lovatelli, 2015). *E.g.*, for a fish cage with $W = 40$ kg/m and $C = 120$ m, the total submerged weight $W_0 = 40 \times 120 \times 9.81 = 47\,088$ N.

Figure 5-2 shows the studied parameters H and C in comparison with the previous studies (Bi and Xu, 2018; Cha and Lee 2018; Cheng 2018; Cheng *et al.* 2020a; Dong *et al.* 2021; Endresen and Klebert 2020; Gansel *et al.* 2018; Huang *et al.* 2007; Huang *et al.* 2020; Lee *et al.* 2010; Winthereig-Rasmussen *et al.* 2016; Zhao *et al.* 2015a). In addition, three newly designed offshore aquaculture structures, *i.e.*, Deep Blue No.1 (Wanzefeng Fisheries, 2018), Ocean Farm 1 (SalMar ASA, 2021) and Havfarm 1 (Nordlaks Produkter AS, 2020), are also shown in this figure for reference. It can be observed that all the studied fish cages satisfy

5.3 The studied parameters and conditions

$\frac{H}{C} \leq \frac{1}{2}$, which is the rule of thumb for the design of gravity type fish cages (Cardia and Lovatelli 2015).

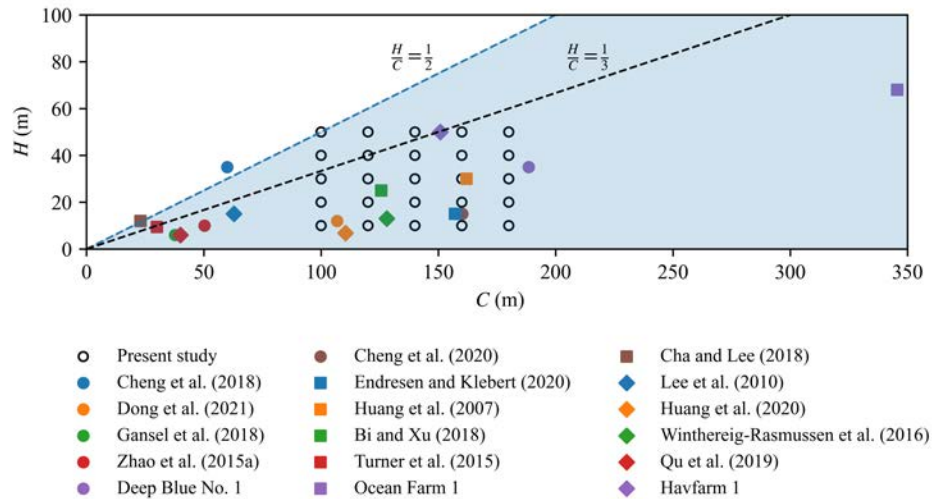


Figure 5-2. The value of H and C for the net bags in the present and previous studies.

According to the report by Halwart *et al.* (2007), most of the gravity type fish farms are located at sheltered sites. In the well-protected sea and freshwater sites, the wave force only accounts for a negligible fraction of environmental loads (Lekang, 2019). Thus, wave-induced forces are not included in this chapter. The maximum current velocity for simulations is set considering biological and environmental aspects. The strong current can wash away a large part of the feed causing unacceptable losses, and force farmed fish to swim causing worthless metabolic expenditure (Nilsen, 2019). For most finfish aquaculture, 0.2 to 0.5 m/s is the optimal current velocity, and 0.75 m/s is the maximum recommended current (Cardia and Lovatelli 2015). Thus, the current

5 Application to the design of traditional fish cages

velocity in the present study is set from 0 m/s to 0.8 m/s with a 0.1 m/s interval.

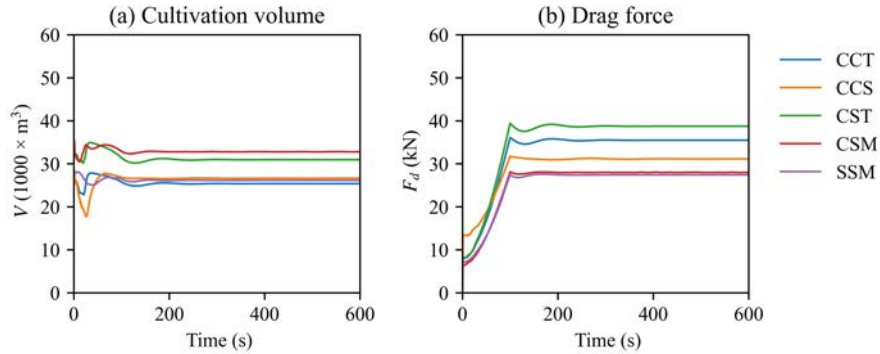


Figure 5-3. Time histories of cultivation volumes and drag for the five gravity type fish cages with $C = 120$ m, $H = 30$ m, $W = 40$ kg/m and $U = 0.3$ m/s.

All the simulations are conducted in the time domain. The settings of time step and mesh size are based on the previous convergence studies by Cheng *et al.* (2020b). All the simulation cases adopt a mesh size of 2.5 m, a time step of 0.2 s and a simulation duration of 600 s. Figure 5-3 shows the time series of numerical results for the five types of fish cages when $C = 120$ m, $H = 30$ m, $W = 40$ kg/m and $U = 0.3$ m/s. In order to reduce initial impact effects, the current velocity in the present study is linearly increased from 0 m/s to the targeted velocity within the first 100 s. All the simulations can reach a steady state after 300 s. The mean value of the drag and cultivation volume is measured from the last 300 s and will be used in the subsequent discussions.

5.3 The studied parameters and conditions

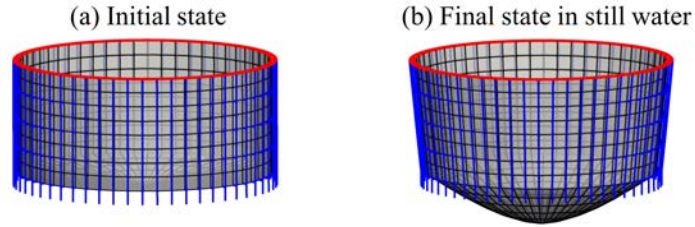


Figure 5-4. The cage shape in still water.

Figure 5-4 shows the shape of the CSM fish cage in still water. Compared to its initial geometrical configuration, the cage is deeper in the final state as the weight can stretch down the bottom net. Meanwhile, the side net moves towards the center of the fish cage due to the lack of support from the sinker tube. Thus, the cultivation volume in still water may be larger than its initial volume in structural analyses. The cultivation volume is calculated based on the divergence method, as described by Eq(5-1). The remaining volume factor is defined as the ratio between the cultivation volume under various current velocities and its corresponding volume in still water: $V_r = \frac{V}{V_0}$.

$$V = \iiint_{\Delta} (\nabla \cdot f) dV = \iint_S (f \cdot n) dA_s \quad (5-1)$$

5.4 Results and discussion

5.4.1 Cultivation volume in still water

5.4.1.1 Volume and total netting area in still water

Traditionally, the dimensions of a fish cage are empirically determined. In order to accurately estimate the cultivation volume in still water and the total netting area for commonly used gravity type fish cage, regression functions are proposed in the present study, as shown in Eqs.(5-2) and (5-3), where a_1 , a_2 are the slopes and b_1 , b_2 are the intercepts. For each regression function, the numerical results from $5 \times 5 \times 5 = 125$ combinations of C , H and W are considered. The regression functions are shown in Figure 5-5 together with the numerical results, and their regression coefficients are listed in Table 5-4 and Table 5-5.

$$V_0 = a_1HC^2 + b_1 \quad (5-2)$$

$$A_{net} = a_2HC + b_2C^2 \quad (5-3)$$

Table 5-4. Regression coefficients for Eq.(5-2).

Cage name	a	b	R^2
CCT	0.0654±0.0003	0.6192±0.1938	0.9998
CCS	0.0585±0.0007	0.8032±0.5035	0.9981
CST	0.0811±0.0006	1.0788±0.4380	0.9992
CSM	0.0755±0.0020	2.9287±1.4324	0.9908
SSM	0.0573±0.0019	2.4335±1.3399	0.9851

5.4 Results and discussion

Table 5-5. Regression coefficients for Eq.(5-3).

Cage name	a	b	R^2
CCT	0.8868±0.0023	0.0573±0.0006	0.9999
CCS	0.8868±0.0023	0.0573±0.0006	0.9999
CST	1.0000±0.0004	0.0801±0.0001	1.0000
CSM	1.0000±0.0004	0.0801±0.0001	1.0000
SSM	1.0015±0.0009	0.0632±0.0002	1.0000

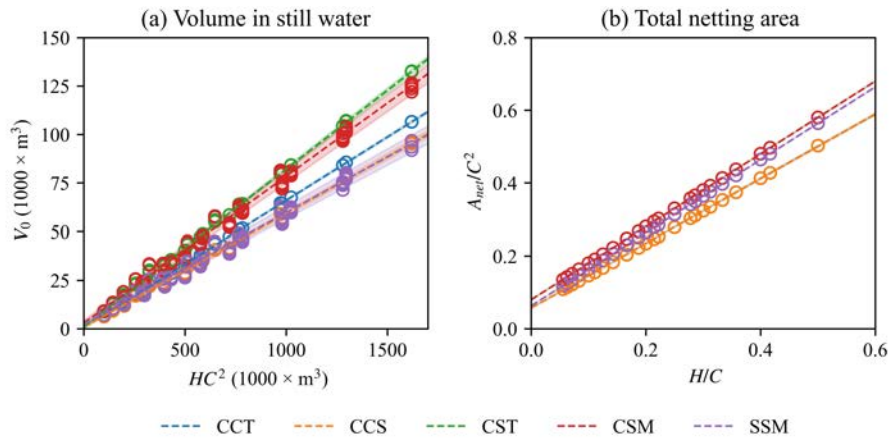


Figure 5-5. Estimations of cultivation volume in still water and total netting area using C and H . The shadows show the 99.7% confidence intervals for the regression functions in Eqs.(5-2) and (5-3).

Figure 5-5(a) shows that the cultivation volume in still water V_0 can be well estimated by Eq.(5-2) using the design parameters C and H . The regression functions of SSM and CCS are almost overlapped coincidentally. The intercept b_1 in the formula for the volume prediction is related to the cone-shaped bottom. As the cone depth is only 3 m in this chapter, the intercept is negligible compared to the predicted V_0 . The total netting area of a fish cage (A_{net}) is only related to the shape of its

5 Application to the design of traditional fish cages

net bag, as shown in Figure 5-5(b). Eq.(5-3) can give high-accurate estimations for A_{net} . Based on these two regression functions, the volume and netting can be easily quantified in the preliminary design process.

5.4.1.2 Effect of cage dimension on cost per unit volume

In order to compare the cost per unit volume of the five types of fish cages in still water, the cultivation volume of the fish cages with varying dimensions and weights are shown in Figure 5-6. Five fitted curves are plotted for the corresponding cage using the same color. The form of the fitted curves is described by Eq.(5-4), and the regression coefficients (a and b) are listed in Table 5-6.

$$V_0 = a(A_{net})^{1.5} + b \quad (5-4)$$

Table 5-6. Regression coefficients for Eq.(5-4).

Cage name	a	b	R^2
CCT	3.4252±0.1099	0.9168±1.5120	0.9861
CCS	3.0585±0.1176	1.1463±1.6172	0.9802
CST	3.3500±0.0835	0.3051±1.4832	0.9916
CSM	3.1107±0.1262	2.3315±2.2408	0.9780
SSM	2.4852±0.1536	3.1715±2.4125	0.9515

5.4 Results and discussion

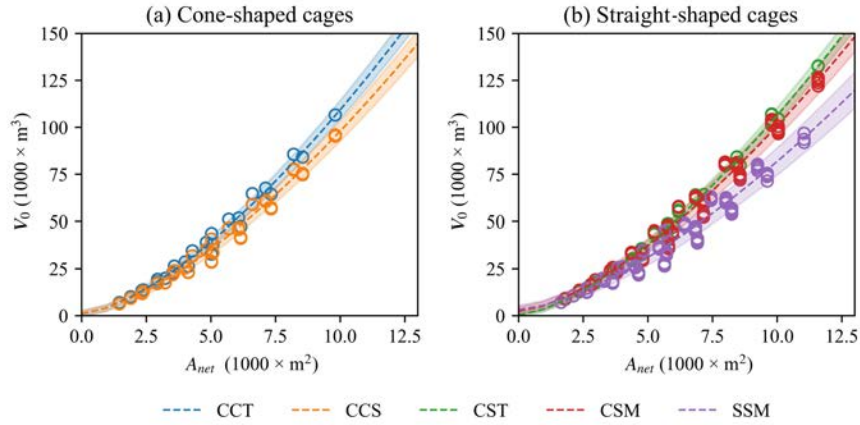


Figure 5-6. Cultivation volumes of fish cages with various dimensions in still water. The shadows show the 99.7% confidence intervals for the regression function Eq.(5-4).

When the cages are located in still water, increasing W cannot bring additional cultivation volume. Thus, W is not included in the regression function. According to Eq.(5-4), the speed of volume increment is faster than the speed of netting area increment when the dimension of a cage is increased. Thus, the construction cost per unit volume of a fish cage is reduced with the increasing dimension. While large cages could improve profitability, they may increase the risk of low dissolved oxygen (DO) conditions due to reduced water exchange (Oldham *et al.*, 2018). Thus, it needs to balance the risk and profitability during the design. Besides, the cost per unit volume of a fish cage also depends on other factors, such as net bag shape and forms of weight. The influences of these factors become significant when the fish cage has a large dimension, *e.g.*, when $A_{net} > 10\,000\text{ m}^2$ or $V_0 > 100\,000\text{ m}^3$. When the cage becomes large, CCT and CST have the lowest cost per unit

5 Application to the design of traditional fish cages

volume among the five studied types, as they can provide the largest cultivation volume with the same area of netting.

5.4.1.3 Effect of net bag shape on cost per unit volume

The net bag shape is mainly determined by the shape of the floating collar, the ratio of bottom circumference to top circumference and the ratio of cage depth to circumference (H/C). H/C can indicate how slim or stout a cage is. A large value of H/C means the cage is slim; otherwise, the cage is stout. According to the Norwegian Standards NS 9415 (Standards Norway, 2009) and Lekang (2019), H/C should not exceed 0.4 for the straight circular cages, and 0.5 for cone-shape cages.

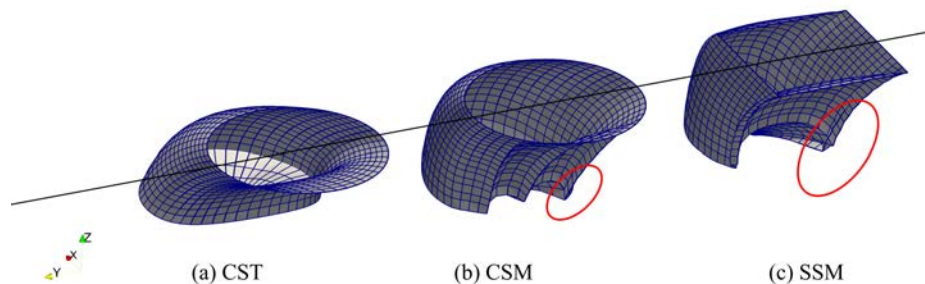


Figure 5-7. The deformations of different net bags. Sharp corners (circled in red) appear in the net bags using multiple-sinker weight with $C = 120$ m, $H = 40$ m, $W = 50$ kg/m and $U = 0.6$ m/s. These sharp corners may not be used by the farmed fish if the fish has a circular swimming pattern.

The shape of the floating collar can affect the efficiency of material usage. With the same length of the floating collar, the circular shape makes the most efficient use of materials and thus can provide a larger surface area and larger cultivation volume than the square shape. In

addition, corners of square structures may be little utilized due to the circular swimming behaviors of fish (Beveridge, 2004), and these corners can be sharper under higher current velocities, as shown in Figure 5-7 (c).

The ratio of bottom circumference to top circumference determines how the cage is tapered. The tapered cages, which get narrow from the top down to the bottom, have similar shapes caused by gravity. Taking CCT and CST as examples, the truncated-cone shape net bag may wisely use the nettings, as the side net usually moves towards the center of a cage (Figure 5-4(b)). In the present study, the ratio of bottom circumference to the circumference is 0.8 for the cone-shaped cages (CCT and CCS), which is similar to the cage employed by Endresen and Klebert (2020). This ratio can be optimized to improve the efficiency of material usage through further parametric study, but it is out of scope in the present work.

Figure 5-8 shows how the H/C affects the cost per unit volume. For a given cultivation volume, the increment of H/C , which makes the cage stouter, can improve the efficiency of materials usage. Besides, this figure can also indicate that among the five cages, the SSM has the highest cost per unit volume for same H , C and W . For sites with small current velocity, it is suggested to enlarge the fish cage vertically, because when $H/C < 0.5$, one meter increment of cage depth can gain more cultivation volume than one meter increment of cage

5 Application to the design of traditional fish cages

circumference. This can be easily proved by assessing the partial derivatives of Eq.(5-2).

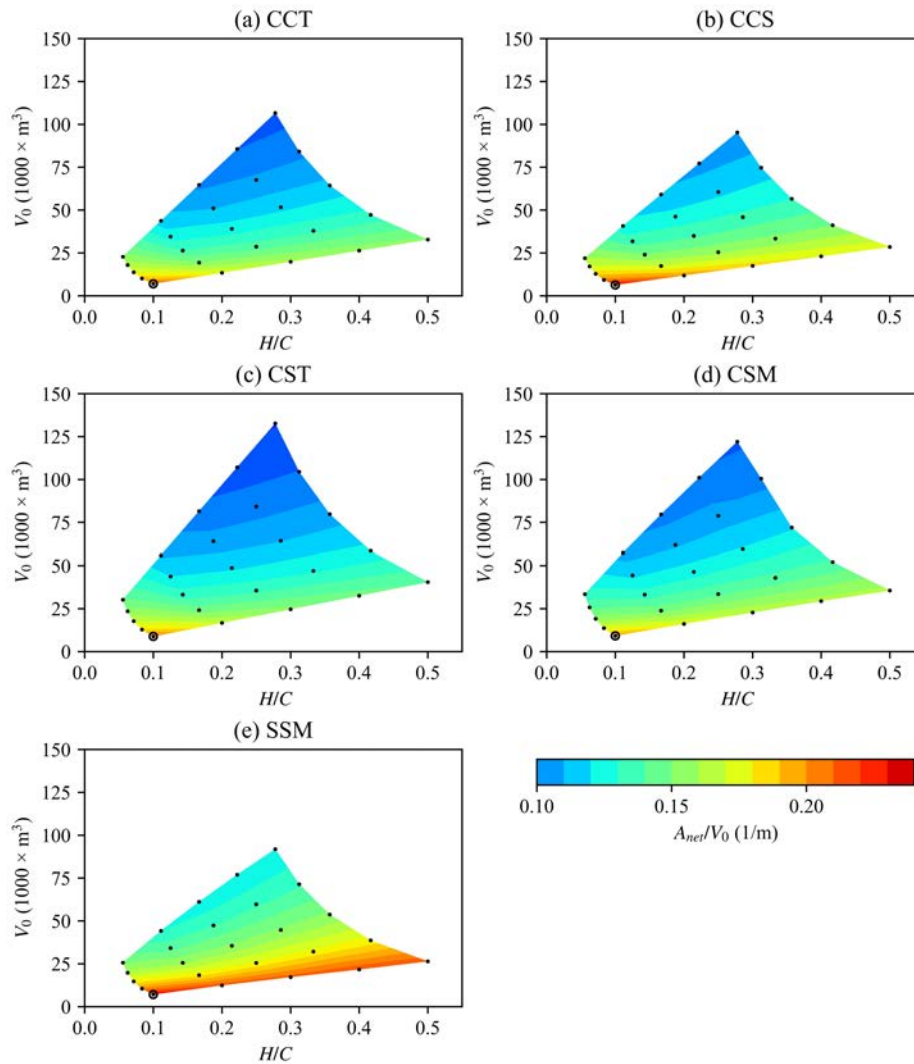


Figure 5-8. Cultivation volumes in still water and netting area to volume ratio for fish cages with different H/C when $W = 40$ kg/m. The black points represent the studied cases. The black circles represent the case with $H = 10$ m and $C = 100$ m.

5.4.1.4 Effect of weight on cost per unit volume

Although increasing the weight cannot bring any additional cultivation volume in still water, the forms of weight can still affect the cultivation volume. As shown in Figure 5-8, when CCT and CCS have the same dimensions, the CCT can gain roughly 10% larger volume than CCS, because its sinker tube can restrict the side net and prevent it from moving towards the cage center, as shown in Figure 5-4 (b). In addition, the comparison between CST and CSM also indicates that the sinker tube can bring more volume to the cage than the multiple-sinker weight. Thus, it is suggested to adopt the sinker tube as the weight for the cage in still water or sites with low current velocities.

5.4.2 Cultivation volume under current conditions

5.4.2.1 Effect of current velocity on cultivation volume

Although cage culture can be carried out successfully even in still water, a certain water current (0.1 - 0.2 m/s) has a good effect on the oxygen supply and the fish muscle development, ensuring permanent water exchange between the water body inside and outside of the cage (Cardia and Lovatelli, 2015). As the gravity type cages do not have rigid nets, strong current velocity can easily reduce the cultivation volume and cause negative impacts on fish welfare. Figure 5-9 shows that the cultivation volumes of the five types of fish cage are reduced significantly with the increasing current velocity but increasing the weight can mitigate the volume reduction.

5 Application to the design of traditional fish cages

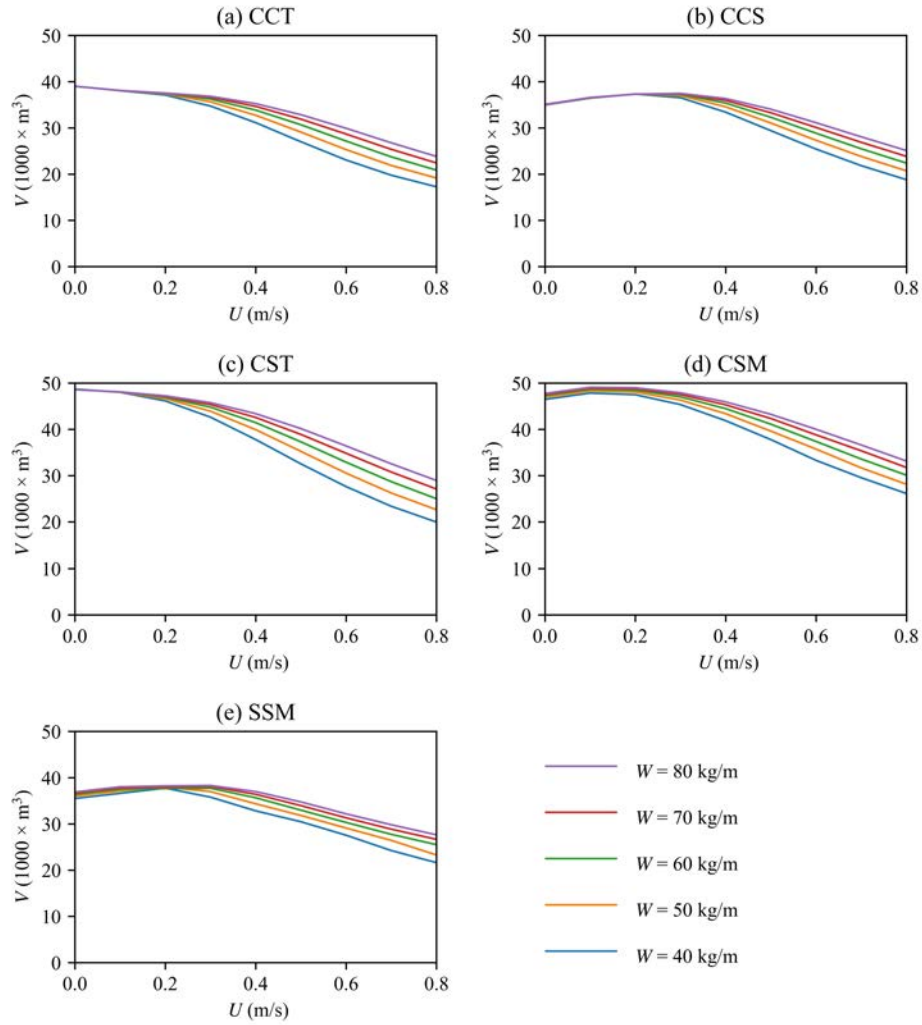


Figure 5-9. Cultivation volumes of the five fish cages with $C = 140$ m and $H = 30$ m under different current velocities.

5.4 Results and discussion

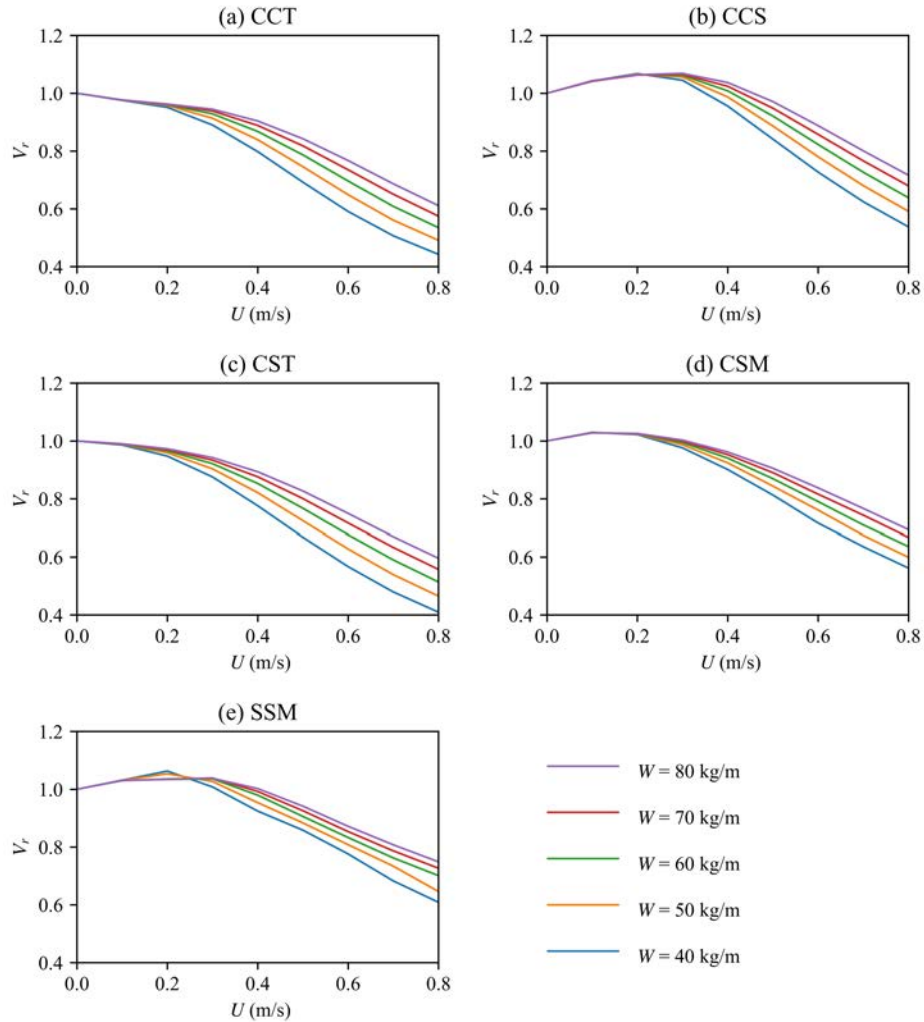


Figure 5-10. The remaining volume factors for the five fish cages with $C = 140$ m and $H = 30$ m under different current velocities.

Figure 5-10 shows V_r for the five types of fish cages under different U . The cultivation volume of a fish cage can reduce to half of its cultivation volume in still water when $U > 0.5$ m/s. Cages using different forms of weight may have different abilities to keep cultivation volume.

5 Application to the design of traditional fish cages

However, when $U < 0.2$ m/s, values of V_r for the five types of cages are all close to 1. For the cages using sinkers as weight, *i.e.*, CCS, CSM and SSM, V_r even increases slightly, up to 1.1, when $U < 0.2$ m/s. This means the cultivation volumes of gravity type fish cages can be well maintained under such small current velocities. According to Halwart *et al.* (2007), with a current velocity of 0.15 m/s, the water in a fish cage can be exchanged more than 100 times per day, which already exceeds the typical amount needed to ensure the levels of nutrients in the water column. Thus, gravity type fish cages are suitable for sites with small current velocities.

5.4.2.2 Effect of weight system on cultivation volume

Faster current velocities usually require heavier weights. As shown in Figure 5-9 and Figure 5-10, the increment of W can mitigate the volume loss caused by strong currents. However, the cost-effectiveness of increasing weight depends on the form of weight and the current velocity in the site. When $U < 0.2$ m/s, the increment of W may not bring obvious benefits to the cultivation volume, but can bring additional costs and burdens to weight-related operations. When $U > 0.2$ m/s, the increment of weight helps to mitigate the fish cage deformation, but at the same time, reduces total buoyancy. Thus, the total weight of a gravity type fish cage should be well designed depending on the site's current velocity and buoyancy. Besides, the forms of weight may also affect cage deformations.

5.4 Results and discussion

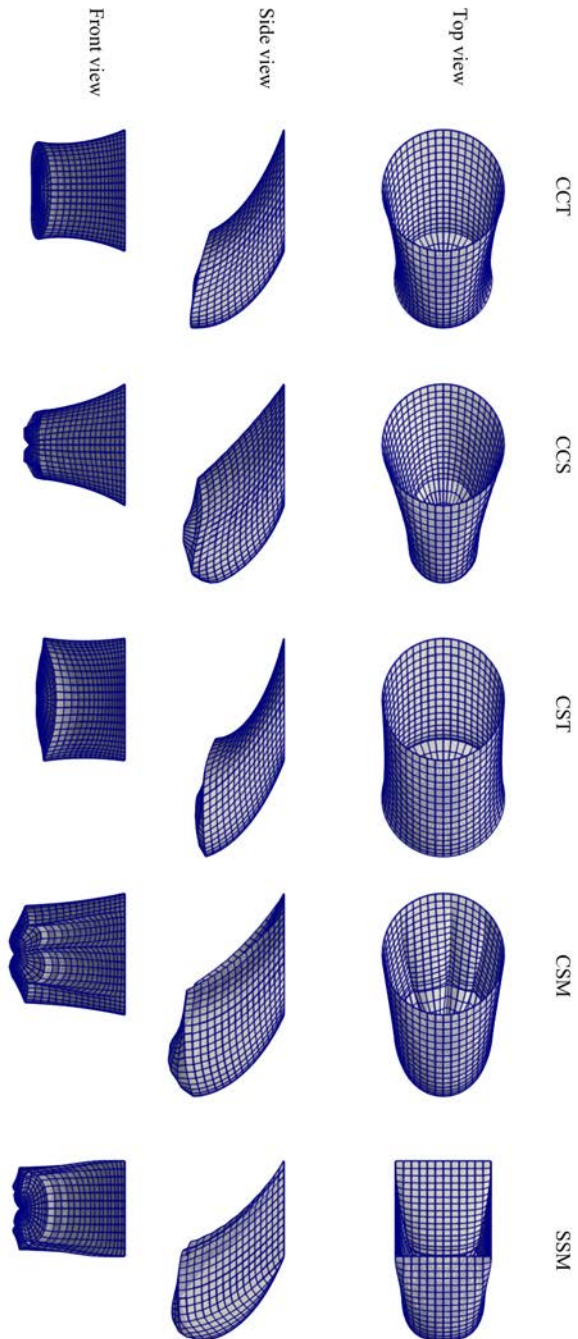


Figure 5-11. Deformations of the five net bags with $C=120$ m, $H=40$ m, $W=50$ kg/m and $U=0.6$ m/s.

5 Application to the design of traditional fish cages

Figure 5-11 shows the deformations of the five net bags with different forms of weight. According to Cardia and Lovatelli (2015), although sinker tubes are more expensive than sinkers, the sinker tubes may better maintain the shape of the cage bag, as the sinker tubes have a certain stiffness. The top and front views in Figure 5-11 also indicate that the bottom nets of the cages using sinker tubes are flatter than those using single-sinker weight or multiple-sinker weight. However, the flatter bottom nets are not enough to guarantee a larger volume than those without flat bottoms. As shown in Figure 5-11, CCS, CSM and SSM may not have a flat bottom, but they can have deeper cage bags. Thus, it is difficult to judge which forms of weight can produce the largest cultivation volume for the same design parameters.

5.4.2.2.1 Sinker tubes versus single-sinker weight (CCT vs. CCS)

Based on the results in Figure 5-10, the cage using single-sinker weight has a larger V_r than that using sinker tube when both have the same C , H , W and under the same U . Figure 5-12 shows how these two forms of weight systems affect the cage deformations. As observed from this figure, the bottom net of CCT is flatter than that of CCS. This is because the tensional ropes between the sinker tube and bottom net can mitigate the vertical stretch of the bottom net. Thus, the bottom net of CCT is almost in the same plane as the sinker tube. The sinker tube can better maintain the shape of net bag compared to the single-sinker weight, but it may result in a smaller cultivation volume due to the flat bottom net. The nearly flat bottom net acts as a porous airfoil that can provide a lift force to raise the bottom net, thus reducing cultivation volume.

5.4 Results and discussion

Therefore, from the perspective of volume maintenance, the sinker tube is no better than the single-sinker weight, which is contrary to the observations by Cardia and Lovatelli (2015). However, considering CCT has a larger initial volume in still water than the CCS when the two cages have the same dimension, the larger V_r of CCS may make the actual cultivation volumes of the two type cages roughly equal. Their similar cultivation volumes are evident in Figure 5-8.

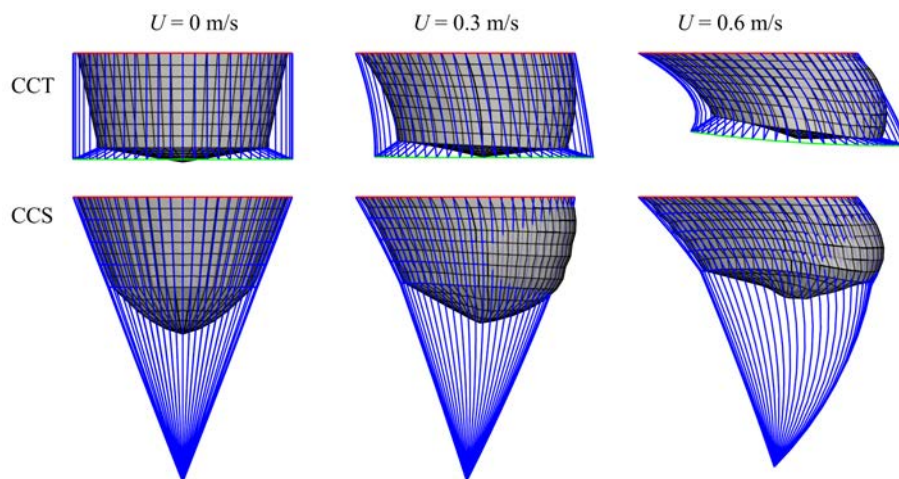


Figure 5-12. Deformations of the two truncated-cone shape fish cages with $C = 140$ m, $H = 20$ m and $W = 50$ kg/m under three current velocities.

5.4.2.2 Sinker tubes versus multiple-sinkers weight (CST vs. CSM)

Figure 5-10 also indicates that the cage using multiple-sinker weight has a larger V_r than that using the sinker tube, but the differences of their V_r are less than 10% which agrees with the previous work by Huang *et al.* (2007). Figure 5-13 shows the deformation of these two types of fish cages under different current velocities. Similar to the observations from

5 Application to the design of traditional fish cages

Figure 5-12, the sinker tube can well maintain the shape of the bottom net but lead to a shallower net bag under strong current than that using multiple-sinker weight. Thus, CST has a larger volume than CSM when they have the same C , H , W and under the same U . However, the volume of sharp corners in CSM (circled in Figure 5-7(b)), although included in the calculation, may not be used by fish due to their circular swimming pattern. In addition, the tension is usually large near the sharp corners, which may increase the risk of net failure. In contrast, as shown in Figure 5-7(a), the sharp corners can be avoided in CST when the fish cage deforms. This can conform with the fish behaviors and may improve the fish welfare. Moreover, the sinker tube is able to better distribute the concentrated weight on the net and the floating collar. Thus, the risk of net failure can be reduced.

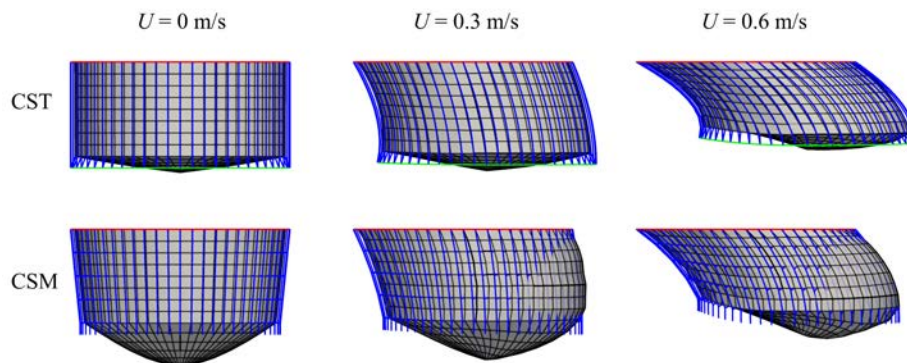


Figure 5-13. Deformations of the two circular straight shape fish cages with $C = 140$ m, $H = 20$ m and $W = 50$ kg/m under three current velocities.

5.4.2.3 Effect of cage dimension on cultivation volume

Fish cages can be enlarged in the horizontal or vertical direction to accommodate more fish. However, the gained volume from the increment of the circumference or depth can significantly reduce with increasing current velocity. Although it is difficult to quantify the influence of circumference or depth on the cultivation volume in Figure 5-14 due to a large number of cases, it can still observe that the cultivation volume of the large cages is reduced faster with the increasing current velocity than those of the small cages. For a better comparison, the effect of changing the circumference or depth on V_r is shown in Figure 5-15.

For the CCT, CCS and CST cages, an increment of H can certainly increase V_0 but can significantly reduce V_r when the current is strong ($U > 0.4$ m/s). This means the volume gained from the increment of H can be lost under strong current, but the cost for construction is increased. However, an increment of C has little effect on V_r for CCT, CCS and CST cages, which means the volume gained from the increment of C can be well maintained even when the current is strong. Thus, it is suggested to enlarge the fish cage horizontally to gain more cultivation volume when the site has a strong current.

5 Application to the design of traditional fish cages

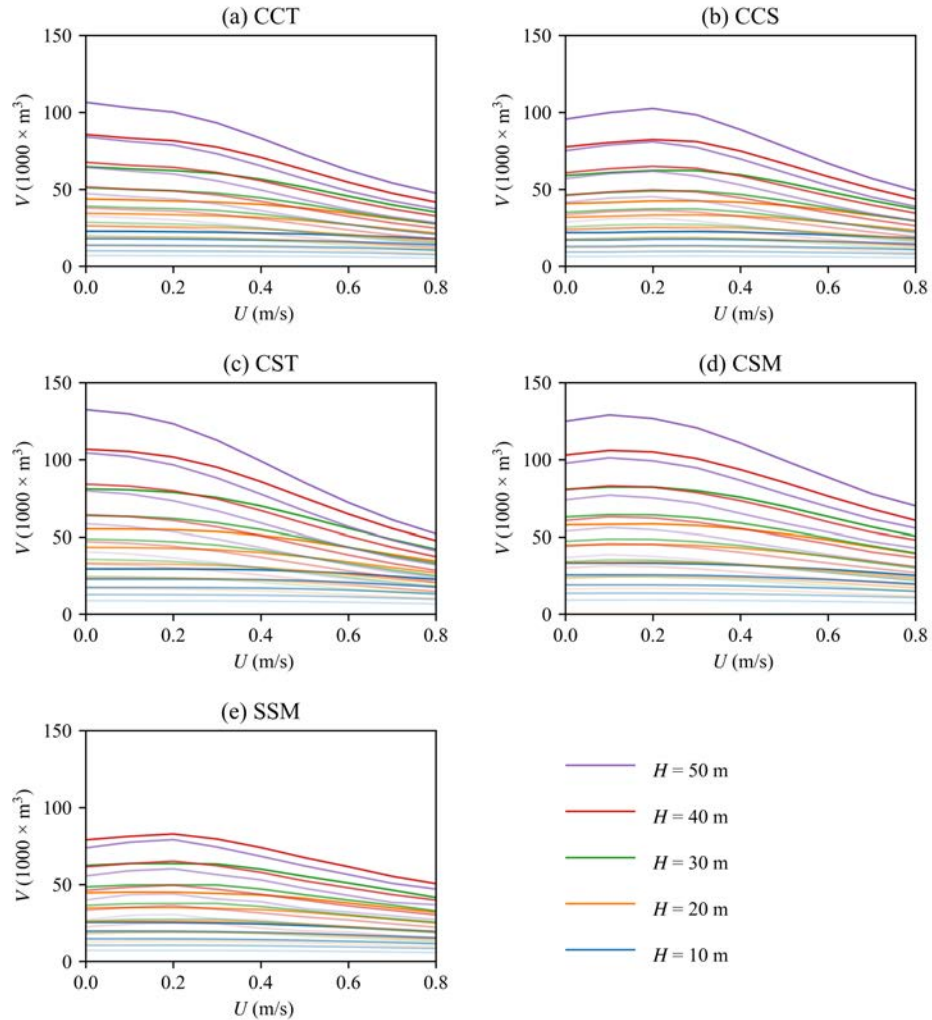


Figure 5-14. Cultivation volumes of the five fish cages with $W = 60$ kg/m under different current velocities. The shades of colors (from light to dark) represent the different circumferences (C is from 100 m to 180 m).

For the other two cages using multiple-sinker weight, *i.e.*, CSM and SSM, the increment of H and C can both reduce V_r , and their effectiveness is roughly equivalent. Thus, the dimensions of these two

5.4 Results and discussion

fish cages may need to be determined based on the site conditions as well as the types of farmed fish.

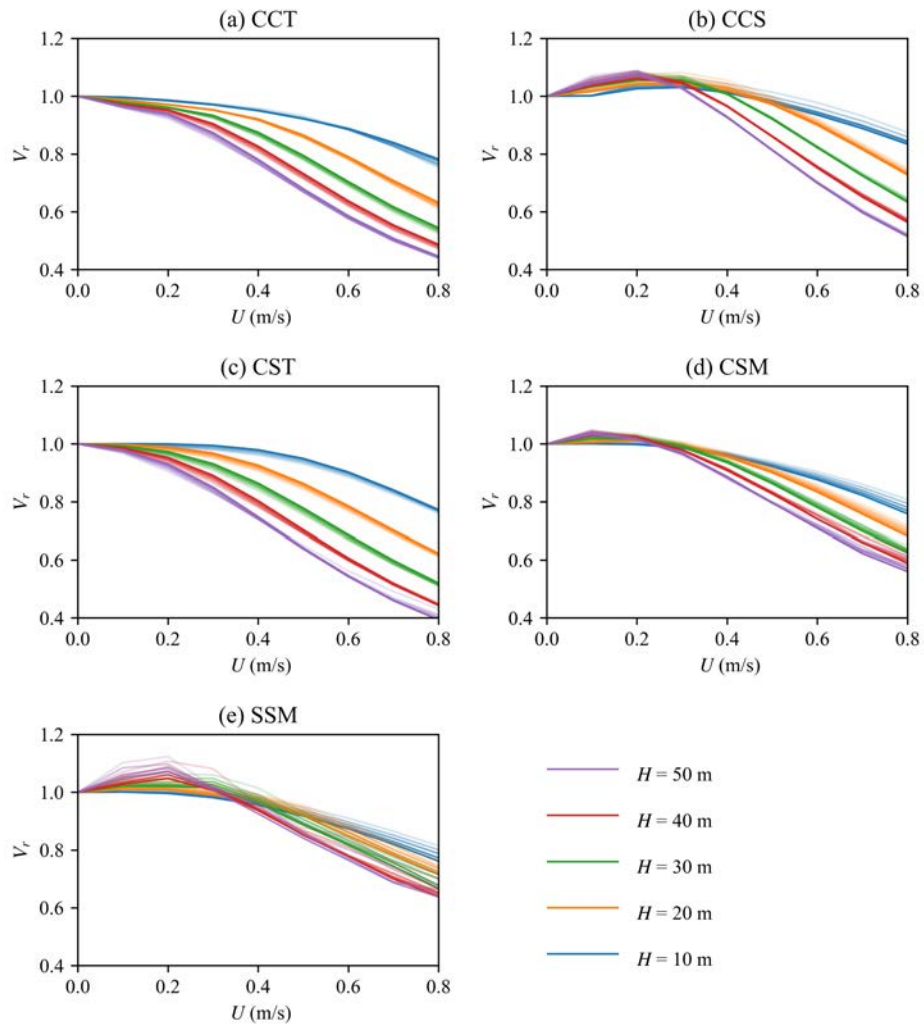


Figure 5-15. Remaining volume factors for the five fish cages with $W = 60$ kg/m under different current velocities. The shades of colors (from light to dark) represent the circumferences (C is from 100 m to 180 m).

5 Application to the design of traditional fish cages

5.4.2.4 Effect of net bag shape on cultivation volume

Although the cultivation volumes are reduced with different speeds under different currents, the trend that the stouter cage has higher efficiency in material usage is still valid, as shown in Figure 5-16. At the same time, increasing the fish cage dimension can also reduce the usage of netting per unit cultivation volume. In addition, it can be observed that CSM has a larger cultivation volume than CST when both net bags have the same dimension and use the same amount of weight. Thus, CSM has a higher efficiency in material usage than CST when the current is strong. The two types of cages using sinker tube, *i.e.*, CCT and CST, have almost the same cultivation volume when both have the same H , C and W under the same U . As CCT uses less netting, A_{net}/V of CCT is smaller than that of CST.

As shown in Figure 5-17, an increment of H/C , which will make the cage slimmer, can reduce V_r in general, meaning that the volume of the slim cage can be easily reduced by the current force. For all the cage types, larger cages have a smaller V_r than the smaller cages, meaning that the larger cages are usually easier to get volume reductions due to the current force. In addition, it can be observed that SSM has a relatively stable V_r , which does not change so much with H/C , compared to the other four cage types. It may be because the cultivation volume of this square cage is relatively small compared to the other cages with the same H , C and W under the same U .

5.4 Results and discussion

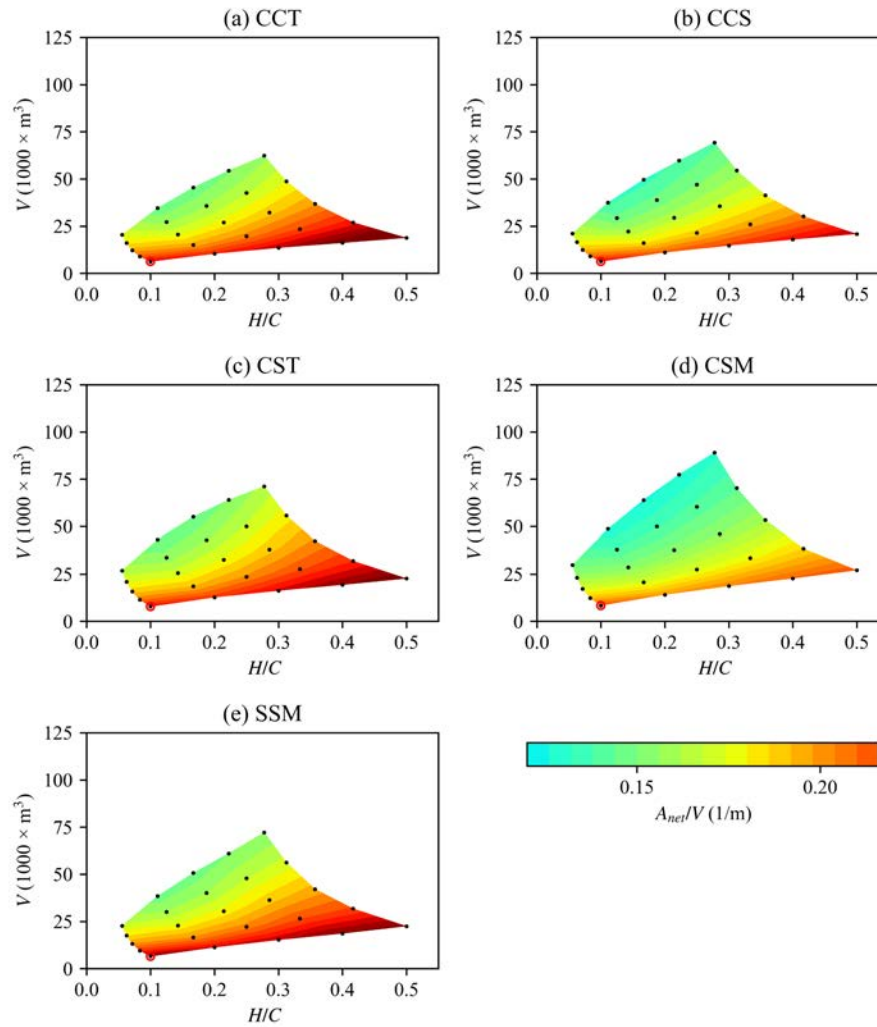


Figure 5-16. Cultivation volumes of the five fish cage with $W = 40$ kg/m when $U = 0.5$ m/s. The black points represent the studied cases. The red circles represent the case with $H = 10$ m and $C = 100$ m.

5 Application to the design of traditional fish cages

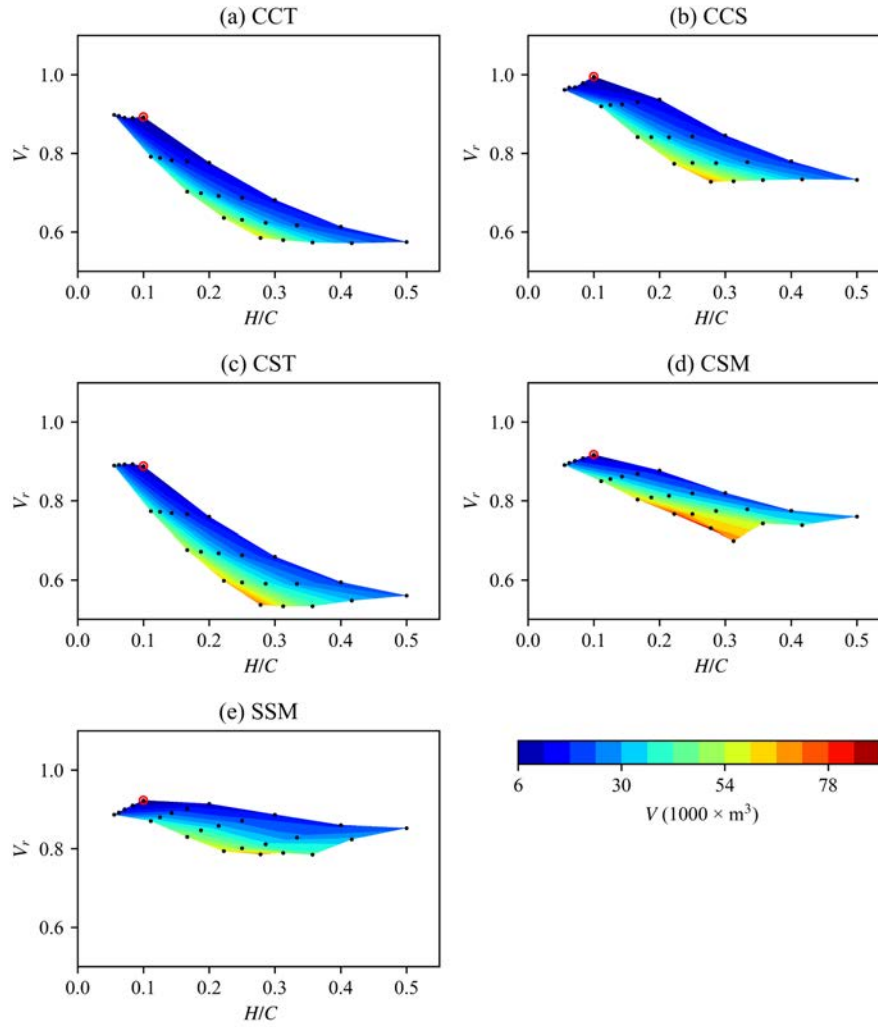


Figure 5-17. Remaining volume factors for the fish cage with $W = 40$ kg/m when $U = 0.5$ m/s. The black points represent the studied cases. The red circles represent the case with $H = 10$ m and $C = 100$ m.

5.4.3 Volume prediction under current conditions

In the preliminary design process, the cultivation volume is one of the most concerning aspects and usually needs to be updated several times based on the biomass and site conditions. Thus, a quick and accurate method to predict the cultivation volume is in need to reduce the workload.

Based on the discussions in Sections 5.4.1 and 5.4.2, the cultivation volume of a fish cage under current conditions highly depends on its dimension, weight and the current-induced drag, which can be characterized by the main design parameters H , C , W and U . According to Dong *et al.* (2021) and Moe-Føre *et al.* (2016), the dimensionless drag F_d/W_0 and the remaining volume factor V_r have a strong negative correlation. Thus, the cultivation volume may be predicted if F_d/W_0 is known. However, the drag F_d is not easy to be directly estimated based on the main design parameters. Usually, in order to get F_d , a series of scaled model experiments or verified numerical simulations need to be conducted, which will be costly and time-consuming. Thus, a superficial drag F_d^* is proposed to replace F_d and employed in the regression function for the volume prediction. F_d^* is defined as Eq.(5-5) and has the same unit as F_d .

$$F_d^* = \frac{1}{2} \rho C_{D(\theta=0^\circ)} U^2 H C \quad (5-5)$$

5 Application to the design of traditional fish cages

where ρ is the density of the water, $C_D (\theta=0^\circ)$ is the drag coefficient of the netting when the current is perpendicular to the net panel, U is the current velocity, H is the designed depth of net bag and C is the designed circumference of floating collar.

$$\frac{1}{V_r} = a \frac{F_d^*}{W_0} + b \quad (5-6)$$

$$V = \frac{V_0 W_0}{a F_d^* + b W_0} \quad (5-7)$$

Table 5-7. Regression coefficients for the volume prediction by Eq.(5-7)

Cage name	a	b	R^2
CCT	0.1710±0.0019	0.9935±0.0054	0.9933
CCS	0.1267±0.0022	0.9047±0.0064	0.9833
CST	0.1992±0.0016	0.9738±0.0047	0.9962
CSM	0.1035±0.0027	0.9805±0.0077	0.9645
SSM	0.0768±0.0035	0.9802±0.0099	0.9035

The regression function for the cultivation volume is shown in Eq.(5-6). In the regression function, W_0 is the total submerged weight on a cage, which can be expressed as $W_0 = C \times g \times W$. Besides, V_r on the left side of Eq.(5-6) is inversed so that both sides of the equation will increase with the increasing current velocity. The regression analysis is conducted based on the data from the present simulation results and using the linear least squares method. The regression coefficients are

5.4 Results and discussion

listed in Figure 5-18, and the regression results are shown in Figure 5-18. Theoretically, the intercept b in regression functions should be 1, as $V = V_0$ when $U = 0$ m/s ($F_d^* = 0$). As shown in Figure 5-18, although the five regression functions have different slopes, their intercepts are around 1.

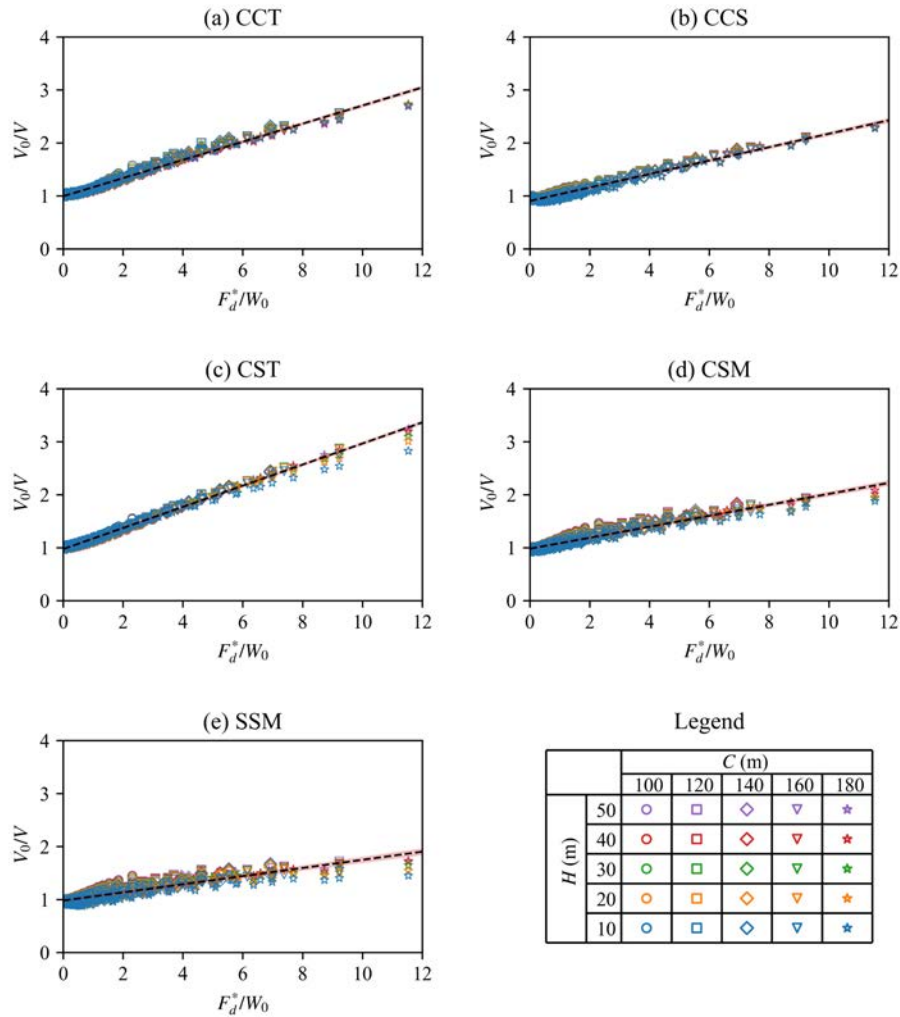


Figure 5-18. Regression functions for volume predictions. The shadows show the 99.7% confidence intervals for the regression function in Eq.(5-7).

5 Application to the design of traditional fish cages

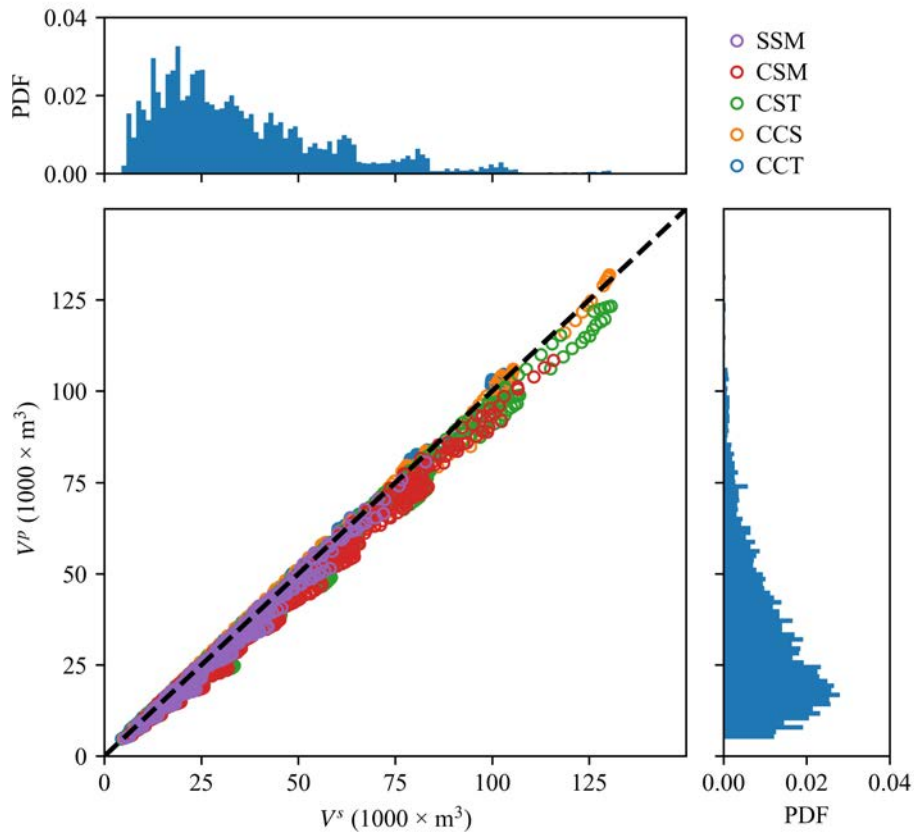


Figure 5-19. The cultivation volumes predicted using Eq.(5-7) and the cultivation volume based on the present numerical simulations. The scatter plot on the left side includes the results from all the simulation cases: $5 \times 5 \times 5 \times 9 = 5\ 625$. The PDF means the probability density function. The right and top subplots show the probability density of the V^p and V^s for the data in the present study, respectively.

Based on the regression function in Eq.(5-6), the predicted cultivation volume can be expressed as a function of V_0 , W_0 and F_d^* in Eq.(5-7), where all the parameters are known in the preliminary design process. Based on this formula, the cultivation volume for different fish cages under different current conditions can be easily predicted for various design purposes.

Figure 5-19 compares the predicted cultivation volume (V^p) using Eq.(5-7) and the cultivation volume from numerical simulations (V^s). The PDF means the probability density function, showing the probability density of V^p and V^s for all the 5 625 simulation cases. For all the five cage types, the difference between V^p and V^s are on average 5%, with a maximum difference of 9%. This indicates that the proposed volume prediction function has high accuracy and can be acceptable for a quick empirical estimation. As shown in Figure 5-19, the probability distributions of V^p and V^s are similar, and most of the studied cases have cultivation volumes $< 80\,000\text{ m}^3$.

The accuracy of predictions using Eq.(5-7) may be different with respect to cage types and the key design parameters. In order to evaluate the accuracy of Eq.(5-7), the distributions of V^p/V^s are presented in Figure 5-20 from the perspectives of cage type, C , H , W and U . In terms of cage type, V^p/V^s of the cages using multiple-sinker weight, *i.e.*, CSM and SSM, have a relatively larger range compared to the other three cage types. This may be because the deformed CSM and SSM have sharp corners, as shown in Figure 5-7, that may bring uncertainties to the volume predictions. In terms of cage dimensions, the accuracy of volume predictions is almost independent of C but can be influenced by H . The accuracy of volume predictions for the deep cages is higher than those for the short cages. In terms of W , the accuracy of volume predictions has almost the same variation for different W . In terms of U , the accuracy of the volume prediction first decreases with the increasing current velocity when $U < 0.3\text{ m/s}$, then increases with the increasing current

5 Application to the design of traditional fish cages

velocity. This nonlinear relationship may be caused by the quadratic velocity term in hydrodynamic force models and wake effects.

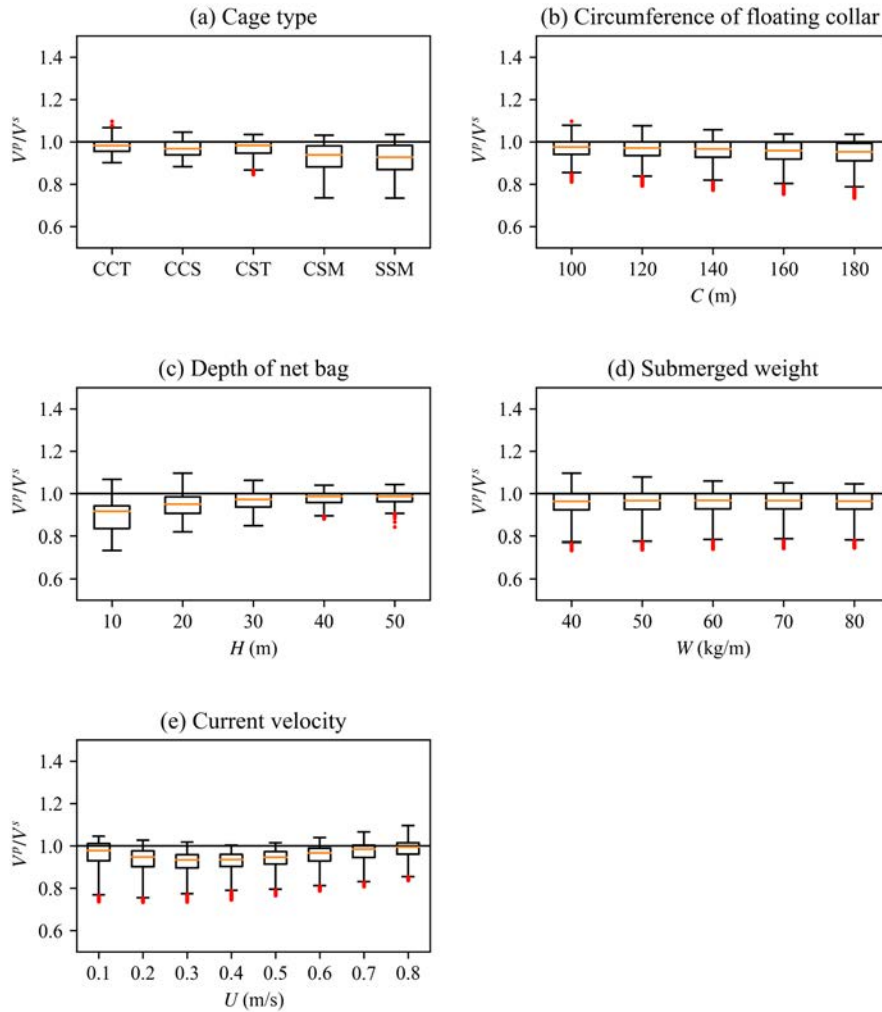


Figure 5-20. Evaluation of the volume prediction fuction from different perspectives. The distributions of V^p/V^s are presented by boxplots.

5.4.4 Drag under current conditions

5.4.4.1 Effect of current velocity on drag

Figure 5-21 shows the drag on the net bag of the five types of fish cages under different current velocities. Their drag loads increase with the increasing current velocity, and the increasing speeds of drag loads decrease with the increasing current velocity. This is caused by the deformations of the flexible cage net as well as the wake effects. Although the velocity is a quadratic term in hydrodynamic force models, the deformed cages cause a reduced projected area of the fish cage net. Together with the wake effects, which cause a reduced velocity on the downstream nets, the drag increases slower with the increasing current velocity.

5.4.4.2 Effect of weight system on drag

Figure 5-21 also shows that increasing the W will increase the F_d on the fish cage, especially when $U > 0.5$ m/s. For the small to moderate current velocity $U < 0.5$ m/s, F_d on a fish cage with W are almost equal because the cages have similar deformed shapes under that small current force. For high current velocity $U > 0.5$ m/s, the increment of W has an obvious effect on the volume maintenance, as discussed in Section 5.4.2.2. However, the additional cultivation volume caused by increasing W is gained in exchange for additional F_d on the fish cages. Thus, the requirement for the mooring system needs to be increased to withstand a larger F_d if the W is increased.

5 Application to the design of traditional fish cages

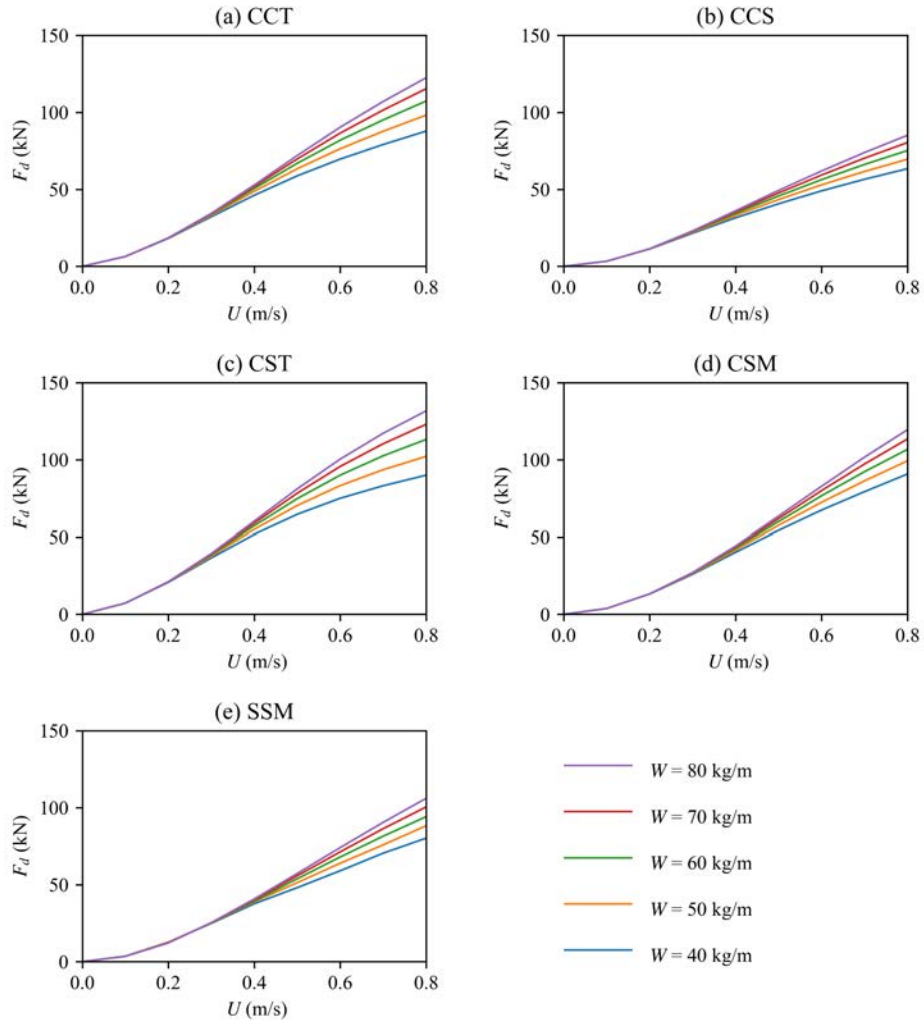


Figure 5-21. Drag on the fish cages with $C = 140$ m and $H = 30$ m under different current velocities.

The forms of weight can affect the F_d on a fish cage. Taking CCT and CCS as examples, F_d on the cage using sinker tube is much larger than that using single-sinker weight when both cages have the same dimension, amount of weight and under the same current velocity. The

reason why the sinker tube causes a larger F_d than the single-sinker weight may be that the net bag's shape of the one using the sinker tube is well kept, and this results in a larger project area than that using single-sinker weight. Subsequently, based on the comparisons between CST and CSM, the sinker tube does not cause a larger F_d than the multiple-sinker weight.

5.4.4.3 Effect of cage dimension on drag

As shown in Figure 5-22, when the dimension of a fish cage is increased, no matter horizontally or vertically, F_d on the net bag will increase significantly, especially when U is large. Due to the large number of simulation cases, curves of F_d overlap each other in Figure 5-22, and it is difficult to quantify the effects of C or H on F_d . Thus, the dimensionless F_d/W_0 is used for a better comparison in Figure 5-23.

As shown in Figure 5-23, except for CCS, the increment of C has negligible effects on F_d/W_0 for the other four types of fish cage. This means the increment of F_d caused by increasing C is roughly equal to the increment of W_0 . As W_0 has a linear relationship with C ($W_0 = C \times g \times W$), the F_d on the net bag should also have almost a linear relationship with C . Because F_d/W_0 is almost independent of C , the value of for the four types of cages may also be independent of C , which is in accordance with the results in Figure 5-15 as well as the observations by Mjåtveit *et al.* (2021). However, the increment of H can certainly increase F_d as well as F_d/W_0 , as W_0 does not depend on H . The increments of F_d (or F_d/W_0) are reduced with the increasing H . This nonlinear relationship between F_d

5 Application to the design of traditional fish cages

(or F_d/W_0) and H may be caused by the deformation of net bags. When H is large, it is easy to have large deformation of the net bag under the current forces. Thus, the cage becomes much shallower than its designed H , and F_d on this shallow net bag is reduced significantly. Consequently, the increments of F_d become smaller with the increasing H . For CCS, increasing C or H can both increase F_d/W_0 in a similar way when $H > 10$ m. This phenomenon may be caused by the truncated-cone shape net bag and the single-sinker weight. As the single-sinker weight is located at a deep position, the fish cage shapes can be well kept, which are in accordance with the results in Figure 5-15. Thus, F_d will increase faster than W_0 with the increasing C .

5.4 Results and discussion

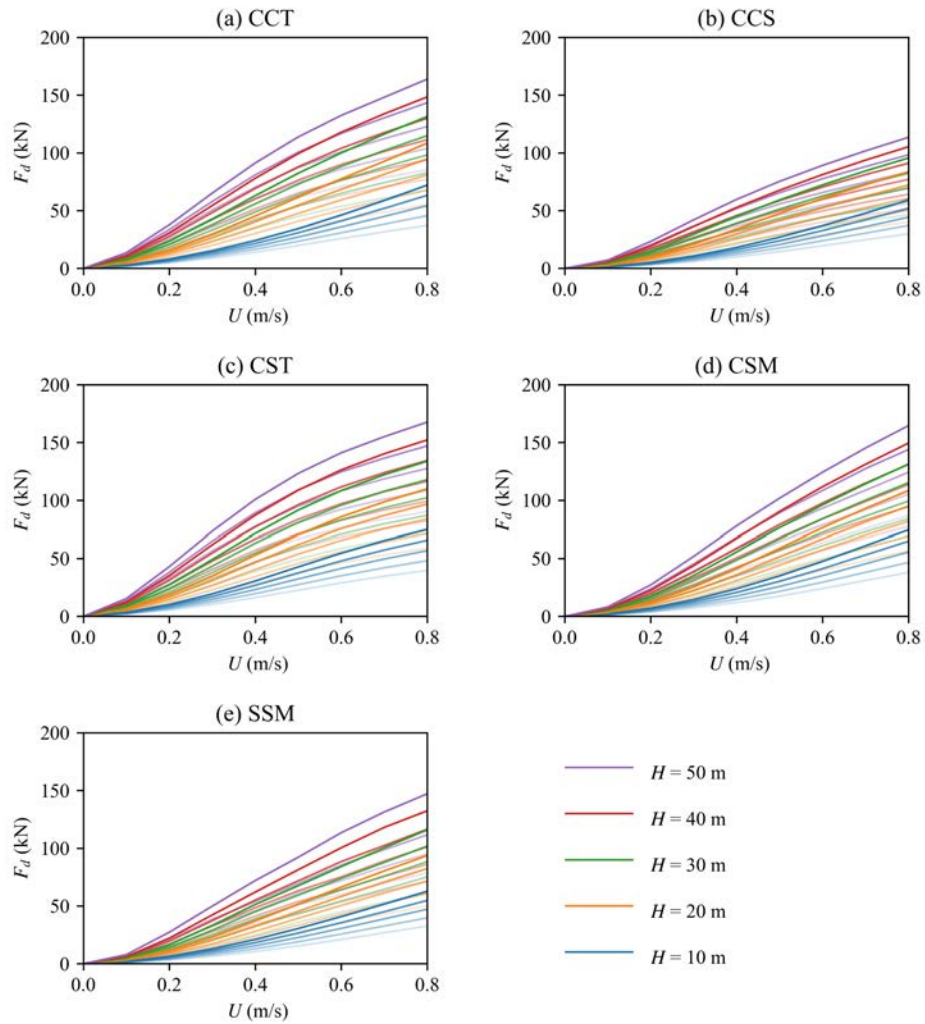


Figure 5-22. Drag on the fish cages with $W = 50$ kg/m under different current velocities. The shades of colors (from light to dark) represent the different circumferences (C is from 100 m to 180 m).

5 Application to the design of traditional fish cages

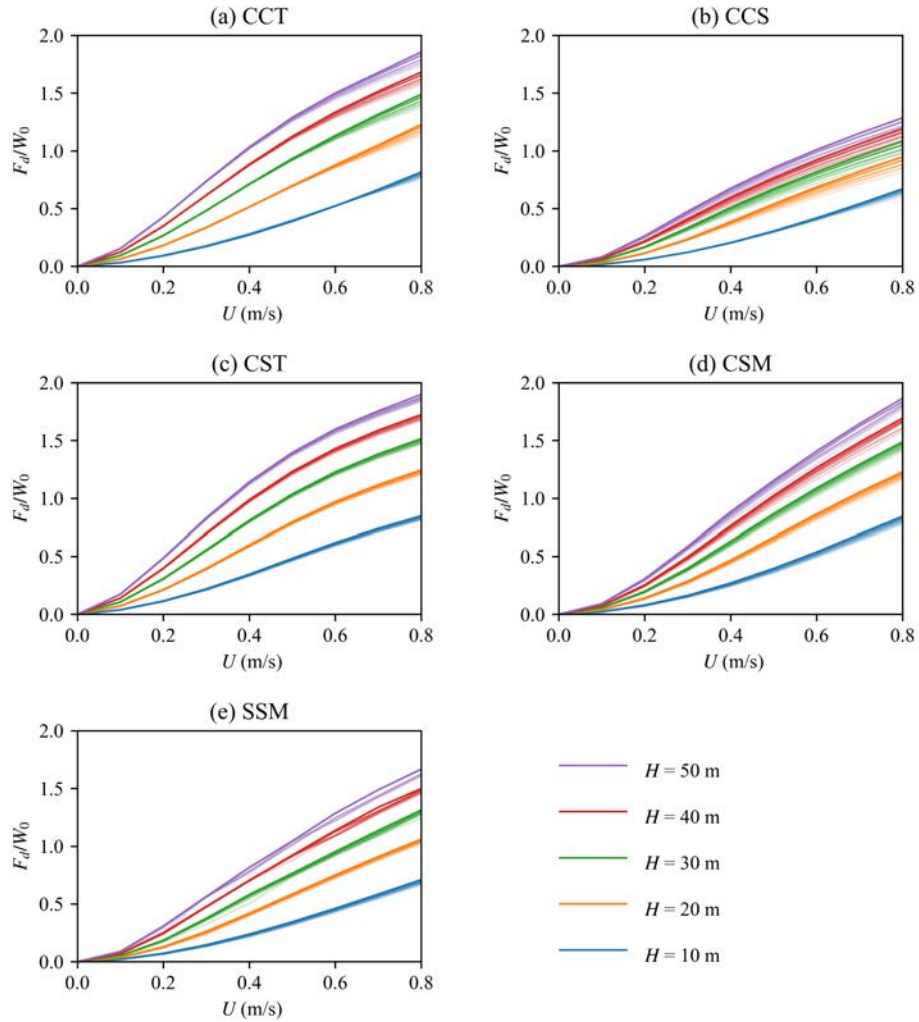


Figure 5-23. F_d/W_0 of the fish cages with $W = 50$ kg/m under different current velocities. The shades of colors (from light to dark) represent the different circumferences (from 100 m to 180 m).

5.4.4.4 Effect of net bag shape on drag

As shown in Figure 5-24(b), F_d on CCS does not have a strong correlation with H/C , which means no matter the CCS cage is slim or stout, its F_d is only proportional to its cultivation volume. The other four types of fish cages also have this similar color shades when their $V > 40\,000\text{ m}^3$. However, when $V < 40\,000\text{ m}^3$, F_d on the net bag is smaller if the cage is stouter (*i.e.*, smaller H/C) with the same cultivation volume. The cage using sinker tube has a relatively smaller V/F_d , compared to the other three types of cage. This indicates that using a sinker tube can significantly increase F_d on a fish cage. In addition, it can be observed that CSM has the largest cultivation volume as well as the largest drag when the five cages have the same C , H , W and under the same U .

5 Application to the design of traditional fish cages

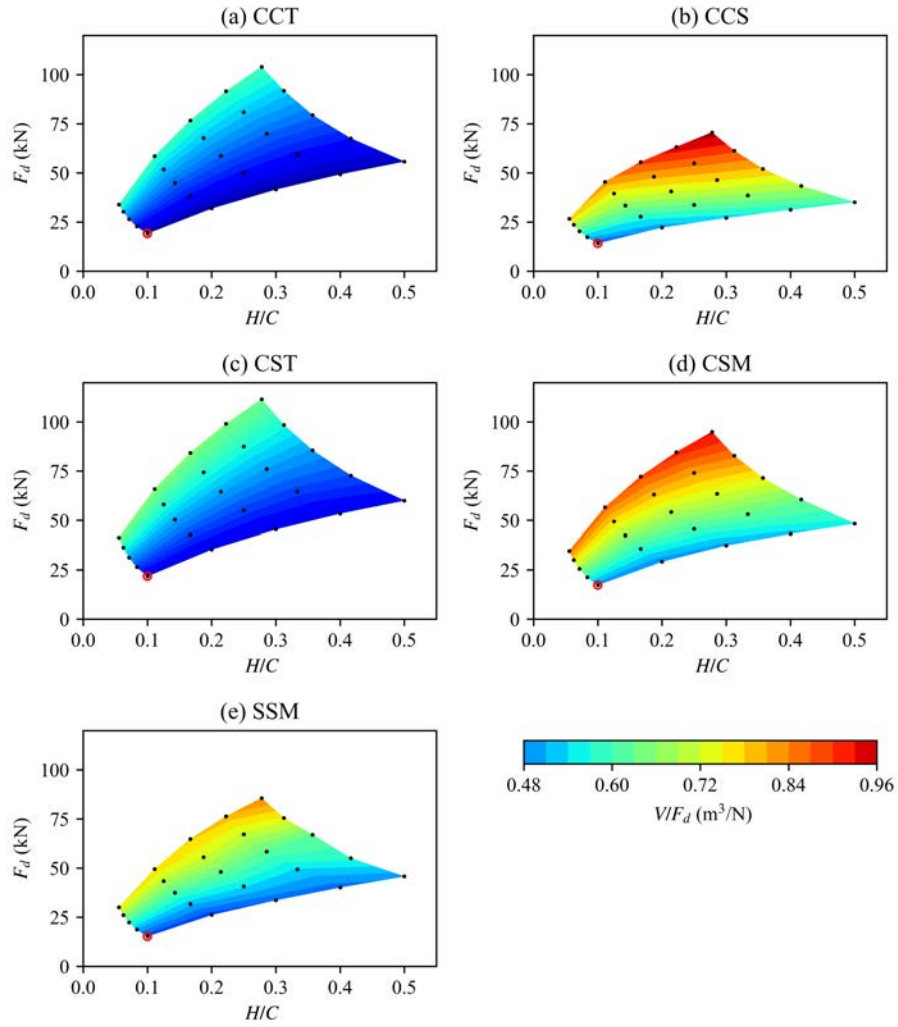


Figure 5-24. Drag on fish cages with $W = 40$ kg/m when $U = 0.8$ m/s. The black points represent the studied cases. The red circles represent the case with $H = 10$ m and $C = 100$ m.

5.4.5 Drag prediction under current conditions

Based on the discussions in Section 5.4.4, the drag on a fish cage highly depends on H , C , W and U . In order to quickly predict the drag on fish cages in the preliminary design process, a formula is proposed based on regression analysis. The regression function is shown in Eq.(5-8). The regression analysis is conducted based on the drag loads from the present simulation results and using the nonlinear least squares method. The regression coefficients are listed in Table 5-8, and the regression results are shown in Figure 5-25. In addition to the present numerical results, published results from experiments (Endresen and Klebert, 2020; Qu *et al.*, 2019) and sea trials (Gansel *et al.*, 2018) are also included in Figure 5-25 for reference.

$$\frac{F_d}{W_0} = a\left(\frac{F_d^*}{W_0}\right)^b \quad (5-8)$$

$$F_d = aW_0\left(\frac{F_d^*}{W_0}\right)^b \quad (5-9)$$

Table 5-8. Regression coefficients for the drag prediction by Eq.(5-9)

Cage name	a	b	RMSE*
CCT	0.5522±0.0081	0.5730±0.0099	0.0686
CCS	0.3781±0.0068	0.5715±0.0120	0.0570
CST	0.6186±0.0093	0.5410±0.0102	0.0787
CSM	0.4837±0.0072	0.6310±0.0098	0.0611
SSM	0.4380±0.0060	0.6287±0.0090	0.0498

*RMSE: Root mean square error.

5 Application to the design of traditional fish cages

Based on the regression function in Eq.(5-8), the predicted drag can be expressed by Eq.(5-9), where all the parameters on the right side of this equation are known in the preliminary design process. Figure 5-26 shows the comparison between the predicted drag (F_d^p) using Eq.(5-9) and the drag from numerical simulations (F_d^s). The PDF means the probability density function, showing the probability density of F_d^p and F_d^s for all the 5 625 simulation cases. On average, F_d^p is 24% higher than F_d^s . However, the difference between F_d^p and F_d^s is less than 2% on average when $F_d > 50$ kN. According to the probability distributions of F_d^s , the drag on the net bag is less than 50 kN for 58% of the studied cases. Due to this considerable proportion of the cases with small drag, the overall difference between F_d^p and F_d^s is relatively large. Thus, when a fish cage has a small dimension or is under a small current, using Eq.(5-9) for the drag prediction can make the structural design conservative. When the fish cage is large and under strong current, Eq.(5-9) can provide high-accuracy predictions on the drag without any time-consuming simulation.

5.4 Results and discussion

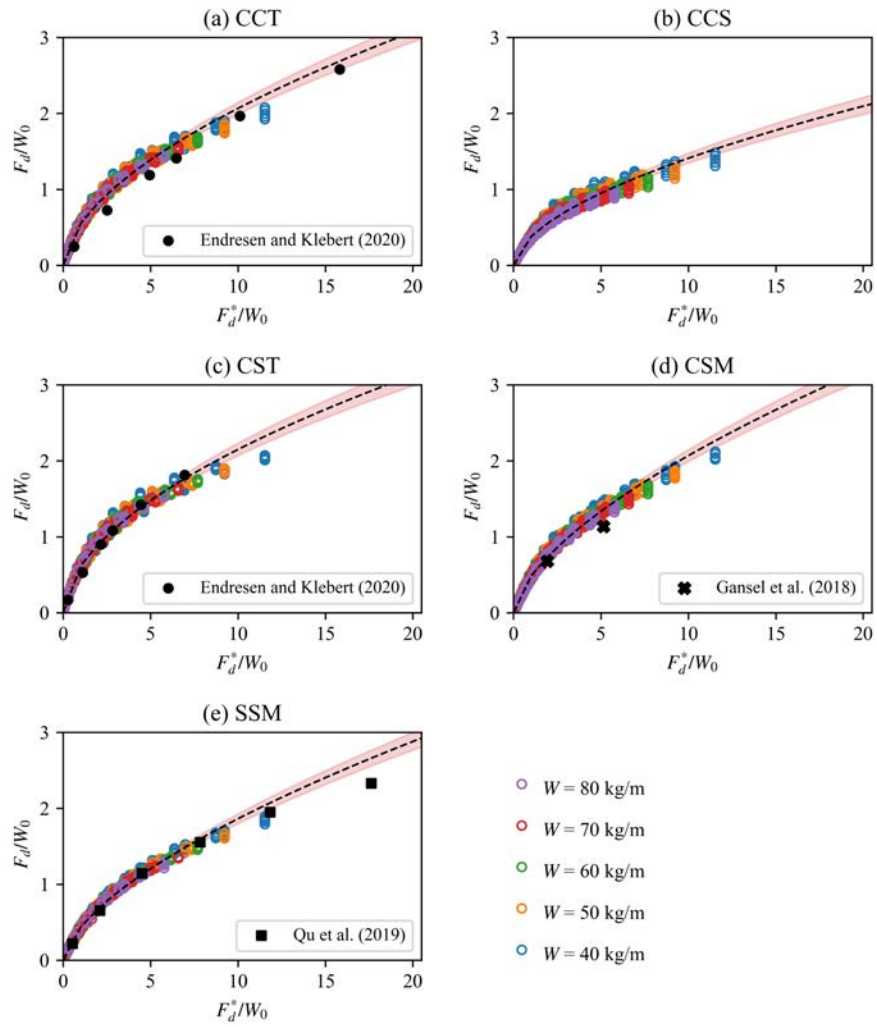


Figure 5-25. Regression functions for drag predictions. The shadows show the 99.7% confidence intervals for the regression function in Eq.(5-9).

5 Application to the design of traditional fish cages

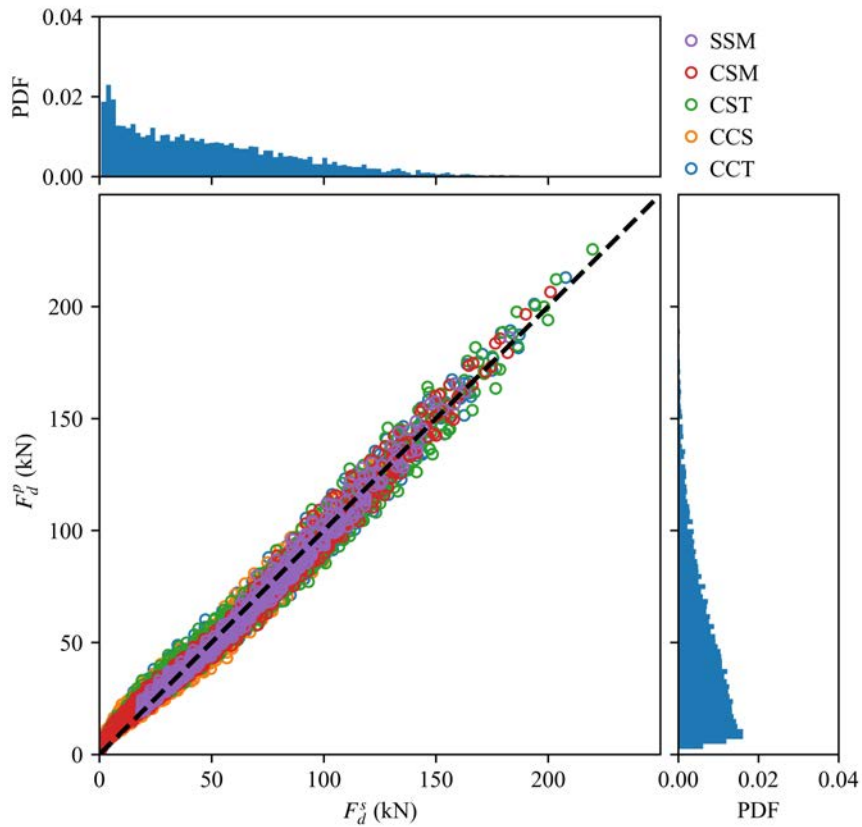


Figure 5-26. The drag predicted using Eq.(5-9) and the drag based on the present numerical simulations. The scatter plot on the left side includes the results from all the simulation cases: $5 \times 5 \times 5 \times 5 \times 9 = 5\ 625$. The PDF means the probability density function. The right and top subplots show the probability density of the F_d^p and F_d^s for the data in the present study, respectively.

In order to evaluate the accuracy of the drag predictions using Eq.(5-9), the distributions of F_d^p/F_d^s are presented in Figure 5-27 from the perspectives of cage type, C , H , W and U . The most noticeable finding is from Figure 5-27(e), in which F_d^p/F_d^s rapidly approaches to 1 with the increasing U . This finding agrees well with the earlier

5.4 Results and discussion

observations in Figure 5-26, which shows that the drag can be overpredicted when $U < 0.3$ m/s, but can be accurately predicted when $U > 0.3$ m/s. Due to these overpredicted drag loads when $U < 0.3$ m/s, there are many data points located above the upper whiskers of the boxplots in Figure 5-27(a)-(d). Although there are so many outliers in Figure 5-27(a)-(d), the boxplots indicate that most of the predicted drag loads using Eq.(5-9) are very close to the drag loads obtained from numerical simulations. Based on Figure 5-27(a)-(b), the accuracy of drag predictions is almost independent of cage types and C . Based on Figure 5-27(c), the accuracy of the drag predictions for the deep fish cages has a smaller variation and is higher than those of shallow fish cages. Based on Figure 5-27(d), the accuracy of the drag predictions for the cage with different W is similar on average, but the accuracy for the cage with larger W has a larger variation.

5 Application to the design of traditional fish cages

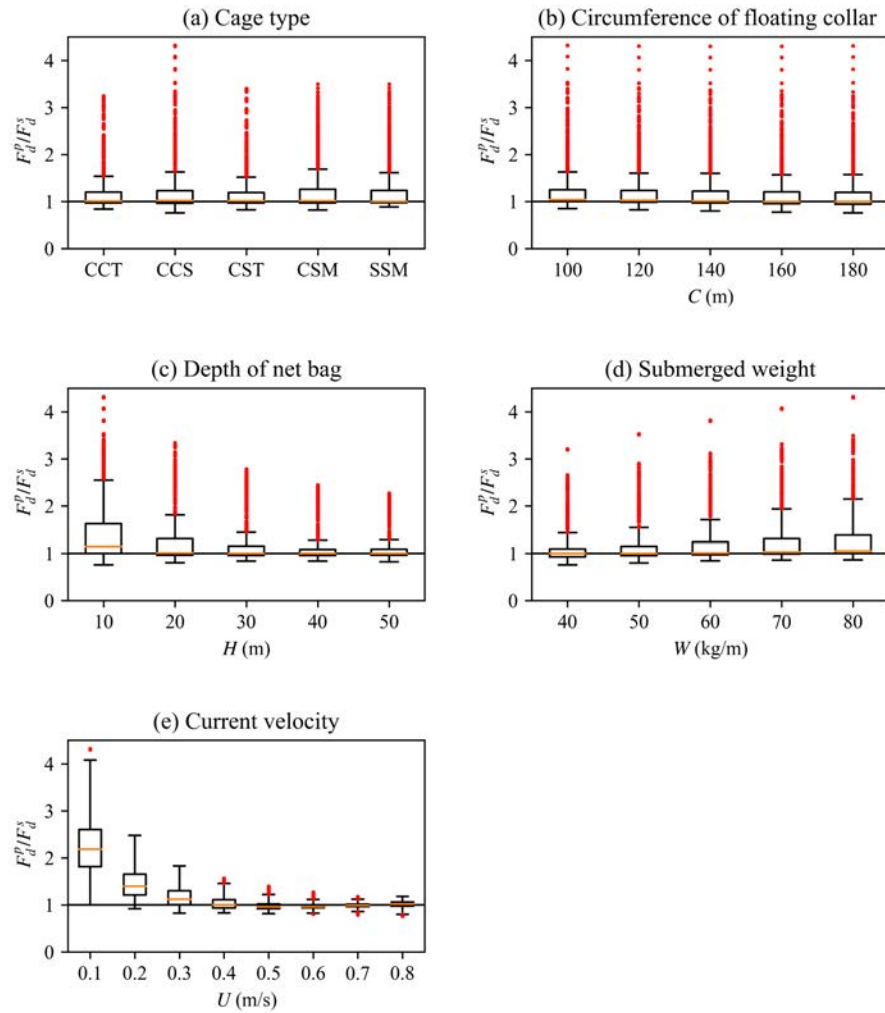


Figure 5-27. Evaluation of the drag prediction function from different perspectives. The distributions of F_d^p/F_d^s are presented by boxplots.

5.5 Conclusions

The main objective of this chapter is to investigate the structural responses of commonly used gravity fish cages and provide guides for future structural design. This chapter provides a comprehensive assessment on the effects of the design parameters, including circumference of the floating collar, depth of net bag, forms of weight and current velocity, on the cultivation volumes and drag loads. The following conclusions are drawn from the results:

1. A stout fish cage, no matter square or circular shape, can efficiently use the materials and provide a larger cultivation volume than a slim fish cage when the two cages use the same amount of netting, weight and are under the same strong current ($U > 0.4$ m/s) condition. Thus, increasing circumference is more effective than increasing the depth of net bag to improve cultivation volume.
2. Given the same circumference of floating collar, depth of net bag, amount of weight and current velocity, the square fish cage has a smaller cultivation volume than the circular one, although it has a slightly larger remaining volume factor.
3. An increment of submerged weight can mitigate the cage deformation and help to maintain cultivation volume under strong current, but bring negligible improvements of cultivation volume when current velocity is lower than 0.2 m/s.

5 Application to the design of traditional fish cages

4. Sinker tube can maintain the net bag shape well under current conditions. However, due to the upward movement of the bottom net, the cultivation volume can significantly decrease under strong current conditions.
5. Multiple-sinker weight shows the best performance in volume maintenance, especially when the current velocity is large. However, multiple-sinker weight can cause irregular bottom and front nets, in which the space may be hardly used by the farmed fish and the risk of net failure may be increased.
6. With a constant submerged weight per meter, the drag on fish cages almost linearly increases with the increasing circumference, but nonlinearly increases with the increasing current velocity and depth of net bag.
7. The drag loads on the cages using sinker tube and multiple-sinker weight are roughly equal, when the five types of fish cage have the same circumference of floating collar, depth of net bag, amount of weight and are under the same current velocity condition. Meanwhile, the drag loads on cages using single-sinker weight are much smaller than those using other forms of weight under the same condition.

In addition to the above findings, multiple regression analyses are conducted based on a large number of numerical results. The regression functions can provide high-accuracy predictions for the most concerning aspects in the preliminary design process, and it can save considerable time for experiments and numerical simulations in the cage design.

5.5 Conclusions

6 Application to the dynamic analysis of grid moored fish farms

The main content in this chapter was created using the numerical program, FhSim and published as follows. Additional results are created using UiS-Aqua in the chapter.

Cheng, H., Li, L., Ong, M.C., Aarsæther, K.G., Sim, J., 2021. Effects of mooring line breakage on dynamic responses of grid moored fish farms under pure current conditions. *Ocean Engineering* 237, 109638.

6.1 Introduction

Fish farming in Norway is regulated through production licenses issued and regulated by the Directorate of Fisheries based on the Aquaculture Act (Norwegian Directorate of Fisheries, 2005). The regulation limits the number of aquaculture farms, but also imposes requirements on planning, design and operation in order to reduce adverse side effects such as waste, parasites and escape of farmed salmon.

Escapes of farmed fish can cause an economic loss for fish farmers, threaten the wild fish populations, and reduce the societal acceptance of the aquaculture industry. Figure 6-1 shows the production of farmed salmon and the number of escaped salmon in Norway in the period between 2000 and 2019 (Statistics Norway, 2020). The salmon production grew rapidly during the years 2000-2013, which led to an increase in the number of fish escapes, especially before 2006. According to Moe-Føre and Thorvaldsen (2021), 92% of fish escapes were triggered by technological factors, such as submergence of the net top and holes in nettings. The Norwegian Standard NS 9415 (Standards Norway, 2009) on the design, operation and installation of fish farms was introduced in 2004 (Berstad *et al.*, 2004) and compliance was ensured through the Aquaculture Act. This technical standard was revised in 2009 and enforced correspondingly in 2011. The implementation of NS 9415 increases technological investments and reduces the number of escaped fish. According to the report by Moe-Føre *et al.* (2019), 82% of fish escapes in the period 2014 -2018 happened during normal operations, such as

6 Application to the dynamic analysis of grid moored fish farms

handling weights and netting (in preparation for delousing). In the last decade, human and organizational factors during in-situ operations, instead of technological factors, have been identified as dominant underlying causes for fish escapes (Thorvaldsen *et al.*, 2018; Thorvaldsen *et al.*, 2015).

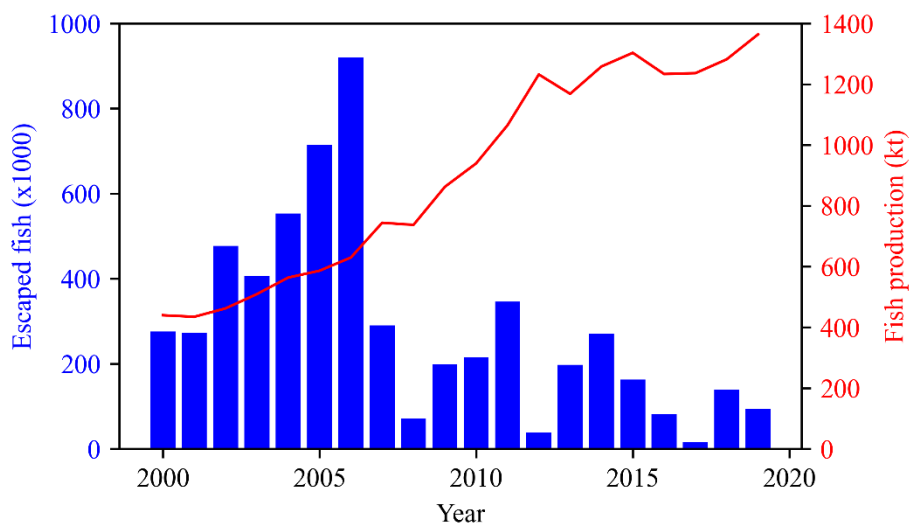


Figure 6-1. Fish production and number of escaped fish in Norway from 2000 to 2019. (Data: Statistics Norway, 2020).

Fish farming is a complex process with various in-situ operations, such as delousing process, changing/cleaning netting and transfer of fish. These operations usually involve a number of operators, different types of equipment and well boats (Høyli, 2016). During operations, well boats can bring substantial forces on mooring lines, as they are moored to aquaculture structures. According to the research by Shen *et al.* (2019), loads on anchor lines can increase 40% due to the existence of well-

boats, even under modest current velocities of 0.3 m/s. Furthermore, underwater structural failures, such as tears on netting and mooring line breakage, may be difficult to detect during operations. These unaware structural failures may lead to fish escapes. Tang *et al.* (2019) investigated structural responses of a single-cage fish farm due to mooring line breakages. The results indicated that tensions in the remaining mooring lines could increase up to 1.75 times compared to those under intact conditions. In order to prevent fish escapes, a quick approach to detect and identify structural failures during operations is necessary (Yang *et al.*, 2020a). This quick approach needs comprehensive analyses in the design phase on the structural responses of fish farms due to various structural failures. When the fish farms are established in exposed and remote areas, understanding how the surface visible parts of the structure are influenced by the combination of current and broken lines can lead to fast identification of failures by remote operators. However, to the best of our knowledge, such analyses are rarely reported in the literature.

A marine fish farm is built to support the containment netting with components, floater, weight system, interconnecting ropes, mooring lines, anchor and supporting buoys. These structures have complex topology regarding the interconnection of structure members, and combinations of elastic, stiff and permeable structures. A comprehensive model is needed to analyze such structures, and considerable research effort has been spent to analyze the physical effects of fish farm structures. Endresen *et al.* (2013) developed a numerical tool to calculate

6 Application to the dynamic analysis of grid moored fish farms

the total drag force and deformation of a fish farm under complex sea conditions. Zhao *et al.* (2013a) employed a porous media model to simulate the flow through a net panel and showed that the velocity reduction downstream from one net panel is 11%. Bi *et al.* (2014) proposed a coupled fluid-structure model to study the wake effect after a fish cage and showed that the maximum velocity reductions downstream from a single fish cage are 17.5%. Zhao *et al.* (2013b) established a numerical model for multi-cage fish farm using a porous media model and showed 69% of velocity reduction when the flow passed through 4 cages. Gutiérrez-Romero *et al.* (2020) comprehensively analyzed a fish farm under combined wave and current conditions using a fluid-structure interaction method. All the above studies proved that the numerical method is accurate enough to predict the structural responses of a fish farm under various current and wave conditions. Thus, the effects of mooring line breakage on dynamic responses of grid moored fish farms are investigated through numerical simulations in the present study.

With complex in-situ operations which can lead to increased loads on different structure members, it is important to understand how the breakage in any part of the fish farm will affect the response and load distribution. In this chapter, the structural responses of a fish farm due to mooring line breakages under operational conditions (*i.e.*, current velocity is less than 0.5 m/s) are comprehensively analyzed.

6.2 Description of the fish farm system

6.2.1 Fish cage description

This study focuses on typical Norwegian fish cages, which include a double-pipe floating collar, a cage net (cylindrical net structure with conical bottom), ropes for supporting the weight system, chains (connecting cage net and sinker tube), a sinker tube and a center point weight. An illustration of the fish cage can be found in Figure 5-1. In order to keep fish cages at targeted locations, a grid mooring system that includes anchors, buoys, connection plates, bridles, buoy lines, anchor lines and frame lines, should be properly designed according to the environmental conditions. Figure 6-2 illustrates how these components are interconnected in a typical Norwegian fish farm. The topological relationship of the aforementioned components in numerical simulations is shown in Figure 6-3. The dimensions and physical properties of the main components used in this chapter are listed in Table 6-1.

6 Application to the dynamic analysis of grid moored fish farms

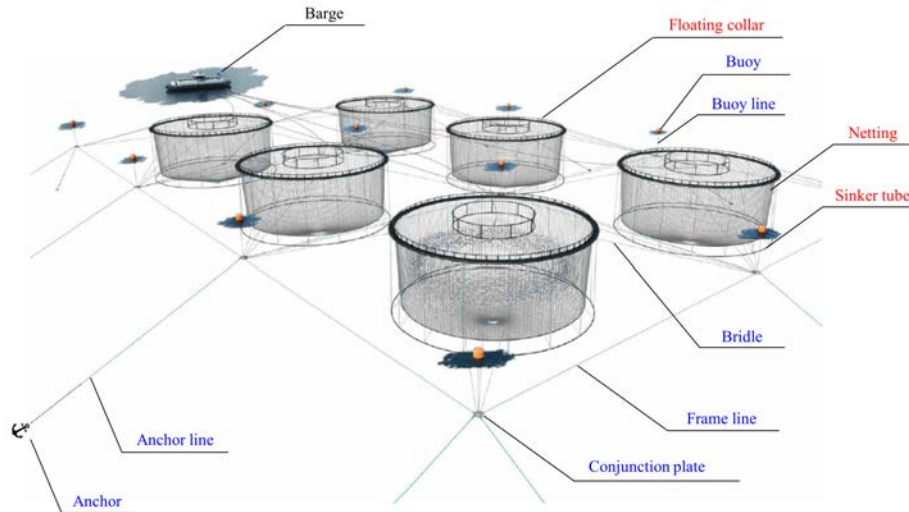


Figure 6-2. Illustration of a typical Norwegian fish farm with 2×3 fish cages (reproduced from AKVA Group, 2020).

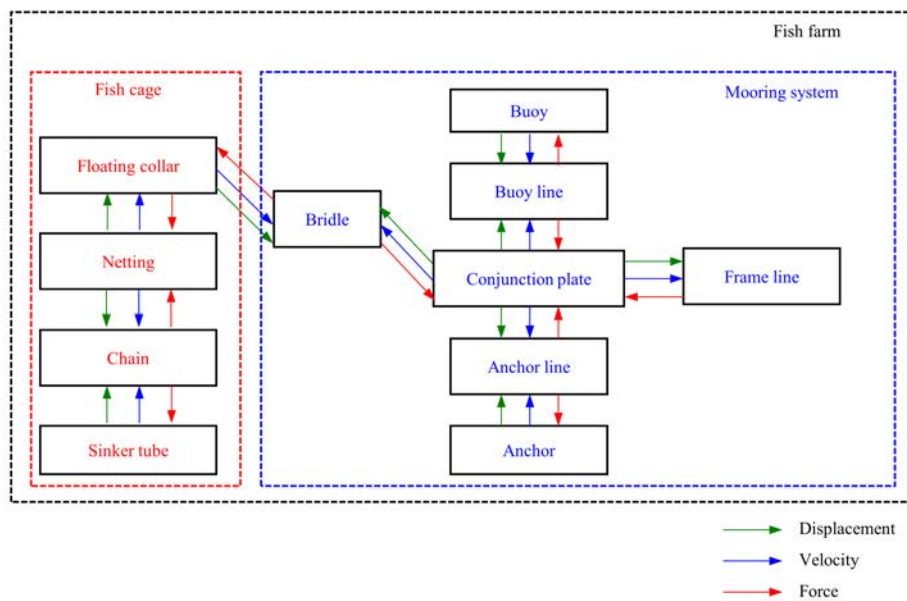


Figure 6-3. Topological relationship for the different components in a fish farm.

6.2 Description of the fish farm system

Table 6-1. Dimensions and properties of the fish cage.

Component	Parameter	Value	Unit
Floating collar	Inside diameter	51	m
	Outside diameter	53	m
	Section diameter	0.25	m
	Wall thickness	28.4	mm
	Young's modulus	0.9	GPa
	Linear density	81	kg/m
Netting	Section diameter	2.5	mm
	Mesh length	25	mm
	Density	1125	kg/m ³
	Young's modulus	0.1	GPa
	Vertical cylinder depth	15	m
	Conical bottom depth	28	m
Sinker Tube	Tube diameter	51	m
	Section diameter	0.25	m
	Center point weight	100	kg
	Linear density	51	kg/m
Mooring line	Initial length of anchor line	120	m
	Initial length of frame line	100	m
	Section diameter	0.05	m
	Young's modulus	1	GPa
	Density	1100	kg/m ³
Buoy	Diameter	2	m
	Vertical cylinder depth	1	m
	Conical bottom depth	2	m

6.2.2 Single-cage fish farm

Figure 6-4 shows an overview of the single-cage fish farm. The mooring lines are named following matrix style, reflecting the matrix-like structure of the grid mooring system. “Mx” represents the mooring lines along X-axis. The first digit of the index number after “Mx” represents the index of the line in the Y-direction, and the second digit represents the index of the line in the X-direction. The “My” lines along Y direction are labeled in a similar fashion. Since this model only contains one fish

6 Application to the dynamic analysis of grid moored fish farms

cage, the mooring lines whose name ends with the number “1” are frame lines, and the rest are anchor lines. The labels of buoys follow the same matrix fashion starting with “B”, with the following two numbers indicating the location in the mooring frame.

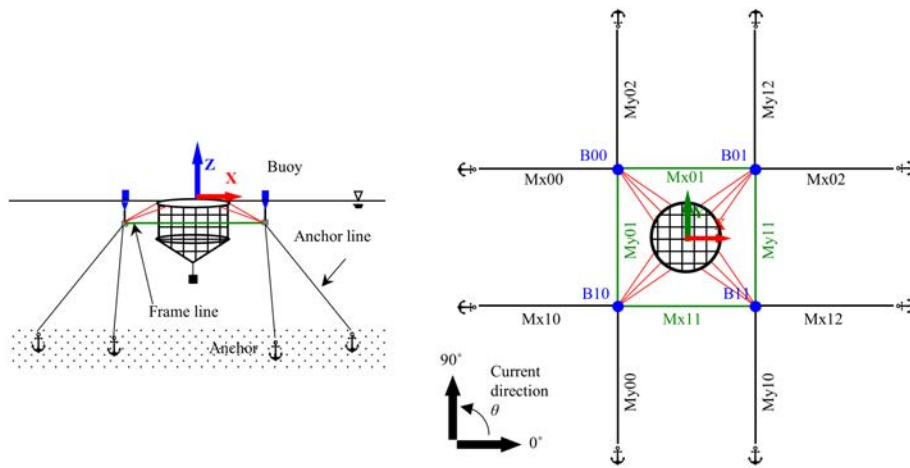


Figure 6-4. Overview of a single-cage fish farm. The current direction is defined as 0° when the current heads to $X+$.

Figure 6-5 shows the time series of the numerical results for this single-cage fish farm with a current velocity of 0.5 m/s and current direction $\theta = 0^\circ$. Although the simulation is under pure current conditions, oscillations are observed in the numerical results. These oscillations come from the nonlinearity of the system, which is also reported by Antonutti *et al.* (2018) and Cheng *et al.* (2021). The oscillations are deemed acceptable, as the standard deviation for the time-series force over the last 100s is 3.1% of the mean force. The time-series results indicate that the simulation reaches the steady-state after 300 s. Hereafter, the tensions in mooring lines and displacements of

6.2 Description of the fish farm system

buoys are time-averaged under steady-state conditions. Figure 6-6 shows the deformation of the single-cage fish farm in a steady-state condition. Due to the pre-tensions in mooring lines, the displacements of other components, such as floating collar and mooring lines, are unnoticeable.

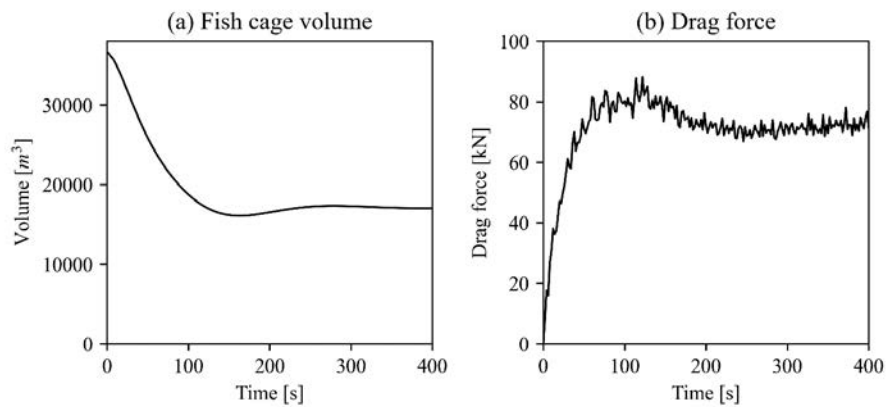


Figure 6-5. Time-series results for the cultivation volume and drag on the fish cage when current velocity is 0.5 m/s and current direction is 0°.

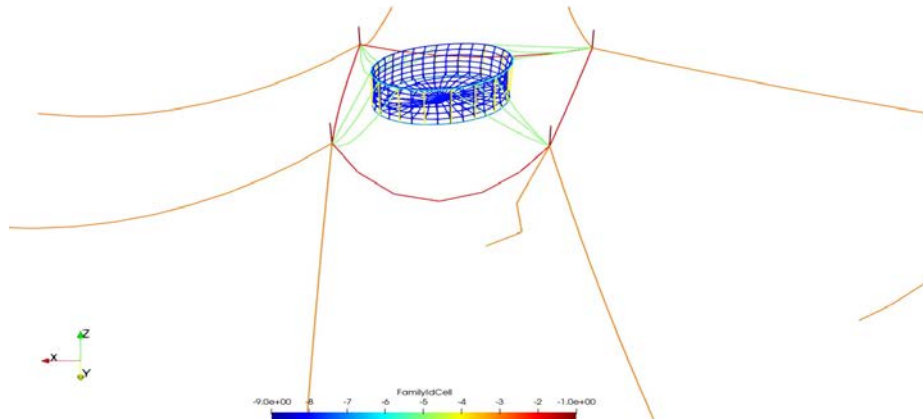


Figure 6-6. The deformation of a fish cage when current velocity is 0.5 m/s and current direction is 0°. For the netting, the grey lines show the undeformed fish cage, and the blue line is the deformed fish cage.

6 Application to the dynamic analysis of grid moored fish farms

6.2.3 1×4 multi-cage fish farm

Figure 6-7 shows the plan view of the 1×4 multi-cage fish farm. The labels of mooring lines and buoys follow the same rule as the single-cage fish farm. The longest axis of this fish farm is along the X-axis. As the four fish cages are arranged along X-axis, these mooring lines along X-axis whose name ends with a number between 1 and 4 are frame lines, and these mooring lines along Y-axis whose name ends with the number “1” are frame lines. The fish cage is named Cage1 to Cage4 from left to right. The labels of buoys also follow the matrix style.

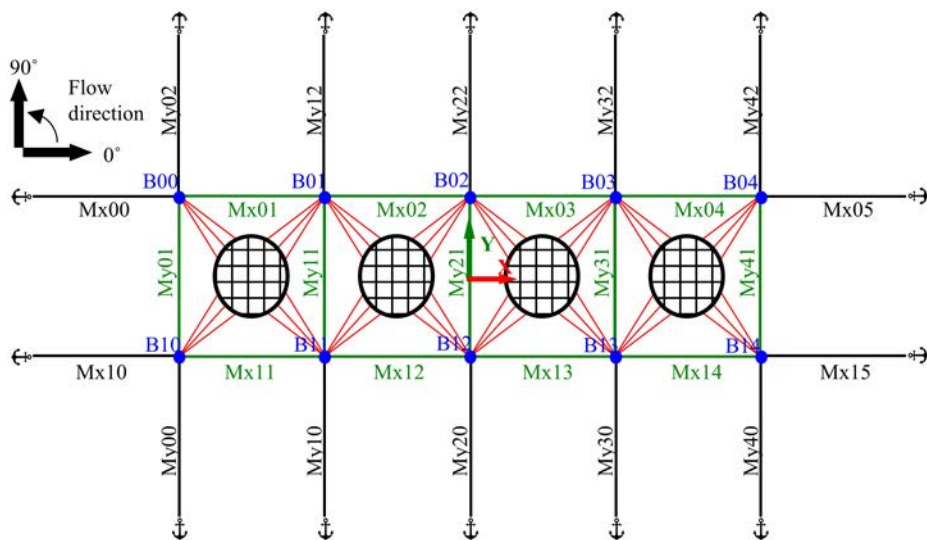


Figure 6-7. Top view of the 1×4 multi-cage fish farm.

6.2 Description of the fish farm system

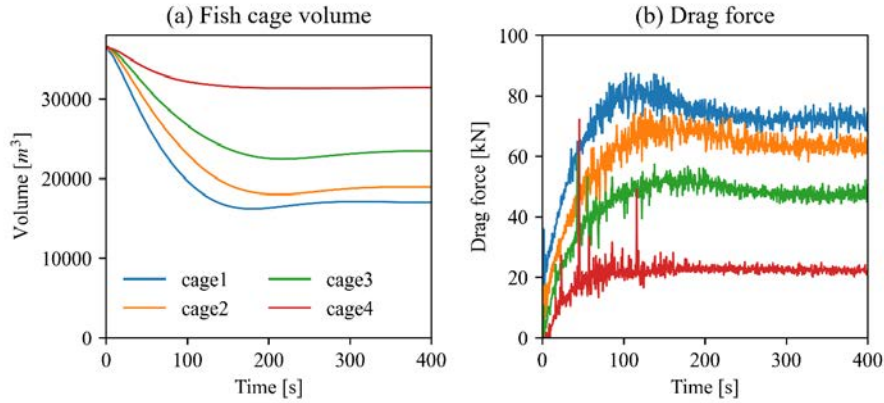


Figure 6-8. Time-series results for the cultivation volume and drag on fish cages when current velocity is 0.5 m/s and current direction is 0° .

Figure 6-8 shows the time series of the numerical results for this 1x4 multi-cage fish farm when current velocity is 0.5 m/s and current direction $\theta = 0^\circ$. Oscillations of drag are also observed in the numerical results. The standard deviation for the drag over the last 100s is up to 5.3% of the mean drag for the four cages. Due to the existence of the upstream fish cages, the current velocity for the downstream fish cage is reduced. The fish cage located downstream, *e.g.*, Cage2, experiences a smaller current velocity compared to Cage1. Thus, Cage2 experiences a smaller current load. The smaller current load makes Cage2 have less deformation and larger cultivation volume than Cage1. Thus, the volume and drag of the four fish cages are different due to the different experienced current velocities. The mechanism that causes the current velocity reduction in the downstream location is the wake effect. The detailed explanations and discussions for the wake effect can refer to Section 2.4, Section 4.6.4 and Sim *et al.* (2021). Here, only the final

6 Application to the dynamic analysis of grid moored fish farms

expression for the current velocity in the rear of a fish cage, $U_{rear}(x, y)$, is presented:

$$U_{rear}(x, y) = (1 - V_{decay})U_{\infty} \quad (6-1)$$

$$V_{decay} = V_r \cdot \frac{S_n}{0.25} \sqrt{\exp\left(-\frac{x/D - 1.5}{25}\right)} \quad (6-2)$$

$$\begin{aligned} V_r = & 0.1201 + 0.2414\cos(\omega y/D) + 0.0115\cos(2\omega y/D) \\ & - 0.0644\cos(3\omega y/D) \\ & + 0.0030\cos(4\omega y/D) \\ & + 0.0294\cos(5\omega y/D) \\ & - 0.0058\cos(6\omega y/D) \\ & - 0.0149\cos(7\omega y/D) \end{aligned} \quad (6-3)$$

where U_{∞} is the incoming current velocity for this fish cage, D is the diameter of this fish cage, and S_n is the solidity of the netting. (x, y) is the coordinate in a local coordinate system where the X+ axis is aligned with the current direction, Z+ is opposite to gravity, and Y-axis is perpendicular to the X-axis and Z-axis. As $U_{rear}(x, y)$ is only meaningful downstream of a fish cage, the value of x is larger than $0.5D$. The constant $\omega = 2.692$ is found by a fit of the experimental data from Gansel *et al.* (2012) and also is also validated using the FSI numerical model in Section 4.6.4. The assumption proposed by Sim *et al.* (2021) that the influence width of the wake is approximately twice of the fish cage diameter is adopted. Hereby, $-1 < y/D < 1$.

6.3 Environmental conditions

According to the report by Halwart *et al.* (2007), most of the conventional fish farms are located at sheltered sites. The sheltered site, according to the Norwegian Standards (Standards Norway, 2009), refers to the location with a significant wave height of 0 - 0.5 m and a peak wave period of 0 - 2 s. According to the previous study by Shen *et al.* (2018), the waves at the sheltered sites can only contribute up to 10 % of the tension forces in mooring lines when the current velocity is 0.5 m/s. As the present study focuses on the structural responses of the conventional fish farms under operational conditions, wave-induced forces are insignificant compared to current-induced forces. Thus, the waves are not included in the present numerical simulations. Pure current conditions with an assumption that the current is steady and uniform over the entire water depth are applied to all the cases. The applied current velocity is 0.5 m/s which corresponds to the velocity for a moderately exposed site, and the water depth is 80 m. As the current direction may vary in fish farms, current directions from 0° to 360° with a 10° interval are considered.

In order to study line breakage, a function was implemented into the existing program, FhSim, to control where and when the breakage occurs in the mooring system. For these mooring line breakage cases, the simulations are conducted under an intact condition until it reaches a steady-state condition, and then the constraint equations between the elements at the desired position are deactivated to simulate the mooring

6 Application to the dynamic analysis of grid moored fish farms

line breakage. Only one broken mooring line is included for each simulation case. For the single-cage fish farm, 12 breakage cases corresponding to the 12 mooring lines, *i.e.*, 8 anchor lines and 4 frame lines, are considered to investigate the influence of breakages at various positions. Together with the different current directions, there are $36 \times 12 = 432$ cases for the single-cage fish farm. Similarly, there are $36 \times 27 = 972$ cases for the 1×4 multi-cage fish farm. A summary of all the simulations in the present study is shown in Table 6-2. Regarding the measurements of structural responses, the tension force in all mooring lines, positions of buoy, drag loads and cultivation volume of the fish cage are recorded before and after breakages occur. Because the two fish farms are symmetric with respect to the Y-axis and the X-axis, many interesting characteristics can be seen in the following results and discussion.

Table 6-2. Summary of simulations cases

		Single-cage fish farm	1×4 multi-cage fish farm
Intact cases	Current velocity	0.5 m/s	0.5 m/s
	Current direction	$0^\circ - 360^\circ$	$0^\circ - 360^\circ$
	Number of cases	36	36
Structural failure cases	Current velocity	0.5 m/s	0.5 m/s
	Current direction	$0^\circ - 360^\circ$	$0^\circ - 360^\circ$
	Breakage positions	$M_{xij} (i = 0, 1; j = 0, 1, 2)$ $M_{yij} (i = 0, 1; j = 0, 1, 2)$	$M_{xij} (i = 0, 1; j = 0, 1, 2, 3, 4, 5)$ $M_{yij} (i = 0, 1, 2, 3, 4; j = 0, 1, 2)$
	Number of cases	$36 \times 12 = 432$	$36 \times 27 = 972$

6.4 Results and discussion

6.4.1 Single-cage fish farm

6.4.1.1 Tension distribution before mooring line breakage

Before the analysis of structural responses due to mooring line breakages, detailed results of tension distribution under intact conditions are presented. Figure 6-9 presents the tension force in each mooring line when the current direction θ is 0° . The dashed lines represent pre-tensions in anchor lines and frame lines. The red color shows that the tension in the anchor line is higher than the pre-tension, and the blue color shows that the tension in the anchor line is lower than the pre-tension. According to the layout in Figure 6-4, all the anchor lines in higher tensions, *i.e.*, Mx00, Mx10, My00 and My02 are located on the negative side of X-axis, which means they are the main contributors to hold the fish farms when the $\theta = 0^\circ$. Tension forces in all the frame lines are much smaller than those in anchor lines. The tension in frame line My01, which is on the upstream side of the fish cage, is reduced compared to the pre-tension. When $\theta = 0^\circ$, the drag on the fish cage is acting along X+ direction, and this drag is transferred to the mooring system through bridles (the red lines in Figure 6-4). According to the equilibrium of forces, the tension in the front frame line My01 is reduced, and the tension in the rear frame line My11 is increased compared to their pre-tension. Together with Figure 6-4 and Figure 6-9, it can be seen that mooring lines which are symmetric with respect to the X-axis experience the same tension forces, such as Mx00 and Mx02 have the same value.

6 Application to the dynamic analysis of grid moored fish farms

When $\theta = 0^\circ$, the environmental loads act along the axis of symmetry for this single-cage fish farm, and these loads can be symmetrically distributed among the mooring lines.

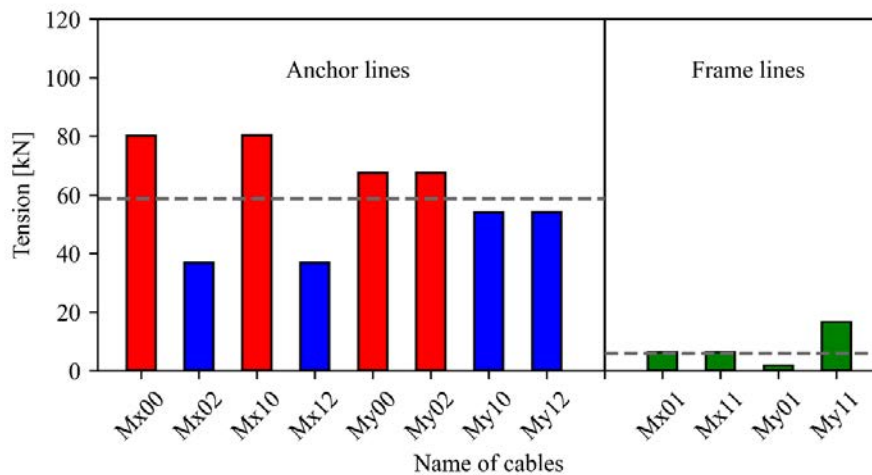


Figure 6-9. Tension distribution in mooring lines, *i.e.*, anchor lines and frame lines, when the mooring system is in intact condition, current direction is 0° and current velocity is 0.5 m/s.

Figure 6-10 shows the influence of different current directions on the tension distribution among anchor lines. This figure is plotted in a polar coordinate system, where the polar angle represents the current direction, and the radius represents the value of tension force. The tensions in anchor lines change with different current directions. Take Mx00 and Mx10 as an example. When $\theta = 0^\circ$, the tension force in Mx00 and Mx10 are the same, which can also be seen in Figure 6-9. With the increasing current direction, the tensions in Mx00 and Mx10 are reduced until $\theta = 180^\circ$. The tension-deduction in Mx00 is first slower than that of Mx10 when $\theta < 90^\circ$, and then faster than that of Mx10 when $\theta > 90^\circ$.

6.4 Results and discussion

When $\theta = 180^\circ$, the tensions in these two anchor lines are the same again. When $0^\circ < \theta < 90^\circ$, Mx10 is relatively located in front of Mx00, and thus Mx10 carries a higher proportion of the current-induced load on the fish farm. Hereby, the tension in Mx10 is larger than that in Mx00 when $0^\circ < \theta < 90^\circ$. For the current direction between 180° and 360° , the change of tensions in Mx00 and Mx10 follows an opposite trend compared to those when $0^\circ < \theta < 180^\circ$. The change of the tensions in other mooring lines can be interpreted in a similar way as with Mx00 and Mx10.

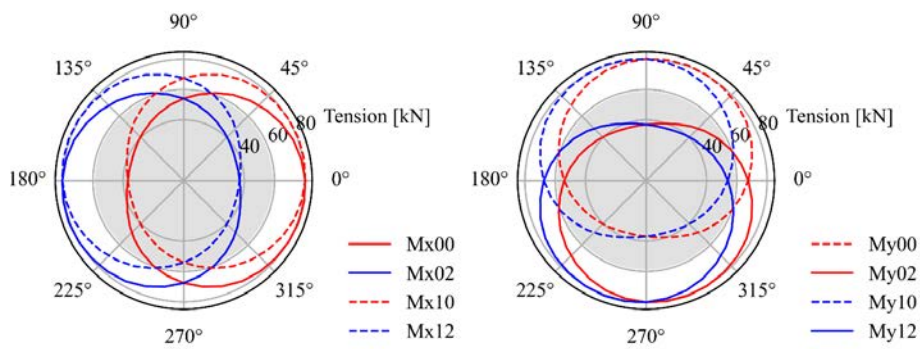


Figure 6-10. Tension distribution in anchor lines under different current directions when the mooring system is in intact condition and current velocity is 0.5 m/s. The grey shadow represents pre-tension in anchor lines.

The tension distribution is symmetric when the environmental loads along the axis of symmetry for this single-cage fish farm. In addition to $\theta = 0^\circ$, the symmetric tension distribution can also be observed when $\theta = n \times 45^\circ$, where n is an integer. In Figure 10, intersections of the curves occur when the tension distribution is symmetric. For $\theta = 45^\circ, 135^\circ, 225^\circ$ and 315° , these intersections can be

6 Application to the dynamic analysis of grid moored fish farms

observed by overlapping the two subplots for anchor lines in X and Y directions in Figure 6-10. All the above symmetric characteristics are related to geometric characteristics of the single-cage fish farm. These symmetric characteristics can simplify fish farm design and structural analysis.

6.4.1.2 Tension distribution after mooring line breakage

When one of the mooring lines breaks, the environmental loads will be distributed among the remaining mooring lines, and consequently, the position of buoys may also change. The changes of tensions in the remaining mooring lines and positions of buoys, due to mooring line breakages, are presented in Figure 6-11. The influence of mooring line breakages on the position of buoys will be discussed in Section 6.4.1.3. Figure 6-11 is divided into six blocks in order to differentiate the influence of breakages in anchor lines and frame lines. Here we define anchor lines and frame lines as two mooring components. The names of the six blocks, which are shown at the lower right of Figure 6-11, indicate the influence of one component on others. For example, M_{AF} represents the influence on tensions in the anchor lines due to the frame line breakages. The influence of breakages at the two components and current directions will be discussed in Section 6.4.1.5.

6.4 Results and discussion

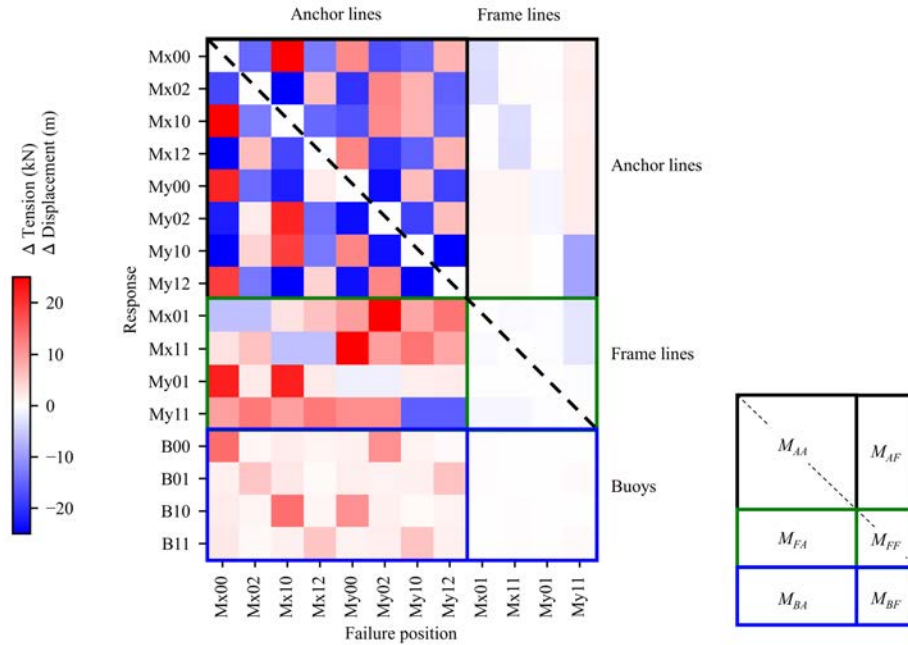


Figure 6-11. The change of tension in mooring lines and the movements of buoys with respect to the different positions of mooring line breakages when current velocity is 0.5 m/s and $\theta = 0^\circ$.

An example of the displacement of the fish farm can be seen in Figure 6-12. When the anchor line Mx00 breaks, the whole fish farm is no longer symmetric with respect to X-axis. Thus, the tensions among the remaining mooring lines are no longer symmetric, as shown in Figure 6-9. The first column of Figure 6-11 shows the changes of tension in the remaining mooring lines after anchor line Mx00 breaks. It is seen that the tension in anchor line Mx10, which is parallel to the broken anchor line Mx00, increases 32 kN (1.4 times of its tension under intact conditions). Similar observations were also reported by Tang *et al.* (2020) and Yang *et al.* (2020). According to Tang *et al.* (2020), the tension in the remaining anchor line can increase up to 1.75 times due to

6 Application to the dynamic analysis of grid moored fish farms

mooring line breakage under the condition with the current velocity of 1.0 m/s and irregular waves corresponding to a 50-year return period. In addition, tensions in anchor lines My00 and My12 are clearly increased as well, which is similar to the results reported by Tang *et al.* (2020) and Yang *et al.* (2020). Except for these three anchor lines, the tensions in the remaining anchor lines are reduced after anchor line Mx00 breaks. As for the frame lines, the tensions in three of the frame lines increase, and tensions in only one frame line reduce. Generally, the changes of tension among the frame lines are smaller than those in anchor lines. The other columns, which indicate the influence of breakages at different mooring lines, will be discussed in Section 6.4.1.4.

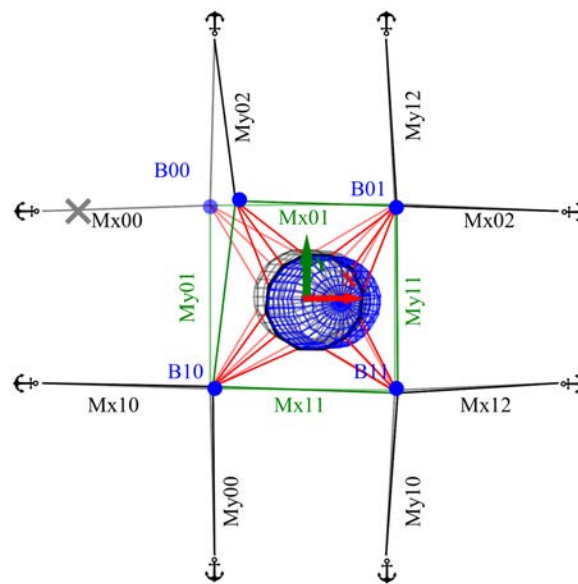


Figure 6-12. Top view of the single-cage fish farm when the anchor line Mx00 breaks, the current velocity is 0.5 m/s and $\theta = 0^\circ$.

6.4.1.3 Movement of buoys after mooring line breakage

As shown in Figure 6-12, due to the breakage of anchor line Mx00, the buoy B00 moves towards the X+ direction significantly. However, the other three buoys have negligible movements as their constraining structures are still intact. The movements of buoys are also shown in Figure 6-11. The movement of a buoy is calculated as the distance between the buoy before and after one of the mooring lines breaks. As the distance is non-negative, the color for the movement of buoys is always red. According to the first column in Figure 6-11, the movements of B00 are clearly larger than the other three buoys.

6.4.1.4 Influence of breakages at different mooring lines

If one of the mooring lines breaks, the fish farm with the remaining components is most likely geometrically asymmetric, and the tension distribution among the remaining mooring lines may lose the symmetric characteristics as shown in Section 6.4.1.1. The breakages at different mooring lines usually cause different tension distributions, but symmetric characteristics of the changes in the structural responses can still be observed between different cases. The different columns in Figure 11 represent the changes in mooring line tensions and buoy movements caused by the breakages at different mooring lines when $\theta = 0^\circ$. The dashed diagonal line for M_{AA} and M_{FF} represents the influence of the broken mooring to itself. Since only the responses of the remaining components are discussed in the present study, the values on this diagonal line are set to zero. Symmetric values with respect to this

6 Application to the dynamic analysis of grid moored fish farms

diagonal line can be observed from M_{AA} . For example, $M_{AA}(3,1) = M_{AA}(1,3)$, $M_{AA}(4,2) = M_{AA}(2,4)$ and $M_{AA}(7,8) = M_{AA}(8,7)$, where the pair numbers in brackets are the index for the row number and the column number. Taking $M_{AA}(3,1) = M_{AA}(1,3)$ for instance, the symmetric values imply that when $\theta = 0^\circ$, the influence from the broken Mx00 on Mx10 is equivalent to the influence from the broken Mx10 to Mx00. This is because of the symmetric characteristics of the intact fish farm, as discussed in Section 6.4.1.1.

Whichever anchor line breaks, the number of mooring lines with increased tension compared to intact conditions is the same. When one of the anchor lines breaks, there are always three anchor lines and three frame lines experiencing increased tensions. More specifically, the tensions in one of the remaining anchor lines which are parallel to the broken anchor line will increase, and the tension in two of the remaining anchor lines which are perpendicular to the broken anchor line will increase. As for the frame lines, the tension always decreases in the frame lines, which are parallel with and directly connected to the broken anchor line, and increases in the rest of the frame lines. However, when one of the frame lines breaks, the changes of tensions in the remaining mooring lines are relatively insignificant. Hereby, the colors in M_{AF} and M_{FF} are lighter than those in M_{FA} and M_{AA} , as shown in Figure 6-11.

Whichever anchor line breaks, the buoy which is directly connected to the broken anchor line has the most significant movement. This is because the constraint which holds this buoy at the desired

position disappears due to the breakage of the anchor line. For the other three buoys, the constraints still work similarly to the condition that before the breakage happens. Thus, the movement of the buoys that are not directly connected to the broken anchor line is negligible. However, when one of the frame lines breaks, the movements of all buoys are negligible. Thus, the colors in M_{BF} are almost white in Figure 6-11.

6.4.1.5 Influence of current directions

As shown in Figure 6-11, the colors in the last four columns corresponding to the breakage of frame lines (*i.e.*, M_{AF} , M_{FF} and M_{BF}) are clearly lighter than the colors in the first eight columns corresponding to the anchor lines breakage cases (*i.e.*, M_{AA} , M_{FA} and M_{BA}). These lighter colors mean that the influence on the mooring system caused by frame lines breakages is smaller than those caused by anchor lines breakages. Thus, it can be considered that frame lines are less crucial than anchor lines regarding the robustness of the fish farm. In order to compare the importance of the two components, *i.e.*, anchor lines and frame lines, the root-mean-square (RMS) value of the changes in the responses is introduced as an indicator. The RMS is calculated based on the values in each block, as shown in Figure 6-11. The values in each block can be considered as a matrix. The RMS value of each matrix can reflect the averaged changes of tensions in the remaining mooring lines or the averaged movements of buoys due to breakages of the two components, and is calculated as follows:

6 Application to the dynamic analysis of grid moored fish farms

$$\|M\|_{RMS} = \left(\frac{1}{m \times n} \sum_{i=1}^n \sum_{j=1}^m (a_{ij})^2 \right)^{1/2} \quad (6-4)$$

where m and n are the row and column numbers for the matrices, respectively. a_{ij} is the value shown by the color in Figure 6-11.

Figure 6-13 presents the RMS value for the six matrices with respect to different current directions. Due to the symmetric characteristics discussed from Sections 6.4.1.1 to 6.4.1.4, the RMS is only given for 0° - 90° . In this figure, all the lines are nearly horizontal, which means that the averaged changes in the responses due to mooring line breakages at different components exhibit little sensitivity to the current direction. In addition, the solid lines are always higher than the dashed lines. This implies that the influence caused by the anchor line breakages is always larger than those caused by the frame line breakages. Meanwhile, the breakages at anchor lines are always easier to notice than those at frame lines, as M_{BA} is always larger than M_{BF} .

6.4 Results and discussion

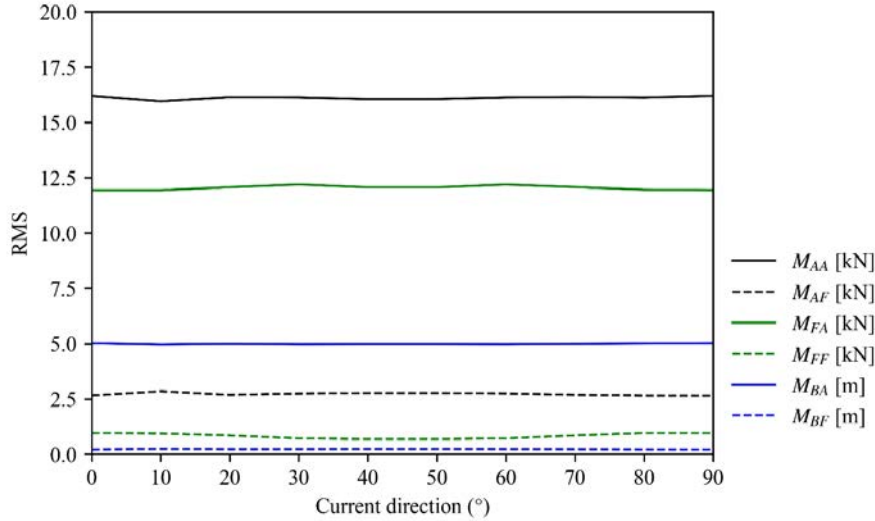


Figure 6-13. The RMS for matrices with respect to different current directions.

6.4.2 Multi-cage fish farm

6.4.2.1 Tension distribution before mooring line breakage

Figure 6-14 presents the tension distribution before mooring line breakage with respect to different current directions. For the tensions in the “My--” anchor lines, only half of them are plotted in the right subplot of Figure 6-14 to make this figure readable. The tensions in the other half mooring lines can be obtained based on symmetry, similar to the single-cage fish farm. Moreover, the left subplot in Figure 6-14 shows that zero-tension appears in “Mx” anchor lines when the angle between the current direction and the longest axis of this 1×4 multi-cage fish farm is less than 45° . Under these current directions, the anchor lines with small tension may become slack and have abrasions with the seabed.

6 Application to the dynamic analysis of grid moored fish farms

According to Cardia and Lovatelli (2015), these abrasions can rapidly abrade the anchor lines to a dangerous condition and should be avoided in the design. The use of floats, attached close to the lower end of the anchor lines, can reduce the possibility of these abrasions.

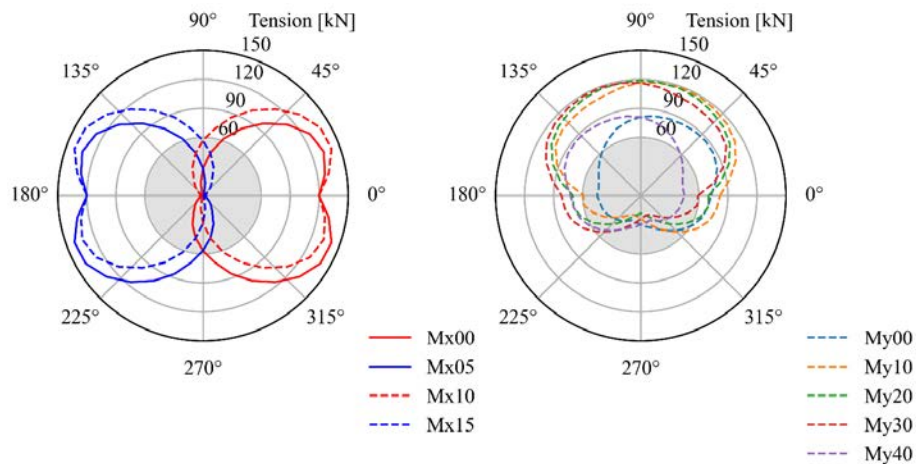


Figure 6-14. Tension distribution in anchor lines under different current directions when the mooring system is in intact condition and current velocity is 0.5 m/s. The grey shadow represents pre-tension in anchor lines.

Figure 6-15 shows the extreme tension in anchor lines under different current directions. The extreme tension represents the largest tension among all the mooring lines. In this 1×4 multi-cage fish farm, the maximum extreme tension (around 140 kN) is almost 2.3 times of the pre-tension (around 60 kN), and it is much higher than that in the single-cage fish farm (around 80 kN) due to higher total environmental loads. For example, the total drag on the four fish cages is around 211 kN when $\theta = 0^\circ$, which is three times larger than that on the single fish cage (72 kN). The maximum extreme tension in this 1×4 multi-cage fish farm occurs when the angle between the current direction and the longest axis

of the fish farm is $20^\circ \sim 30^\circ$. However, the extreme tension is not sensitive to the current direction in the single-cage fish farm. According to the explanation by Sim *et al.* (2021), the layout of the two fish farms together with the wake effect can cause different reactions of extreme tension under different current directions. Due to the wake effect, the current velocity is reduced after the current passes through a fish cage (Zhao *et al.*, 2015). The reduced current velocity can lead to a smaller drag on these fish cages, which locate in the wake region of the upstream cages. When the current direction increases from 0° to 90° , the total drag on the four fish cages first increases from the smallest value (around 211 kN) at 0° to around 320 kN at 30° , and then remains at the maximum value. It should be noted that the drag is the maximum does not necessarily mean that the extreme tension in the mooring system is the maximum, as the number of effective anchor lines also changes with the current direction. The effective anchor lines are the main lines that hold the fish farm in position. For example, when $\theta = 0^\circ$, Mx00 and Mx10 are the main effective anchor lines to hold this 1×4 fish farm in position. When $\theta = 90^\circ$, Myi0 ($i = 0, 1, 2, 3$ and 4) are the main effective anchor lines. Under the same total drag, more effective anchor lines can lead to smaller extreme tension in the mooring system. Due to the total drag and the number of effective anchor lines, the highest tension happens when the current direction is around $20^\circ \sim 30^\circ$. For other current directions ($90^\circ \sim 360^\circ$), similar observations can be seen due to the geometric symmetry of this fish farm. As for the single-cage fish farm, the total drag loads and effective anchor lines do not change with the current

6 Application to the dynamic analysis of grid moored fish farms

directions. Thus, the extreme tension in this single-cage fish farm is always around 80 kN.

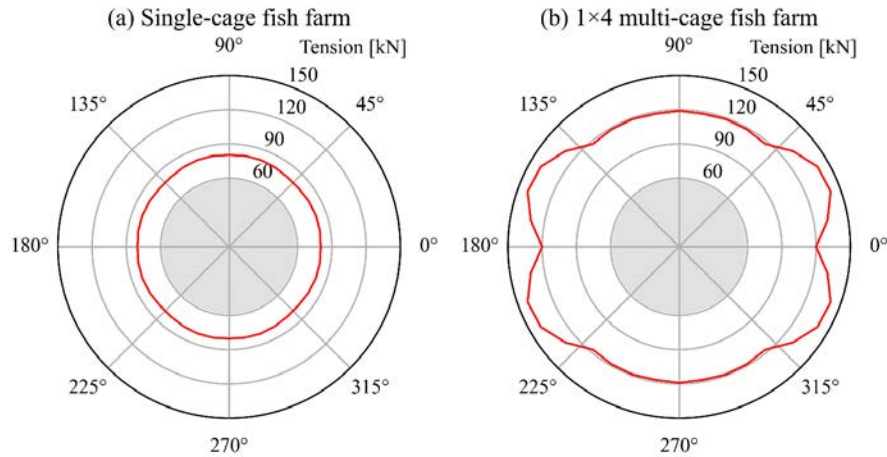


Figure 6-15. Extreme tension in mooring lines under different current directions when the mooring system is in intact condition and current velocity is 0.5m/s. The grey shadow represents pre-tension in anchor lines.

6.4.2.2 Tension distribution and movement of buoys after mooring line breakage

Figure 6-17 shows the tension distribution and the movement of buoys after one of the mooring lines breaks when the current velocity is 0.5 m/s and $\theta = 30^\circ$. The symmetric characteristics which are discussed in Figure 6-11 cannot be observed in this figure, as the current is not along the axis of symmetry for this 1×4 multi-cage fish farm. Usually, the breakages at different mooring lines can cause different tension increments or decrements in the remaining mooring lines. However, some mooring lines, *e.g.*, Mx05, Mx04 and Mx14, are always white, as shown in Figure 6-17. That white color means that whichever mooring lines break, the tensions in these mooring lines are always the same as theirs under intact

6.4 Results and discussion

conditions. Actually, these mooring lines are zero-tension and slack under the intact condition when $\theta = 30^\circ$. As the remaining mooring lines can still hold the whole fish farm, these zero-tension mooring lines are still slack. Thus, the tensions in these mooring lines have no change after mooring line breakages.

Figure 6-16 shows the top view of this 1×4 multi-cage fish farm after anchor line My30 breaks when current velocity is 0.5 m/s and $\theta = 30^\circ$. It can be observed that the buoy B13 has a significant movement towards Y+ direction, and the other buoys have relatively smaller movements. Figure 6-18 shows the bird view of this multi-cage fish farm after anchor line My30 breaks. The distances of these movements are shown in Figure 6-17.

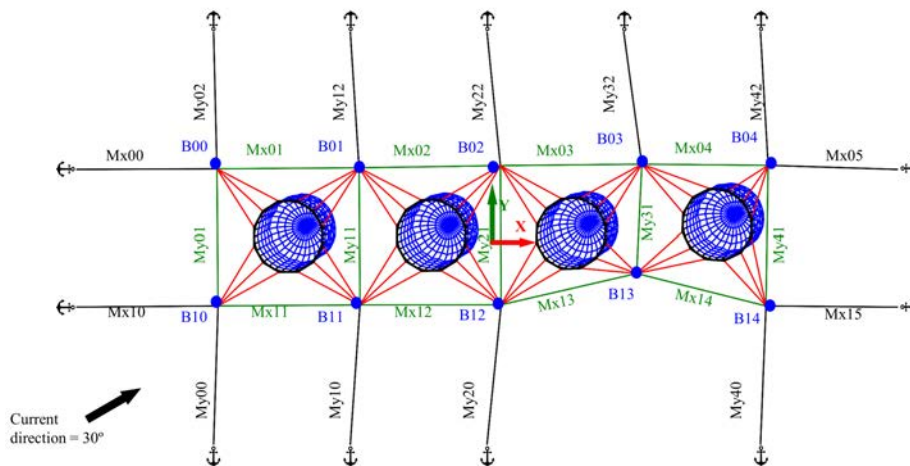


Figure 6-16. Top view of the 1×4 multi-cage fish farm when the anchor line My30 breaks, current velocity is 0.5 m/s and $\theta = 30^\circ$.

6 Application to the dynamic analysis of grid moored fish farms

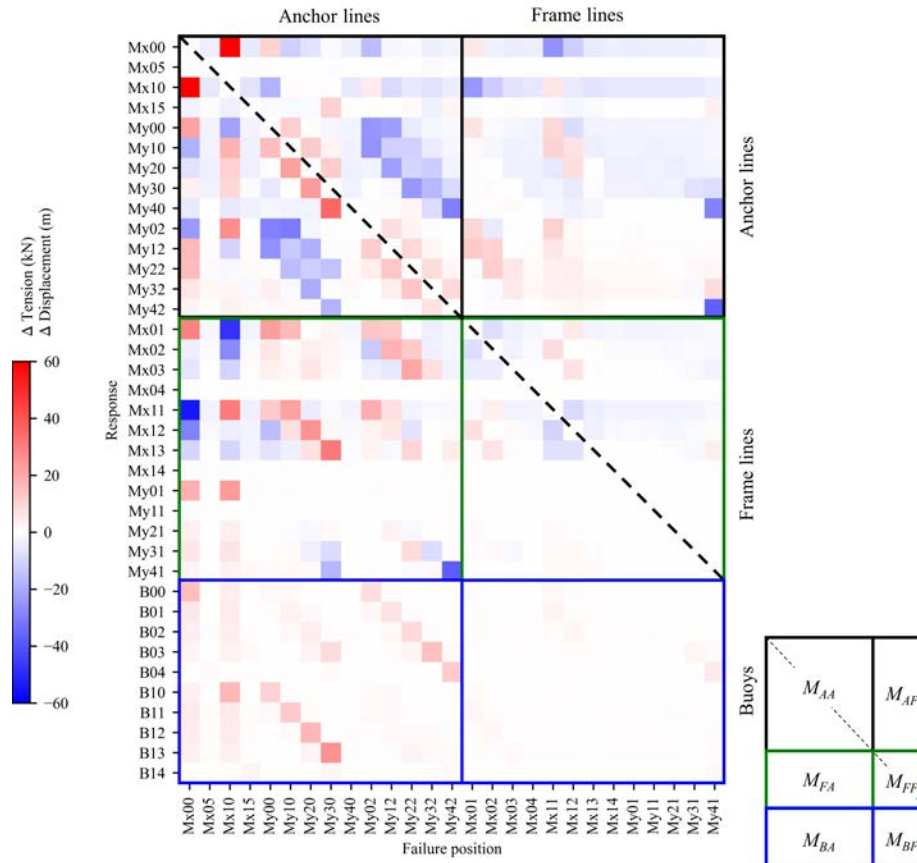


Figure 6-17. The changes of tensions in mooring lines and the movements of buoys in the 1×4 multi-cage fish farm with respect to the different positions of mooring line breakages, when current velocity is 0.5 m/s and $\theta = 30^\circ$.

6.4 Results and discussion

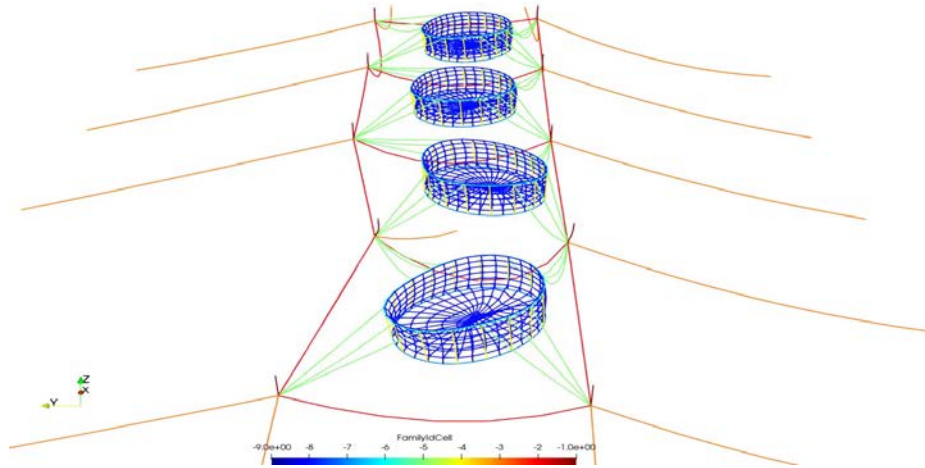


Figure 6-18. Brid view of the 1×4 multi-cage fish farm when the anchor line My30 breaks, current velocity is 0.5 m/s and $\theta = 30^\circ$.

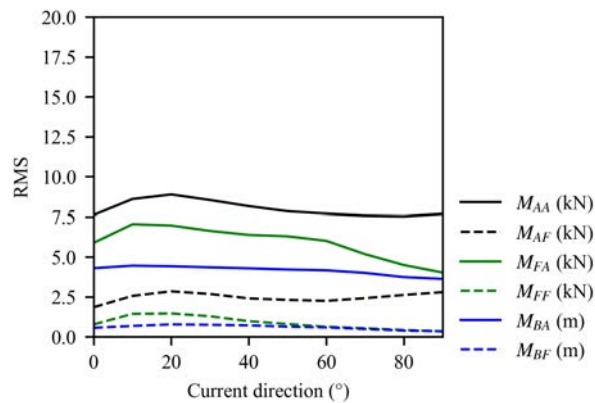


Figure 6-19. The RMS for matrices under different current directions.

6.4.2.3 Influence of current directions

As shown in Figure 6-19, the influence due to frame line breakages is less serious than that due to anchor line breakages. Unlike the single-cage fish farm, for this 1×4 multi-cage fish farm, the influence on the changes of tensions in the remaining mooring lines due to mooring line

6 Application to the dynamic analysis of grid moored fish farms

breakages is dependent on the current direction. When $20^\circ < \theta < 30^\circ$, the influence on the changes of tensions in the remaining mooring lines due to anchor line breakages is strongest among all current directions. When $20^\circ < \theta < 30^\circ$, the extreme tension is also the maximum under intact conditions, as shown in Figure 6-15. This implies that the influence is related to the extreme tensions before mooring line breakages. If the extreme tension in the intact condition is high, a stronger influence on the changes of the tensions is expected after mooring line breakages. As for the influence on the movements of buoys, M_{BA} is always larger than M_{BF} , and both are independent of current directions.

6.4.3 Mooring system design consideration

Usually, a fish farm consists of several fish cages, and these fish cages are arranged in arrays using a grid-like mooring system. According to Cardia and Lovatelli (2015), the most common layouts of a fish farm are 2×3 , 2×4 and 2×6 . During the design of a mooring system, the ratio between the number of fish cages and the number of anchor lines is a useful indicator to measure the robustness of the fish farm. As shown in Table 6-3, a fish farm with a small number of fish cage usually has a relatively larger number of anchor lines per fish cage. A larger number of anchor lines per fish cage is preferred in an exposed site, as the position of the fish farm can be kept more securely. As shown in Figure 6-20, the maximum increment of tension in the single-cage fish farm is less than half of that in the 1×4 multi-cage fish farm. Thus, the fish farm with a larger number of anchor lines per fish cage has a higher chance to

6.4 Results and discussion

sustain the fish farm after one of the mooring lines breaks. While in a sheltered site, a fish farm with more fish cages and small anchor lines per fish cage is preferable, as it requires relatively fewer anchors and mooring lines, and subsequently lower installation costs.

Table 6-3. Fish farm with grid mooring system.

Layout of fish farm	Number of fish cage	Number of anchor line	Number of anchor line per fish cage
1×1	1	8	8
1×4	4	14	3.5
1×8	8	22	2.75
2×2	4	12	3
2×3	6	14	2.33
2×4	8	16	2
2×6	12	20	1.66

In some cases, additional anchor lines are required to reinforce the mooring system, particularly in an exposed site. Figure 6-20 shows the relationship between the maximum tension increment in the mooring system and the maximum buoy movement after one mooring line breaks. For example, one point in the left scatterplot is extracted based on the first column of Figure 6-10. The X-value in the scatter plot corresponds to the maximum movement, which is from B00, and the Y-value corresponds to the maximum tension increment, which is from MX10. The figure summarizes the results for all the cases with different breakage situations. Due to the symmetry of the fish farm set-up, the scatter plots only include results for current directions of $0^\circ \leq \theta \leq 90^\circ$. Thus, there are $10 \times 12 = 120$ points in the left subplot and $10 \times 27 = 270$

6 Application to the dynamic analysis of grid moored fish farms

points in the right subplot. According to the right subplot, the breakages at the “Mx” anchor lines can lead to a higher tension increment in the mooring system, compared to the breakages at the “My” anchor lines. In order to reinforce the mooring system, additional anchor lines should be added as a backup for the “Mx” anchor lines. According to Figure 6-15 and Figure 6-19, When $20^\circ < \theta < 30^\circ$, the extreme tension in the mooring system is the maximum, and the influence of mooring line breakages is also the strongest. Thus, the most effective way to improve the security and reliability of this 1x4 multi-cage fish farm is to add additional anchor lines in the four corners, as shown in Figure 6-21.

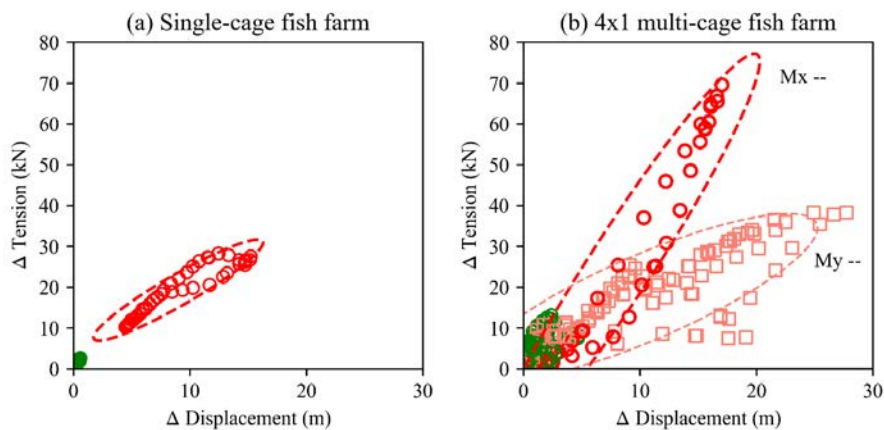


Figure 6-20. The extreme change of tension among mooring lines after one of the mooring lines breaks. The green color represents the conditions when the frame line breaks. For subplot (a), the red circles represent the conditions when one anchor line breaks. For subplot (b), the red circles represent the conditions when one “Mx” anchor line breaks, and the light red squares represent the conditions when one “My” anchor line breaks. Confidence ellipse with 95% confidence is plotted for these anchor line breaks.

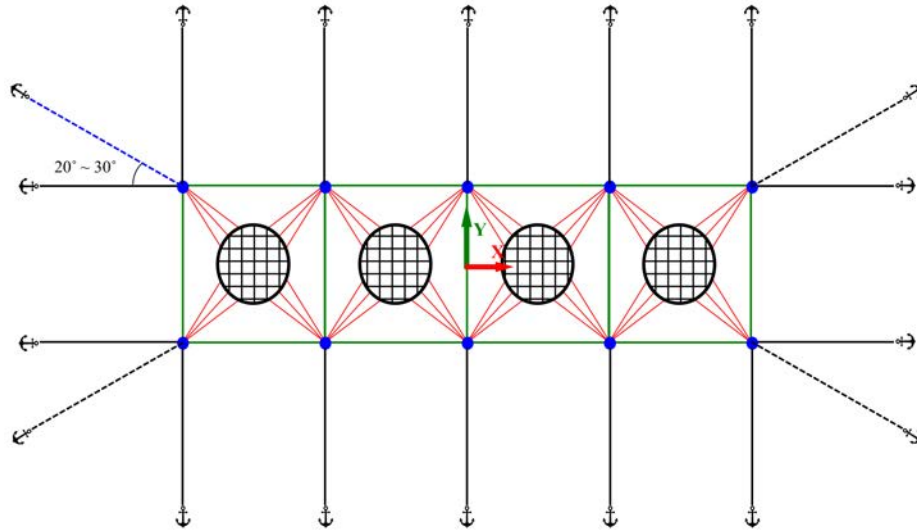


Figure 6-21. The 1×4 multi-cage fish farm with additional corner mooring lines.

6.4.4 Observations during operation

The breaking strength for the considered anchor lines (50mm three-strand PolysteelTM rope) is around 360 kN, which is larger than the extreme tension (around 220 kN) in the remaining mooring lines of the 1x4 multi-cage fish farm after one of the mooring lines breaks. Thus, the mooring system should not have progressive collapse under operational conditions. However, if this breakage is not detected, the damaged mooring system may not be able to keep the fish farm in position during higher currents and waves. Consequently, the undetected mooring line breakage can lead to a structural collapse and fish escape, which is a serious accident. As reported by Føre and Thorvaldsen (2021), the most serious fish escape in the period of 2010 - 2018 occurred because of the breakages in the mooring system. In order to avoid this serious fish

6 Application to the dynamic analysis of grid moored fish farms

escape, one way is to increase the conservativeness during the design, which means to increase the breaking strength of anchor lines by using stronger material or larger diameter of the ropes. This improvement can increase the initial financial investment for a fish farm. Another way is to monitor the positions of buoys during or after in-situ operations.

According to NS9415 (Standards Norway, 2009), the regular inspections of a fish farm only emphasize the structural integrity of netting and floating collar. Monitoring the positions of buoys has not been given enough attention. However, based on the results from Sections 6.4.1.1 and 6.4.1.2, the displacements of the buoys can act as a good indicator to detect the mooring line breakage. As shown in Figure 6-20, the tension increment in the mooring system has a strong correlation with the movement of buoys. If one of the buoys is observed to have a large movement, it is most likely that one of the mooring lines breaks. The present analysis shows that the broken mooring line is most likely the one directly connected to the buoy with the largest movement.

In Norway, most of the in-situ operations in a fish farm are handled by various auxiliary equipment, such as net cleaners, buoy ropes for crowding of fish, tarpaulins for parasite treatment and netting for fish handling. It may not be easy to notice the movement of buoys while the equipment operators are working. From a practical point of view, it is useful to install a Global Positioning System (GPS) device on each buoy. The GPS device can record the locations of buoys and send the information back to the operators and administrators. Based on the

movements of buoys, a warning system to detect mooring line breakages can be established. According to the previous studies by Zhao *et al.* (2019) and Bi *et al.* (2020), a warning system for mooring line breakages can be established through a deep learning method based on more simulations as presented in the present study. By then, the breakages in the mooring system can be quickly and automatically discovered and precisely located, and the tension distribution in the remaining mooring system can be predicted with seconds. The administrator can make a corresponding decision based on these predictions, such as: (1) stop the operation immediately or (2) continue the operation and repair the damaged mooring line later. With more data training, the autonomous fish farming system for early prediction proposed by Yang *et al.* (2020b) can also be achieved in the future.

6.5 Conclusions

In this chapter, the structural responses of the two fish farms, *i.e.*, a single-cage fish farm and a 1×4 multi-cage fish farm, are comprehensively analyzed with respect to combinations of mooring line breakages and current directions. Due to the symmetry of the two fish farms, symmetric results are shown and discussed. Based on these results, suggestions to improve the design of the mooring system are given. It is also recommended to monitor the positions of buoys during operation to detect the mooring line breakages. Besides, the following conclusions are drawn from this chapter:

1. Breakage at one mooring line is unlikely to cause a progressive collapse of the fish farm under operational conditions, such as current velocity < 0.5 m/s. The extreme tension in the remaining mooring lines of the 1×4 multi-cage fish farm is around 220 kN after one of the mooring lines breaks under operational conditions. This value is 3.6 times larger than the pre-tension and 60% of the designed breaking strength. However, mooring line breakages may cause structural collapse and fish escape when the current and waves become stronger, if the breakages remain undetected.
2. Monitoring the positions of buoys during and after in-situ operations is recommended and could be emphasized in the operational handbook, since mooring line breakages can be discovered and located from the movement of buoys. The

6.5 Conclusions

broken mooring line is usually directly connected to the buoy with the largest movement.

The increment of tension in the mooring system due to mooring line breakages has a strong positive correlation with the movement of buoys. Based on the displacement of the buoys with the largest movement, the maximum tension increment in the mooring system can be estimated. This estimation can help the operators of fish farms to decide whether or not to repair the damaged mooring line immediately.

7 Application to offshore aquaculture structure

The content is partly published as:

Cheng, H., Ong, M.C., Li, L., 2022. Dynamic simulations of an offshore aquaculture structure under combined wave and current conditions (accepted by 2022OMAE).

7.1 Introduction

Offshore aquaculture has gained momentum in recent years, and the production of marine finfish species is being relocated offshore (Morro *et al.*, 2021). The reliability of offshore aquaculture structure (OAS), which may be subjected to strong currents and waves in offshore areas, is one of the keys to achieving the sustainability of offshore aquaculture. Norway and China lead in offshore aquaculture with the introduction of massive semi-submersible fish cages, *e.g.*, “Ocean Farm 1” (Jin *et al.*, 2021) and “Shen Lan 1” (Wang *et al.*, 2021). These two OASs are illustrated in Figure 7-1. Given the large capital costs, offshore aquaculture is growing slowly in these two countries and has been confined mainly to small-scale pilot projects in other countries (Naylor *et al.*, 2021).



Figure 7-1. Illustration of two offshore aquaculture structures. (a) “Ocean Farm 1” (reproduced from SalMar ASA, 2021). (b) “Shen Lan 1” (reproduced from Wanzefeng Fisheries, 2021).

7 Application to offshore aquaculture structure

In order to study the dynamic responses of aquaculture structures, considerable research works have been done using experimental and numerical methods. Bi *et al.* (2015) conducted a series of laboratory experiments to investigate the damping effect of the net cage on wave propagation. Zhao *et al.* (2015a) investigated the hydrodynamic characteristics of a large fish farm containing eight fish cages with a model scale of 1:40. Their results showed that obvious flow-velocity reduction exists inside and also outside the cages of the multi-cage configuration. Zhao *et al.* (2015b) conducted a series of experiments to investigate the motion responses of an offshore fish farm in regular waves. Jin *et al.* (2021) conducted a series of experiments and developed a numerical model using commercial computer software, SIMO, to study the motion responses of “Ocean Farm 1” in waves and currents. Li *et al.* (2018, 2019) and Li and Ong (2017) analyzed the hydrodynamic properties of semi-submersible and vessel-shaped offshore aquaculture structures using SIMO, based on linear potential theory. While these experiments offer controllable conditions for reliable dynamic analysis, the dynamic behavior of a full-scale fish cage is still largely unclear from a quantitative point of view (Klebert *et al.*, 2013; Ruzzo *et al.*, 2021). It is mainly due to that the influence of Reynolds number is often non-negligible in the scaling process using the Froude laws. A detailed discussion can be found in the article (Ruzzo *et al.*, 2021). Thus, advanced numerical tools are essential in the design process to understand the structural responses of the full-scale OAS.

7.1 Introduction

In order to understand the dynamic responses of OAS under the action of currents and waves, a numerical model of an OAS is developed in this chapter for dynamic analyses in the time domain. In addition, the submodule in UiS-Aqua, *enviromentModules*, is invoked in this chapter to generate irregular waves. A validation study is first carried out to test the accuracy of the newly developed OAS numerical model, and then the dynamic responses of the OAS are analyzed under the action of irregular waves and currents.

7 Application to offshore aquaculture structure

7.2 Description of the offshore aquaculture structure

The validation data for the present numerical model is from the physical model (see Figure 7-2), similar to Ocean Farm 1, consisting of the primary frame, net, weight, and mooring systems. The experiments were performed with a 1:120 model scale under regular wave conditions. The numerical model (see Figure 7-3) in the present study is reproduced according to the physical model by Zhao *et al.* (2019). The detailed parameters of the numerical model are presented in Table 7-1. All results are presented in model scale hereafter, unless otherwise indicated.

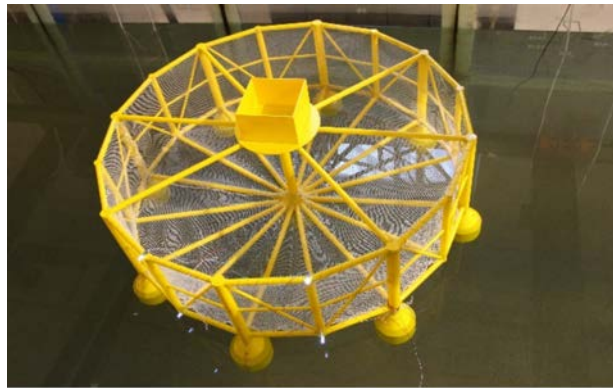


Figure 7-2. Physical model of the OAS by Zhao *et al.* (2019).

7.2 Description of the offshore aquaculture structure

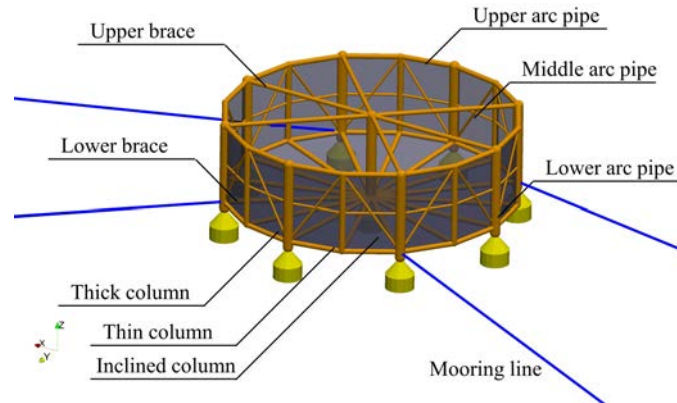


Figure 7-3. Numerical model of the OAS in the present study.

Table 7-1. The main parameters of the OAS model.

Component	Length (cm)	Diameter (mm)	Thickness (mm)
Thick column	30	30	2.5
Thin column	28	20	3.1
Inclined column	30	8	2.1
Upper arc pipe	20	16	2.3
Middle arc pipe	20	8	2.1
Lower arc pipe	20	16	2.3
Upper brace	50	16	2.3
Lower brace	50	16	2.3
Mooring line	4.2	1	-

7.3 Validation of the numerical model

7.3.1 Free decay test

A free decay test is usually conducted at the first step of the dynamic simulations. The information about the natural periods and the damping levels can be used to calibrate the present numerical model. However, according to the experiments by Zhao *et al.* (2019), the free decay test is not conducted. Thus, the experimental results from Jin *et al.* (2021), in which the physical model is also similar to Ocean Farm 1, are converted to the present model scale, in order to calibrate the present numerical model.

In the numerical model, the mass is assumed uniformly distributed along with the frames, and two different draughts are reached by adjusting the total mass. The calculated natural periods are present in Table 7-2, and the heave responses in the free decay test are plotted in Figure 7-4. The results in Table 7-2 indicate that the natural period of heave motion increases with the increasing draught, which is physically sound, according to Næss and Moan (2013). As shown in Figure 7-4, the present numerical model and the physical model from Jin *et al.* (2021) have a similar natural period of heave motion and damping level, which confirms that the numerical model is correctly built in this section.

Table 7-2. Natural periods of the present numerical model under different draught conditions.

Draught (cm)	28	36
Total mass (kg)	10.29	11.06
Heave (s)	2.049	2.104

7.3 Validation of the numerical model

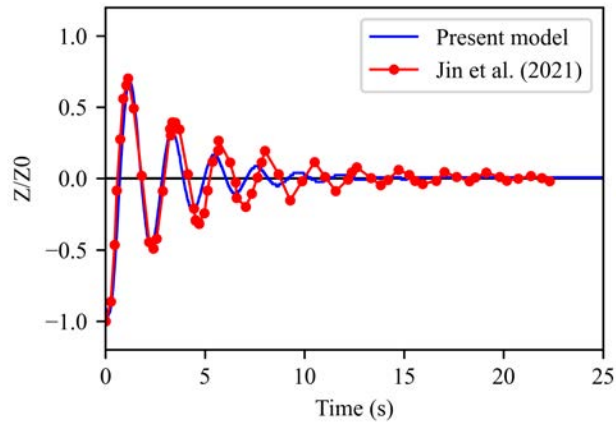


Figure 7-4. Free decay tests for the OAS model.

7.3.2 Dynamic responses under pure wave conditions

The validation simulations are conducted under regular wave conditions that are taken from the experiment by Zhao *et al.* (2019). Six cross-combinations with three wave periods (1.0s, 1.2 and 1.4s) and two draughts (28 cm and 36 cm) are employed as the environmental conditions. The wave height is 10 cm, and there is no current for all the experimental conditions. Figure 7-5 shows the numerical setup for the simulations under regular wave conditions, where the wave direction is towards X+.

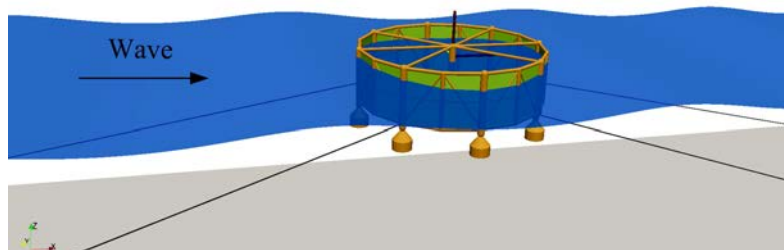


Figure 7-5. Numerical setup for the simulation of the OAS in waves.

7 Application to offshore aquaculture structure

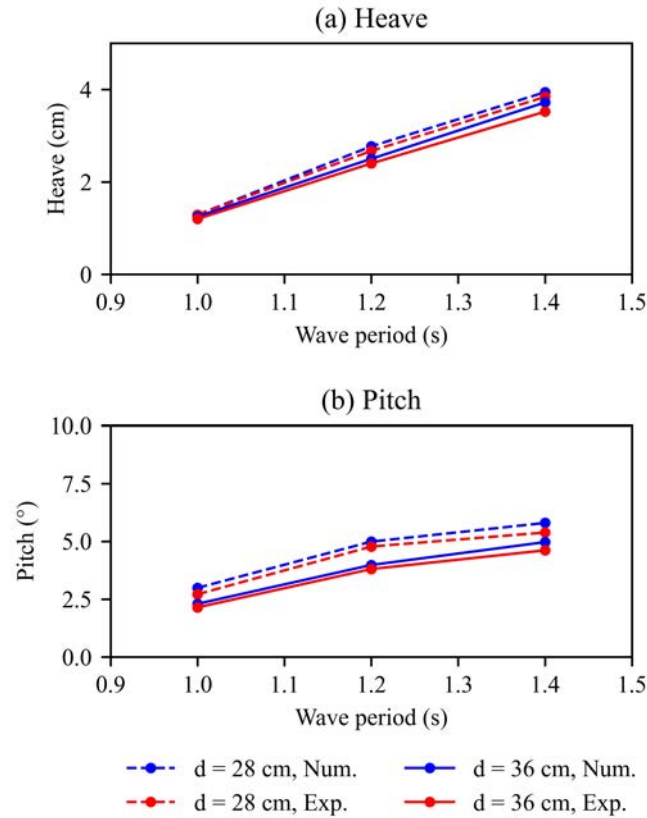


Figure 7-6. Comparison of the hydrodynamic responses between the numerical and experimental values. Exp. represents the experimental values from Zhao *et al.* (2019). Num. represents the numerical results in the present study.

As shown in Figure 7-6, increasing the draught can reduce the amplitudes of heave and pitch motions. The reason might be that when the draught increases, the water particle velocity and the influence of waves will decrease around the pontoon, causing the force on the bottom of the OAS model to decrease. Thus, the global hydrodynamic responses of the structure will decrease with the increasing draught. In addition, Figure 7-6 indicates that the amplitudes of heave and pitch motion are

7.3 Validation of the numerical model

nearly proportional to the wave period for the two draughts, which is also observed in the experimental and numerical analyses by Liu *et al.* (2020).

Figure 7-7 shows the time series of the tension force in mooring lines when the wave height is 10 cm, the wave period is 1.4 s and the draught is 36 cm. The mooring line tension in the pure waves is calculated with the subtraction of the pre-tension. It is observed that the predicted tension forces are generally close to the experimental results reported by Zhao *et al.* (2019). The relative difference for the extreme tension force is 10.5%. The maximum motion responses of the fish farm with different wave periods and draughts are shown in Figure 7-6. The maximum relative difference of the heave and pitch motions are 7.5 and 11.5% compared with the experimental results from Zhao *et al.* (2019), respectively. These differences between the numerical and experimental results may be due to that the influence from the movement of the structure on the wave field is not considered in the present model.

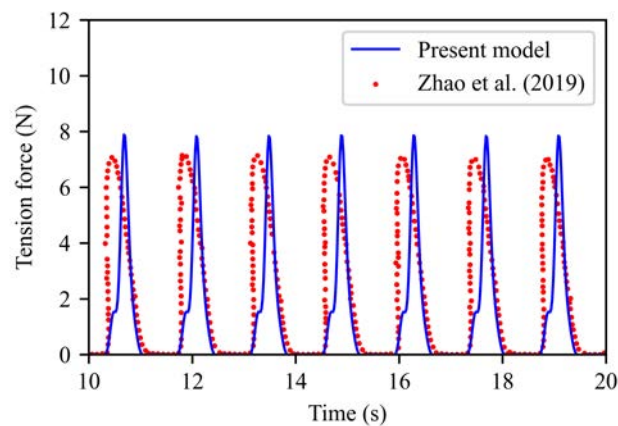


Figure 7-7. Time-series results for the mooring line tensions.

7.4 Application in irregular waves and currents

In order to better understand the global responses of the OAS under a condition close to a real offshore site, additional simulations are conducted under irregular waves and current conditions. The environmental conditions from the field measurements by Bore and Amdahl (2017) at an offshore aquaculture site are employed in the present application. Figure 7-8 shows the environmental contour lines at the considered location. The irregular waves are described by the significant wave height (H_s) and the spectral peak period (T_p), and the JONSWAP spectrum with a peak enhancement factor depending on H_s and T_p are applied in the simulations. The combination of H_s and T_p are selected from the contour lines described sea states with a probability of exceedance corresponding to a return period of 50 years, according to Bore and Amdahl (2017). The current (U_c) is assumed uniform over the water depth, and the current direction is the same with wave direction. The value of U_c is also corresponding to a return period of 50 years based on the deterministic method in NS 9415 (2009). Additionally, simulations without current and without nets are conducted to investigate the influence of the current and the nets on the motion of the structure, respectively. A summary of the environmental conditions for applications is shown in Table 7-3, where the values of H_s , T_p and U_c are given in the model scale. The draught is 36 cm in the six environmental conditions.

7.4 Application in irregular waves and currents

Table 7-3. Summary of the environmental conditions.

EC no.	H_s (cm)	T_p (s)	U_c (cm/s)	Nets
EC1	3.67	1.05	9.22	Included
EC2	3.67	1.29	9.22	Included
EC3	3.67	1.05	0	Included
EC4	3.67	1.29	0	Included
EC5	3.67	1.05	9.22	Excluded
EC6	3.67	1.29	9.22	Excluded

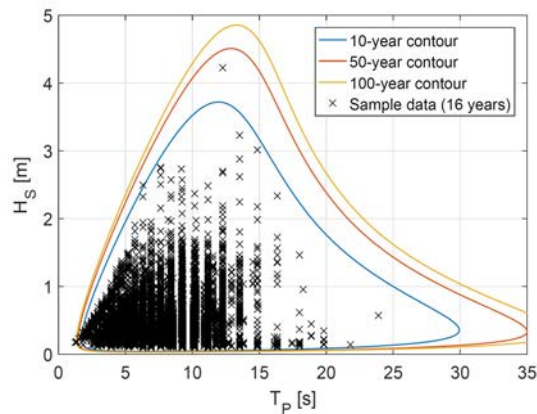


Figure 7-8. Environmental contour lines at the considered location (Bore and Amdahl, 2017).

Figure 7-10 shows the selected time-series results of the wave elevation, structural motions (including surge, heave and pitch), and tension forces in the mooring lines. It can be observed that the mean values of the structural motions and tension forces are nonzero. The statistics for the motions and tension forces are given in Table 7-4. For the surge motion, a mean drift is generated due to the current loads. Due to the restrictions of mooring lines, the mean horizontal movement is only 1/25 of that using catenary mooring lines (Jin *et al.*, 2020). For the

7 Application to offshore aquaculture structure

heave motion, it can be observed that the vertical movement of the structure is restricted by the pre-tensioned mooring lines. Due to the large stiffness of the mooring lines, the structure can hardly move higher than its initial position. Thus, the heave motion of this model may be different from that using catenary mooring lines (Jin *et al.*, 2020). For the pitch motion, the mean value of pitch is -1.1° . This negative pitch motion is shown in Figure 7-9. Due to the relatively large project area of the pontoon, the current loads on the bottom of the OAS model are larger than those on the top. Thus, a negative torque is generated, and this negative torque causes a negative mean pitch angle. For the tension forces, the mean tension force in the windward mooring lines is larger than that in the leeward mooring lines. This is caused by the current loads. In addition, Figure 7-10(e) indicates that all the mooring lines are under tension.

Table 7-4. Mean values, standard deviations and maximum values of structural motions and tension forces in mooring lines under EC1.

	Mean	Std.	Max.
Surge	0.75 cm	0.38 cm	-
Heave	-0.26 cm	0.33 cm	-
Pitch	-1.1°	0.49°	-
Windward mooring line	4.00 N	0.54 N	6.62 N
Leeward mooring line	1.77 N	0.66 N	4.32 N

7.4 Application in irregular waves and currents

Time : 149.18 s

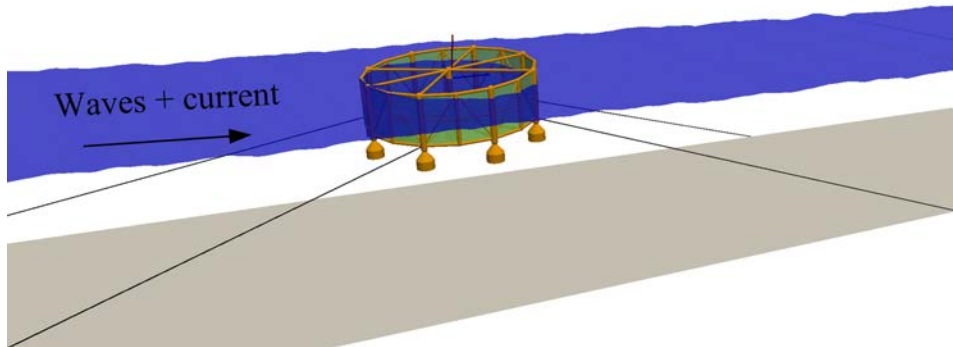


Figure 7-9. An instantaneous state of the OAS model under EC1.

7 Application to offshore aquaculture structure

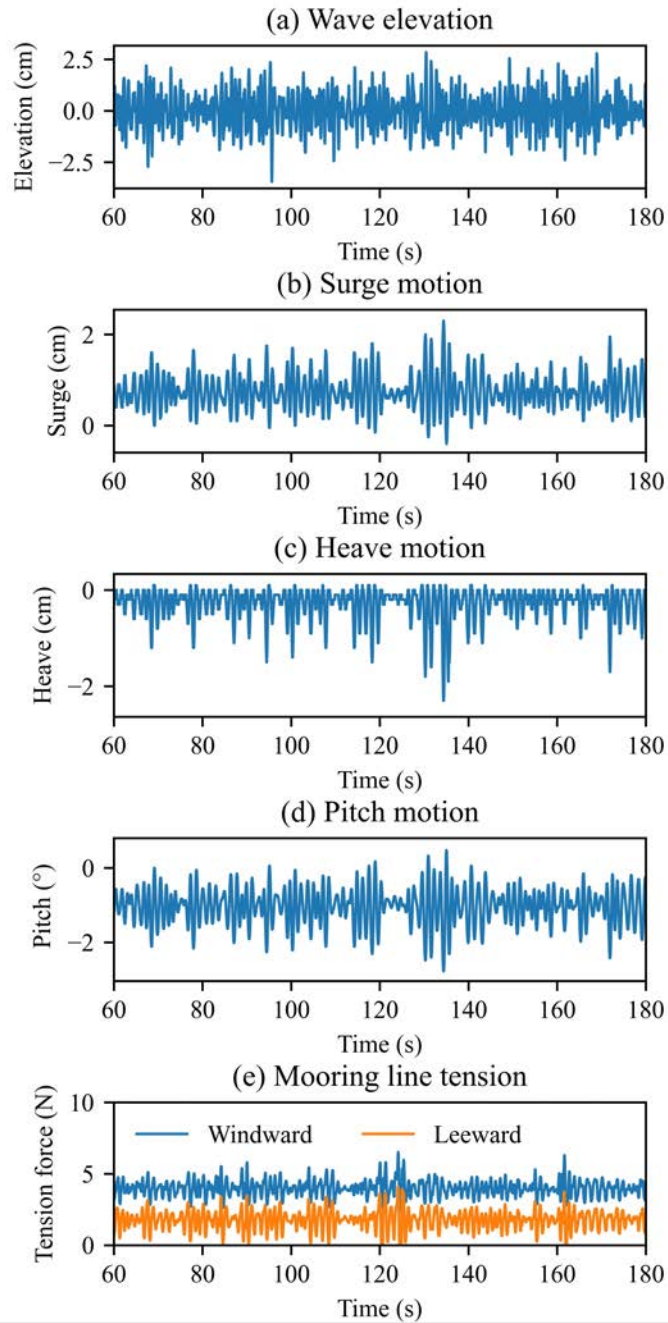


Figure 7-10. Selected time-series results for the OAS model in under EC1.

Figure 7-11 ~ Figure 7-13 present the structural motions and tension forces under the six environmental conditions in Table 7-3. The mean values are represented by the heights of bar, and the standard deviations are represented by the error bars. The influence of different T_p , with/without current and with/without nets will be discussed based on these figures.

As shown in Figure 7-11, the mean values and standard deviations of surge motion slightly increase with the increasing T_p , because the wave drift forces acting on nets increase with the increasing wave periods according to the research by Zhao *et al.* (2011). The current causes a clear influence on the surge motion. The mean values of the surge are close to zero when there is no current. The existence of nets also has a clear influence on the surge motion. When the nets are removed from the model, a large part of the environmental loads on the structure is reduced. Therefore, the mean values of surge motion are reduced. However, since the significant damping effect of the nets also disappear with the removal of the nets from the model, the standard deviation of surge motion increases.

Figure 7-12 shows the mean values and standard deviation of pitch motions under EC1 ~ EC6. The influence of different T_p , with/without current and with/without nets on the pitch motions can be interpreted in a similar way as with surge motions. The different T_p has a negligible influence on the mean values of pitch, which indicates that the current loads dominate the mean value of pitch motions.

7 Application to offshore aquaculture structure

As shown in Figure 7-13, the mean values and standard deviations of the tension force in all the mooring lines increase with the increasing T_p . When the current is included in the numerical simulations, the mean values of the tension force in the windward mooring lines are significantly larger than those in the leeward mooring lines. However, the mean values of the tension force in all the mooring lines are almost the same when the current is not included. The reasons for these are the same as the interpretation given in Figure 7-11.

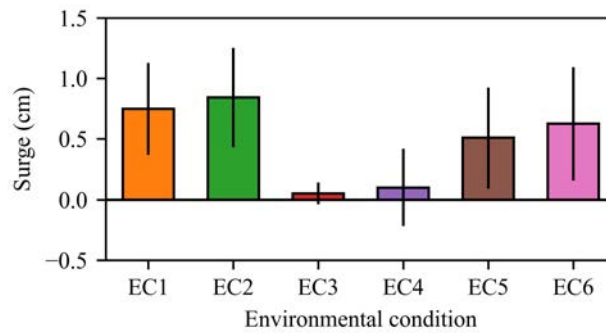


Figure 7-11. Mean values and standard deviations of surge motions under different environmental conditions.

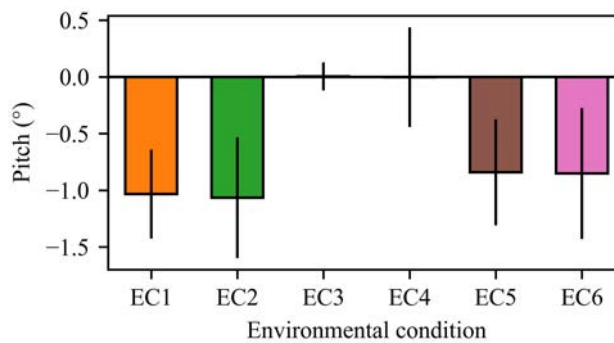


Figure 7-12. Mean values and standard deviations of pitch motions under different environmental conditions.

7.4 Application in irregular waves and currents

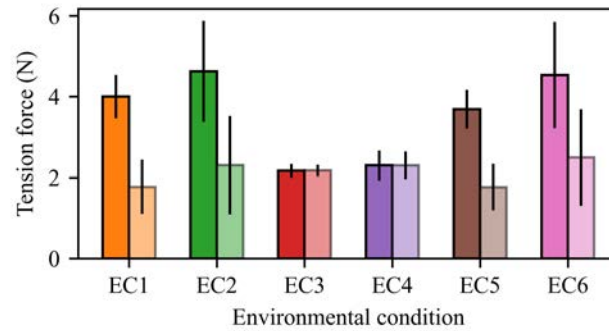


Figure 7-13. Mean values and standard deviations of tension forces in mooring line under different environmental conditions. The tension forces in the windward and leeward mooring lines are represented by dark and light colors, respectively.

7.5 Conclusions

In this chapter, a new numerical model is developed for modelling the global responses of offshore aquaculture structures in waves and current. The dynamic analyses are carried out under the framework of Code_aster with the implementation of UiS-Aqua. Reasonable agreements with published experimental results demonstrate the accuracy of the present model. Moreover, the dynamic responses of a semi-submersible offshore aquaculture structure under irregular waves and current conditions are investigated thoroughly. For the studied model, a relatively small vertical motion is observed. However, the mean horizontal motion caused by the current loads is large. A negative mean pitch angle is observed when the current is included in the simulations.

7.5 Conclusions

8 Conclusions and future work

8.1 Conclusions

This thesis comprehensively investigates dynamic responses of different marine aquaculture structures, including traditional fish cages, grid moored fish farms and a large semi-submersible aquaculture structure, under the action of currents and waves. The main conclusions of this thesis are summarized as follows:

- (1) For modelling the hydrodynamic loads on nets, the Morison model has a significant defect compared to the Screen model. Since the Morison model does not include the twine-to-twine wake effect, the hydrodynamic loads on a net panel can be overestimated when the inflow angle is large. This will make the dynamic analyses inaccurate and unreliable for the structural design.
- (2) The engineering approach provided by Løland (1991) is insufficient to address the changes in the flow field around a fish cage. As shown in Section 4.6, the existence of nets can affect both the magnitude and direction of the water flow. However, the engineering approach only approximates the wake effect as a flow velocity reduction without considering the direction changes.
- (3) A new wake model is proposed to address the net-to-net wake effect inside fish cages. With the help of this new wake model, the discrepancy between the predicted and experimental drag loads on a fish cage can be reduced from 30% to 5%.

8.1 Conclusions

- (4) For the designs of traditional fish cages, a stout fish cage, no matter square or circular shape, can efficiently use the netting and provide a larger cultivation volume than a slim fish cage, when the two cages use the same amount of netting and weight under the same strong current condition ($U > 0.4$ m/s). Thus, increasing circumference is more effective than increasing the depth of net bag to improve the cultivation volume.
- (5) During in-situ operations in a fish farm, when one of the mooring lines in a fish farm breaks, the maximum increment of tension in the mooring system has a strong positive correlation with the movement of buoys. Based on the displacement of buoys, the maximum tension increment in the mooring system can be estimated, and the position of breakage can be located.
- (6) The UiS-Aqua can be applied to dynamic analyses of offshore aquaculture structures. The numerical model shows good agreements with published experimental results. When the studied structure is under the environmental conditions corresponding to a return period of 50 years, the structure will have a relatively small vertical motion (standard deviation = 0.4 m) and a negative mean pitch angle (mean value = -1.1°).

8.2 Recommendations for the future work

(1) Improve the computational efficiency

In this thesis, the structural responses are calculated by a FEM program, which has an abundant element library and can be applied to many engineering questions. However, the standard FEM program is not fast enough to conduct real-time simulations of marine aquaculture structures. Different spatial discretization techniques, such as lumped mass method, can be considered in the future development to improve the calculation speed. In addition, different time integration methods, such as the Verlet algorithm, can also be included in the future development.

(2) Extend the code for wider industrial usages

The Code_Aster, together with UiS-Aqua, can be utilized to investigate dynamic motions of many other marine structures, such as wave buoy, wind turbine, floating barge and various fishing gears. In order to meet the industrial usages, a user-friendly Graphical User Interface (GUI) needs to be developed. In addition, numerical models for the commonly used marine structures are also required further developments and validations for the industry.

(3) High-quality experimental data for hydrodynamic characteristics of different nets

The hydrodynamic characteristics of nets are one of the most critical inputs for dynamic analyses of marine aquaculture structures. These characteristics usually come from a series of well-designed and well-

8.2 Recommendations for the future work

documented experiments that approximate the ideal conditions of a finite net panel in an infinite flow field. The experimental conditions and measurements, such as net materials, mesh shapes, twine shapes, net weaving methods, twine roughness, net solidities under submerged conditions, water flow turbulence intensities and water temperatures, should be documented in the future work.

References

- Aarsnes, J.V., Rudi, H., Løland, G., 1990. Current forces on cage, net deflection. Engineering for offshore fish farming. Proceedings of a conference organised by the Institution of Civil Engineers, Glasgow, UK, 17-18 October 1990. 137–152.
- AKVA Group, 2020. Pen Farming Aquaculture Catalogue (English).
- Alver, M.O., Skøien, K.R., Føre, M., Aas, T.S., Oehme, M., Alfredsen, J.A., 2016. Modelling of surface and 3D pellet distribution in Atlantic salmon (*Salmo salar* L.) cages. *Aquacultural Engineering* 72–73, 20–29. <https://doi.org/10.1016/j.aquaeng.2016.03.003>
- Antonutti, R., Peyrard, C., Incecik, A., Ingram, D., Johanning, L., 2018. Dynamic mooring simulation with Code_Aster with application to a floating wind turbine. *Ocean Engineering* 151, 366–377. <https://doi.org/10.1016/j.oceaneng.2017.11.018>
- Arnold, D.N., Logg, A., 2014. Periodic Table of the Finite Elements. *SIAM News* 47(9).
- Aryai, V., Abbassi, R., Abdussamie, N., Salehi, F., Garaniya, V., Asadnia, M., Baksh, A.-A., Penesis, I., Karampour, H., Draper, S., Magee, A., Keng, A.K., Shearer, C., Sivandran, S., Yew, L.K., Cook, D., Underwood, M., Martini, A., Heasman, K., Abrahams, J., Wang, C.-M., 2021. Reliability of multi-purpose offshore-facilities: Present status and future direction in Australia. *Process Safety and Environmental Protection* 148, 437–461. <https://doi.org/10.1016/j.psep.2020.10.016>
- Aubry, J.-P., 2019. Beginning with Code_Aster: a practical introduction to finite element method using Code_Aster Gmsh and Salome ; Version 2.1.2.
- Balash, C., Colbourne, B., Bose, N., Raman-Nair, W., 2009. Aquaculture Net Drag Force and Added Mass. *Aquacultural*

- Engineering 41, 14–21.
<https://doi.org/10.1016/j.aquaeng.2009.04.003>
- Berstad, A.J., Heimstad, L.F., Walaunet, J., 2014. Model Testing of Fish Farms for Validation of Analysis Programs. Presented at the ASME 2014 33rd International Conference on Ocean, Offshore and Arctic Engineering, American Society of Mechanical Engineers Digital Collection. <https://doi.org/10.1115/OMAE2014-24647>
- Berstad, A.J., Tronstad, H., Sivertsen, S.-A., Leite, E., 2008. Enhancement of Design Criteria for Fish Farm Facilities Including Operations. Presented at the ASME 2005 24th International Conference on Offshore Mechanics and Arctic Engineering, American Society of Mechanical Engineers Digital Collection, pp. 825–832. <https://doi.org/10.1115/OMAE2005-67451>
- Berstad, A.J., Tronstad, H., Ytterland, A., 2004. Design Rules for Marine Fish Farms in Norway: Calculation of the Structural Response of Such Flexible Structures to Verify Structural Integrity, in: 23rd International Conference on Offshore Mechanics and Arctic Engineering, Volume 3. Presented at the ASME 2004 23rd International Conference on Offshore Mechanics and Arctic Engineering, ASMEDC, Vancouver, British Columbia, Canada, pp. 867–874. <https://doi.org/10.1115/OMAE2004-51577>
- Berstad, A.J., Walaunet, J., Heimstad, L.F., 2013. Loads From Currents and Waves on Net Structures. Presented at the ASME 2012 31st International Conference on Ocean, Offshore and Arctic Engineering, American Society of Mechanical Engineers Digital Collection, pp. 95–104. <https://doi.org/10.1115/OMAE2012-83757>
- Bessonneau, J.S., Marichal, D., 1998. Study of the dynamics of submerged supple nets (applications to trawls). Ocean Engineering 25, 563–583. [https://doi.org/10.1016/S0029-8018\(97\)00035-8](https://doi.org/10.1016/S0029-8018(97)00035-8)

- Beveridge, M.C.M., 2004. Cage aquaculture, 3rd ed. ed. Oxford, UK : Blackwell Pub. ; Ames, Iowa.
- Bi, C.-W., Xu, T.-J., 2018. Numerical study on the flow field around a fish farm in tidal current. *Turk. J. Fish. Aquat. Sci.* 18.
https://doi.org/10.4194/1303-2712-v18_5_06
- Bi, C.-W., Zhao, Y.-P., Dong, G.-H., 2020a. Experimental study on the effects of farmed fish on the hydrodynamic characteristics of the net cage. *Aquaculture* 524, 735239.
<https://doi.org/10.1016/j.aquaculture.2020.735239>
- Bi, C.-W., Zhao, Y.-P., Dong, G.-H., Cui, Y., Gui, F.-K., 2015. Experimental and numerical investigation on the damping effect of net cages in waves. *Journal of Fluids and Structures* 55, 122–138.
<https://doi.org/10.1016/j.jfluidstructs.2015.02.010>
- Bi, C.-W., Zhao, Y.-P., Dong, G.-H., Wu, Z.-M., Zhang, Y., Xu, T.-J., 2018. Drag on and flow through the hydroid-fouled nets in currents. *Ocean Engineering* 161, 195–204.
<https://doi.org/10.1016/j.oceaneng.2018.05.005>
- Bi, C.-W., Zhao, Y.-P., Dong, G.-H., Xu, T.-J., Gui, F.-K., 2014a. Numerical simulation of the interaction between flow and flexible nets. *Journal of Fluids and Structures* 45, 180–201.
<https://doi.org/10.1016/j.jfluidstructs.2013.11.015>
- Bi, C.-W., Zhao, Y.-P., Dong, G.-H., Xu, T.-J., Gui, F.-K., 2013. Experimental investigation of the reduction in flow velocity downstream from a fishing net. *Aquacultural Engineering* 57, 71–81. <https://doi.org/10.1016/j.aquaeng.2013.08.002>
- Bi, C.-W., Zhao, Y.-P., Dong, G.-H., Zheng, Y.-N., Gui, F.-K., 2014b. A numerical analysis on the hydrodynamic characteristics of net cages using coupled fluid–structure interaction model. *Aquacultural Engineering* 59, 1–12.
<https://doi.org/10.1016/j.aquaeng.2014.01.002>

- Bi, C.-W., Zhao, Y.-P., Sun, X.-X., Zhang, Y., Guo, Z.-X., Wang, B., Dong, G.-H., 2020b. An efficient artificial neural network model to predict the structural failure of high-density polyethylene offshore net cages in typhoon waves. *Ocean Engineering* 196, 106793. <https://doi.org/10.1016/j.oceaneng.2019.106793>
- Blevins, R.D., 1984. *Applied Fluid Dynamics Handbook*. Van Nostrand Reinhold Company.
- Bondevik, H.L., 2019. *Fish Escape and Models to Assess Influential Factors* (Master Thesis). Norwegian University of Science and Technology, Trondheim, Norway.
- Bore, P.T., Amdahl, J., 2017. Determination of Environmental Conditions Relevant for the Ultimate Limit State at an Exposed Aquaculture Location. Presented at the ASME 2017 36th International Conference on Ocean, Offshore and Arctic Engineering, American Society of Mechanical Engineers Digital Collection. <https://doi.org/10.1115/OMAE2017-61413>
- Bos, W.J.T., 2020. Production and dissipation of kinetic energy in grid turbulence. *Phys. Rev. Fluids* 5, 104607. <https://doi.org/10.1103/PhysRevFluids.5.104607>
- Brizzi, G., Sabbagh, M., 2021. A new criterion for multi-purpose platforms siting: Fish endurance to wave motion within offshore farming cages. *Ocean Engineering* 224, 108751. <https://doi.org/10.1016/j.oceaneng.2021.108751>
- Buck, B.H., Langan, R. (Eds.), 2017. *Aquaculture Perspective of Multi-Use Sites in the Open Ocean*. Springer International Publishing, Cham. <https://doi.org/10.1007/978-3-319-51159-7>
- Cardia, F., Lovatelli, A., 2015. *Aquaculture operations in floating HDPE cages: a field handbook*. Food and Agriculture Organization of the United States, Rome.

- Cha, B.-J., Lee, C.-W., 2002. Dynamic Simulation of a Midwater Trawl System's Behavior. *Fisheries science* 68, 1865–1868.
https://doi.org/10.2331/fishsci.68.sup2_1865
- Cha, B.-J., Lee, G.-H., 2018. Performance of a model fish cage with copper-alloy net in a circulating water channel and wave tank. *Ocean Engineering* 151, 290–297.
<https://doi.org/10.1016/j.oceaneng.2018.01.053>
- Chen, D., Wang, C.M., Zhang, H., 2021. Examination of net volume reduction of gravity-type open-net fish cages under sea currents. *Aquacultural Engineering* 92, 102128.
<https://doi.org/10.1016/j.aquaeng.2020.102128>
- Chen, H., Christensen, E.D., 2017. Development of a numerical model for fluid-structure interaction analysis of flow through and around an aquaculture net cage. *OCEAN ENG* 142, 597–615.
<https://doi.org/10.1016/j.oceaneng.2017.07.033>
- Chen, H., Christensen, E.D., 2016. Investigations on the porous resistance coefficients for fishing net structures. *Journal of Fluids and Structures* 65, 76–107.
<https://doi.org/10.1016/j.jfluidstructs.2016.05.005>
- Cheng, H., 2017. Study on the anti-current characteristics of a new type gravity fish cage and design optimising (Master Thesis). Ocean University of China, Qingdao, China.
- Cheng, H., Aarsæther, K.G., Li, L., Ong, M.C., 2020a. Numerical Study of a Single-Point Mooring Gravity Fish Cage with Different Deformation-Suppression Methods. *Journal of Offshore Mechanics and Arctic Engineering* 142, 041301.
<https://doi.org/10.1115/1.4046115>
- Cheng, H., Huang, L., Ni, Y., Xu, Q., Zhao, F., Wang, X., Liang, Z., 2018a. Numerical and Experimental Study of SPM Fish Cage: Comparison and Validation, in: Volume 7B: Ocean Engineering.

- Presented at the ASME 2018 37th International Conference on Ocean, Offshore and Arctic Engineering, American Society of Mechanical Engineers, Madrid, Spain, p. V07BT06A053.
<https://doi.org/10.1115/OMAE2018-78204>
- Cheng, H., Huang, L., Ni, Y., Zhao, F., Wang, X., Tang, Y., Liang, Z., 2018b. Study on the Flow Characteristics of Rope and Cylinder With Large-Eddy Simulation, in: Volume 7A: Ocean Engineering. Presented at the ASME 2018 37th International Conference on Ocean, Offshore and Arctic Engineering, American Society of Mechanical Engineers, Madrid, Spain, p. V07AT06A029.
<https://doi.org/10.1115/OMAE2018-78212>
- Cheng, H., Li, L., Aarsæther, K.G., Ong, M.C., 2020b. Typical hydrodynamic models for aquaculture nets: A comparative study under pure current conditions. *Aquacultural Engineering* 90, 102070. <https://doi.org/10.1016/j.aquaeng.2020.102070>
- Cheng, H., Li, L., Ong, M.C., Aarsæther, K.G., Sim, J., 2021. Effects of mooring line breakage on dynamic responses of grid moored fish farms under pure current conditions. *Ocean Engineering* 237, 109638. <https://doi.org/10.1016/j.oceaneng.2021.109638>
- Cheng, H., Ong, M.C., Li, L., Chen, H., 2022. Development of a coupling algorithm for fluid-structure interaction analysis of submerged aquaculture nets. *Ocean Engineering* 243, 110208. <https://doi.org/10.1016/j.oceaneng.2021.110208>
- Chu, Y.I., Wang, C.M., Park, J.C., Lader, P.F., 2020. Review of cage and containment tank designs for offshore fish farming. *Aquaculture* 519, 734928.
<https://doi.org/10.1016/j.aquaculture.2020.734928>
- Costello, C., Cao, L., Gelcich, S., Cisneros-Mata, M.Á., Free, C.M., Froehlich, H.E., Golden, C.D., Ishimura, G., Maier, J., Macadam-Somer, I., Mangin, T., Melnychuk, M.C., Miyahara, M., de Moor, C.L., Naylor, R., Nøstbakken, L., Ojea, E., O'Reilly, E., Parma,

- A.M., Plantinga, A.J., Thilsted, S.H., Lubchenco, J., 2020. The future of food from the sea. *Nature* 588, 95–100.
<https://doi.org/10.1038/s41586-020-2616-y>
- Davis, K.F., Gephart, J.A., Emery, K.A., Leach, A.M., Galloway, J.N., D’Odorico, P., 2016. Meeting future food demand with current agricultural resources. *Global Environmental Change* 39, 125–132.
<https://doi.org/10.1016/j.gloenvcha.2016.05.004>
- de Tullio, M.D., Pascazio, G., 2016. A moving-least-squares immersed boundary method for simulating the fluid–structure interaction of elastic bodies with arbitrary thickness. *Journal of Computational Physics* 325, 201–225. <https://doi.org/10.1016/j.jcp.2016.08.020>
- DeCew, J., 2011. Development of engineering tools to analyze and design flexible structures in open ocean environments. Doctoral Dissertations.
- DeCew, J., Tsukrov, I., Risso, A., Swift, M.R., Celikkol, B., 2010. Modelling of dynamic behavior of a single-point moored submersible fish cage under currents. *Aquacultural Engineering* 43, 38–45. <https://doi.org/10.1016/j.aquaeng.2010.05.002>
- DNV GL, 2018. Aquaculture going offshore- seizing the opportunity, managing the risk.
- Dong, S., You, X., Hu, F., 2021. Experimental investigation on the fluid–structure interaction of a flexible net cage used to farm Pacific bluefin tuna (*Thunnus orientalis*). *Ocean Engineering* 226, 108872. <https://doi.org/10.1016/j.oceaneng.2021.108872>
- Drach, A., Tsukrov, I., DeCew, J., Celikkol, B., 2016. Engineering procedures for design and analysis of submersible fish cages with copper netting for exposed marine environment. *Aquacultural Engineering* 70, 1–14.
<https://doi.org/10.1016/j.aquaeng.2015.11.001>

- Edwards, P., 2015. Aquaculture environment interactions: Past, present and likely future trends. *Aquaculture* 447, 2–14.
<https://doi.org/10.1016/j.aquaculture.2015.02.001>
- Electricité de France (EDF), 1989. Finite Element Code_Aster, Analysis of Structures and Thermomechanics for Studies and Research.
- Endresen, P.C., Birkevold, J., Føre, M., Fredheim, A., Kristiansen, D., Lader, P., 2014. Simulation and Validation of a Numerical Model of a Full Aquaculture Net-Cage System, in: Volume 7: Ocean Space Utilization; Professor Emeritus J. Randolph Paulling Honoring Symposium on Ocean Technology. Presented at the ASME 2014 33rd International Conference on Ocean, Offshore and Arctic Engineering, American Society of Mechanical Engineers, San Francisco, California, USA, p. V007T05A006.
<https://doi.org/10.1115/OMAE2014-23382>
- Endresen, P.C., Føre, M., Fredheim, A., Kristiansen, D., Enerhaug, B., 2013. Numerical Modelling of Wake Effect on Aquaculture Nets, in: Volume 3: Materials Technology; Ocean Space Utilization. Presented at the ASME 2013 32nd International Conference on Ocean, Offshore and Arctic Engineering, American Society of Mechanical Engineers, Nantes, France, p. V003T05A027.
<https://doi.org/10.1115/OMAE2013-11446>
- Endresen, P.C., Klebert, P., 2020. Loads and response on flexible conical and cylindrical fish cages: A numerical and experimental study based on full-scale values. *Ocean Engineering* 216, 107672.
<https://doi.org/10.1016/j.oceaneng.2020.107672>
- Enerhaug, B., Føre, M., Endresen, P.C., Madsen, N., Hansen, K., 2012. Current Loads on Net Panels with Rhombic Meshes, in: Volume 7: Ocean Space Utilization; Ocean Renewable Energy. Presented at the ASME 2012 31st International Conference on Ocean, Offshore and Arctic Engineering, American Society of Mechanical

- Engineers, Rio de Janeiro, Brazil, pp. 49–60.
<https://doi.org/10.1115/OMAE2012-83394>
- Faltinsen, O.M., Shen, Y., 2018. Wave and Current Effects on Floating Fish Farms. *J. Marine. Sci. Appl.* 17, 284–296.
<https://doi.org/10.1007/s11804-018-0033-5>
- FAO, 2020. The State of World Fisheries and Aquaculture 2020: Sustainability in action, The State of World Fisheries and Aquaculture (SOFIA). FAO, Rome, Italy.
<https://doi.org/10.4060/ca9229en>
- FAO, 1984. Inland Aquaculture Engineering: Lectures Presented at the ADCP Inter-regional Training Course in Inland Aquaculture Engineering, Budapest, 6 June-3 September 1983. Food & Agriculture Org.
- FAO, IFAD, UNICEF, WFP, WHO, 2020. The State of Food Security and Nutrition in the World 2020, Transforming food systems for affordable healthy diets. FAO, IFAD, UNICEF, WFP and WHO.
<https://doi.org/10.4060/ca9692en>
- Févotte, F., Lathuilière, B., 2017. Studying the Numerical Quality of an Industrial Computing Code: A Case Study on Code_aster, in: Abate, A., Boldo, S. (Eds.), *Numerical Software Verification, Lecture Notes in Computer Science*. Springer International Publishing, Cham, pp. 61–80. https://doi.org/10.1007/978-3-319-63501-9_5
- Føre, M., Frank, K., Norton, T., Svendsen, E., Alfredsen, J.A., Dempster, T., Eguiraun, H., Watson, W., Stahl, A., Sunde, L.M., Schellewald, C., Skøien, K.R., Alver, M.O., Berckmans, D., 2018. Precision fish farming: A new framework to improve production in aquaculture. *Biosystems Engineering, Advances in the Engineering of Sensor-based Monitoring and Management Systems for Precision Livestock Farming* 173, 176–193.
<https://doi.org/10.1016/j.biosystemseng.2017.10.014>

- Fredheim, A., Reve, T., 2018. Future Prospects of Marine Aquaculture, in: OCEANS 2018 MTS/IEEE Charleston. Presented at the OCEANS 2018 MTS/IEEE Charleston, pp. 1–8.
<https://doi.org/10.1109/OCEANS.2018.8604735>
- Fredriksson, D.W., DeCew, J., Lader, P., Volent, Z., Jensen, Ø., Willumsen, F.V., 2014. A finite element modelling technique for an aquaculture net with laboratory measurement comparisons. *Ocean Engineering* 83, 99–110.
<https://doi.org/10.1016/j.oceaneng.2014.03.005>
- Frenkiel, F.N., Klebanoff, P.S., Huang, T.T., 1979. Grid turbulence in air and water. *The Physics of Fluids* 22, 1606–1617.
<https://doi.org/10.1063/1.862820>
- Fridman, A.L., 1973. Theory and Design of Commercial Fishing Gear. Israel Program for Scientific Translations.
- Froehlich, H.E., Gentry, R.R., Halpern, B.S., 2018. Global change in marine aquaculture production potential under climate change. *Nat Ecol Evol* 2, 1745–1750. <https://doi.org/10.1038/s41559-018-0669-1>
- Gansel, L.C., McClimans, T.A., Myrhaug, D., 2012. The Effects of Fish Cages on Ambient Currents. *J. Offshore Mech. Arct. Eng* 134.
<https://doi.org/10.1115/1.4003696>
- Gansel, L.C., Oppedal, F., Birkevold, J., Tuene, S.A., 2018. Drag forces and deformation of aquaculture cages—Full-scale towing tests in the field. *Aquacultural Engineering* 81, 46–56.
<https://doi.org/10.1016/j.aquaeng.2018.02.001>
- Gijón Mancheño, A., Jansen, W., Winterwerp, J.C., Uijttewaal, W.S.J., 2021. Predictive model of bulk drag coefficient for a nature-based structure exposed to currents. *Sci Rep* 11, 3517.
<https://doi.org/10.1038/s41598-021-83035-0>

- Griffith, B.E., Patankar, N.A., 2020. Immersed Methods for Fluid–Structure Interaction. *Annual Review of Fluid Mechanics* 52, 421–448. <https://doi.org/10.1146/annurev-fluid-010719-060228>
- Guo, Y.C., Mohapatra, S.C., Guedes Soares, C., 2020. Review of developments in porous membranes and net-type structures for breakwaters and fish cages. *Ocean Engineering* 200, 107027. <https://doi.org/10.1016/j.oceaneng.2020.107027>
- Gutiérrez-Romero, J.E., Lorente-López, A.J., Zamora-Parra, B., 2020. Numerical analysis of fish farm behaviour in real operational conditions. *Ships and Offshore Structures* 15, 737–752. <https://doi.org/10.1080/17445302.2019.1671674>
- Guyonnet, B., Grall, J., Vincent, B., 2008. Modified otter trawl legs to reduce damage and mortality of benthic organisms in North East Atlantic fisheries (Bay of Biscay). *Journal of Marine Systems, Oceanography of the Bay of Biscay* 72, 2–16. <https://doi.org/10.1016/j.jmarsys.2007.05.017>
- Halwart, M., Soto, D., Arthur, J.R. (Eds.), 2007. *Cage aquaculture: regional reviews and global overview*, FAO fisheries technical paper. FAO, Rome.
- Hilber, H.M., Hughes, T.J.R., Taylor, R.L., 1977. Improved numerical dissipation for time integration algorithms in structural dynamics. *Earthquake Engineering & Structural Dynamics* 5, 283–292. <https://doi.org/10.1002/eqe.4290050306>
- Holen, S.M., Yang, X., Utne, I.B., Haugen, S., 2019. Major accidents in Norwegian fish farming. *Safety Science* 120, 32–43. <https://doi.org/10.1016/j.ssci.2019.05.036>
- Høyli, R., 2016. *Assessing the Risk of Escape from Marine Fish Farms - Improving Data Collection Strategies and Development of Risk Indicators* (Master Thesis). UiT The Arctic University of Norway, Tromsø, Norway.

- Huang, C.-C., Tang, H.-J., Liu, J.-Y., 2007. Modelling volume deformation in gravity-type cages with distributed bottom weights or a rigid tube-sinker. *Aquacultural Engineering* 37, 144–157.
<https://doi.org/10.1016/j.aquaeng.2007.04.003>
- Huang, C.-C., Tang, H.-J., Liu, J.-Y., 2006. Dynamical analysis of net cage structures for marine aquaculture: Numerical simulation and model testing. *Aquacultural Engineering* 35, 258–270.
<https://doi.org/10.1016/j.aquaeng.2006.03.003>
- Huang, L., Li, Y., Ni, Y., Cheng, H., Wang, X., Wang, G., Zhao, F., 2019. Study on the Influence of Mesh Grouping on Numerical Simulation Results of Fish Cages. Presented at the ASME 2019 38th International Conference on Ocean, Offshore and Arctic Engineering, American Society of Mechanical Engineers Digital Collection. <https://doi.org/10.1115/OMAE2019-95706>
- Huang, X.-H., Liu, H.-Y., Hu, Y., Yuan, T.-P., Tao, Q.-Y., Wang, S.-M., Liu, Z.-X., 2020. Hydrodynamic performance of a semi-submersible offshore fish farm with a single point mooring system in pure waves and current. *Aquacultural Engineering* 90, 102075.
<https://doi.org/10.1016/j.aquaeng.2020.102075>
- Huguenin, J.E., 1997. The design, operations and economics of cage culture systems. *Aquacultural Engineering* 16, 167–203.
[https://doi.org/10.1016/S0144-8609\(96\)01018-7](https://doi.org/10.1016/S0144-8609(96)01018-7)
- Hvas, M., Folkedal, O., Oppedal, F., 2021. Fish welfare in offshore salmon aquaculture. *Rev. Aquacult.* 13, 836–852.
<https://doi.org/10.1111/raq.12501>
- Jensen, B., Jacobsen, N.G., Christensen, E.D., 2014. Investigations on the porous media equations and resistance coefficients for coastal structures. *Coastal Engineering* 84, 56–72.
<https://doi.org/10.1016/j.coastaleng.2013.11.004>

- Jiang, C., Yao, J.-Y., Zhang, Z.-Q., Gao, G.-J., Liu, G.R., 2018. A sharp-interface immersed smoothed finite element method for interactions between incompressible flows and large deformation solids. *Computer Methods in Applied Mechanics and Engineering* 340, 24–53. <https://doi.org/10.1016/j.cma.2018.04.032>
- Jin, J., Su, B., Dou, R., Luan, C., Li, L., Nygaard, I., Fonseca, N., Gao, Z., 2021. Numerical modelling of hydrodynamic responses of Ocean Farm 1 in waves and current and validation against model test measurements. *Marine Structures* 78, 103017. <https://doi.org/10.1016/j.marstruc.2021.103017>
- Johannesen, Á., Patursson, Ø., Kristmundsson, J., Dam, S.P., Mulelid, M., Klebert, P., 2021. Waves and currents decrease the available space in a salmon cage (preprint). *Animal Behavior and Cognition*. <https://doi.org/10.1101/2021.07.23.453560>
- Johansen, V., 2007. Modelling of flexible slender systems for real-time simulation and control applications (Doctoral thesis). Norwegian University of Science and Technology, Trondheim, Norway.
- Jones, W.P., Launder, B.E., 1972. The prediction of laminarization with a two-equation model of turbulence. *International Journal of Heat and Mass Transfer* 15, 301–314. [https://doi.org/10.1016/0017-9310\(72\)90076-2](https://doi.org/10.1016/0017-9310(72)90076-2)
- Jónsdóttir, K.E., Hvas, M., Alfredsen, J.A., Føre, M., Alver, M.O., Bjelland, H.V., Oppedal, F., 2019. Fish welfare based classification method of ocean current speeds at aquaculture sites. *Aquaculture Environment Interactions* 11, 249–261. <https://doi.org/10.3354/aei00310>
- Kajishima, T., Taira, K., 2017. *Computational Fluid Dynamics*. Springer International Publishing, Cham. <https://doi.org/10.1007/978-3-319-45304-0>

- Kebede, G.E., Winger, P.D., DeLouche, H., Legge, G., Cheng, Z., Kelly, D., Einarsson, H., 2020. Flume tank evaluation of the hydrodynamic lift and drag of helix ropes compared to conventional ropes used in midwater trawls. *Ocean Engineering* 195, 106674. <https://doi.org/10.1016/j.oceaneng.2019.106674>
- Klebert, P., Lader, P., Gansel, L., Oppedal, F., 2013. Hydrodynamic interactions on net panel and aquaculture fish cages: A review. *Ocean Engineering* 58, 260–274. <https://doi.org/10.1016/j.oceaneng.2012.11.006>
- Klebert, P., Su, B., 2020. Turbulence and flow field alterations inside a fish sea cage and its wake. *Applied Ocean Research* 98, 102113. <https://doi.org/10.1016/j.apor.2020.102113>
- Knysh, A., Coyle, J., DeCew, J., Drach, A., Swift, M.R., Tsukrov, I., 2021. Floating protective barriers: evaluation of seaworthiness through physical testing, numerical simulations and field deployment. *Ocean Engineering* 227, 108707. <https://doi.org/10.1016/j.oceaneng.2021.108707>
- Knysh, A., Tsukrov, I., Chambers, M., Swift, M.R., Sullivan, C., Drach, A., 2020. Numerical modelling of submerged mussel longlines with protective sleeves. *Aquacultural Engineering* 88, 102027. <https://doi.org/10.1016/j.aquaeng.2019.102027>
- Kollmannsberger, S., Geller, S., Düster, A., Tölke, J., Sorger, C., Krafczyk, M., Rank, E., 2009. Fixed-grid fluid–structure interaction in two dimensions based on a partitioned Lattice Boltzmann and p-FEM approach. *International Journal for Numerical Methods in Engineering* 79, 817–845. <https://doi.org/10.1002/nme.2581>
- Kristiansen, T., 2013. A Numerical Parameter Study on Current Forces on Circular Aquaculture Net Cages. Presented at the ASME 2013 32nd International Conference on Ocean, Offshore and Arctic

- Engineering, American Society of Mechanical Engineers Digital Collection. <https://doi.org/10.1115/OMAE2013-10915>
- Kristiansen, T., Faltinsen, O.M., 2012. Modelling of current loads on aquaculture net cages. *Journal of Fluids and Structures* 34, 218–235. <https://doi.org/10.1016/j.jfluidstructs.2012.04.001>
- Krogstad, P.-Å., Davidson, P.A., 2011. Freely decaying, homogeneous turbulence generated by multi-scale grids. *Journal of Fluid Mechanics* 680, 417–434. <https://doi.org/10.1017/jfm.2011.169>
- Kumar, V., Karnatak, G., 2014. Engineering consideration for cage aquaculture. *IOSR Journal of Engineering* 4, 11–18. <https://doi.org/10.9790/3021-04661118>
- Kurian, T., Fransson, J.H.M., 2009. Grid-generated turbulence revisited. *Fluid Dyn. Res.* 41, 021403. <https://doi.org/10.1088/0169-5983/41/2/021403>
- Lader, P., Dempster, T., Fredheim, A., Jensen, Ø., 2008. Current induced net deformations in full-scale sea-cages for Atlantic salmon (*Salmo salar*). *Aquacultural Engineering* 38, 52–65. <https://doi.org/10.1016/j.aquaeng.2007.11.001>
- Lader, P., Enerhaug, B., Fredheim, A., Klebert, P., Pettersen, B., 2014. Forces on a cruciform/sphere structure in uniform current. *Ocean Engineering* 82, 180–190. <https://doi.org/10.1016/j.oceaneng.2014.03.007>
- Lader, P., Jensen, A., Sveen, J.K., Fredheim, A., Enerhaug, B., Fredriksson, D., 2007a. Experimental investigation of wave forces on net structures. *Applied Ocean Research* 29, 112–127. <https://doi.org/10.1016/j.apor.2007.10.003>
- Lader, P., Olsen, A., Jensen, A., Sveen, J.K., Fredheim, A., Enerhaug, B., 2007b. Experimental investigation of the interaction between waves and net structures—Damping mechanism. *Aquacultural*

- Engineering 37, 100–114.
<https://doi.org/10.1016/j.aquaeng.2007.03.001>
- Lader, P.F., Enerhaug, B., 2005. Experimental Investigation of Forces and Geometry of a Net Cage in Uniform Flow. *IEEE J. Oceanic Eng.* 30, 79–84. <https://doi.org/10.1109/JOE.2004.841390>
- Lader, P.F., Enerhaug, B., Fredheim, A., Krokstad, J., 2003. Modelling of 3D net structures exposed to waves and current. Presented at the Proceedings of the 3rd International Conference on Hydroelasticity in Marine Technology, Department of Engineering Science, The University of Oxford, Oxford, UK.
- Lader, P.F., Fredheim, A., 2006. Dynamic properties of a flexible net sheet in waves and current—A numerical approach. *Aquacultural Engineering* 35, 228–238.
<https://doi.org/10.1016/j.aquaeng.2006.02.002>
- Lader, P.F., Fredheim, A., Lien, E., 2001. Dynamic behaviour of 3D nets exposed to waves and current. Presented at the Proceedings of the 20th International Conference on Offshore Mechanics and Arctic Engineering, Rio de Janeiro, Brazil.
- Laws, E.M., Livesey, J.L., 1978. Flow Through Screens. *Annual Review of Fluid Mechanics* 10, 247–266.
<https://doi.org/10.1146/annurev.fl.10.010178.001335>
- Lee, C.-W., 2002. Dynamic Analysis and Control Technology in a Fishing Gear System. *Fisheries science* 68, 1835–1840.
https://doi.org/10.2331/fishsci.68.sup2_1835
- Lee, C.-W., Kim, Y.-B., Lee, G.-H., Choe, M.-Y., Lee, M.-K., Koo, K.-Y., 2008. Dynamic simulation of a fish cage system subjected to currents and waves. *Ocean Engineering* 35, 1521–1532.
<https://doi.org/10.1016/j.oceaneng.2008.06.009>
- Lee, C.W., Lee, G.H., Choe, M.Y., Song, D.H., Hosseini, S.A., 2010. Dynamic Behavior of a Submersible Fish Cage. Presented at the

- ASME 2009 28th International Conference on Ocean, Offshore and Arctic Engineering, American Society of Mechanical Engineers Digital Collection, pp. 201–206.
<https://doi.org/10.1115/OMAE2009-79328>
- Lee, C.W., Lee, J., Park, S., 2015. Dynamic behavior and deformation analysis of the fish cage system using mass-spring model. *China Ocean Eng* 29, 311–324. <https://doi.org/10.1007/s13344-015-0022-2>
- Lee, C.-W., Lee, Ju-Hee, Cha, B.-J., Kim, H.-Y., Lee, Ji-Hoon, 2005. Physical modelling for underwater flexible systems dynamic simulation. *Ocean Engineering* 32, 331–347.
<https://doi.org/10.1016/j.oceaneng.2004.08.007>
- Lekang, O.-I., 2019. *Aquaculture Engineering*, Third edition. ed. Wiley-Blackwell, Hoboken.
- Lester, S.E., Gentry, R.R., Kappel, C.V., White, C., Gaines, S.D., 2018. Opinion: Offshore aquaculture in the United States: Untapped potential in need of smart policy. *PNAS* 115, 7162–7165.
<https://doi.org/10.1073/pnas.1808737115>
- Li, L., Brusset, M., Ong, M.C., Wu, X., 2020. Numerical Analysis of a Floating Fish Cage With Feeding Systems. Presented at the ASME 2020 39th International Conference on Ocean, Offshore and Arctic Engineering, American Society of Mechanical Engineers Digital Collection. <https://doi.org/10.1115/OMAE2020-18112>
- Li, L., Fu, S., Xu, Y., Wang, J., Yang, J., 2013. Dynamic responses of floating fish cage in waves and current. *Ocean Engineering* 72, 297–303. <https://doi.org/10.1016/j.oceaneng.2013.07.004>
- Li, L., Jiang, Z., Høiland, A.V., Ong, M.C., 2018. Numerical Analysis of a Vessel-Shaped Offshore Fish Farm. *Journal of Offshore Mechanics and Arctic Engineering* 140.
<https://doi.org/10.1115/1.4039131>

- Li, L., Jiang, Z., Ong, M.C., Hu, W., 2019. Design optimization of mooring system: An application to a vessel-shaped offshore fish farm. *Engineering Structures* 197, 109363.
<https://doi.org/10.1016/j.engstruct.2019.109363>
- Li, L., Ong, M.C., 2017. A Preliminary Study of a Rigid Semi-Submersible Fish Farm for Open Seas. Presented at the ASME 2017 36th International Conference on Ocean, Offshore and Arctic Engineering, American Society of Mechanical Engineers Digital Collection. <https://doi.org/10.1115/OMAE2017-61520>
- Li, Y., Zhao, Y., Gui, F., Teng, B., Guan, C., 2006. Numerical analysis of the effects of sinker weight on the hydrodynamics behaviour of gravity cage net in uniform flow. *Journal of Hydrodynamics, Ser. B* 18, 77–83. [https://doi.org/10.1016/S1001-6058\(06\)60034-6](https://doi.org/10.1016/S1001-6058(06)60034-6)
- Li, Y.-C., Zhao, Y.-P., Gui, F.-K., Teng, B., Dong, G.-H., 2006. Numerical simulation of the influences of sinker weight on the deformation and load of net of gravity sea cage in uniform flow. *hyxb* 125–137.
- Little, D.C., Newton, R.W., Beveridge, M.C.M., 2016. Aquaculture: a rapidly growing and significant source of sustainable food? Status, transitions and potential. *Proceedings of the Nutrition Society* 75, 274–286. <https://doi.org/10.1017/S0029665116000665>
- Liu, H.-F., Bi, C.-W., Zhao, Y.-P., 2020. Experimental and numerical study of the hydrodynamic characteristics of a semisubmersible aquaculture facility in waves. *Ocean Engineering* 214, 107714.
<https://doi.org/10.1016/j.oceaneng.2020.107714>
- Liu, H.-Y., Huang, X.-H., Wang, S.-M., Hu, Y., Yuan, T., Guo, G.-X., 2019. Evaluation of the structural strength and failure for floating collar of a single-point mooring fish cage based on finite element method. *Aquacultural Engineering* 85, 32–48.
<https://doi.org/10.1016/j.aquaeng.2018.12.007>

- Løland, G., 1991. Current forces on and flow through fish farms (Doctoral thesis). Norwegian Institute of Technology, Trondheim, Norway.
- Løland, G., Slaattelid, O.H., 1993. NETSIM, PC program for calculation of motion and tension in net cages. MARINTEK Report MT40-F93-0021, Trondheim, Norway.
- Lupandin, A.I., 2005. Effect of Flow Turbulence on Swimming Speed of Fish. *Biol Bull Russ Acad Sci* 32, 461–466.
<https://doi.org/10.1007/s10525-005-0125-z>
- Martin, T., Kamath, A., Bihs, H., 2020. A Lagrangian approach for the coupled simulation of fixed net structures in a Eulerian fluid model. *Journal of Fluids and Structures* 94, 102962.
<https://doi.org/10.1016/j.jfluidstructs.2020.102962>
- Martin, T., Tsarau, A., Bihs, H., 2021. A numerical framework for modelling the dynamics of open ocean aquaculture structures in viscous fluids. *Applied Ocean Research* 106, 102410.
<https://doi.org/10.1016/j.apor.2020.102410>
- Mjåtveit, M.A., Cheng, H., Ong, M.C., Lee, J., 2021. Numerical study of two typical gravity-based fish cages with different dimensions under pure current conditions. *Aquacultural Engineering*.
- Moe, H., Fredheim, A., Hopperstad, O.S., 2010. Structural analysis of aquaculture net cages in current. *Journal of Fluids and Structures* 26, 503–516. <https://doi.org/10.1016/j.jfluidstructs.2010.01.007>
- Moe-Føre, H., Christian Endresen, P., Gunnar Aarsæther, K., Jensen, J., Føre, M., Kristiansen, D., Fredheim, A., Lader, P., Reite, K.-J., 2015. Structural Analysis of Aquaculture Nets: Comparison and Validation of Different Numerical Modelling Approaches. *Journal of Offshore Mechanics and Arctic Engineering* 137.
<https://doi.org/10.1115/1.4030255>

- Moe-Føre, H., Lader, P.F., Lien, E., Hopperstad, O.S., 2016. Structural response of high solidity net cage models in uniform flow. *Journal of Fluids and Structures* 65, 180–195.
<https://doi.org/10.1016/j.jfluidstructs.2016.05.013>
- Moe-Føre, H., Thorvaldsen, T., 2021. Causal analysis of escape of Atlantic salmon and rainbow trout from Norwegian fish farms during 2010–2018. *Aquaculture* 532, 736002.
<https://doi.org/10.1016/j.aquaculture.2020.736002>
- Moe-Føre, H., Thorvaldsen, T., Astrid, B., Eivind, L., Fagertun, J.T., 2019. Tekniske årsaker til rømming av oppdrettslaks og regnbueørret for perioden 2014–2018. SINTEF Ocean AS.
- Moore, G.E., 1968. Cramming more components onto integrated circuits. *IEEE Solid-State Circuits Society Newsletter* 38, 114.
<https://doi.org/10.1109/N-SSC.2006.4785860>
- Morison, J.R., Johnson, J.W., Schaaf, S.A., 1950. The Force Exerted by Surface Waves on Piles. *Journal of Petroleum Technology* 2, 149–154. <https://doi.org/10.2118/950149-G>
- Morro, B., Davidson, K., Adams, T.P., Falconer, L., Holloway, M., Dale, A., Aleynik, D., Thies, P.R., Khalid, F., Hardwick, J., Smith, H., Gillibrand, P.A., Rey-Planellas, S., 2021. Offshore aquaculture of finfish: Big expectations at sea. *Rev Aquac raq*.12625.
<https://doi.org/10.1111/raq.12625>
- Næss, A., Moan, T., 2013. *Stochastic dynamics of marine structures*. Cambridge University Press, New York, NY.
- Naylor, R.L., Goldberg, R.J., Primavera, J.H., Kautsky, N., Beveridge, M.C.M., Clay, J., Folke, C., Lubchenco, J., Mooney, H., Troell, M., 2000. Effect of aquaculture on world fish supplies. *Nature* 405, 1017–1024. <https://doi.org/10.1038/35016500>
- Naylor, R.L., Hardy, R.W., Buschmann, A.H., Bush, S.R., Cao, L., Klinger, D.H., Little, D.C., Lubchenco, J., Shumway, S.E., Troell,

- M., 2021. A 20-year retrospective review of global aquaculture. *Nature* 591, 551–563. <https://doi.org/10.1038/s41586-021-03308-6>
- Nilsen, A., 2019. Production of Atlantic salmon (*Salmo salar*) in closed confinement systems (CCS) : salmon lice, growth rates, mortality and fish welfare. Norwegian University of Life Sciences, Ås.
- Nordlaks Produkter AS, 2020. Transport of Hav Farm. URL <https://www.nordlaks.no/nyheter-fra-nordlaks/2020/5/28/mediekit-transport-av-havfarmen>
- Norway Royal Salmon ASA, 2017. Arctic Offshore Farming. URL <https://www.arcticoffshorefarming.no/>
- Norwegian Directorate of Fisheries, 2005. Aquaculture Act [WWW Document]. URL <http://fiskeridir.no/English/Aquaculture/Aquaculture-Act> (accessed 11.22.20).
- Okereke, M., Keates, S., 2018. Finite element applications: a practical guide to the FEM process.
- Oldham, T., Oppedal, F., Dempster, T., 2018. Cage size affects dissolved oxygen distribution in salmon aquaculture. *Aquaculture Environment Interactions* 10, 149–156. <https://doi.org/10.3354/aei00263>
- O’Neill, F.G., 2006. Source models of flow through and around screens and gauzes. *Ocean Engineering* 33, 1884–1895. <https://doi.org/10.1016/j.oceaneng.2005.10.009>
- Oppedal, F., Dempster, T., Stien, L.H., 2011. Environmental drivers of Atlantic salmon behaviour in sea-cages: A review. *Aquaculture* 311, 1–18. <https://doi.org/10.1016/j.aquaculture.2010.11.020>
- Park, S., Lee, J., Lee, C.-W., 2021. Design evaluation of a fish cage mooring system with different bridle line connections using model experiments and simulations. *Aquacultural Engineering* 94, 102177. <https://doi.org/10.1016/j.aquaeng.2021.102177>

- Patursson, Ø., 2008. Flow Through and Around Fish Farming Nets. University of New Hampshire, Durham, USA.
- Patursson, Ø., Swift, M.R., Tsukrov, I., Simonsen, K., Baldwin, K., Fredriksson, D.W., Celikkol, B., 2010. Development of a porous media model with application to flow through and around a net panel. *Ocean Engineering* 37, 314–324.
<https://doi.org/10.1016/j.oceaneng.2009.10.001>
- Pepona, M., Favier, J., 2016. A coupled Immersed Boundary – Lattice Boltzmann method for incompressible flows through moving porous media A coupled Immersed Boundary -Lattice Boltzmann method for incompressible flows through moving porous media. *Journal of Computational Physics* 321, 1170–1184.
<https://doi.org/10.1016/j.jcp.2016.06.026>
- Peskin, C.S., 1972. Flow patterns around heart valves: A numerical method. *Journal of Computational Physics* 10, 252–271.
[https://doi.org/10.1016/0021-9991\(72\)90065-4](https://doi.org/10.1016/0021-9991(72)90065-4)
- Piperno, S., Farhat, C., 2001. Partitioned procedures for the transient solution of coupled aeroelastic problems - part II: Energy transfer analysis and three-dimensional applications. *Computer Methods in Applied Mechanics and Engineering* 190, 3147–3170.
[https://doi.org/10.1016/S0045-7825\(00\)00386-8](https://doi.org/10.1016/S0045-7825(00)00386-8)
- Priour, D., 2014. Modelling axisymmetric codends made of hexagonal mesh types. *Ocean Engineering* 92, 1–11.
<https://doi.org/10.1016/j.oceaneng.2014.09.037>
- Priour, D., 2013. A Finite Element Method for Netting: Application to fish cages and fishing gear, 1st ed. 2013. ed. Springer Netherlands, Dordrecht. <https://doi.org/10.1007/978-94-007-6844-4>
- Priour, D., 2005. FEM modelling of flexible structures made of cables, bars and nets, in: *Maritime Transportation and Exploitation of Ocean and Coastal Resources*.

- Priour, D., 1999. Calculation of net shapes by the finite element method with triangular elements. *Communications in Numerical Methods in Engineering* 15, 755–763. [https://doi.org/10.1002/\(SICI\)1099-0887\(199910\)15:10<755::AID-CNM299>3.0.CO;2-M](https://doi.org/10.1002/(SICI)1099-0887(199910)15:10<755::AID-CNM299>3.0.CO;2-M)
- Provot, X., 1995. Deformation Constraints in a Mass-Spring Model to Describe Rigid Cloth Behavior. undefined.
- Puvanendran, V., Mortensen, A., Johansen, L., Kettunen, A., Hansen, Ø.J., Henriksen, E., Heide, M., 2021. Development of cod farming in Norway: Past and current biological and market status and future prospects and directions. *Rev Aquacult* raq.12599. <https://doi.org/10.1111/raq.12599>
- Qu, X., Hu, F., Kumazawa, T., Takeuchi, Y., Dong, S., Shiode, D., Tokai, T., 2019. Deformation and drag force of model square fish cages in a uniform flow. *Ocean Engineering* 171, 619–624. <https://doi.org/10.1016/j.oceaneng.2018.12.016>
- Reite, K.-J., Føre, M., Aarsæther, K.G., Jensen, J., Rundtop, P., Kyllingstad, L.T., Endresen, P.C., Kristiansen, D., Johansen, V., Fredheim, A., 2014. FHSIM — Time Domain Simulation of Marine Systems. Presented at the ASME 2014 33rd International Conference on Ocean, Offshore and Arctic Engineering, American Society of Mechanical Engineers Digital Collection, San Francisco, California, USA. <https://doi.org/10.1115/OMAE2014-23165>
- Reynolds, A.J., 1969. Flow Deflection by Gauze Screens. *Journal of Mechanical Engineering Science* 11, 290–294. https://doi.org/10.1243/JMES_JOUR_1969_011_036_02
- Rickard, G., 2020. Three-dimensional hydrodynamic modelling of tidal flows interacting with aquaculture fish cages. *Journal of Fluids and Structures* 93, 102871. <https://doi.org/10.1016/j.jfluidstructs.2020.102871>

- Robertson, E., Choudhury, V., Bhushan, S., Walters, D.K., 2015. Validation of OpenFOAM numerical methods and turbulence models for incompressible bluff body flows. *Computers & Fluids* 123, 122–145. <https://doi.org/10.1016/j.compfluid.2015.09.010>
- Roelofs, F., Shams, A., 2019. “CFD—Introduction,” in: Roelofs, Ferry (Ed.), *Thermal Hydraulics Aspects of Liquid Metal Cooled Nuclear Reactors*. Woodhead Publishing, pp. 213–218. <https://doi.org/10.1016/B978-0-08-101980-1.00006-5>
- Ruzzo, C., Muggiasca, S., Malara, G., Taruffi, F., Belloli, M., Collu, M., Li, L., Brizzi, G., Arena, F., 2021. Scaling strategies for multi-purpose floating structures physical modelling: state of art and new perspectives. *Applied Ocean Research* 108, 102487. <https://doi.org/10.1016/j.apor.2020.102487>
- SalMar ASA, 2021. Salmar Gallery. URL <https://www.salmar.no/en/gallery/>
- Schubel, J.R., Thompson, K., 2019. Farming the Sea: The Only Way to Meet Humanity’s Future Food Needs. *GeoHealth* 3, 238–244. <https://doi.org/10.1029/2019GH000204>
- Shainee, M., Ellingsen, H., Leira, B.J., Fredheim, A., 2013. Design theory in offshore fish cage designing. *Aquaculture* 392–395, 134–141. <https://doi.org/10.1016/j.aquaculture.2013.02.016>
- Shainee, Mohamed, Leira, B.J., Ellingsen, H., Fredheim, A., 2013. An Optimum Design Concept for Offshore Cage Culture. Presented at the ASME 2012 31st International Conference on Ocean, Offshore and Arctic Engineering, American Society of Mechanical Engineers Digital Collection, pp. 85–93. <https://doi.org/10.1115/OMAE2012-83601>
- Shen, Y., Greco, M., Faltinsen, O.M., 2019a. Numerical study of a well boat operating at a fish farm in current. *Journal of Fluids and*

- Structures 84, 77–96.
<https://doi.org/10.1016/j.jfluidstructs.2018.10.006>
- Shen, Y., Greco, M., Faltinsen, O.M., 2019b. Numerical study of a well boat operating at a fish farm in long-crested irregular waves and current. *Journal of Fluids and Structures* 84, 97–121.
<https://doi.org/10.1016/j.jfluidstructs.2018.10.007>
- Shen, Y., Greco, M., Faltinsen, O.M., Nygaard, I., 2018. Numerical and experimental investigations on mooring loads of a marine fish farm in waves and current. *Journal of Fluids and Structures* 79, 115–136. <https://doi.org/10.1016/j.jfluidstructs.2018.02.004>
- Shimizu, H., Mizukami, Y., Kitazawa, D., 2018. Experimental study of the drag on fine-mesh netting. *Aquacultural Engineering* 81, 101–106. <https://doi.org/10.1016/j.aquaeng.2018.03.005>
- Shimizu, T., Takagi, T., Korte, H., Hiraishi, T., Yamamoto, K., 2007. Application of NaLA, a fishing net configuration and loading analysis system, to bottom gill nets. *Fish Sci* 73, 489–499.
<https://doi.org/10.1111/j.1444-2906.2007.01361.x>
- Sievers, M., Korsøen, Ø., Warren-Myers, F., Oppedal, F., Macaulay, G., Folkedal, O., Dempster, T., 2021. Submerged cage aquaculture of marine fish: A review of the biological challenges and opportunities. *Rev Aquacult* raq.12587.
<https://doi.org/10.1111/raq.12587>
- Sim, J., Cheng, H., Aarsæther, K.G., Li, L., Ong, M.C., 2021. Numerical Investigation on the Cage-to-Cage Wake Effect: A Case Study of a 4×2 Cage Array. *Journal of Offshore Mechanics and Arctic Engineering* 143, 051301.
<https://doi.org/10.1115/1.4049831>
- Simonsen, K., Tsukrov, I., Baldwin, K., Swift, M.R., Patursson, O.E., Simonsen, K., Tsukrov, I., Baldwin, K., Swift, M.R., Patursson, O.E., 2006. Modelling Flow Through and Around a Net Panel

- Using Computational Fluid Dynamics, in: OCEANS 2006. Presented at the OCEANS 2006, pp. 1–5.
<https://doi.org/10.1109/OCEANS.2006.306909>
- Skjong, S., Reite, K.J., Aarsæther, K.G., 2021. Lumped, Constrained Cable Modelling With Explicit State-Space Formulation Using An Elastic Version of Baumgarte Stabilization. *Journal of Offshore Mechanics and Arctic Engineering* 143.
<https://doi.org/10.1115/1.4050422>
- Skøien, K.R., 2017. Feed Distribution in Large Scale Sea Cage Aquaculture: Experiments, modelling and simulation. Norwegian University of Science and Technology, Trondheim, Norway.
- Standards Norway, 2009. NS 9415 marine fish farms—requirements for design. In: *Dimensioning, Production, Installation and Operation*.
- Statistics Norway, 2020. Aquaculture [WWW Document]. URL <https://www.ssb.no/en/jord-skog-jakt-og-fiskeri/statistikker/fiskeoppdrett/aar/2020-10-29> (accessed 11.22.20).
- Su, B., Reite, K.-J., Føre, M., Aarsæther, K.G., Alver, M.O., Endresen, P.C., Kristiansen, D., Haugen, J., Caharija, W., Tsarau, A., 2019. A Multipurpose Framework for Modelling and Simulation of Marine Aquaculture Systems. Presented at the ASME 2019 38th International Conference on Ocean, Offshore and Arctic Engineering, American Society of Mechanical Engineers Digital Collection, Glasgow, Scotland, UK.
<https://doi.org/10.1115/OMAE2019-95414>
- Su, B., Tsarau, A., Endresen, P.C., Kristiansen, D., Lader, P.F., 2021. Numerical study of closed rigid fish cages in waves and comparison with experimental data. *Ocean Engineering* 233, 109210. <https://doi.org/10.1016/j.oceaneng.2021.109210>

- Suzuki, K., Takagi, T., Shimizu, T., Hiraishi, T., Yamamoto, K., Nashimoto, K., 2003. Validity and visualization of a numerical model used to determine dynamic configurations of fishing nets. *Fisheries science* 69, 695–705. <https://doi.org/10.1046/j.1444-2906.2003.00676.x>
- Takagi, T., Miyata, S., Fusejima, I., Oshima, T., Uehara, T., Suzuki, K., Nomura, Y., Kanechiku, M., Torisawa, S., 2014. Effect of Mesh Size on Sinking Characteristics of Purse Seine Net. *Journal of Fisheries Engineering* 51, 11–19. https://doi.org/10.18903/fisheng.51.1_11
- Takagi, T., Shimizu, T., Suzuki, K., Hiraishi, T., Yamamoto, K., 2004. Validity and layout of “NaLA”: a net configuration and loading analysis system. *Fisheries Research* 66, 235–243. [https://doi.org/10.1016/S0165-7836\(03\)00204-2](https://doi.org/10.1016/S0165-7836(03)00204-2)
- Takagi, T., Suzuki, K., Hiraishi, T., 2002. Modelling of net for calculation method of dynamic fishing net shape. *Fisheries science* 68, 1857–1860. https://doi.org/10.2331/fishsci.68.sup2_1857
- Tang, H., Hu, F., Xu, L., Dong, S., Zhou, C., Wang, X., 2019. Variations in hydrodynamic characteristics of netting panels with various twine materials, knot types, and weave patterns at small attack angles. *Sci Rep* 9, 1923. <https://doi.org/10.1038/s41598-018-35907-1>
- Tang, H., Xu, L., Hu, F., 2018a. Hydrodynamic characteristics of knotted and knotless purse seine netting panels as determined in a flume tank. *PLOS ONE* 13, e0192206. <https://doi.org/10.1371/journal.pone.0192206>
- Tang, H.-J., Yang, R.-Y., Huang, C.-C., 2019. Numerical Modelling of the Mooring Line Failure Induced Performance Changes of a Marine Fish Cage in Irregular Waves and Currents. Presented at the ASME 2019 38th International Conference on Ocean, Offshore and Arctic Engineering, American Society of Mechanical

- Engineers Digital Collection. <https://doi.org/10.1115/OMAE2019-95730>
- Tang, H.-J., Yeh, P.-H., Huang, C.-C., Yang, R.-Y., 2020. Numerical study of the mooring system failure of aquaculture net cages under irregular waves and current. *Ocean Engineering* 216, 108110. <https://doi.org/10.1016/j.oceaneng.2020.108110>
- Tang, M.-F., Dong, G.-H., Xu, T.-J., Zhao, Y.-P., Bi, C.-W., Guo, W.-J., 2018b. Experimental analysis of the hydrodynamic coefficients of net panels in current. *Applied Ocean Research* 79, 253–261. <https://doi.org/10.1016/j.apor.2018.08.009>
- Theret, F., 1993. Etude de l'équilibre de surfaces réticulées placées dans le courant uniforme. Application aux chaluts. Université de Nantes.
- Thorvaldsen, T., Holmen, I.M., Moe, H.K., 2015. The escape of fish from Norwegian fish farms: Causes, risks and the influence of organisational aspects. *Marine Policy* 55, 33–38. <https://doi.org/10.1016/j.marpol.2015.01.008>
- Thorvaldsen, T., Moe Føre, H., Tinmannsvik, R.K., Okstad, E.H., 2018. Menneskelige og organisatoriske årsaker til rømming av oppdrettslaks og regnbueørret (SINTEF Report).
- Tsukrov, I., Drach, A., DeCew, J., Robinson Swift, M., Celikkol, B., 2011. Characterization of geometry and normal drag coefficients of copper nets. *Ocean Engineering* 38, 1979–1988. <https://doi.org/10.1016/j.oceaneng.2011.09.019>
- Tsukrov, I., Eroshkin, O., Fredriksson, D., Swift, M.R., Celikkol, B., 2003. Finite element modelling of net panels using a consistent net element. *Ocean Engineering* 30, 251–270. [https://doi.org/10.1016/S0029-8018\(02\)00021-5](https://doi.org/10.1016/S0029-8018(02)00021-5)
- Turner, A.A., Jeans, T.L., Reid, G.K., 2016. Experimental Investigation of Fish Farm Hydrodynamics on 1:15 Scale Model Square

- Aquaculture Cages. *Journal of Offshore Mechanics and Arctic Engineering* 138. <https://doi.org/10.1115/1.4034176>
- Turner, A.A., Jeans, T.L., Reid, G.K., 2015. Experimental Investigation of Fish Farm Hydrodynamic Wake Properties on 1:15 Scale Model Circular Aquaculture Cages. Presented at the ASME 2015 34th International Conference on Ocean, Offshore and Arctic Engineering, American Society of Mechanical Engineers Digital Collection. <https://doi.org/10.1115/OMAE2015-42140>
- Turner, A.A., Steinke, D.M., Nicoll, R.S., 2017. Application of Wake Shielding Effects With a Finite Element Net Model in Determining Hydrodynamic Loading on Aquaculture Net Pens. Presented at the ASME 2017 36th International Conference on Ocean, Offshore and Arctic Engineering, American Society of Mechanical Engineers Digital Collection. <https://doi.org/10.1115/OMAE2017-61330>
- van Doorn, E., White, C.M., Sreenivasan, K.R., 1999. The decay of grid turbulence in polymer and surfactant solutions. *Physics of Fluids* 11, 2387–2393. <https://doi.org/10.1063/1.870100>
- Vassilicos, J.C., 2015. Dissipation in Turbulent Flows. *Annu. Rev. Fluid Mech.* 47, 95–114. <https://doi.org/10.1146/annurev-fluid-010814-014637>
- Vincent, B., 1999. A new generation of tools for trawls Dynamic numerical simulation, in: DEMaT '99 - Fourth International Workshop on Methods for the Development and Evaluation of Maritime Technologies. Rostock.
- Wan, R., Guan, Q., Li, Z., Hu, F., Dong, S., You, X., 2020. Study on hydrodynamic performance of a set-net in current based on numerical simulation and physical model test. *Ocean Engineering* 195, 106660. <https://doi.org/10.1016/j.oceaneng.2019.106660>

- Wang, D., Zhang, D., Wang, S., Ge, S., 2013. Finite element analysis of hoisting rope and fretting wear evolution and fatigue life estimation of steel wires. *Engineering Failure Analysis* 27, 173–193. <https://doi.org/10.1016/j.engfailanal.2012.08.014>
- Wang, G., Martin, T., Huang, L., Bihs, H., 2021a. Modelling the flow around and wake behind net panels using large eddy simulations. *Ocean Engineering* 239, 109846. <https://doi.org/10.1016/j.oceaneng.2021.109846>
- Wang, G., Martin, T., Huang, L., Bihs, H., 2021b. A Numerical Study of the Hydrodynamics of an Offshore Fish Farm Using REEF3D. *Journal of Offshore Mechanics and Arctic Engineering* 144. <https://doi.org/10.1115/1.4052865>
- Wang, S., Zhang, G., Zhang, Z., Hui, D., Zong, Z., 2017. An immersed smoothed point interpolation method (IS-PIM) for fluid-structure interaction problems. *International Journal for Numerical Methods in Fluids* 85, 213–234. <https://doi.org/10.1002/flid.4379>
- Wang, X., Wan, R., Zhao, F., Huang, L., Sun, P., Tang, Y., 2016. Comparative Study of Dynamics of Gravity Cages With Different Meshes in Waves and Current. Presented at the ASME 2016 35th International Conference on Ocean, Offshore and Arctic Engineering, American Society of Mechanical Engineers Digital Collection. <https://doi.org/10.1115/OMAE2016-54549>
- Wang, X., Zhang, L.T., 2009. Interpolation functions in the immersed boundary and finite element methods. *Comput Mech* 45, 321. <https://doi.org/10.1007/s00466-009-0449-5>
- Wanzefeng Fisheries, 2018. Salmon farming. URL <http://www.wanzefeng.com/product/sanwenyuyangzhi/>
- Winthereig-Rasmussen, H., Simonsen, K., Patursson, Ø., 2016. Flow through fish farming sea cages: Comparing computational fluid dynamics simulations with scaled and full-scale experimental data.

- Ocean Engineering 124, 21–31.
<https://doi.org/10.1016/j.oceaneng.2016.07.027>
- Xu, Z., Qin, H., 2020. Fluid-structure interactions of cage based aquaculture: From structures to organisms. Ocean Engineering 217, 107961. <https://doi.org/10.1016/j.oceaneng.2020.107961>
- Yan, B., Wang, S., Zhang, G., Jiang, C., Xiao, Q., Sun, Z., 2020. A sharp-interface immersed smoothed point interpolation method with improved mass conservation for fluid-structure interaction problems. J Hydrodyn 32, 267–285.
<https://doi.org/10.1007/s42241-020-0025-1>
- Yang, R.-Y., Tang, H.-J., Huang, C.-C., 2020. Numerical Modelling of the Mooring System Failure of an Aquaculture Net Cage System Under Waves and Currents. IEEE J. Oceanic Eng. 45, 1396–1410.
<https://doi.org/10.1109/JOE.2019.2941768>
- Yang, X., Utne, I.B., Holmen, I.M., 2020a. Methodology for hazard identification in aquaculture operations (MHIAO). Safety Science 121, 430–450. <https://doi.org/10.1016/j.ssci.2019.09.021>
- Yang, X., Utne, I.B., Sandøy, S.S., Ramos, M.A., Rokseth, B., 2020b. A systems-theoretic approach to hazard identification of marine systems with dynamic autonomy. Ocean Engineering 217, 107930.
<https://doi.org/10.1016/j.oceaneng.2020.107930>
- Yao, Y., Chen, Y., Zhou, H., Yang, H., 2016. Numerical modelling of current loads on a net cage considering fluid–structure interaction. Journal of Fluids and Structures 62, 350–366.
<https://doi.org/10.1016/j.jfluidstructs.2016.01.004>
- Zhao, F., Kinoshita, T., Bao, W., Wan, R., Liang, Z., Huang, L., 2011. Hydrodynamics identities and wave-drift force of a porous body. Applied Ocean Research 3, 169–177.
<https://doi.org/10.1016/j.apor.2011.04.001>

- Zhao, Y., Guan, C., Bi, C., Liu, H., Cui, Y., 2019. Experimental Investigations on Hydrodynamic Responses of a Semi-Submersible Offshore Fish Farm in Waves. *Journal of Marine Science and Engineering* 7, 238. <https://doi.org/10.3390/jmse7070238>
- Zhao, Y.-P., Bi, C.-W., Chen, C.-P., Li, Y.-C., Dong, G.-H., 2015a. Experimental study on flow velocity and mooring loads for multiple net cages in steady current. *Aquacultural Engineering* 67, 24–31. <https://doi.org/10.1016/j.aquaeng.2015.05.005>
- Zhao, Y.-P., Bi, C.-W., Dong, G.-H., Gui, F.-K., Cui, Y., Guan, C.-T., Xu, T.-J., 2013a. Numerical simulation of the flow around fishing plane nets using the porous media model. *Ocean Engineering* 62, 25–37. <https://doi.org/10.1016/j.oceaneng.2013.01.009>
- Zhao, Y.-P., Bi, C.-W., Dong, G.-H., Gui, F.-K., Cui, Y., Xu, T.-J., 2013b. Numerical simulation of the flow field inside and around gravity cages. *Aquacultural Engineering* 52, 1–13. <https://doi.org/10.1016/j.aquaeng.2012.06.001>
- Zhao, Y.-P., Bi, C.-W., Sun, X.-X., Dong, G.-H., 2019. A prediction on structural stress and deformation of fish cage in waves using machine-learning method. *Aquacultural Engineering* 85, 15–21. <https://doi.org/10.1016/j.aquaeng.2019.01.003>
- Zhao, Y.-P., Li, Y.-C., Dong, G.-H., Gui, F.-K., Teng, B., 2007a. Numerical simulation of the effects of structure size ratio and mesh type on three-dimensional deformation of the fishing-net gravity cage in current. *Aquacultural Engineering* 36, 285–301. <https://doi.org/10.1016/j.aquaeng.2007.01.003>
- Zhao, Y.-P., Li, Y.-C., Dong, G.-H., Gui, F.-K., Teng, B., 2007b. A numerical study on dynamic properties of the gravity cage in combined wave-current flow. *Ocean Engineering* 34, 2350–2363. <https://doi.org/10.1016/j.oceaneng.2007.05.003>

- Zhao, Y.-P., Li, Y.-C., Gui, F., Dong, G., 2007c. Numerical Simulation of the Effects of Weight System on the Hydrodynamic Behavior of 3-D Net of Gravity Cage in Current. *J Hydrodyn* 19, 442–452. [https://doi.org/10.1016/S1001-6058\(07\)60138-3](https://doi.org/10.1016/S1001-6058(07)60138-3)
- Zhao, Y.-P., Wang, X.-X., Decew, J., Tsukrov, I., Bai, X.-D., Bi, C.-W., 2015b. Comparative study of two approaches to model the offshore fish cages. *China Ocean Eng* 29, 459–472. <https://doi.org/10.1007/s13344-015-0032-0>
- Zhong, W., Li, X., Liu, F., Tao, G., Lu, B., Kagawa, T., 2014. Measurement and Correlation of Pressure Drop Characteristics for Air Flow Through Sintered Metal Porous Media. *Transp Porous Med* 101, 53–67. <https://doi.org/10.1007/s11242-013-0230-2>